The Kaos Spectrometer at the Mainz Microtron and First Measurements of Kaon Electro-Production

Patrick Achenbach

Habilitationsschrift

zur Erlangung der *venia legendi*
im Fach Experimentalphysik
vorgelegt beim
Fachbereich Physik, Mathematik und Informatik
der Johannes Gutenberg-Universität Mainz

2010

Deutsche Zusammenfassung

Experimente zur Photo- und Elektroproduktion von Hadronen am Mainzer Mikrotron MAMI dienen dazu, einen tieferen Einblick in die Niederenergiestruktur der Theorie der starken Wechselwirkung (QCD) zu gewinnen. Seit Dezember 2006 beschleunigt die Stufe MAMI-C Elektronen auf über 1500 MeV Strahlenergie und eröffnet durch die Überschreitung der Energieschwelle für assoziierte Kaonenerzeugung neue Möglichkeiten, Hadronen mit offener Seltsamkeit und ihre Wechselwirkungen in nuklearen Systemen zu studieren.

Die Beschreibung der Anregung des Nukleons in $(e, e'K)$-Reaktionen läßt trotz vorausgegangenen Messungen an auswärtigen Beschleunigern eine Reihe von Fragen offen. So sind zum Beispiel gemessene Wirkungsquerschnitte in kinematischen Regionen, die an MAMI-C zugänglich sind, inkonsistent und verschiedene Modelle des Nukleons sagen grundsätzlich unterschiedliche Amplituden vorher.

Im Rahmen dieser Arbeit wurde die Spektrometeranlage der Kollaboration A1 an MAMI um das von der GSI in Darmstadt übernommene KAOS-Spektrometer erweitert. Dieses Spektrometer dient mit seiner kurzen Bauart insbesondere dem Nachweis von Kaonen. In den Jahren 2002–8 konnte durch umfangreiche Installationen die notwendige Infrastruktur geschaffen und das Spektrometer in Betrieb genommen werden, so dass seit Herbst 2008 erstmals an MAMI die Kaonen-Elektroproduktion studiert wird. Die erreichte Winkel- und Impulsauflösung ist ausreichend, um Λ- und Σ^0-Hyperonen im Spektrum der fehlenden Masse leicht trennen zu können. Für Messungen am Wasserstoff-Target wurden aus den gewonnenen Daten Wirkungsquerschitte extrahiert, um phänomenologische Modelle differenzieren zu können.

In den kommenden Jahren kann mit dem KAOS-Spektrometer auch die kaonassoziierte Produktion von Hyperkernen nachgewiesen werden. Das Studium von Hyperkernen kann Strukturen beleuchten, die in konventioneller Kernmaterie verborgen bleiben, denn für das Hyperon gilt nicht das Pauli-Prinzip der Nukleonen und so kann es auch tief liegende Kernniveaus bevölkern.

Für dieses Programm wurde das Spektrometer mit einem zweiten Arm ausgestattet, in dem knapp 20 000 szintillierende Fasern für eine schnelle Koordinaten- und Zeitmessung in der Bildebene sorgen. Dieses seit dem Jahr 2009 betriebene Instrument gehört weltweit zu den modernsten Bildebenen-Detektoren.

Das mit dem KAOS-Spektrometer an MAMI-C in den letzten Jahren ermöglichte Studium von Systemen mit Seltsamkeit wird auch in Zukunft dem Verständnis der inneren Struktur des Nukleons dienen.

Aus der Wiese

kommt ein Blümlein hervorgesprießt,

zeigt seine Blüten.

Preface

In the cores of stars and the depths of interstellar space, phenomena are observed which, on earth, only occur under artificial circumstances such as created in particle accelerators. A landmark in our understanding of the microscopic world has been the development of the "standard model". Quantum Chromodynamics (QCD) classifies all elementary particles into two categories: leptons, with the electron and electron-neutrino as best-known examples, and quarks, which form the constituents of hadrons such as the proton and the neutron. A firm grasp of these fundamental building blocks is essential to understand the multitude of processes occurring throughout our universe.

Modern theories of the strong interaction would certainly be incomplete if we ignored the necessity to understand hadronic interactions at the mass scale of the proton and its resonances. Due to the non-perturbative nature of QCD at such energies, hadrons are complex systems which cannot be described by the fundamental equations for the dynamics of asymptotically free quarks and gluons.

Instead, hadronic descriptions are common, where the hadrons are treated as effective degrees-of-freedom. These models consider a multitude of mesons and baryons, such as pions, kaons, protons, neutrons, Δ-resonances, Λ-, and Σ-hyperons to be the fundamental objects which interact with one another. The properties of the particles and strengths of the interactions between them are determined by experiments, *e.g.* hadron-hadron scattering, photo-production, radiative capture, electro-production, and the use of symmetry relations like duality, and crossing symmetry between reactions.

The idea of multiple scales in nuclear physics is made clear in the following scheme of a proton and a kaon at different energy, *i.e.* length scales (Fig. from [1]). At low energies, the hadrons can be treated as structureless particles. With increasing energy, part of the substructure of the hadrons is revealed and the concept of constituent quarks turns out to be effective for understanding their major properties like magnetic moments. Upon further decreasing of the length scale, the full QCD dynamics and the partonic nature of hadronic matter in terms of quarks and gluons becomes accessible. Hence, one of the most intriguing areas of nucleon resonance physics is the interface between a hadron description and a quark description.

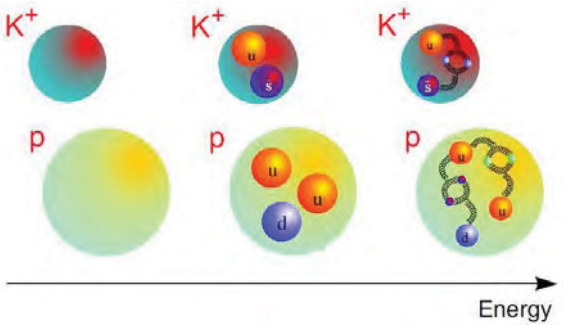

The partonic constituents can also be considered along the lines of chiral models, which take the chiral symmetry of the QCD Lagrangian and its spontaneous breakdown into account. However, practical methods tested in the pion sector like chiral perturbation theory are in general not amenable to strangeness production. Lattice QCD, which is expected to alleviate this problem, has only recently begun to contribute to this field. It is anticipated that this technique will gain importance in hadron physics with increasing pace.

Though, hadronic physics continues to be a challenging field of investigation, especially in the strangeness sector. Electromagnetic reactions with either "open" or "closed" strangeness in the final state are particularly interesting because of the involvement of a strange–antistrange pair. In this work, the focus is on the open strangeness case, particularly the production of a ground-state kaon and hyperon (*i.e.* a baryon with non-zero strangeness, commonly abbreviated as Y) from the proton. Although the largest cross-sections are found in hadronic processes, the use of an electromagnetic probe has a distinct advantage. Indeed, all electromagnetic ingredients in the reaction amplitude can be expressed in the context of quantum electrodynamics or QED, the well-established theory of electromagnetic interactions. The scattering of photons and electrons from nucleons and nuclei constitutes the backbone of the physics programme at the MAMI facility.

Strangeness electrophoto-production is experiencing a renewed interest in its 40-year-old history. Technical and methodical development made it possible that today strange systems can also be produced copiously using electromagnetic processes, and detected in a clean way using magnetic spectrometers in counter experiments. A new era started with the application of high-energy, high-intensity electron beams produced at Jefferson Laboratory, Newport News, and at the Mainz Mikrotron MAMI. These beams are the ideal probes to study the hadronic structure of nuclei and nucleons. The experimental capabilities of both accelerators make them well suited to the task of studying sub-nuclear dynamics in this

energy regime. The electron beams at Jefferson Lab and MAMI are of high intensity, capable of more then 100 μA beam current, with 100 % duty factor. In the experimental halls the facilities utilize high-resolution large-acceptance focusing spectrometers, high-power cryogenic targets, and high-resolution detectors with fast electronics. Magnetic spectrometers with high resolving powers tend to be long, which makes them hard to use for measurements of particles as short-lived as kaons. Consequently, for the detection of kaons dedicated strangeness spectrometers with short particle orbits were developed. These instruments make measurements of fairly low cross-sections possible which lead to improved statistical and systematic errors relative to earlier facilities.

This thesis documents the installation and operation of the spectrometer KAOS at the Mainz Mikrotron during the period 2002–9 and reports on the first kaon electro-production experiments performed at MAMI. The thesis begins with the underlying physics motivation behind the strangeness programme at MAMI. It includes a brief discussion of kaon and hypernuclei electro-production experiments. The following part of the work describes in detail the experimental apparatus used for data-taking. The final part presents an analysis of data from the $p(e,e'K^+)Y$ electro-production reaction in two hyperon channels, $Y = (\Lambda, \Sigma^0)$, taken during the years 2008–9.

The spectrometer was officially inaugurated with a ceremony on 5 June 2009. The event got a broad news coverage in the press and in TV, which was part of the outreach activities that accompanied the project with a first press release on 10 December 2008, *„Neues Instrument zur Untersuchung von Kernreaktionen mit seltsamen Teilchen an MAMI in Betrieb genommen"*, followed a year later by a press invitation on 25 May 2009 *„Einweihung des Magnetspektrometers Kaos"* and the press release on 5 June 2009 *„Ein weiteres Großgerät für die Kernphysik"*.

Since 2002 Prof. J. Pochodzalla shared his responsibility for the supervision of students with me. During the last years 4 diploma theses and 1 doctorate thesis were written on a subject related to the KAOS spectrometer, 2 doctorate students in the group are in their final year, and 2 more students are in the progression of the work. A student from Ljubljana, Slovenia, was advised by me in his diploma work which is continued in his doctorate work. In 2006–7, I was supervising a Danish student during his one-year long research project, comparable to a diploma work. These academic works, compiled in the following list, were a great support to the work presented in this habilitation thesis:

[a] S. Sánchez Majos, *Measurement of $K^+\Lambda$ and $K^+\Sigma^0$ electroproduction cross-sections off the proton at low Q^2 with the Kaos-Spectrometer (prelim. title)*, doctorate thesis, Johannes Gutenberg-Universität, Mainz (to appear in 2011).

[b] C. Ayerbe Gayoso, *Instrumentation of the Kaos spectrometer's electron arm for forward angle*

measurements (prelim. title), doctorate thesis, Johannes Gutenberg-Universität, Mainz (to appear in 2011).

[c] A. Esser, *Teilchennachweis und Spurerkennung mit dem Faserdetektor im Kaos-Spektrometer am Mainzer Mikrotron*, diploma thesis, Johannes Gutenberg-Universität, Mainz (Jan. 2010).

[d] L. Nungesser, *Aufbau und Simulation des Kaos-Spektrometers an MAMI für Koinzidenzmessungen in der assoziierten Kaonproduktion*, doctorate thesis, Johannes Gutenberg-Universität, Mainz (Apr. 2009).

[e] M. Bösz, *Datenerfassung und Spurerkennung mit den Vieldrahtproportionalkammern für das Kaos-Spektrometer an MAMI*, diploma thesis, Johannes Gutenberg-Universität, Mainz (Mar. 2009).

[f] M. Gómez Rodríguez de la Paz, *Strahltest und Betrieb von Vieldrahtproportionalkammern für das Kaos-Spektrometer*, diploma thesis, Johannes Gutenberg-Universität, Mainz (May 2008).

[g] L. Debenjak, *Measurements with scintillating fibres for prototype detectors of the Kaos spectrometer*, diploma thesis, University of Ljubljana, Slovenia (May 2007).

[h] J. Wellendorf Pedersen, *Operation of Multiwire Proportional Chambers for the kaon spectrometer at MAMI*, project thesis, Johannes Gutenberg-Universität, Mainz (Jan. 2007).

[i] C. Ayerbe Gayoso, *Development of a fibre detector for the Kaos spectrometer*, diploma thesis, Johannes Gutenberg-Universität, Mainz (Apr. 2004).

To me, the strangeness physics programme and the technical project of the KAOS spectrometer set-up has formed a symbiosis with a very fruitful outcome. In 2009, after long years of construction and commissioning, the KAOS spectrometer has become the workhorse of the collaboration with several months of production beam-time, prevailing other activities at the spectrometer facility.

For all mistakes, apocryphal contents, and wild inaccuracies in this text I feel fully responsible.

Mainz,
February 2o1o

Patrick Achenbach

During the course of the habilitation process following the submission of the thesis some corrections and updates were included in the text.

CONTENTS

a strange flower
for birds and butterflies
the autumn sky

Matsuo Bashō (1644–94)

1 Strangeness Production

1.1. Introducing Kaons and Hyperons

Strange particles were first observed in 1946 and 1947 by a team at Manchester University in the UK under the direction of Clifford C. Butler [2]. They appeared as a completely unexpected new phenomenon in the study of cosmic rays. Since then, interest in the strangeness degree-of-freedom has remained alive, with investigations covering a broad range of systems from quarks and nuclei to neutron stars.

Butler and George Rochester were examining images of tracks of particles in a cloud chamber shielded by lead plates and immersed in a magnetic field. On 15 October 1946 they found two tracks apparently not connected to any incoming cosmic particle, but curved symmetrically away from each other from their point of origin, showing that the particles had opposite electric charges [3]. Butler and Rochester pointed out that the two particles could have been produced by the decay of a neutral particle and the examination of the tracks suggested that their progenitor had a mass of about half of that of the proton. According to the recorded pattern of the tracks in the chamber they named it the "V"-particle. Today we assume they were the first to detect the decay of the lightest strange meson, called kaon.

The main instruments in use to study particle interactions in the 1940s were cloud chambers and counter arrays, often used in combination with each other and with magnets, and somewhat later nuclear photographic emulsions. The discovery of kaons was only possible because of a strong electromagnet that was built and brought to Manchester by Patrick Blackett [3]. It was the combination of this powerful equipment with the good tracking capability of the cloud chamber that enabled the experimenters to study kaons. In fact, the magnet could not be operated during World War II because of its high coil current.

In the following years positive, negative, and neutral charge states of the kaon

Table 1.1.: Decay modes and branching fractions of charged kaons, extracted from the Review of Particle Physics [4]. The $K^{\pm}$ decays with a mean life of $\tau_K = 12\,\text{ns}$ and a proper decay length of $c\tau_K = 3.71\,\text{m}$.

branching ratio	decay mode
63.5 %	$K^+ \to \mu^+ + \nu$
	$K^- \to \mu^- + \nu$
21 %	$K^+ \to \pi^+ + \pi^0$
	$K^- \to \pi^- + \pi^0$
5.5 %	$K^+ \to \pi^+ + \pi^+ + \pi^-$
	$K^- \to \pi^- + \pi^+ + \pi^-$
4.8 %	$K^+ \to e^+ + \pi^0 + \nu$
	$K^- \to e^- + \pi^0 + \nu$
3.2 %	$K^+ \to \mu^+ + \pi^0 + \nu$
	$K^- \to \mu^- + \pi^0 + \nu$
1.7 %	$K^+ \to \pi^+ + \pi^0 + \pi^0$
	$K^- \to \pi^- + \pi^0 + \pi^0$

were discovered. Their life-time was strangely much longer than expected. It was known that the kaon is created by the strong nuclear force, and it was expected to decay mediated by the same force, which by a consideration of the its range means that it should decay in about 10^{-23} s. The actual half-life is about 10^{15} times longer. Today, we know that kaons are stable against strong and electromagnetic decays, and decay only weakly into two or three pions or into leptons, most often into $\mu^{\pm}$ and the corresponding neutrino. Several decay modes are listed in Table 1.1 in decreasing order of probability. The mass of the charged kaon, $M_{K^{\pm}} = 493.677\,\text{MeV}$, is known with an accuracy of 13 keV [4]. The neutral kaon has a slightly greater mass, $M_{K^0} = 497.61\,\text{MeV}$ [4], and two different decay half-lives: there is a K^0 with a long decay time or K^0_L, and a K^0 with a short decay time or K^0_S. The K^0_L has a decay half-life of 51 ns, about four times longer than that of the charged kaons. The K^0_S has a decay half-life that is much shorter than that of the K^0_L, namely 89 fs. The decay modes of neutral kaons are shown in Table 1.2.

Many more strange particles were found in cloud chamber tracks in the following years, when the experiments were repeated in much higher altitude. In 1951 the Manchester group brought its magnet, weighing 11 tons, and associated equipment up the 2 850 m high Pic du Midi de Bigorre in the French Pyrenees.

Table 1.2.: Decay modes and branching fractions of neutral kaons, extracted from the Review of Particle Physics [4]. The longer living neutral kaon has a decay half-life of 51 ns, the shorter living a decay half-life of 89 fs.

branching ratio	decay mode
21.5 %	$K_L^0 \to \pi^0 + \pi^0 + \pi^0$
19.4 %	$K_L^0 \to \pi^+ + e^- + \nu$
19.4 %	$K_L^0 \to \pi^- + e^+ + \nu$
13.5 %	$K_L^0 \to \pi^+ + \mu^- + \nu$
13.5 %	$K_L^0 \to \pi^- + \mu^+ + \nu$
12.4 %	$K_L^0 \to \pi^+ + \pi^- + \pi^0$
68.6 %	$K_S^0 \to \pi^+ + \pi^-$
31.4 %	$K_S^0 \to \pi^0 + \pi^0$

Simultaneously Carl Anderson and Eugene Cowan made observations on the White Mountain in California. The found tracks were showing the "V"-pattern characteristic of charged particles coming from the decay of a neutral particle. A closer analysis revealed the existence of two different neutral particles producing the tracks. The first one being the neutral kaon, while the other was a more massive neutral particle, which was named Λ. The Λ turned out to have a mass 2 250 times as heavy as the electron and 1.2 times as heavy as the proton. It was the first particle to be found that was heavier than the proton and the neutron, the building blocks of matter, making it the first of the so-called "hyperons" to be discovered. However, at this time the Λ hyperon was known as the V_1^0 characterized by its decay scheme. Like the kaon, the Λ seemed strange, decaying in about 10^{-10} s when it should have decayed in 10^{-23} s. The main decay modes of charged hyperons are purely hadronic with pions and nucleons as the final states. These modes and their branching fractions are listed in Table 1.3. The mass of the Λ hyperon is $M_\Lambda = 1\,115.68\,\text{MeV}$.

In 1952, observations of cosmic ray tracks by the group from the University of Manchester led to the discovery of a new massive negatively charged particle, which featured a two-stage decay process, first decaying to the Λ and a pion, with the Λ decaying in turn to a proton and a pion. The new particle was named the Cascade or Ξ particle. It was another strange particle, with a long decay half-

Table 1.3.: Main decay modes and branching fractions of charged $S = -1$ hyperons, extracted from the Review of Particle Physics [4]. The Λ hyperon has a mean life of $\tau = 2.63 \times 10^{-10}$ s.

branching ratio	decay mode
64 %	$\Lambda \to p + \pi^-$
36 %	$\Lambda \to n + \pi^0$
52 %	$\Sigma^+ \to p + \pi^0$
48 %	$\Sigma^+ \to n + \pi^+$
100 %	$\Sigma^- \to n + \pi^-$

life of about 10^{-10} s, and one of its decay products was itself strange. In 1953, Italian physicists discovered yet another strange, slow-decaying positively-charged particle, about 30 % heavier than the proton. It seemed to be like a "superproton" and was appropriately named with the Greek letter Σ. The discovery of the positively charged Σ led to the discovery of a negatively charged Σ. It is slightly heavier than its positive partner and takes about twice as long to decay, almost exclusively into a neutron and a negative pion. Not too surprisingly, a neutral Σ was found as well. Its mass is between that of the charged states, and it decays much faster, with a half-life of about 10^{-19} s, into a Λ and a γ-ray. The neutral Σ was hard to detect because its direct decay products were both neutral. The $\Sigma^{\pm}$ hyperons have masses of $M_{\Sigma^+} = 1\,189\,\text{MeV}$ and $M_{\Sigma^-} = 1\,197\,\text{MeV}$.

In 1953, Tadao Nakano and Kazuhiko Nishijima in Japan and, independently, Murray Gell-Mann [5] in the USA, gave a definite formulation of the quantum number that was conserved in the production of strange particles, but violated in their decay, called *strangeness*. Four different strange particles were known at that time with their strangeness content described by the new quantum number. The associated production characteristic with its pairs of strange particles of opposite strangeness was confirmed in 1954 using the first proton accelerators that were energetic enough to cross the strange particle energy thresholds. Especially in the analysis of bubble chamber photographs from the Lawrence Berkeley Laboratory it was found that kaons were produced in association with hyperons.

Only few years later the observation of kaon decay modes and the famous τ–θ puzzle led to the discovery of violation of parity, $\mathcal{P}$, and violation of the combined charge-conjugation and parity, $\mathcal{CP}$. These ground breaking findings

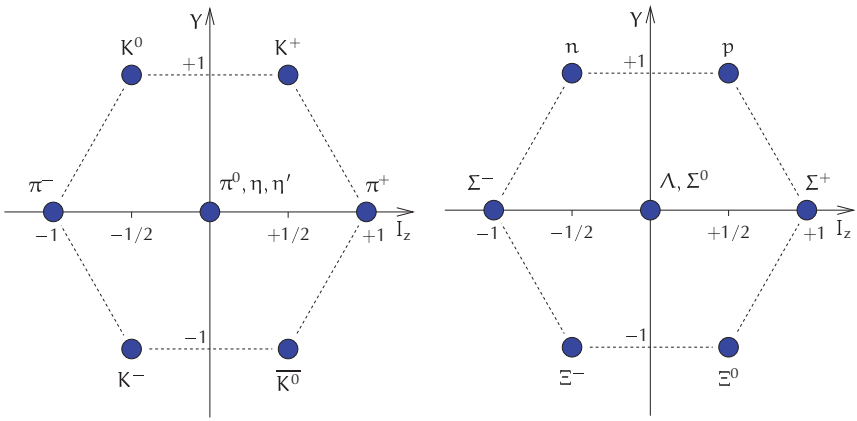

Figure 1.1.: Flavour $SU(3)$ ground state multiplets of isospin z-component I_z versus hypercharge $Y = \mathcal{B} + S$ for the spin-0 mesons with baryon number $\mathcal{B} = 0$ and the spin-1/2 baryons with $\mathcal{B} = 1$. The pseudoscalar meson octet contains the lightest strange mesons, the baryon decuplet contains the lightest hyperons.

were honoured by Nobel prizes awarded to Tsung-Dao Lee and Chen Ning Yang in 1957 [6, 7] and to James Cronin and Val Fitch in 1980 [8, 9], who gave the concepts of right-handedness, left-handedness, matter, and anti-matter a definite meaning in physics.

In February 1964, Gell-Mann and George Zweig [10–12] described a new classification scheme that has put all particles known at that time into order using an abstract symmetry. It was based on fictional building blocks of matter that were named "aces" by Zweig. Gell-Mann, instead, preferred the name "quark", taken from a passage of the novel Finnegans Wake by James Joyce. In this scheme, the lightest strange particles are the kaons, which are mesons carrying the quantum number *strangeness* S of the s-quark. Mesons are classified in J^{PC} multiplets according to their spin J, parity P, and C-parity C. In the quark model the $q\overline{q}'$ quark-antiquark bound states with orbital angular momentum $\ell = 0$ are the pseudoscalar mesons (0^{-+}) and the vector mesons (1^{--}). The strangeness quantum number $S = +1$ is assigned to the positively charged kaon, the K^+. The number $S = -1$ is then assigned to K^-. Other members of the kaon family are the neutral K^0 and its antiparticle $\overline{K}^0$. The kaons can be regarded as an isospin

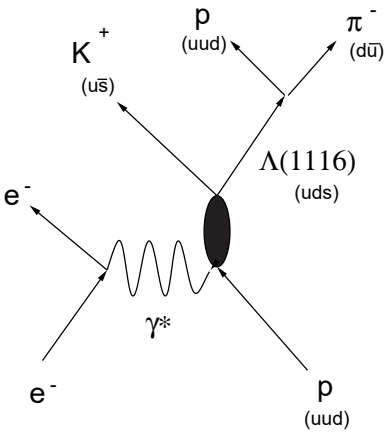

Figure 1.2.: Open strangeness production at MAMI. The coupling of the virtual photon to the nucleon is represented by the ellipse, which needs to be described by phenomenological models or other effective approaches. A kaon is produced associated to a Λ hyperon, a typical decay of the latter is depicted. The quark structure of the hadrons is written in parenthesis beneath each particle.

($I = 1/2$) doublet of particles K^+ and K^0 with antiparticles K^- and $\overline{K}^0$. The underlying symmetry of the structure of the hadrons can be seen in the multiplets showing the isospin component I_z plotted against hypercharge $Y = \mathcal{B} + S$ with $\mathcal{B}$ being the baryon number separating between baryons and mesons. Following flavour $SU(3)$, the nine possible $q\overline{q}'$ combinations containing the light u-, d-, and s-quarks are grouped into an octet and a singlet of light mesons. The baryons, three-quark fermions (qqq) with baryon number $\mathcal{B} = 1$, are grouped into an $SU(3)$ quark-symmetric decuplet, such as the decuplet that includes the Λ and Σ hyperons, two mixed-symmetric octets and a singlet. Hyperons, in the $SU(3)$ quark model classification, are baryons with at least one strange quark in the qqq structure. Fig. 1.1 shows the ground state multiplets for the spin-0 mesons and spin-1/2 baryons. The pseudoscalar meson octet contains the lightest strange mesons, the baryon decuplet contains the lightest hyperon, the Λ with strangeness $S = -1$ and isospin $I = 0$ quantum numbers.

Based on these concepts the standard model of particle physics emerged during the 1970s and Quantum Chromodynamics (QCD) became the theory to study the strong interactions of particles. In this framework all hadrons, *i.e.* the class of particles that interact strongly, are made out of quarks, and strange particles are

the ones which are composed of at least one strange quark. In our understanding of the microscopic world the standard model is the fundamental theory, which unites the weak, electromagnetic and strong interactions, which in turn govern the seemingly infinite variety of processes occurring in nature.

Since its initial formulation, QCD has been thoroughly probed in reactions at very high energies. However, efforts to apply it to hadronic processes have been complicated, one very basic obstacle being the non-perturbative nature of the strong interaction at the energy scales typical to bound many-body systems like hadrons. Although significant progress has been made in *ab initio* computations of QCD on the lattice, at this point only static hadron properties have been computed with a reasonable level of confidence. The interpretation of dynamical hadronic processes thus continues to hinge on models containing some phenomenological ingredients.

It is well established that QCD is at the basis of the composite structure of the hadrons, but it turns out that in many cases QCD does not provide the appropriate degrees-of-freedom to describe the properties of hadronic matter at a larger scale. For example, the concept of structureless hadrons turns out to be much more efficient in describing the properties of nuclei. At intermediate energies, though, some of the properties of the hadrons are surprisingly well explained in terms of constituent quarks without taking explicitly the gluons into account.

The electromagnetic interaction has turned out to be the ideal probe to investigate the hadronic structure of nuclei and nucleons [13]. All electromagnetic ingredients in the transition amplitudes can be described by quantum electrodynamics (QED), the well-established theory of electromagnetic interactions. At low energies the electromagnetic interaction is governed by the fine structure constant $\alpha = e^2/4\pi\epsilon_0\hbar c \approx 1/137$. At this value of α the interaction is sufficiently weak to be treated by perturbation theory. In the one-photon exchange approximation of QED, reaction and structure aspects can be separated in a model-independent way, and the scattering of electrons off light nuclei or nucleons is described with an accuracy of about 1% [14]. In this approximation a virtual photon mediates a well-defined energy and momentum transfer to the hadronic system and probes hadronic currents.

Over the years, considerable effort has been invested into improving the existing picture of the nucleon by electron scattering. Like the exited states of atoms are reflecting the governing interactions, knowledge of the nucleon excitations or resonances is providing essential information at the hadronic energy scale. Most of the available information concerning the nucleon excitation spectrum was gathered through experiments involving pion-nucleon final states. It turns out that many of the resonances predicted by constituent-quark models have not been experimentally confirmed. As several of these so-called "missing

resonances" are predicted to couple weakly to the πN channel and some states are predicted to have a larger probability of coupling to alternative channels like ωN, ηN, $\pi\pi N$, $K\Lambda$, and $K\Sigma$, electromagnetic reactions with strangeness in the final state are particularly interesting. At MAMI, a primary reaction of interest is the electro-production of kaons, shown in Fig. 1.2 in a cartoon form including the decay of the associated Λ hyperon and the strange quark content of the hadrons.

1.2. FORMALISM OF ELECTRON SCATTERING EXPERIMENTS

The kinematics of elementary strangeness electro-production, *i.e.* off a nucleon, may be written in the following way [15]

$$N(p^{\mu}_{targ}) + e(q^{\mu}_{e}) \rightarrow e'(q^{\mu}_{e'}) + K(p^{\mu}_{K}) + Y(p^{\mu}_{Y}), \tag{1.1}$$

where the initial state is described by the incident electron $q^{\mu}_{e} = (E_e, \vec{q}_e)$ and the stationary target $p^{\mu}_{targ} = (M_{targ}, \vec{0})$ and three particles final state by:

$$q^{\mu}_{e'} = (E_{e'}, \vec{q}_{e'}), \quad p^{\mu}_{K} = (E_K, \vec{p}_K), \quad p^{\mu}_{Y} = (E_Y, \vec{p}_Y). \tag{1.2}$$

In the one-boson exchange approximation the process involves the exchange of a virtual photon, γ^*, between beam electron and target with its four-momentum $q^{\mu} = (\omega, \vec{q})$ defined by the difference of the four-vectors of the incoming and outgoing electron, $q^{\mu} = q^{\mu}_{e} - q^{\mu}_{e'}$.

In a typical two-arm strangeness electro-production experiment the produced meson is a charged kaon that is detected in coincidence with the scattered electron and the recoiling hadronic system remains unobserved. Fig. 1.3 illustrates the process in the one-photon exchange approximation: an incident electron, labelled e, scatters by radiating a virtual photon, γ^*. The scattered electron, e', is emitted at a polar angle θ_e with respect to the direction of the incident beam and is detected in a spectrometer. The plane defined by the incident electron and scattered electron is referred to as the scattering plane. The virtual photon carries momentum and energy from the electron beam and interacts with a proton target to form a charged kaon, K^+, and a hyperon, Y, which is either a Λ or Σ^0. The kaon is emitted at a polar angle θ_{qK} with respect to the virtual photon direction and is detected in a second spectrometer. The plane defined by the produced kaon and produced hyperon is referred to as the reaction plane. The azimuthal angle, ϕ, is the angle between the scattering plane and reaction plane. The complementary

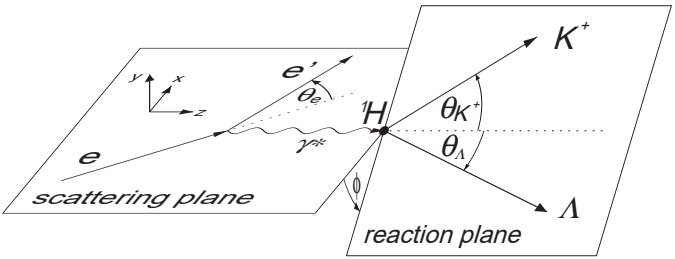

Figure 1.3.: Electron scattering geometry off the proton with the definition of some kinematic variables in the one-photon exchange approximation. In a two-arm experiment the scattered electron e' and the kaon K^+ are detected. Through the measurement of the scattering angles θ_e and θ_K the scattering and the reaction planes are determined, which are rotated by the angle ϕ. The photon transfers a four-momentum of Q^2 and excites a hadronic system of energy W, see also Fig. 1.4.

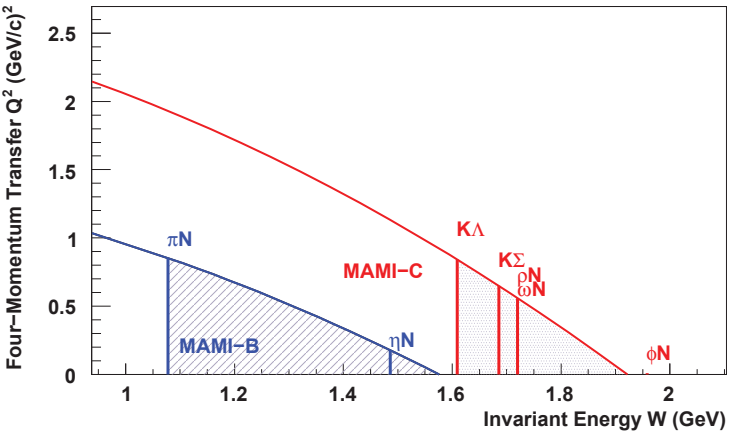

Figure 1.4.: Kinematic region accessible in electro-production by the accelerator stages MAMI-B (end-point energy of 855 MeV) and MAMI-C (end-point energy of 1508 MeV). The threshold energies for $\pi/\eta/\rho/\omega$ and ϕ production off the nucleon and for the associated strangeness channels $K\Lambda$ and $K\Sigma$ are indicated. Electro-production experiments at MAMI-B were devoted often to pion production and $N\Delta$ transitions, whereas at MAMI-C the electro-production of open strangeness in the Q^2-range below 1 $(\mathrm{GeV}/c)^2$ is possible.

process $e + n \rightarrow e' + K^0 + \Lambda$ is possible, which would require a nuclear target and the detection of the neutral kaon by its decay products.

With the definition of $Q^2 = -q^\mu q_\mu$ the four-vector momentum transfer can be deduced in the approximation for massless electrons scattered into the angle θ to be:

$$Q^2 = 2E_e E_{e'}(1 - \cos\theta') = 4E_e E_{e'} \sin^2 \theta/2 \,. \tag{1.3}$$

Using Eq. 1.3 the relation between the energy of the scattered electron and the angle of the virtual photon in the laboratory frame follows:

$$\cos\theta_\gamma = \frac{E_e - E_{e'}(1 - Q^2/2E_e E_{e'})}{|\vec{q}|} \,, \tag{1.4}$$

where $|\vec{q}| = \sqrt{\omega^2 + Q^2}$ is the modulus of the photon three-momentum. The four-vector momentum transfer to the nucleon is given by the so-called Mandelstam variable t,

$$t = (q^\mu - p_K^\mu)^2 = (\omega - E_K)^2 - |\vec{q}|^2 - |\vec{p}_K|^2 + 2|\vec{q}||\vec{p_K}| \cos\theta_{qK} \,, \tag{1.5}$$

which complements the total centre-of-mass energy

$$s = (q^\mu + p_{targ}^\mu)^2 = (p_K^\mu + p_Y^\mu)^2 \,, \tag{1.6}$$

and the third independent combination of four-vectors:

$$u = (q^\mu - p_Y^\mu)^2 = (p_{targ}^\mu - p_K^\mu)^2 \,. \tag{1.7}$$

The threshold laboratory energy E_{thr} for kaon electro-production associated to a hyperon Y is, neglecting the electron mass:

$$E_{thr}(e + A \rightarrow e' + X + K^+ + Y) = \frac{(M_K + M_Y)^2 - M_{targ}^2}{2M_{targ}} \,, \tag{1.8}$$

with A being the target of mass M_{targ} and X being the system recoiling against the associated strangeness pair.

The accelerator facility MAMI can now be used to study strange hadronic systems as the threshold energy for the elementary processes on a proton target was crossed by the 1508 MeV energy of MAMI stage C:

$$\begin{aligned} E_{thr}(ep \rightarrow e'K^+\Lambda) &= 912\,\text{MeV}, \quad \text{and} \\ E_{thr}(ep \rightarrow e'K^+\Sigma^0) &= 1\,047\,\text{MeV} \,. \end{aligned}$$

The kinematic region accessible in electro-production by the electron accelerator stages MAMI-B (end-point energy of 855 MeV) and MAMI-C (end-point energy of 1508 MeV) is shown in Fig. 1.4.

If momentum and energy of the hadronic system, $p^{\mu}_{KY} = p^{\mu}_{K} + p^{\mu}_{Y}$, are defined as follows:

$$\vec{p}_{KY} = \vec{q}_e - \vec{q}_{e'} = \vec{q} \tag{1.9}$$

$$E_{KY} = E_e + M_{targ} - E_{e'} = M_{targ} + \omega \tag{1.10}$$

the modulus of the kaon momentum is related to the electron kinematics by the relativistic relation:

$$E_{KY} = E_K + E_Y = \sqrt{p_K^2 + M_K^2} + \sqrt{p_Y^2 + M_Y^2} \quad \text{with} \tag{1.11}$$

$$p_Y^2 = p_{KY}^2 - 2\vec{p}_{KY} \cdot \vec{p}_K + p_K^2 \tag{1.12}$$

With the kaon angles known in the laboratory system and the following definitions

$$D = \vec{p}_{KY} \cdot \vec{e}_K \tag{1.13}$$

$$a = 4\left(D^2 - E_{KY}^2\right) \tag{1.14}$$

$$b = 4D\left(E_{KY}^2 - p_{KY}^2 + M_K^2 - M_Y^2\right) \tag{1.15}$$

$$c = \left(E_{KY}^2 - p_{KY}^2\right)^2 + \left(M_K^2 - M_Y^2\right)^2 + 2p_{KY}^2\left(M_Y^2 - M_K^2\right) - 2E_{KY}^2\left(M_K^2 + M_Y^2\right) \tag{1.16}$$

Eq. 1.11 is solved for the kaon momentum to be

$$p_K^{\pm} = \frac{-b \pm \sqrt{b^2 - 4ac}}{2a} \tag{1.17}$$

Fig. 1.5 shows these kinematic correlations in kaon electro-production at forward kaon and electron angles. The actual energies and angles resemble the measurements performed in 2008 and 2009 with the spectrometer set-up as described in Chapter 3 of this thesis.

For an unpolarised electron beam and an unpolarised target, the five-fold differential cross-section for the $\mathrm{p}(e, e'K^+)\Lambda$ process can be written, see *e.g.* [16], in a very intuitive form:

$$\frac{\mathrm{d}\sigma}{\mathrm{d}E_{e'}\mathrm{d}\Omega_e\mathrm{d}\Omega_K^*} = \Gamma_v \frac{\mathrm{d}\sigma_v}{\mathrm{d}\Omega_K^*}, \tag{1.18}$$

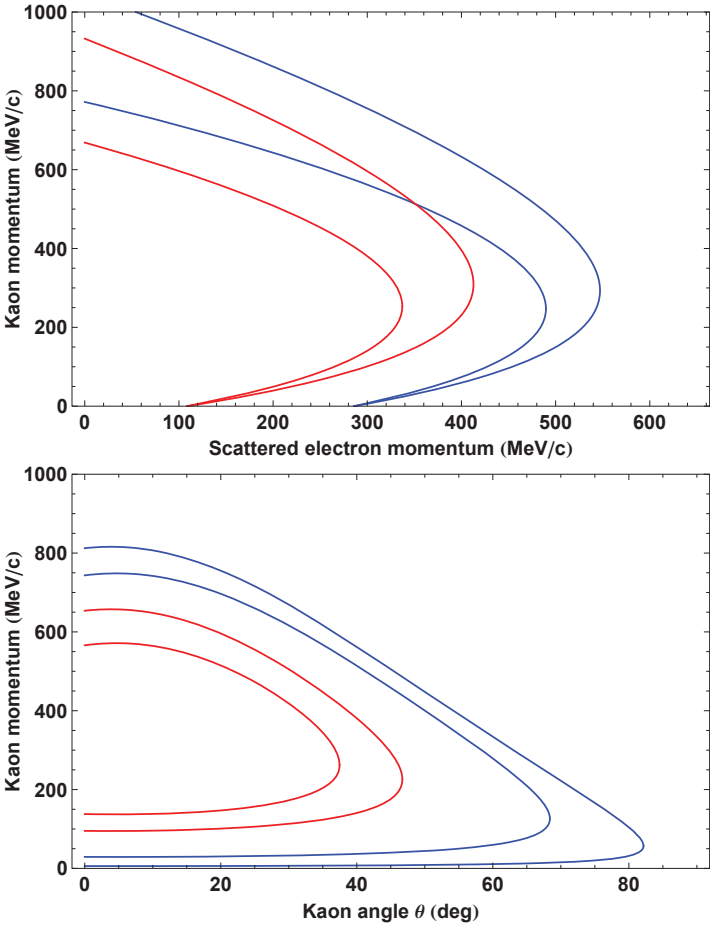

Figure 1.5.: Top: Kinematic correlation between scattered electron momentum and kaon momentum in strangeness electro-production at forward kaon angles, a scattered electron angle $\theta = -15.8\,^{\circ}$, a beam energy of $E_e = 1508\,\text{MeV}$, and a scattered electron energy of $E_{e'} = 318\,\text{MeV}$. Bottom: kinematic correlation between kaon momenta and kaon angles for the same electron kinematics. Blue lines: kinematic limits in the $K\Lambda$ reaction channel; Red lines: kinematic limits in the $K\Sigma^0$ reaction channel.

where the virtual photo-production cross-section is conventionally expressed as

$$\frac{\mathrm{d}\sigma_v}{\mathrm{d}\Omega_K^*} = \frac{\mathrm{d}\sigma_T}{\mathrm{d}\Omega_K^*} + \epsilon\frac{\mathrm{d}\sigma_L}{\mathrm{d}\Omega_K^*} + \sqrt{2\epsilon(1+\epsilon)}\,\frac{\mathrm{d}\sigma_{LT}}{\mathrm{d}\Omega_K^*}\cos\phi + \epsilon\frac{\mathrm{d}\sigma_{TT}}{\mathrm{d}\Omega_K^*}\cos 2\phi\,. \tag{1.19}$$

The kaon solid angle differential Ω_K^* is given in the hadronic centre-of-mass system and ϕ is the angle between the electron-scattering and hadron-production planes. In the centre-of-mass system ω^* is the energy of the virtual photon. The terms indexed by T, L, LT, TT are the transverse, longitudinal and interference cross-sections. Different conventions for Eq. 1.19 exist in the literature. Instead of the degree-of-polarisation ϵ, the transverse and longitudinal polarisation factors of the virtual photon can be distinguished, that can be related to the amplitudes of the electromagnetic field A:

$$\epsilon = \frac{|A_x|^2 - |A_y|^2}{|A_x|^2 + |A_y|^2} = \left(1 + 2\frac{|\vec{q}|^2}{Q^2}\tan^2\theta/2\right)^{-1} \quad \text{and} \tag{1.20}$$

$$\epsilon_L = \frac{|A_z|^2}{|A_x|^2 + |A_y|^2} = \epsilon\frac{Q^2}{(\omega^*)^2}\,. \tag{1.21}$$

It should be noted that in the discussion of the data measured at MAMI, a definition of the longitudinal and interference terms is followed which makes use of the transverse polarisation only and which absorbs the longitudinal polarisation into the structure functions. In electro-production, longitudinal polarisation components are possible. For real photons, where the longitudinal polarisation and the four-vector momentum transfer vanish, only the transverse term remains.

The flux of virtual photons per scattered electron into $\mathrm{d}E_{e'}\mathrm{d}\Omega$ is given by

$$\Gamma_v = \frac{\alpha}{2\pi^2}\frac{E_{e'}}{E_e}\frac{k_\gamma}{Q^2}\frac{1}{1-\epsilon}\,, \tag{1.22}$$

and evaluated with electron kinematics in the laboratory frame. The photon equivalent energy, $k_\gamma = (W^2 - M_{targ}^2)/2M_{targ} = \omega - Q^2/(2M_{targ})$, is the energy a real photon would have in the laboratory frame to excite a hadronic state of energy W.

The maximum photon flux produced by the (e, e') reaction occurs when the scattered electron is detected at very forward angles and the virtual photon direction is almost parallel. In this kinematical situation the photons can be considered almost on-shell, *i.e.* real. For low-Q^2 electro-production, Eq. 1.19 provides a connection to photo-production, with the photon flux factor, Γ_v, multiplying the on-shell photon cross-section. Especially for the electro-production of strange

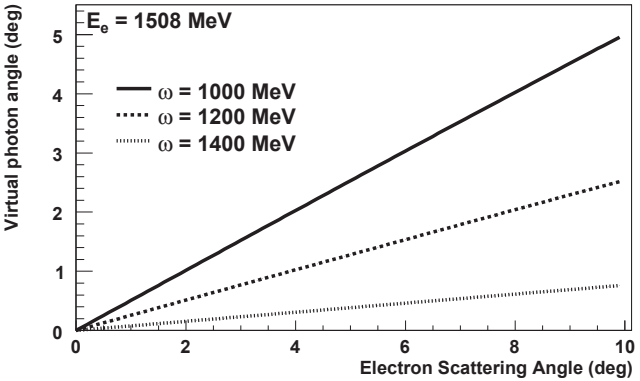

Figure 1.6.: The virtual photon angle as a function of electron scattering angle, for different photon energies. The incident electron beam energy is 1508 MeV.

systems with low cross-sections, *e.g.* strange nuclear systems, only forward scattering angle geometries will experimentally be possible. Fig. 1.6 shows the direction of virtual photons of different energies as a function of the scattered electron angle. In parallel kinematics, with kaons emitted close to the direction of the virtual photons, the interference terms σ_{LT} and σ_{TT} vanish due to their $\sin\theta_K^*$ and $\sin^2\theta_K^*$ dependence, respectively. However, for experiments at small kaon angles the electron and kaon spectrometers could physically interfere with each other or with the electron beam-line.

1.3. PROBING HADRONIC DEGREES-OF-FREEDOM WITH STRANGENESS

1.3.1. THEORETICAL SITUATION

The earliest attempt to explain kaon photo- and electro-production theoretically was proposed by Kawaguchi and Moravcsik more than 50 years ago [17]. Over the past few decades a large number of different attempts have been devoted to the modelling of the electromagnetic strangeness production. The theoretical approaches generally fall into two categories. In parton-based models the quark-gluon structure of the interaction hadrons is explicitly tied in with the reaction

dynamics. A successful example of such a strategy is the work of Li [18] and co-workers, in which the interaction vertices are constructed directly from a chiral constituent-quark model. Alternatively, hadrodynamic approaches express the kaon production amplitudes in terms of hadronic degrees-of-freedom, see (*e.g.* [19–21]). Thereby, the strong inter-particle interactions are modelled by effective Lagrangians. Because the mathematical structure of these Lagrangians is not *a priori* known, their construction relies for the most part on symmetry arguments.

ISOBAR AND COUPLED-CHANNEL APPROACHES

Starting from the late eighties, various groups have developed a particular type of effective Lagrangian model, commonly referred to as the "isobar" approach, which was inspired by the successful description of pion photo-production in the Δ-resonance region or η photoproduction in the second resonance region. In the isobaric models the reaction amplitudes are constructed from lowest-order (so-called tree-level) Born terms with the addition of extended Born terms for intermediate particles, N, K, or Y resonances, exchanged in the s-, t-, and u-channels as shown in Fig. 1.7. The squared masses of the exchange particle in the three types of diagrams are equivalent to the three Mandelstam variables defined in Eqs. 1.6, 1.5, and 1.7. Each intermediate state enters into the model through its strong coupling constant and strong decay width. Diagrams containing intermediate nucleon resonances can produce peaks at given hadronic energies W, or equivalently $\sqrt{s}$, in the cross-sections at the pole masses of the s-channel intermediate states. Intermediate kaons and hyperons cause no such peaking behaviour, and are often called background contributions.

A complete description of the reaction process would require all possible channels that could couple to the initial and final state. Most of the model calculations for kaon electrophoto-production have been performed in the framework of tree-level isobar models [19, 22, 23], however, only few coupled-channels calculations exist [24]. In the tree-level framework higher-order mechanisms like final-state interactions and channel couplings are not treated explicitly.

The advantages of the one-channel, tree-level approach are its limited complexity and the identification of the dominant trends. Even so, several dozen parameters remain. One reason is that, in contrast to pion and eta production, the kaon production process in the s-channel is not dominated by a single resonant state. Although the choice of the resonances is guided by existing πN data and quark model predictions, the models differ in the use of specific nucleon, hyperon, and kaon resonances. The coupling constants for each of the included resonances are extracted from global fits of the model calculations to the existing data base. The

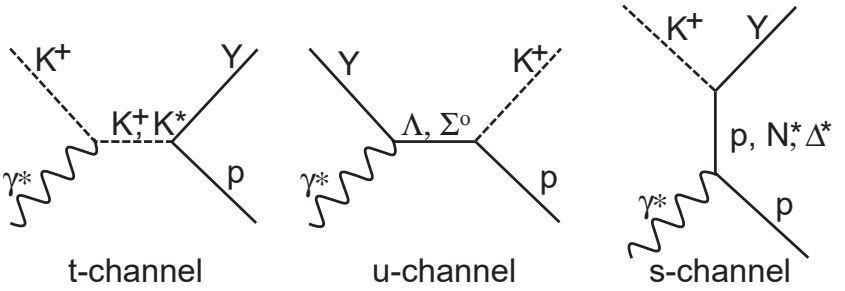

Figure 1.7.: Lowest-order Feynman diagrams of *s*-, *t*-, and *u*-channel exchanges for the $p(e,e'K^+)Y$ reaction. The vertices enter into the models through strong coupling constants and form-factors. The squared masses of the intermediate states in the three channels equal the corresponding Mandelstam variables. The different resonance contributions are subject to model variations and global fits.

tree-level coupling constants obtained from these fits should be regarded as effective values. They cannot be compared to quark-model predictions, because the latter are related to untruncated amplitudes instead. To account for the finite lifetimes of the resonances, decay widths must be introduced which break unitarity.

The drawback of the isobaric models is the large and unknown number of exchanged hadrons that can contribute in the intermediate state of the reaction. Depending on which set of resonances is included, very different conclusions about the strengths of the contributing diagrams for resonant baryon formation and kaon exchange may be reached.

The various unknown kaon-hyperon-nucleon coupling strengths can be incorporated by resorting to more fundamental models or can be determined from experiment. In this respect, effective field approaches provide a direct link between quark-model predictions for mesonic or baryonic properties and experimentally accessible quantities, such as scattering cross-sections. The strong coupling constants in the $K^0\Lambda$ and $K^+\Lambda$ channels are related via the $SU(2)$ isospin symmetry: $g_{K^+\Lambda p} = g_{K^0\Lambda n}$ and $g_{K^+\Sigma^0 p} = -g_{K^0\Sigma^0 n}$. In the electromagnetic vertices the ratio of the neutral to charged coupling constants have to be known. For the nucleon and its resonances the ratio can be related to the known helicity amplitudes of the nucleons, whereas for the kaon resonances the ratio relates to the decay widths known only for the K^* meson.

Model predictions for laboratory and centre-of-mass kaon photo-production

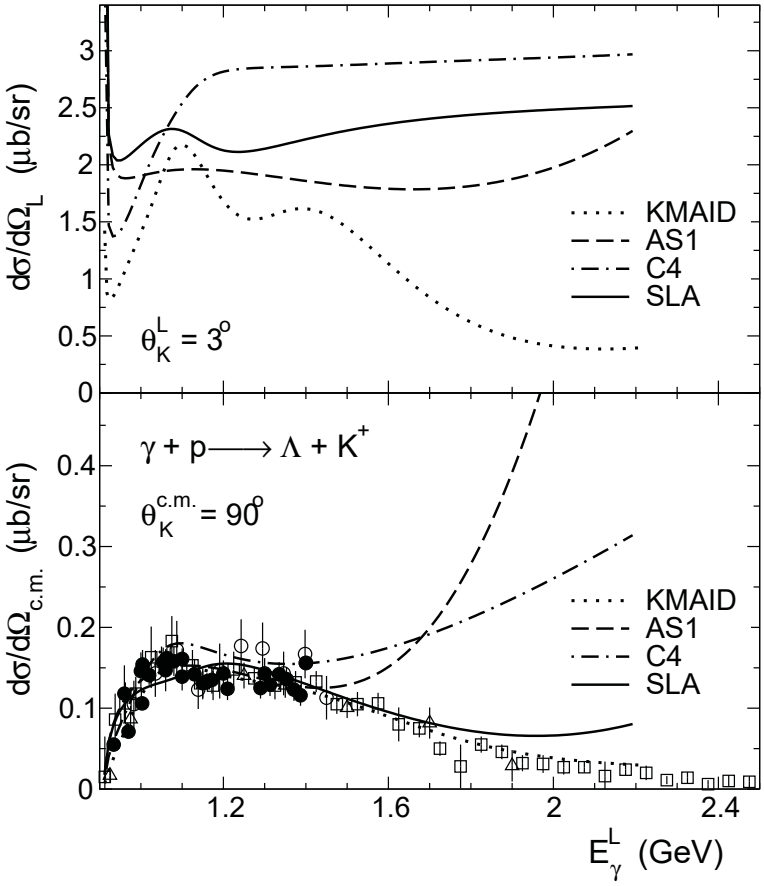

Figure 1.8.: Differential kaon photo-production cross-sections as a function of the photon energy at fixed kaon angles in the laboratory (top) and centre-of-mass (bottom) reference frame (Fig. from [25]). Predictions from models Kaon-Maid (KMAID), Adelseck and Saghai (AS1), Williams-Ji-Cotanch (C4), and Saclay Lyon A (SLA). In the laboratory frame only the theoretical curves for $\theta_K^{lab} = 3^\circ$ are shown.

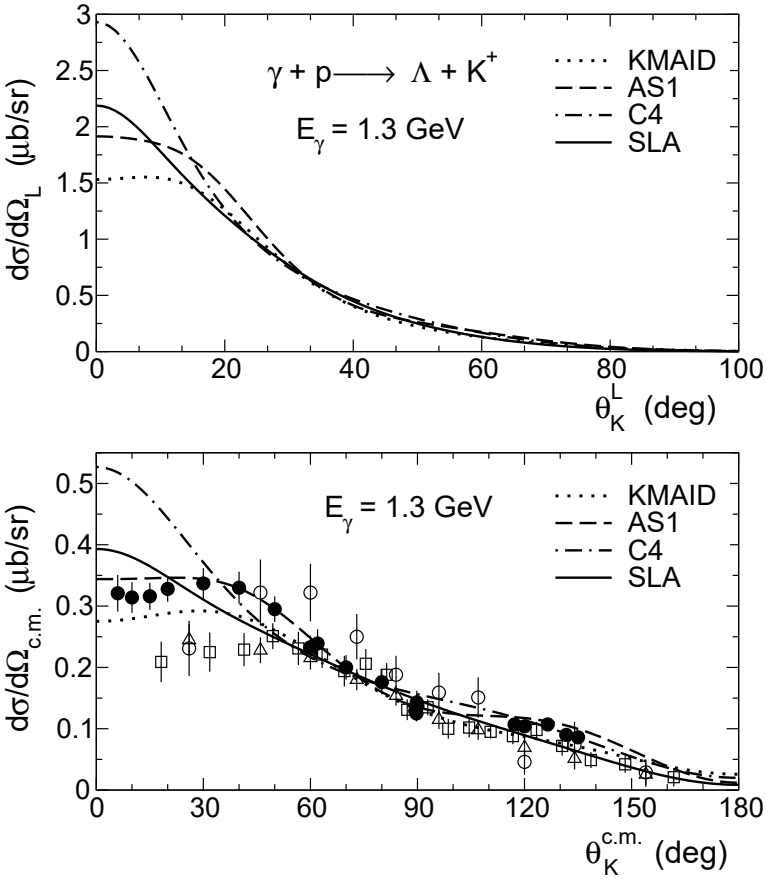

Figure 1.9.: Differential kaon photo-production cross-sections as a function of the kaon angle at fixed photon energy in the laboratory (top) and centre-of-mass (bottom) reference frame (Fig. from [25]). Predictions from models Kaon-Maid (KMAID), Adelseck and Saghai (AS1), Williams-Ji-Cotanch (C4), and Saclay Lyon A (SLA). In the laboratory frame only the theoretical curves are shown.

cross-sections as a function of the photon energy at fixed kaon angles and at fixed photon energy are shown in Figs.1.8 and 1.9. The predictions are from the models Kaon-Maid, Adelseck and Saghai, Williams-Ji-Cotanch, and Saclay Lyon A. These models characterise our present understanding of kaon photoproduction reactions at photon energies below 1.5 GeV. The model SLA is a simplified version of the full Saclay-Lyon model in which a nucleon resonance with spin-$^5/_2$ appears in addition. Since predictions of both models are very similar for the cross-sections one can use the simpler version SLA here [26]. The variations in the models in the resonance region are clearly visible which lead to the conclusion, that our description of the process still lacks considerable insight. Concerning the differential cross-section with respect to the kaon centre-of-mass angle the variations are strongest at small angles.

The electro-production of strangeness introduces two additional contributions, that are vanishing for the kinematic point at $Q^2 = 0$: the longitudinal coupling of the photons in the initial state, and the electromagnetic and hadronic form factors of the exchanged particles. The expression for the unpolarised electro-production cross-section includes the longitudinal-transverse and transverse-transverse interference terms and the non-separated sum of the transverse and longitudinal cross-sections, $\sigma_u = \sigma_T + \epsilon\sigma_L$. If the interaction Lagrangian describes the coupling of a hadron to the photon field, one talks about electromagnetic form factors. In the case of a vertex Lagrangian describing the coupling of hadron fields to each other, one has to include strong or hadronic form factors. The introduction of form factors has a serious impact on the properties of a model. It is common practice to use phenomenological form factors to account for the extension of the point-like interactions at the hadronic vertices [27]. It is a well-known phenomenon that the insertion of strong form factors breaks the gauge invariance of isobar models for meson photo- and electro-production. Different models typically have different prescriptions for restoring gauge invariance. A variant of the Kaon-Maid model uses identical phenomenological electromagnetic form-factors for baryons and their resonances.

Common to the Kaon-Maid and Saclay-Lyon models is that, besides the extended Born diagrams, they also include kaon resonances $K^*(890)$ and $K_1(1270)$. In Kaon-Maid, four nucleon resonances, the $S_{11}(1650)$, $P_{11}(1710)$, $P_{13}(1720)$, and the "missing resonance" $D_{13}(1900)$ have been included. This D_{13} state has never been observed in pionic reactions but the existence of this resonance with considerable branching into the strange channel was predicted by the constituent quark model calculations. For $K\Sigma$ production further contributions from the $S_{31}(1900)$ and $P_{31}(1910)$ Δ-resonances were added. Note, that Kaon-Maid was fitted to the older SAPHIR data [28]. An interactive version of this version of the model is available through the internet [29]. The electromagnetic form-factor

of the $D_{13}(1900)$ was introduced into Kaon-Maid and fixed to the data taken at Jefferson Lab [30, 31] to produce a sharp peak in σ_L as a function of Q^2 at one hadronic energy ($W = 1.84\,\mathrm{GeV}$). Nevertheless, there is common agreement on the fact that the reproduction of a visual bump in the total cross-section should not be interpreted as rock solid evidence for the occurrence of a missing resonance.

For the electro-production processes, the longitudinal couplings and the electromagnetic form-factors need to be fixed to a very limited set of data for each resonance. The $SU(3)$ symmetry, governing the baryon and meson multiplets, can be exploited to establish relations between the coupling constants that connect the particles of the different sets. As such, these $SU(3)$ relations will permit to connect the coupling constants of the ud-sector, which are mostly very well determined, to the coupling constants of the strange sector. Since there is a substantial mass difference between the mass of the neutron and the Λ mass, which essentially originate from interchanging an u- into a s-quark, it is well known that the $SU(3)$ flavour symmetry is broken and the symmetry relations are not exact. However, it is not unambiguously determined how to define a scale parameter for this symmetry breaking and how to implement this breaking in the coupling constants. Nevertheless, it is commonly assumed that a symmetry breaking of 20 % at the level of the coupling constants is reasonable. With this 20 % deviation from the exact $SU(3)$ predictions, the following ranges for $g_{K\Lambda N}$ and $g_{K\Sigma N}$ emerge:

$$-4.5 \leq g_{K\Lambda N}/\sqrt{4\pi} \leq -3.0 \tag{1.23}$$

$$0.9 \leq g_{K\Sigma N}/\sqrt{4\pi} \leq 1.3 \tag{1.24}$$

The values of resonance couplings are known *a priori* and must be adapted from the data. Table 1.4 lists the coupling constants in the version of the Kaon-Maid model used in the interpretation of the data. Four coupling constants were set to zero in a variant of the model that excludes arguable large longitudinal couplings in the Λ reaction channel, which is further discussed in Chapter 3.

In Figs. 1.10 and 1.11 the energy dependence of the transversal and longitudinal cross-sections for $Q^2 = 2.35$ and $1.9\,(\mathrm{GeV}/c)^2$ and zero kaon angle are shown. The calculations were performed by P. Bydžovský for the analysis of data taken by the Rosenbluth separation experiment E98-108 at Jefferson Lab. The data are not published yet. The calculations are made with several models using various electromagnetic form factors. The Kaon-Maid model gives arguable results which are due to the longitudinal coupling of the $D_{13}(1900)$ resonance. In Fig. 1.12 the dependence of the predicted cross-sections on the four-vector momentum transfer is shown, revealing very large values for σ_L in Kaon-Maid at small Q^2.

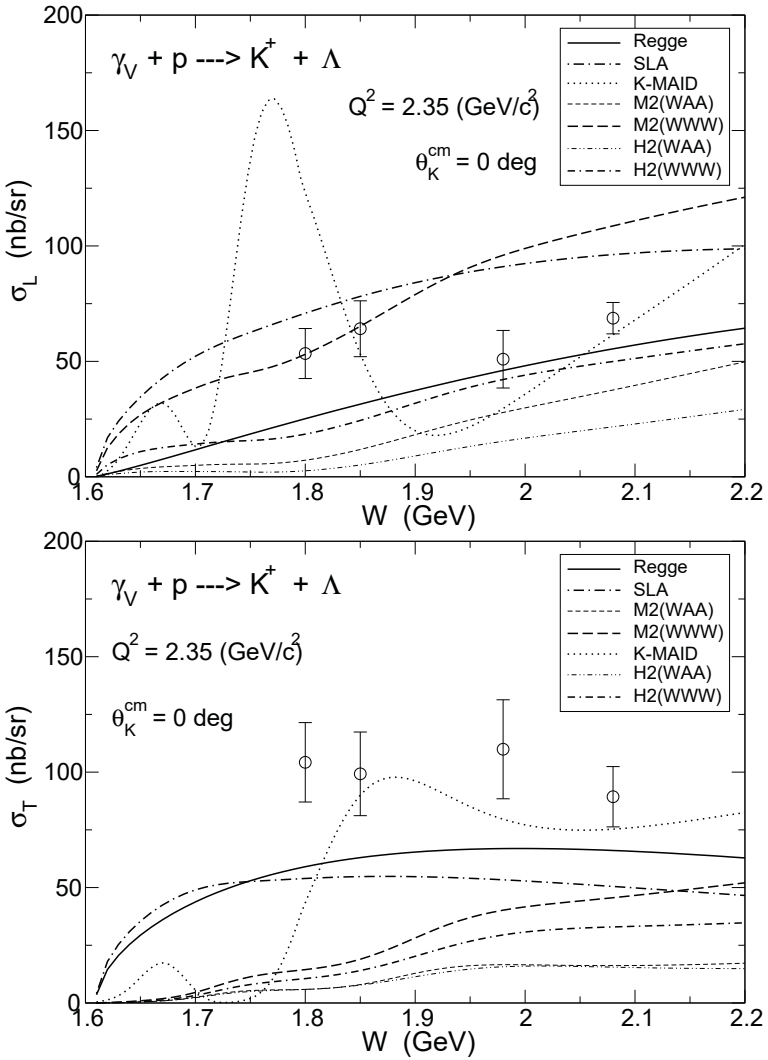

Figure 1.10.: Model description of kaon electroproduction longitudinal (top) and transversal (bottom) cross-sections at zero kaon angle, $\theta_K^* = 0°$, at $Q^2 = 2.35\,(\mathrm{GeV}/c)^2$ (Fig. from P. Bydžovský). The striking resonance structure of the Kaon-Maid model is to be compared to the smooth fall-off of other models like Saclay-Lyon A or Regge phenomenology.

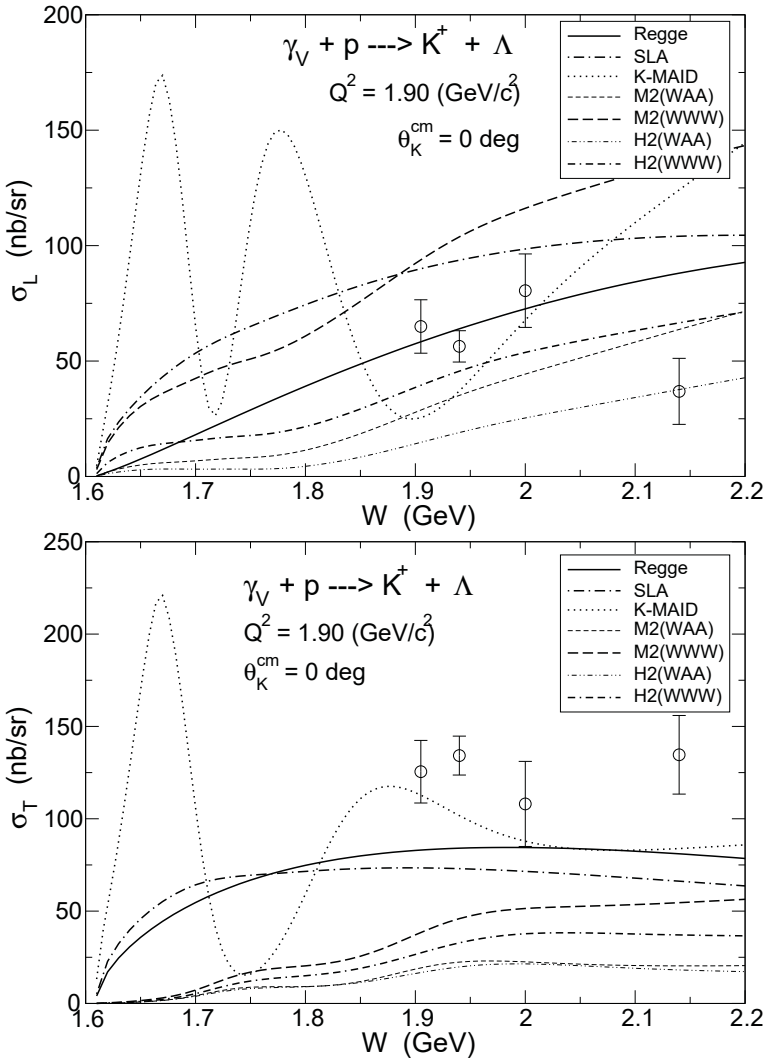

Figure 1.11.: Model description of kaon electro-production longitudinal (top) and transversal (bottom) cross-sections at zero kaon angle, $\theta^*_K = 0°$, at $Q^2 = 1.90\,(\mathrm{GeV}/c)^2$ (Fig. from P. Bydžovský); The striking resonance structure of the Kaon-Maid model is even more pronounced, *cf.* Fig. 1.10 for larger four-vector momentum transfer.

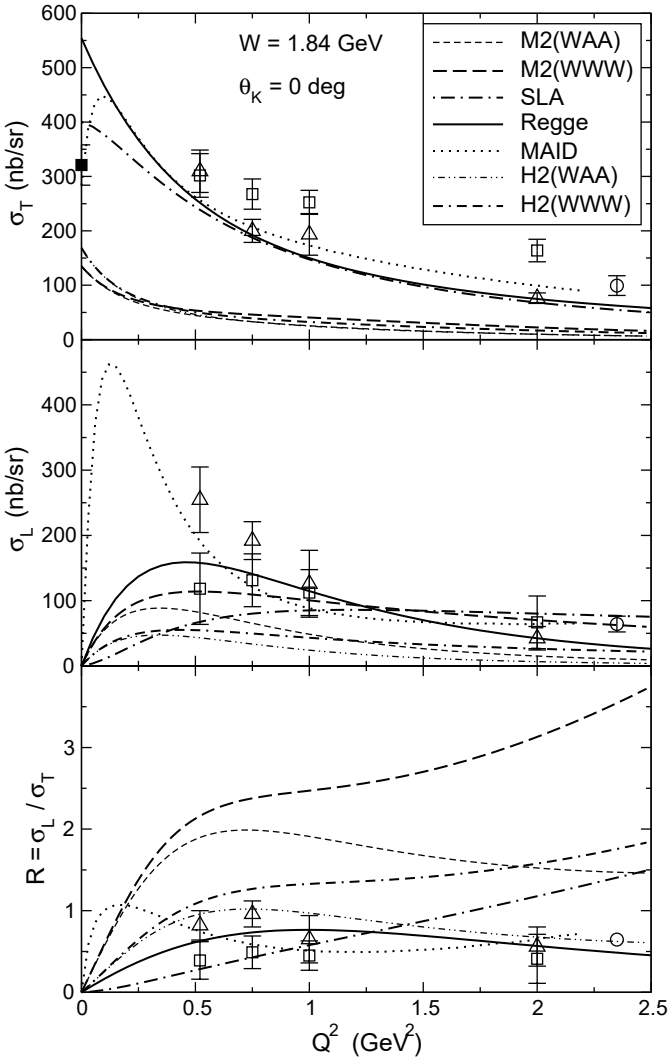

Figure 1.12.: Model description of the dependence of transverse (top) and longitudinal (middle) cross-sections on the four-vector momentum transfer and cross-section ratio (bottom) at zero kaon angle, $\theta_K^* = 0°$, (Fig. from P. Bydžovský).

Table 1.4.: Coupling constants in the version of the Kaon-Maid model used in the interpretation of the data. Coupling constants marked by † were set to zero in a variant of the model that excludes arguable large longitudinal couplings in the Λ reaction channel, see Chapter 3.

coupling constant	$\times\sqrt{4\pi}$		
$g_{K\Lambda N}$	-3.80		
$g_{K\Sigma N}$	1.20		
$K\Lambda$ coupling	$\times 4\pi$	$K\Sigma$ coupling	$\times 4\pi$
$g_{K^*K\gamma}\, g^V_{K^*\Lambda N}$	-0.79	$g_{K^*K\gamma}\, g^V_{K^*\Sigma N}$	-0.31
$g_{K^*K\gamma}\, g^T_{K^*\Lambda N}$	-2.63	$g_{K^*K\gamma}\, g^T_{K^*\Sigma N}$	-0.17
$g_{K^*K\gamma}\, g^V_{K_1\Lambda N}$	3.8	$g_{K_1K\gamma}\, g^V_{K_1\Sigma N}$	-1.36
$g_{K^*K\gamma}\, g^T_{K_1\Lambda N}$	-2.4	$g_{K_1K\gamma} g^T_{K_1\Sigma N}$	-0.51
$K\Lambda$ coupling	$\times\sqrt{4\pi}$	$K\Sigma$ coupling	$\times\sqrt{4\pi}$
$g^{(1)}_{N^*(1650)N\gamma}\, g_{K\Lambda N^*(1650)}$	-0.13	$g^{(1)}_{N^*(1650)N\gamma}\, g_{K\Sigma N^*(1650)}$	-0.03
$g^{(2)}_{N^*(1650)N\gamma}\, g_{K\Lambda N^*(1650)}$	1.23 †	$g^{(2)}_{N^*(1650)N\gamma}\, g_{K\Sigma N^*(1650)}$	-1.27
$g^{(1)}_{N^*(1710)N\gamma}\, g_{K\Lambda N^*(1710)}$	-0.26	$g^{(1)}_{N^*(1710)N\gamma}\, g_{K\Sigma N^*(1710)}$	0.16
$g^{(2)}_{N^*(1710)N\gamma}\, g_{K\Lambda N^*(1710)}$	-0.18 †	$g^{(2)}_{N^*(1710)N\gamma}\, g_{K\Sigma N^*(1710)}$	12.9
$g^{(1)}_{N^*(1720)N\gamma}\, g_{K\Lambda N^*(1720)}$	1.10	$g^{(1)}_{N^*(1720)N\gamma}\, g_{K\Sigma N^*(1710)}$	-0.06
$g^{(2)}_{N^*(1720)N\gamma}\, g_{K\Lambda N^*(1720)}$	0.63	$g^{(2)}_{N^*(1720)N\gamma}\, g_{K\Sigma N^*(1710)}$	0.24
$g^{(3)}_{N^*(1720)N\gamma}\, g_{K\Lambda N^*(1720)}$	10.3 †	$g^{(3)}_{N^*(1720)N\gamma}\, g_{K\Sigma N^*(1710)}$	4.98
$g^{(1)}_{N^*(1900)N\gamma}\, g_{K\Lambda N^*(1900)}$	0.05	$g^{(1)}_{\Delta(1900)N\gamma}\, g_{K\Sigma\Delta(1900)}$	0.10
$g^{(2)}_{N^*(1900)N\gamma}\, g_{K\Lambda N^*(1900)}$	0.61	$g^{(2)}_{\Delta(1900)N\gamma}\, g_{K\Sigma\Delta(1900)}$	0.51
$g^{(3)}_{N^*(1900)N\gamma}\, g_{K\Lambda N^*(1900)}$	-9.0 †	$g^{(1)}_{\Delta(1910)N\gamma}\, g_{K\Sigma\Delta(1910)}$	0.32
		$g^{(2)}_{\Delta(1910)N\gamma}\, g_{K\Sigma\Delta(1910)}$	-1.2
$g_{K_1^0K^0\gamma}$ / $g_{K_1^+K^+\gamma}$		-0.45	

REGGE PHENOMENOLOGY AND HYBRID MODELS

While adopting hadronic degrees-of-freedom near the strangeness energy threshold is a well-justified strategy, the quark-gluon structure of the interacting particles is bound to manifest itself as higher energies are probed. Consequently, all hadrodynamic approaches, both isobar and coupled-channels models, are deficient in their high-energy behaviour. While the measured cross-sections gradually decrease as the energy of the incoming photon increases, the computed cross-sections exhibit an unrealistic rise with energy. At energies more than 1 GeV above threshold, Regge phenomenology provides a method for describing the data with very few free parameters [32, 33]. This approach was developed in the late fifties as an alternative to quantum-mechanical potential scattering [34], where the orbital momentum J is allowed to take complex values. In its simplest form, the Regge model can be formulated as a modified version of the isobar approach. It is distinguished by the property that each intermediate state in the Regge amplitude comprises an entire family of hadrons, rather than a single meson or baryon. The members of such a family are characterized by a linear relation between their spins and squared masses, and are said to lie on a "Regge trajectory". The exchange of these trajectories is formally described through the introduction of Regge propagators.

While the Regge model is suitable for the CEBAF energy range beyond a few GeV, in particular, the MAMI-C energy range is complementary and Regge phenomenologies were up to the present not considered for describing near-threshold data taken at MAMI. Fig. 1.13 illustrates schematically the KY photoproduction cross-section. The number of resonant structures are gradually washed out as the photon energy increases and the number of overlapping states grows. At energies where all visible traces of individual resonances have vanished the amplitude can be described by a pure background model. The Regge amplitude is then considerably simpler than its isobar-model counterpart, as it does not contain any intermediate resonance states but consists solely of background diagrams. The latter can be explained through the duality hypothesis which roughly states that, on average, the sum of all contributing resonances equals the sum of all possible K^*- or Y^*-trajectory exchanges.

Although Regge phenomenology is a high-energy framework by construction, it has been observed to reproduce the trends of experimental meson production cross-sections down to photon energies of a few GeV. It can therefore be assumed that, even in the low-energy domain, the background part of the production amplitudes can be adequately described in the Regge framework. On the other hand, the low-energy structures, which cannot be reproduced in a pure background model, need to be accounted for by adding a number of Feynman diagrams con-

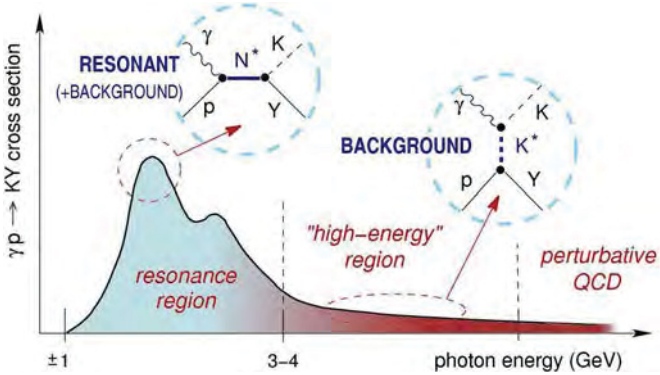

Figure 1.13.: Schematic representation of the total KY photoelectro-production cross-section as a function of photon energy in the laboratory frame (Fig. from [35]). In the resonance region up to a few GeV photon energy, the cross-section exhibits resonance structures. At higher energies a smooth fall-off is observed, which results from a large number of overlapping resonances, and which can be modelled assuming only background diagrams.

taining intermediate nucleon resonances. These resonant contributions should vanish at high energies, where the pure Regge model is valid. This "Regge-plus-resonance" (RPR) model for strangeness production processes was developed in recent years by a group in Ghent [36, 37].

CHIRAL PERTURBATION THEORY

Relative to the energy scale of QCD, $\Lambda_{QCD} \simeq$ several hundred MeV, that is associated with the confinement phenomenon, the u- and d-quarks are light, the c-, b- and t-quarks are heavy, and the s-quark has intermediate mass. Heavy quarks are typically taken as non-relativistic in calculations of heavy hadron spectra [38]. At low energies the chiral symmetry of QCD and its spontaneous and explicit breakdown governs the dynamics of light quarks. An elegant description of data on kaon electro-production close to threshold is provided by chiral perturbation theory [39]. The $SU(2)$ chiral transformations

$$\Psi_{L,R} \equiv \begin{pmatrix} u \\ d \end{pmatrix} \rightarrow \exp(-i\boldsymbol{\theta}_{L,R} \cdot \boldsymbol{\tau})\Psi_{L,R} \qquad (1.25)$$

almost give rise to an invariance of the QCD Lagrangian for small u and d quark masses [38]. The $SU(2)_L \times SU(2)_R$ symmetry has been broken to vectorial isospin symmetry $SU(2)$, *i.e.*, simultaneous $SU(2)$ transformations of Ψ_L and Ψ_R. The isospin symmetry is seen from the near equality of masses in the multiplets. The effective Lagrangian for pions at very low energy has been applied to the process $\gamma p \to \pi^0 p$ and was not only a phenomenological success, but also showed the relevance of chiral (pion) loops [40, 41].

Including the strange quark mass term,

$$\mathcal{L}_{mass} = \overline{\Psi}_L \mathbf{m} \Psi_R + \overline{\Psi}_R \mathbf{m} \Psi_L, \qquad \mathbf{m} = \begin{pmatrix} m_u & 0 & 0 \\ 0 & m_d & 0 \\ 0 & 0 & m_s \end{pmatrix} \tag{1.26}$$

the QCD Lagrangian has an approximate $SU(3)_L \times SU(3)_R$ global symmetry [38]. If the u, d, and s quarks were massless, the dynamical breaking of $SU(3)_L \times SU(3)_R$ to vector $SU(3)$ would produce eight Goldstone bosons, one for each generator of $SU(3)$. These would be the three pions $\pi^{\pm}$, π^0, the four kaons $K^{\pm}$, K^0, $\overline{K}^0$, and one neutral particle η of the octet. Due to non-zero quark masses, these mesons are not actually massless, but small compared to the confinement scale of QCD. The addition of the strange quark produces, if its mass is not too large, low mass kaons associated with the breaking of chiral symmetry. The content of chiral $SU(3)$ is contained in an effective Lagrangian expressed in terms of an exponential parametrisation. Chiral perturbation theory is then formulated in terms of the asymptotic fields, here the octet of Goldstone bosons and the ground state baryon octet. It proceeds in a low energy expansion. Beyond leading order, the effective Lagrangian contains parameters not fixed by chiral symmetry, the so-called low-energy constants (LEC). In principle, these LECs should be extracted from data or calculated by means of lattice gauge theory. To some extent, their values reflect the spectrum of QCD [42].

From the effective Lagrangian and using Eq. 1.26 for the quark masses the relation to the meson masses

$$\frac{\hat{m}}{m_s} = \frac{M_\pi^2}{2M_K^2 - M_\pi^2} = \frac{1}{26} \tag{1.27}$$

can be obtained, where $\hat{m} \equiv (m_u + m_d)/2$. The corresponding small values of the u, d masses are responsible in QCD for the light pion, and for the usefulness of chiral symmetry techniques. Evidently, while for $SU(2)$ the pertinent expansion parameter is small, $M_\pi / 4\pi F_\pi = 0.12$ (with M_π and F_π the pion mass and decay constant, respectively), the larger strange quark mass leads to $M_K / 4\pi F_\pi = 0.43$

(with M_K the kaon mass). Therefore, it is *a priori* not clear whether the expansion in small momenta and meson masses is applicable in the presence of baryons. How much the dynamical behaviour of strange quarks is constrained by the chiral symmetry of massless particles remains open.

The extension from the flavour $SU(2)$ to the strangeness sector needs precision data for the threshold production of mesons and meson pairs. However, only one calculation of the $K^+\Lambda$ total cross-section from threshold to 100 MeV above has been performed so far. From a generalisation of the Adler-Gilman relation [43, 44] to the $SU(3)$ sector one may expect that K^+ electro-production close to threshold also gives access to the $\langle \Lambda | A^{\mu,a} | p \rangle$ axial-vector current matrix element. The Adler-Gilman relation is the basis of extracting information on the axial and induced pseudoscalar form-factors of the nucleon from threshold pion electro-production experiments. Clearly, because of the rather large kaon mass, a careful investigation of corrections due to the strange quark mass is required for such an interpretation.

1.3.2. EXPERIMENTAL SITUATION

The electromagnetic production of kaons off the nucleon provides an important tool for understanding the dynamics of hyperon-nucleon systems. Before the 1990's, kaon electro-production in the nucleon resonance region has remained largely unexplored. Several low-statistics measurements were carried out in the 1970's at Cambridge University, the Wilson Synchrotron Laboratory at Harvard-Cornell, and at DESY (Deutsches Elektronen-Synchrotron), which focused mainly on cross-section measurements to explore differences in the production dynamics between Λ and Σ^0 hyperons. The first experiment was performed at the Cambridge Electron Accelerator (CEA) [45] using small-aperture spectrometers in kinematics spanning four-vector momentum transfers Q^2 below 1.2 $(\mathrm{GeV}/c)^2$, hadronic energies $W \approx 1.8$–2.6 GeV, and forward kaon angles ($\theta^*_K < 28°$). It was noted that the $K^+\Lambda$ channel dominated the $K^+\Sigma^0$ channel, with signs of a large longitudinal component in the $K^+\Lambda$ channel. Subsequent results from Cornell [46] for $Q^2 < 2.0\,(\mathrm{GeV}/c)^2$ and $W = 2.15$ and 2.67 GeV seemed to confirm this observation.

Other measurements made at Cornell were reported [47] for kaons produced at very small angles relative to the virtual photon ($\theta^*_K < 15°$). The results for hadronic energies, W, ranging from 2.15 to 3.1 GeV included improved measurements of the Q^2 dependence of the differential cross-sections over the range from 0.6 to 4.0 GeV^2, showing that the $K^+\Sigma^0$ cross-section falls off much faster than the $K^+\Lambda$ cross-section. A Rosenbluth separation of longitudinal, σ_L, and transverse,

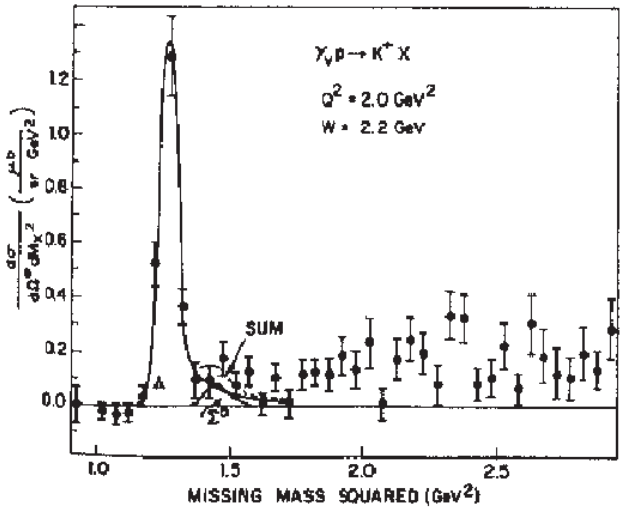

Figure 1.14.: Spectrum of squared missing mass measured at Harvard in 1977 (Fig. from [47]). Note the broad Λ resolution and the Σ^0 peak appearing as a small shoulder on the Λ peak.

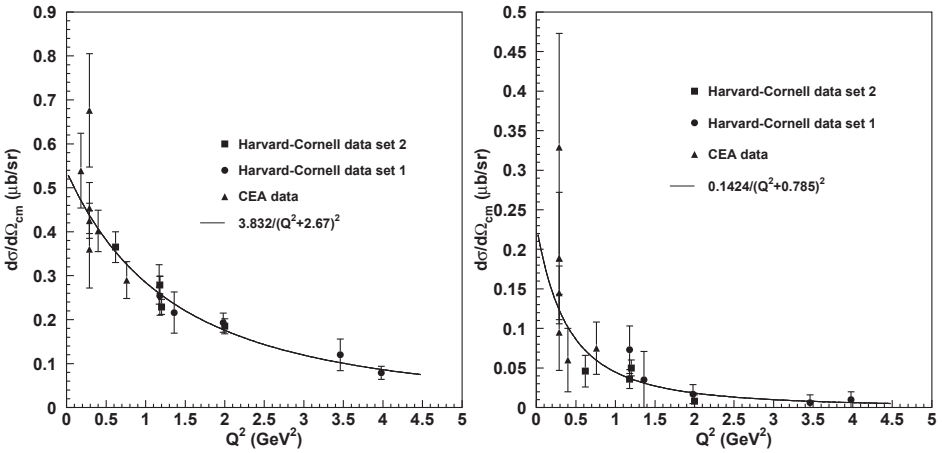

Figure 1.15.: Old kaon electro-production data for $p(e,e'K^+)\Lambda,\Sigma^0$ scaled in the hadronic energy W to 2.16 GeV (Fig. from [47]). Note that already before the 1990's the cross-section was well described at high hadronic energies.

σ_T, terms was first applied to the kaon electro-production data from Harvard in 1977 [47]. The separation was severely limited by systematic uncertainties. Because of its poor precision this experiment provided virtually no constraints for available theories and models.

An experiment at DESY [48] used a large-aperture spark-chamber spectrometer to measure both reaction channels at higher W ($1.9 < W < 2.8\,\mathrm{GeV}$) and lower Q^2 ($0.1 < Q^2 < 0.6\,(\mathrm{GeV}/c)^2$). That experiment managed the first separations of interference terms, σ_{LT} and σ_{TT}, albeit with large error bars, few data points, and considerable kinematic extrapolations to extract results at fixed values of W, Q^2, and $t = (q - p_K)^2$. The results were consistent with zero for these interference cross-sections because of the large uncertainties.

Another survey experiment from DESY [49] at $W = 2.2\,\mathrm{GeV}$ and $0.06 < Q^2 < 1.35\,\mathrm{GeV}^2$, which measured differential cross-sections for the $K + \Lambda$ and $K + \Sigma^0$ final states, confirmed the measured Q^2 dependence of the cross-sections, but with improved statistics. The quality of the 1979 data from DESY were comparable to the Harvard data. Fig. 1.14 shows a typical missing mass spectrum of that time from the $\mathrm{p}(e, e'K^+)\Lambda, \Sigma^0$ reaction, the overlap of Λ and Σ^0 contributions in the spectrum is significant. Most electro-production data taken before 1980 were taken at electron accelerators with low duty cycles and low kaon counting rates. These electro-production experiments tended to have an average hadronic energy of $W = 2.2\,\mathrm{GeV}$, above the resonance region. In fact, the assumption of non-resonant production lead to the smooth description of the cross-section in terms of

$$\frac{\mathrm{d}\sigma}{\mathrm{d}\Omega} = \frac{|p_K^*|}{(W^2 - M^2)W}|\mathcal{M}|^2 \qquad (1.28)$$

where $\mathcal{M}$ represents the assumed W-independent matrix element and p_K^* the momentum of the kaon in the centre-of-mass frame [47]. In Fig. 1.15 the Q^2-dependences of Λ- and Σ^0-cross-sections at central kaon angles extracted by Bebek [47] is shown.

First new photo-production results from ELSA, the Electron Stretcher Accelerator in Bonn, were published in 1994 by the SAPHIR collaboration [28, 50]. Kaon photo-production at ELSA was studied close to threshold ($W_{th} < W < W_{th} + 25\,\mathrm{MeV}$) and data with photon energies up to 2 GeV were taken and analysed. Results on Σ^- photo-production on the neutron, cross-sections of $K^+\Lambda$ and $K^+\Sigma^0 / K^0\Sigma^+$ and beam polarisation asymmetries have been published. The elementary electro-production cross-sections of kaons were used mainly as a test of production mechanisms [23].

Since 1996 the Jefferson Laboratory (Thomas Jefferson National Accelerator Facility, formerly known as the Continuous Electron Beam Accelerator Facility CE-

BAF) is contributing with a rich experimental programme to the kaon electro-production studies. In Hall C, there is a high momentum spectrometer (HMS) capable of detecting scattered electrons with momenta up to 6 GeV/c, and a short-orbit spectrometer (SOS) capable of detecting decaying secondaries with a maximum central momentum of 1.5 GeV/c in the angular range 12°–165°. Both spectrometers were designed for moderate energy and angular resolutions. The length of HMS from target to detector hut is $\sim$ 25 m, for SOS the distance to the last hodoscope plane is $\sim$ 10 m. The HMS has four superconducting magnets, three focusing quadrupoles followed by a momentum-analysing dipole with a central bend of 25°. The SOS has three normal-conducting magnets, a horizontally focusing quadrupole and two dipole magnets with +33° bend followed by −15° bend. In Hall A there is a pair of identical high resolution spectrometers (HRS) with all magnetic elements superconducting. The momentum range is 0.3–4.0 GeV/c and the angular coverage starts at 12.5° up to large angles.

Jefferson Lab Experiment E03-018 carried out at Jefferson Lab Hall C measured kaon electro-production on hydrogen in the two hyperon channels $\mathrm{p}(e,e'K^+)\Lambda$ and $\mathrm{p}(e,e'K^+)\Sigma^0$. Data in both channels were taken at different values of the virtual photon transverse linear polarization, ϵ, for each of four values of $Q^2 =$ 0.52, 0.75, 1.00, 2.00 $(\mathrm{GeV}/c)^2$. Cross-sections averaged over the angle ϕ were extracted at each point for each hyperon. The first precise Rosenbluth separation of cross-sections into longitudinal and transverse terms were performed with the data taken at this experiment E93-018 [30, 31]. E93-018 achieved a precision of 45% in the separated cross section σ_L and 13% in σ_T at the smallest Q^2. E93-018 resulted in a systematic error on the ratio in the range from 17% to 45% depending on the kinematic bin studied. Experiment E98-108 in Hall A took more data in a kinematic region of higher $Q^2 = 2.35\,(\mathrm{GeV}/c)^2$ and $W \geq 1.80$ [51].

In the low-Q^2 region the ratio of Σ^0 to Λ cross-section may be of interest for further study [31]. The Rosenbluth separated electro-production data from Jefferson Laboratory show a ratio $\Sigma^0/\Lambda \sim 0.2$ for $Q^2 > 0.5\,(\mathrm{GeV}/c)^2$, whereas the photo-production point is at $\Sigma^0/\Lambda \sim 0.5$.

Several measurements have been performed with the CLAS detector at Jefferson Lab Hall B. Measurements on the longitudinal coupling of the photons in the initial state performed by the CLAS collaboration show that $K^+\Lambda$ dominance only occurs at forward kaon angles, and the longitudinal strength is only important at forward angles and higher W [57, 58]. A first measurement of transferred polarisation in the exclusive $\mathrm{p}(\vec{e},e'K^+)\vec{\Lambda}$ reaction has been achieved [57]. New measurements at CLAS have been performed with improved statistical significance and wider energy coverage compared to previous results [59]. However, the CLAS detector has a limited acceptance for four-vector momentum transfers

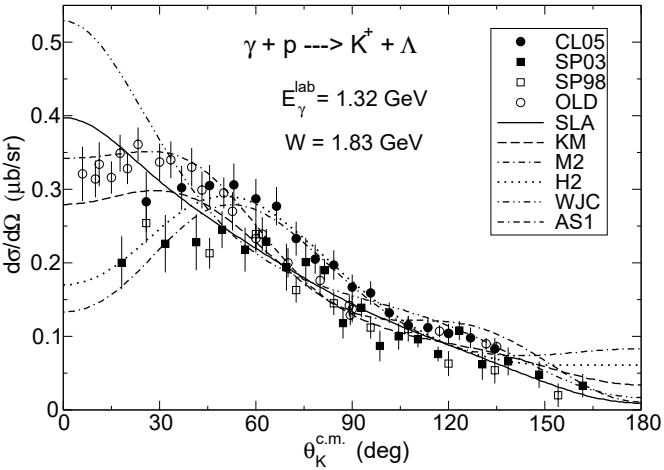

Figure 1.16.: Detailed comparison of the world data set on the differential cross-section for kaon photo-production with effective Lagrangian models (Fig. from [52]). The data points were adopted from Refs. [53] (CL05), [50] (SP03), [28] (SP98), and [22] (OLD). Model predictions are from Saclay-Lyon A (SLA) [26], Kaon-Maid (KM) [21, 29, 54, 55], M2, H2 [56], Williams-Ji-Cotanch (WJC) [19], and Adelseck-Saghai (AS1) [22]. Especially at small kaon angles the effective models differ strongly and the data points are inconsistent.

$Q^2 < 0.5\,(\mathrm{GeV}/c)^2$ and for forward angles.

In spite of the stream of data coming from Jefferson Lab there are still a number of open problems in the interpretation of kaon photoelectro-production data and the description of the process, see Ref. [60] for a recent discussion. Fig. 1.16 shows the comparison of the world data set on the differential cross-section for kaon photo-production with effective Lagrangian models [52]. Especially at small kaon angles the effective models differ strongly and the data points are inconsistent. The most precise experimental data points were published by the CLAS collaboration [53] and the SAPHIR collaboration [28, 50]. However, the two results are inconsistent. The unresolved quest for the kaon production cross-section at forward angles has lead to numerous model predictions which is illustrated in the figure. Measurements of the differential cross-section at small kaon angles from LEPS are available for higher excitations, produced by photon beams with energies from 1.5 to 2.4 GeV. The older data, [50] (SP03), and [22] (OLD),

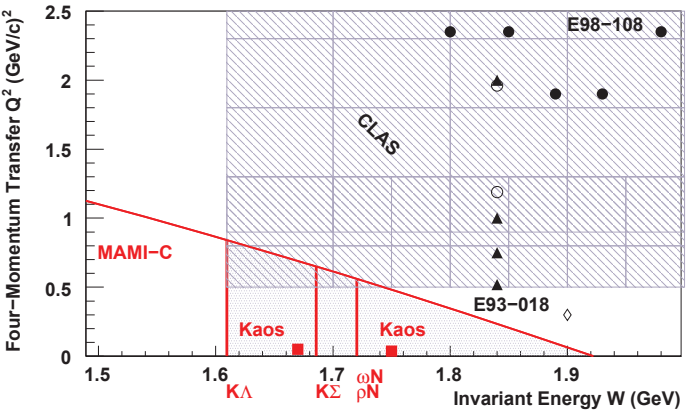

Figure 1.17.: Kinematic coverage of world-data on kaon electro-production showing in red the region accessible with an 1500 MeV electron beam at MAMI-C.

are also considered as being in discrepancy [52]. This situation clearly indicates, that an additional, independent measurement close to this kinematics under forward kaon angles is necessary for a reliable determination of the parameters of the model for the elementary process.

Fig. 1.17 shows the $Q^2 - W$ kinematic region covered by the world data published so far. The measurements reached a number of preliminary conclusions about the production mechanisms. Additional data points at low four-vector momentum transfers would significantly improve the world data-base and resolve the remaining uncertainties.

For calculating hypernuclear production cross-sections, precise data from kaon electro-production processes are urgently required. The elementary amplitude serves as the basic input, which determines the accuracy of predictions for hypernuclei [52, 61]. In the kinematics of the experiments, small kaon and electron angles, only very small values of $Q^2 < 0.1\,(\mathrm{GeV}/c)^2$ are reached which results in a small effect on the amplitudes.

Compared to photo-production, where a good data set of unpolarised and polarised cross-sections exists, the situation in experiments on kaon electro-production in the threshold region seems to be still unsatisfactory. The data collected with electron and photon beams have improved our knowledge of kaon production amplitudes, but their quality is not comparable in terms of statistics and resolution to pion and eta production. One of the main goals of the open strangeness

programme with the KAOS spectrometer remains to provide electro-production data at preferably small kaon angles and small momentum transfers. The lower end-point energy of the MAMI-C machine in comparison with beams from ELSA and CEBAF is of no disadvantage, because the kinematic situation at threshold is well suited for measurements with the KAOS spectrometer.

To conclude, it is fair to say that new experimental data on strangeness production will challenge and improve our understanding of the strong interaction in the low energy regime of QCD.

1.4. THE HYPERON AS A PROBE OF BARYONS

A very interesting phenomenon is the existence of nuclei containing hyperons. Since hyperons in nuclei do not suffer from Pauli blocking by other nucleons, they can penetrate into the nuclear interior and form deeply bound hypernuclear states. As they can decay only weakly they live long enough in the nuclear cores to become bound. When a hyperon, specifically a Λ-hyperon, replaces one of the nucleons in the nucleus, the original nuclear structure changes to a system composed by the hyperon and the core of the remaining nucleons. The hyperon–core system is rearranged quickly by the strong interaction in order to generate a bound state, maximising the binding energy. In its most simplistic form a hypernucleus can be considered as a conventional nuclear core with a hyperon in a single-particle state of the hyperon-nuclear effective potential. However, new nuclear structures, which cannot be seen in ordinary nuclei consisting only of nucleons, may manifest themselves in hypernuclei, providing indispensable information on the flavour $SU(3)$ basis for baryonic matter. The shrinkage of the nuclear size induced by the Λ particle was first confirmed by high-resolution γ-ray experiments [62] in systems composed of a stable nucleus and a Λ particle. Hence, the study of strange nuclear systems provides invaluable information on both, the structure of nuclei as many-body hadronic systems and the structure of baryons in the nuclear medium.

Complementary information on baryon-baryon interactions is mainly obtained from nuclear experiments with projectiles and targets out of ordinary nucleons, addressing interactions in flavour $SU(2)$ only. Hyperon-nucleon (YN) scattering experiments can, in principle, provide basic data on the interactions. The difficulties to study YN interactions by reaction experiments is related to the practical problems in the preparation of low energy hyperon beams and that no hyperon targets are available due to the short lifetimes of hyperons.

Recent calculations of light nuclei based on modern nucleon–nucleon potentials, which also incorporate multi-nucleon interactions, are able to describe the excitation spectra of light nuclei with a very high precision of 1–2 %. The density dependent relativistic hadron field theory (DDRH) has attempted to explain in a unified and self-consistent way the suppression of spin-orbit strength in light hypernuclei as well as the spin-orbit structure observed in more massive nuclei [63]. This is a full quantum field theory enabling an *ab initio* description of strongly interacting many-body systems in terms of mesons and baryons by deriving the in-medium baryon–baryon interactions from free-space interactions by means of Dirac-Brückner theory.

In a phenomenological approach an effective interaction is introduced in which the ΛN interaction is reduced to a hyperon–nucleus potential. In the case of the

ΛN strong potential, the spin-orbit term is known to be much smaller than in NN interactions. In particular, the structure of p-shell hypernuclei was studied by this approach. A deeper understanding of the Λ potential relies on obtaining high quality data for hypernuclei.

The first track of a hypernucleus was observed by M. Danysz and J. Pniewski in a balloon-flown, 600 μm thick, glass-backed Ilford G5 emulsion plate. They reported the observation in October 1952 at a meeting of the Polish Academy of Sciences [64]. This marked the beginning of hypernuclear physics. The phenomenon observed consisted of two "stars" linked by a very heavily ionizing track which in most cases was very short, of the order of 100 μm. The heavy ionization indicates that the particle is heavy and highly charged. The short length of the tracks precludes interaction with another nucleus and indicates spontaneous disintegration. In most cases, a considerable amount of energy was released in the second disintegration; in about half the cases, a pion was also emitted.

Λ-hypernuclei ($S = -1$), being the most stable hypernuclei, have been extensively studied during the past 60 years [65]. Until now, around 40 different Λ-hypernuclear isotopes have been identified. In reaction spectroscopy ground and excited hypernuclear states can be identified by a missing mass analysis of the incident beam and the associated meson. Since these reactions require stable target nuclei, hypernuclei accessible by these reactions are limited. Fig. 1.18 shows the chart of known Λ-hypernuclides today with proton numbers up to $Z = 18$. The convention is to designate the hypernucleus as ${}^{A}_{Y}Z$, where A is the number of baryons (nucleons plus hyperons), Z is the element symbol which designates the charge of the hypernucleus, and Y is the symbol of the bound hyperon. The drip-lines for single Λ hypernuclei were predicted by [66]. The different colors indicate $n \to \Lambda$, $p \to \Lambda$ and $pp \to n\Lambda$ reactions. For $Z < 16$ the reactions populate distinct regions of hypernuclei without overlap. This nicely illustrates the complementarity of the various production mechanisms and the need to study hypernuclei with different reactions. From this chart it is obvious that particularly the production of mirror nuclei — needed to study *e.g.* the charge symmetry breaking in the hyperon-nucleon interaction — requires electro-production experiments.

The production and detection of hypernuclei at accelerators can proceed with different beams using different experimental techniques. In Fig. 1.19 quark flow diagrams of the most relevant reactions mechanisms that have been used in this field are depicted. These diagrams are shown to visualize the processes on the quark level, but are not intended to represent procedures for the calculations. More isotopes are believed to be accessible through heavy ion induced reactions [67]. The present experimental data on hypernuclear binding energies and detailed spectroscopic levels are limited in quantity and quality and refer mostly

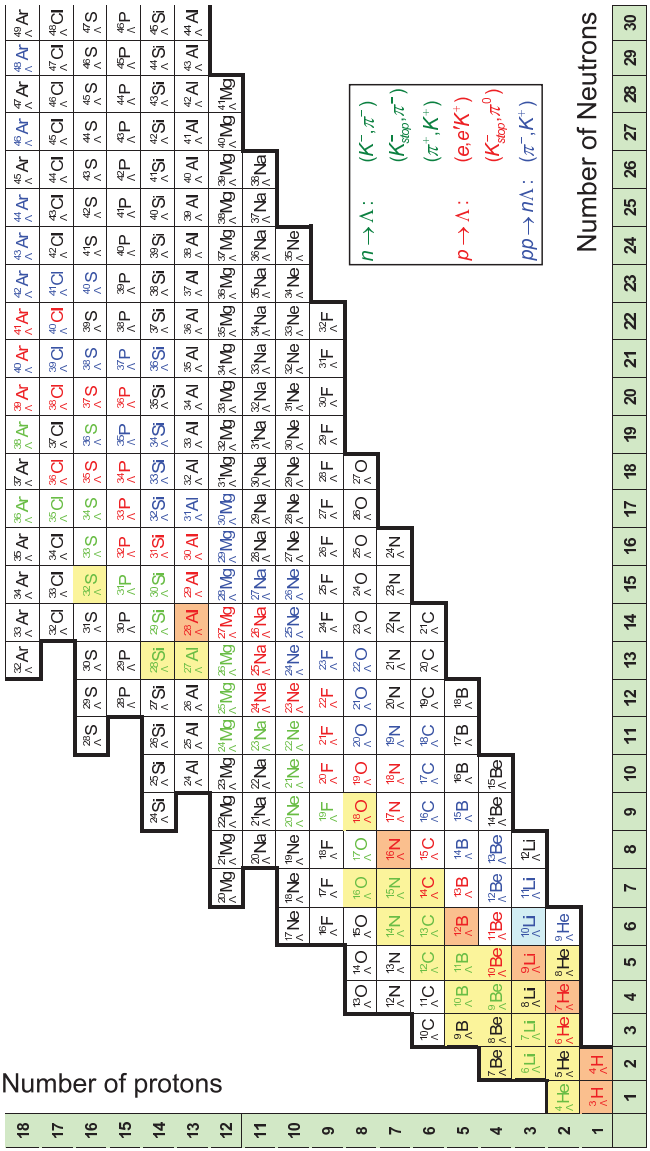

Figure 1.18.: Chart of known Λ-hypernuclides. Green colour: conversion of n→ Λ; red colour: conversion of p→ Λ; blue colour: conversion of pp→nΛ. Isotopes accessible through the different production reactions are almost completely separated in the chart. More isotopes are believed to be accessible through heavy ion induced reactions.

to light (s- and p-shell) hypernuclei. Even though an increasing number of new experiments are now being performed in hypernuclear spectroscopy, our knowledge on hypernuclei is still limited to a small number of isotopes.

The earliest studies were carried out using the aforementioned nuclear emulsions in which kaons have been stopped. Mainly the ground state binding energies of a series of hypernuclei have been determined. From these measurements the depth of the ΛN potential was established to be of the order of $^2/_3$ of the nucleon-nucleon potential. In the 1970s a series of counter experiments started at the proton synchrotrons at CERN and at the Brookhaven National Laboratory (BNL) in the US. The (K^-, π^-) reaction utilized in these experiments made use of the strangeness exchange in flight and led to an energy resolution that was relatively poor ($\Delta E \sim 5\,\mathrm{MeV}$) compared to modern experiments.

One of the factors decisive for the feasibility of an hypernuclei experiment is of course the reaction rate. In order to form a hypernucleus, the hyperon produced in the reaction has to be bound by the core nucleus. The transition form factor depends very much on the transferred momentum to the hyperon. If the momentum transfer is large compared with typical nuclear Fermi momenta, the hyperon will emerge from the nucleus.

The kinematics of the elementary process not only defines the scattering geometry, but can also used to determine the relative "sticking probability" of the recoiling hyperon to the nucleus, which is, of course, included in the nuclear transition form factor. Fig. 1.21 shows the recoil momentum of Λ- and Σ^0-hyperons for three different emission angles of the meson in $\gamma\mathrm{p} \to \mathrm{K}^+\mathrm{Y}$ photo-production, in $\pi^+\mathrm{n} \to K^+\mathrm{Y}$ pion induced production, in $\mathrm{K}^-\mathrm{n} \to \pi^-\mathrm{Y}$ kaon induced production, as well as of Ξ^--hyperons in $K^-\mathrm{p} \to \Xi^- K^+$ charge exchange reaction. The (K^-, π^-) reaction is esoenergetic and is characterised by the existence of a "magic momentum" where the recoil momentum of the hyperon essentially becomes zero. It populates, consequently, substitutional states in which a nucleon is converted to a hyperon in the same orbital state. In these states the neutron hole and the hyperon, namely the Λ, are coupled to $J^P = 0^+$ states with $\Delta L = 0$. By increasing the detection angle of the emitted pion the relative importance of $\Delta L = 1, 2$ transitions increases and hypernuclear states with higher spin can be produced. The spectrum of populated hypernuclear levels is directly reflected in the energy spectrum of the emitted pion. Depending on the momentum of the incident kaon the production proceeds in-flight or at rest. These processes differ both in the branching ratio for the hyperon production and in the kinematics. Since both the initial K^- and the final-state pion are strongly absorbed in the nuclear medium, the kaon induced reactions preferentially populate shallow bound single-particle levels and the reaction has been mainly employed for s- and p-shell hypernuclear studies. In the last 20 years the strangeness exchange reaction

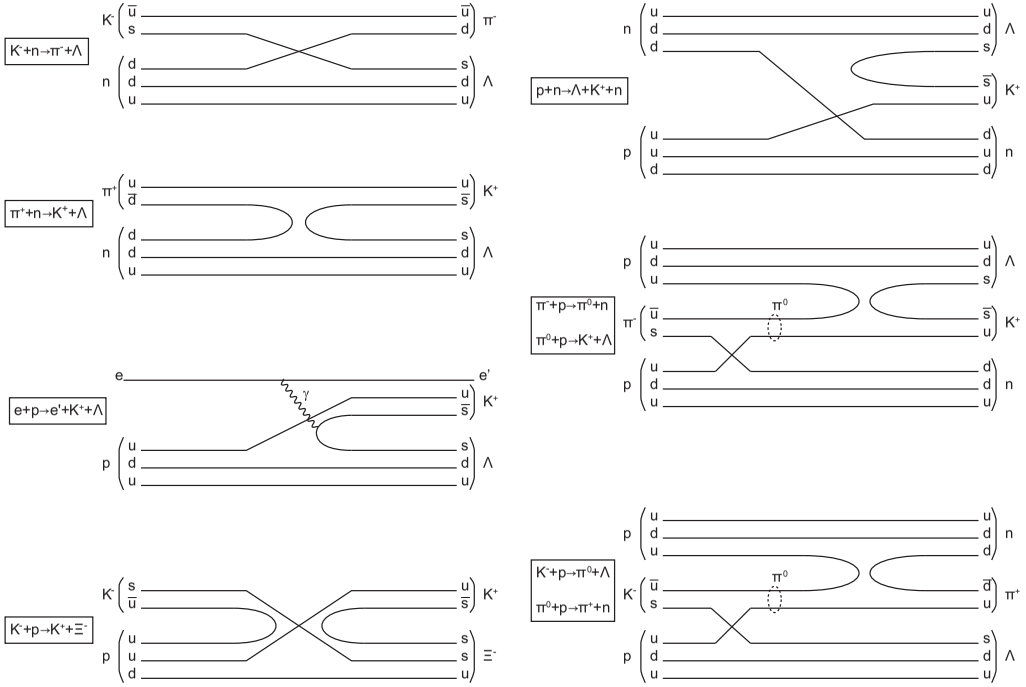

Figure 1.19.: Quark flow diagrams of possible hypernuclei production mechanisms. Kaon and pion induced single Λ-hypernuclei production reactions are shown on the top left side, the corresponding electro-production reaction below, and Ξ-production, leading to double strange hypernuclei, on the bottom left side. On the top right side a possible hadro-production reaction is shown, double charge exchange reactions to produce neutron richer hypernuclei are depicted below.

has been used for production and decay studies of light hypernuclei. However, because of the small momentum transfer and the large background coming from in-flight kaon decays, the measurements could not be extended to heavier hypernuclei.

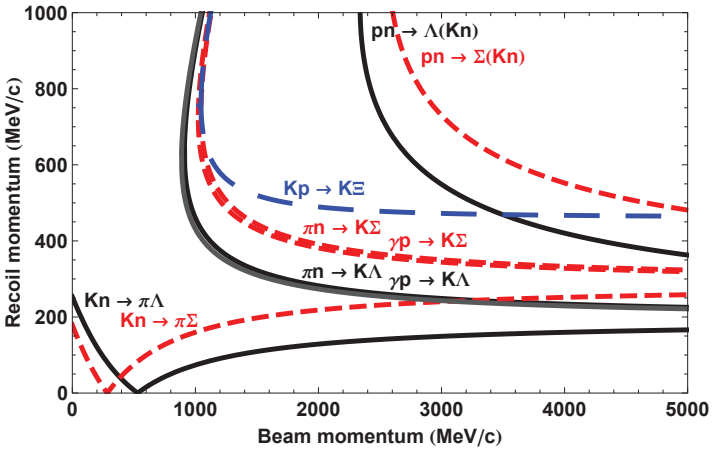

Figure 1.20.: Minimum recoil momentum of Λ, Σ^0, and Ξ^--hyperons in $\gamma p \rightarrow K^+Y$ photo-production, in $\pi^+ n \rightarrow K^+Y$ pion induced production, in $K^- n \rightarrow \pi^- Y$ kaon induced production, in $pn \rightarrow (K^+ n)Y$ hadron induced production, as well as in $K^- p \rightarrow \Xi^- K^+$ charge exchange reaction.

In Fig. 1.20 the minimum momentum transfer to the hyperon $Y = (\Lambda, \Sigma^0, \Xi^-)$ in the reaction $(i, f)Y$ is shown as a function of the projectile momentum p_i at $\theta_f = 0^\circ$ in the laboratory frame. With the exception of the $(K^-, \pi^\pm)$ process the reactions are endoenergetic, the hyperon cannot be produced at rest. The recoil momentum, q_Y, decreases as the projectile momentum increases but remains finite for high q_Y. In this kinematic situation the hyperon is produced with a non-negligible probability above its emission threshold, namely with $B_\Lambda > 0$, in a quasi-free production. Some hypernuclear states in the continuum may be quasi-bound states, not emitting nucleons or clusters of nucleons.

The (K^-_{stop}, π^-) reaction has been studied at KEK and at Frascati, where the non-focusing magnetic spectrometer FINUDA (FIsica NUcleare a DAFNE) was available for the study of Λ hypernuclei levels and life-times, and of their non-mesonic decays. Λ-hypernuclei were produced by stopping negative kaons from ϕ decays in a thin target. The kaons were captured in an atomic level and then

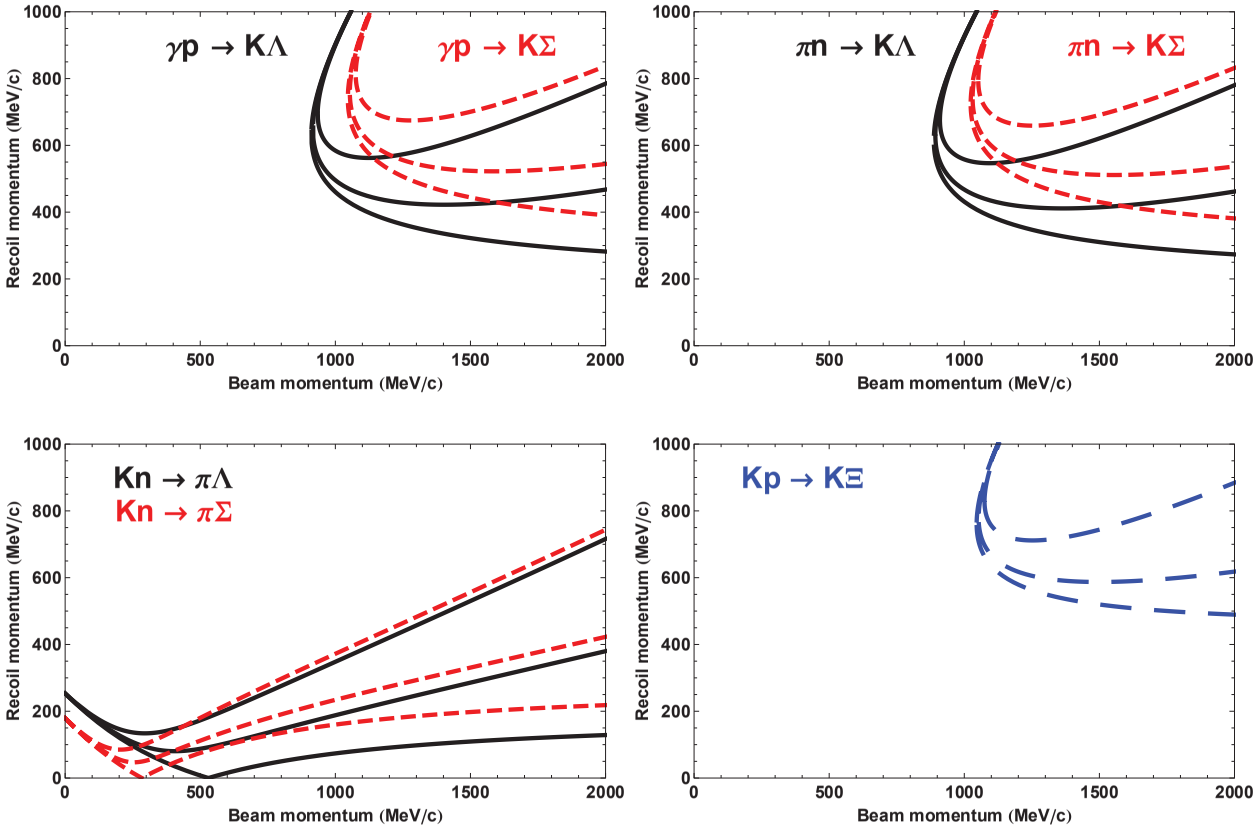

Figure 1.21.: Recoil momentum of Λ- and Σ^0-hyperons for three different emission angles of the final-state meson (θ = 0°, 10°, and 20°) in $\gamma p \to K^+ Y$ photo-production (top left), in $\pi^+ n \to K^+ Y$ pion induced production (top right), in $K^- n \to \pi^- Y$ kaon induced production (bottom left), as well as of Ξ^--hyperons in $K^- p \to \Xi^- K^+$ charge exchange reaction (bottom right).

were cascading down to inner levels, from where they are absorbed at the nuclear surface, converting a nucleon into a hyperon with a prompt negative pion whose momentum is uniquely related to the energy level of the hypernucleus [68]. The transferred momentum is close to the Fermi momentum, $q_\Lambda \simeq 250\,\mathrm{MeV}/c$, and yields a large number of hypernuclear states. Moreover, in contrast to the in-flight reaction, the quasi-free production can cleanly separated, resulting in a good determination of weak decay rates, especially in light systems.

The study of hypernuclei through the (π^+, K^+) and $(K^-, \pi^-\gamma)$ reactions began in the mid-1980s at the alternating gradient synchrotron (AGS) of BNL [69, 70]. Another experimental facility included the 12 GeV proton synchrotron (PS) of the High Energy Accelerator Organization (KEK) in Japan [71–75]. The associated production is complementary to the strangeness exchange reaction and it preferentially populates bound states with high spin configurations. It produces almost background free spectra and it has the advantage of utilizing a pion beam with better definition and higher intensity than available kaon beams. Since the mass of the final hadron pair is sizeable larger than the mass of the initial particle, the reaction is endothermic with a quite large momentum transfer to the hyperon of $q_\Lambda \simeq 300$–$400\,\mathrm{MeV}/c$ at 0° scattering angle.

New experimental techniques have been developed in the 1990s. One major breakthrough was the hypernuclear γ-ray spectroscopy with high-resolution germanium detectors [76]. Through the use of the Hyperball detector array precision spectroscopy with unprecedented resolution of a few keV could have been carried out which provided a wealth of quantitative new information on hyperon-nucleon interactions. Although spin-orbit splittings can now be observed using γ-spectroscopy [77], reaction spectra are equally important because they provide the complete spectrum of excitations with a strength that not only gives the spectroscopic factor, but the transition matrix.

Finally, hypernuclei can also be formed in heavy ion collisions which was first studied by Kerman and Weiss [78]. Neutron or proton rich hypernuclei at extreme isospin have never been so far experimentally accessed. However, information on very neutron rich hypernuclei is essential to understand the nature of neutron stars because several model calculations predict that hyperons are even dominant ingredients in the core of neutron stars [79]. In high energy heavy ion collisions, it is well known that the participant–spectator model explains the general feature of the reaction. The overlapping region between the two nuclei (participants) experiences the collision dynamics, while the nucleons in the off-overlapping region (spectators) pass by each other without experiencing a large disturbance. Hyperons are produced in the participants region at around mid-rapidity. Due to their wide rapidity distribution, hypernuclei may be produced in coalescence with projectile fragments. Because of the energy threshold of $E_{thr} \approx$

1.6 GeV for Λ-production from an elementary process of $NN \to \Lambda KN$, the produced hypernuclei have a large velocity with $\beta > 0.9$, and their effective life-time is longer than at rest due to a large Lorentz factor. Decays of hypernuclei can then be studied in-flight, and most of their decay vertices are a few tens of centimetres behind the target at which the hypernuclei were produced. The HypHI Phase 0 experiment was established to demonstrate the feasibility of hypernuclear spectroscopy with induced reactions of heavy ion beams at GSI. First experiments have been performed in August and October 2009 with a projectile of ^{6}Li at 2 AGeV impinging on carbon graphite target with a thickness of 8 g/cm^2 and a continuation is planned for 2010 [67, 80, 81]. The experiment mainly aims to reconstruct events of ${}^{3}_{\Lambda}$H, ${}^{4}_{\Lambda}$H and ${}^{5}_{\Lambda}$He by observing the π^- decay channel.

Few-body hypernuclear systems with $A = 5$ can be calculated directly from free two-body interactions, in which the calculated binding energies of ground and excited states are compared precisely with experimental data. Studies of hyperon-nucleon (YN) and hyperon-hyperon (YY) interactions provide a unique approach to explore the baryon-baryon interaction. In such studies, information on Λ hypernuclear structure obtained by spectroscopic measurements plays an essential role in testing and improving YN interaction models. Through a quantitative understanding of YN and YY interactions we expect to be better positioned to investigate new aspects and new forms of hadronic matter. In particular, detailed information on YN and YY interactions is indispensable for our understanding of high-density nuclear matter inside neutron stars, where hyperons are possibly mixed and playing a crucial role.

Hypernuclei with mass number $A = 6$ result from the binding of the Λ to an unbound mass-5 core: ^{5}He ($\alpha + n +$ 0.89 MeV) and ^{5}Li ($\alpha + p +$ 1.8 MeV). Although the ground state of ${}^{6}_{\Lambda}$He becomes weakly bound by 0.17 MeV below the ${}^{5}_{\Lambda}$He $+n$ threshold. The three-body binding energy of 3.29 MeV is mostly exhausted to bind the $\alpha + \Lambda$ subsystem [$B_{\Lambda}^{\rm expt}({}^{5}_{\Lambda}{\rm He}) = 3.12$ MeV], and the coupling between the subsystem and the valence neutron is very weak. Hiyama and coworkers took a ${}^{6}_{\Lambda}$He $= \alpha + \Lambda + n$ three-body model and reproduced the observed Λ binding energies [82]. They expect an interesting three-layered structure in ${}^{6}_{\Lambda}$He: α-core, Λ-skin and neutron-halo.

The p-shell $A = 7$ hypernuclei are considered appropriate systems to study the ΛN interaction and in particular its spin dependence. While the ${}^{7}_{\Lambda}$Li and ${}^{7}_{\Lambda}$Be nuclei have been experimentally studied quite well, at the present there is no reliable ${}^{7}_{\Lambda}$He spectra measured. Preliminary experimental data of excitation states in the ${}^{7}_{\Lambda}$He nucleus spectra are available [83, 84]. The data indicates that new experiments are necessary to obtain a reliable value for the ground state energy.

In the low-mass sector there is a long standing interest in the ${}^{9}_{\Lambda}$Be hypernucleus that can be explained by its role in the study of baryon-nucleon interaction, in particular the spin-orbit component of this interaction [85] and by its application to cluster systems [86–90]. Another aspect of interest is related to the possible existence of so-called "genuine" hypernuclear states [91, 92] which do not exist in the $\alpha\alpha$ (^{8}Be) and $\alpha\alpha$N (^{9}Be) nuclear systems. The ${}^{9}_{\Lambda}$Be spectrum was measured in the E336 experiments at BNL [65]. Theoretical results for the ${}^{9}_{\Lambda}$Be spectra were presented a long time ago [86, 87] by Bandō, Ikeda, and Motoba who had used variational calculations in framework of the α-cluster model, as well as $\alpha\alpha\Lambda$, and ^{8}Be + Λ.

1.5. ELECTRO-PRODUCTION OF STRANGE NUCLEAR SYSTEMS

Another new technical development is the use of the $(e, e'K^+)$ reaction for hypernuclear spectroscopy. Electron beams have excellent spatial and energy definitions, and targets can be physically small and thin (10–50 mg/cm^2) which is of great practical advantage in the study of many isotopes. The electron beams available at the Thomas Jefferson National Accelerator Facility permitted the first successful $(e, e'K^+)$ spectroscopy measurements [93]. The study of single Λ-hypernuclei in light targets is also planned at MAMI [94]. The $\mathrm{p}(e, e', K^+)$ reaction, in contrast to most meson-induced reactions, produces hypernuclei by converting a proton into a hyperon and transfers a large momentum to a hypernucleus. The small cross-section for the reaction, $\sigma \sim 140$ nb/sr on a ^{12}C target, compared to strangeness exchange $\mathrm{n}(K^-, \pi^-)\Lambda$ or to associated production $\mathrm{n}(\pi^+, K^+)\Lambda$ is well compensated by the available high electron beam intensities.

In electro-production the angular distribution of kaons associated with a given hypernuclear state is sensitive to the Λ wave function inside the nucleus [23, 95]. A hypernuclear Λ-probe samples the nuclear core where there is little direct information on the single particle structure. In addition, high resolution spectroscopic studies of hypernuclei can be performed in order to provide the most valuable experimental information on the Λ dynamics in nuclei. The electro-production process has the unique characteristic of providing large amplitudes for the population of spin-flip hypernuclear states with unnatural parities [96]. The experimental technique is now fully developed for Λ hypernuclear investigations and is used by the E01-011 Collaboration [84, 97, 98]. Indeed, the high precision of electron beams can considerable improve the quality of experimental data. These developments are expected to greatly expand the possibilities for strangeness nu-

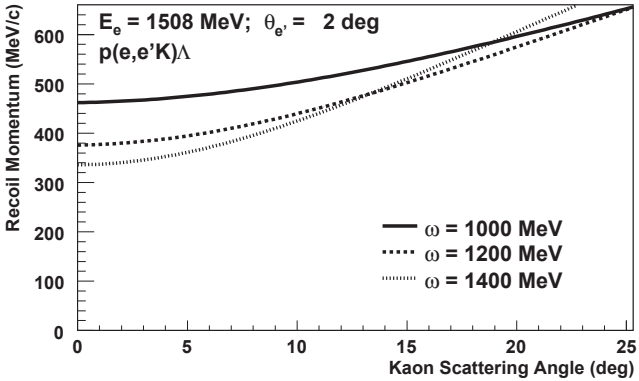

Figure 1.22.: Recoil momentum in $p(e,e'K^+)\Lambda$ electro-production as a function of kaon angle for varying photon energies. The incident electron energy, E_e = 1508 MeV, and the scattering angle, $\theta = 2^\circ$, were fixed.

clear physics in the coming years.

The recoil momentum of the hyperon is:

$$\vec{p}_Y = \vec{p}_{KY} - \vec{p}_K \tag{1.29}$$

and can be solved for a given kaon electro-production kinematics following the relations of Eq. 1.9. Fig. 1.22 shows the recoil momentum as a function of the relative kaon angle for several incident photon energies for fixed electron incident energy and scattering angle. Typical momentum transfers range from 350 MeV to 500 MeV.

In Fig. 1.23 the scattered electron momentum is plotted versus the maximum kaon momentum, where Λ- and Σ-hyperon production has been calculated for the elementary reaction on the proton and ${}^{12}_{\Lambda}$B hypernuclei production has been calculated on a carbon target.

Assuming three-momentum conservation at the vertices of the Feynman diagram in impulse approximation the transferred momentum can be written as the difference between Λ momentum, $\vec{p}_\Lambda$, and core nucleus momentum, $\vec{p}_{A-1}$, and is a function of the momentum of the virtual proton, $\vec{k}$, and the recoil momentum of the hypernucleus, $\vec{p}_Y$: $q(k) \equiv \left|\vec{p}_\Lambda - \vec{p}_{A-1}\right| = \left|\vec{p}_Y + 2\vec{k}\right|$. For the kinematic optimization an approximate Fermi Gas distribution for the virtual proton, $F = 2\pi \int_0^\infty n(k)k^2\,dk$ was assumed, where the distribution function, $n(k)$, is Gaus-

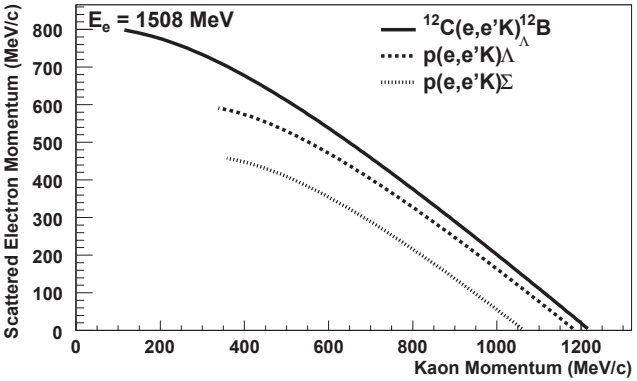

Figure 1.23.: Kinematic correlation between scattered electron momentum and maximum kaon momentum in elementary $p(e,e'K^+)Y$ and ${}^{12}_{\Lambda}$B hypernuclear reactions.

sian,

$$n(k) = (2^{-4}k_F\sqrt{\pi})^{-3}\exp -\sqrt{2}k^2/k_F^2\,. \tag{1.30}$$

By modeling the transition form factor with an exponential function,

$$S_\Lambda = \iint \exp(-q(k)/\sigma_p)n(k)\,k^2\,\mathrm{d}k\,\mathrm{d}\cos\theta\,, \tag{1.31}$$

the function can be evaluated for given kinematic variables:

$$\begin{aligned} S_\Lambda = \; & \tfrac{1}{2p_Y\sigma_p}\Big\{\exp\tfrac{k_F^2}{\sqrt{2}\sigma_p^2} - \tfrac{p_Y}{\sigma_p}\Big(\\ & \big(-\sqrt{2}k_F^2 + p_Y\sigma_p\big)\,\mathrm{Erfc}\big[-\frac{p_Y}{\sqrt{2\sqrt{2}}k_F} + \frac{k_F}{\sqrt{\sqrt{2}}\sigma_p}\big] \\ & + \exp\frac{2p_Y}{\sigma_p}\left(\sqrt{2}k_F^2 + p_Y\sigma_p\right)\,\mathrm{Erfc}\big[\frac{p_Y}{\sqrt{2\sqrt{2}}k_F} + \frac{k_F}{\sqrt{\sqrt{2}}\sigma_p}\big]\Big)\Big\}\,. \end{aligned} \tag{1.32}$$

Since electro-production is a high momentum transfer reaction similar to the (π^+,K^+) process, the transition form factor takes a minimum at threshold and increases as the virtual photon energy increases. An interpretation of the transition form factor in terms of a sticking probability is given, for example, in [92], for the case of harmonic oscillator wave functions. Using this interpretation the sticking probability prevails at low q and substitutional states are exclusively popu-

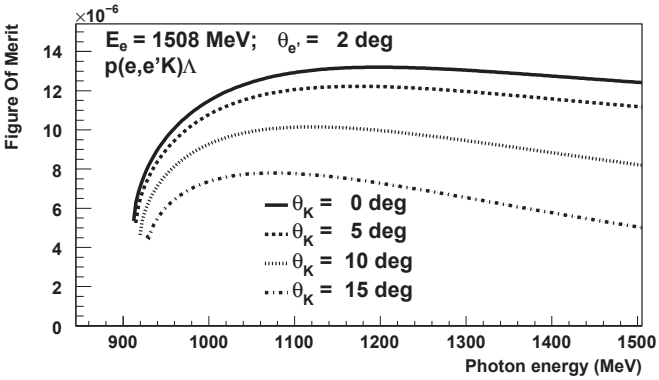

Figure 1.24.: Figure-of-merit for the hypernuclei formation rate as a function of the virtual photon energy calculated from the virtual photon flux times a transition form factor. The incident electron energy, E_e = 1508 MeV, and the scattering angle, $\theta = 2^\circ$, were fixed. The yield decreases with increasing kaon angle.

lated, whereas at $q \sim k_F$, high quantum numbers and spin-stretched states are favoured.

One can perform a kinematic optimisation using a *F*igure *O*f *M*erit for the formation rate defining $FOM = S_\Lambda \times \Gamma$. Fig. 1.24 shows the figure-of-merit as a function of the virtual photon energy, ω, for the $e+^{12}\mathrm{C} \rightarrow e' + K^+ + ^{11}_{\Lambda}\mathrm{B}$ reaction. In this model typical values of $\sigma_p = 100\,\mathrm{MeV}/c$ and $k_F = 200\,\mathrm{MeV}/c$ were assumed.

In 2000, first electro-production experiments were performed at Jefferson Lab on carbon targets demonstrating the feasibility of spectroscopy of $^{12}_{\Lambda}\mathrm{B}$ hypernuclei [83, 93]. In these pioneering experiments the error in the reconstructed kaon scattering angle was about 13 mrad (FWHM), and was dominated by the horizontal angular measurement error, when the short orbit spectrometer (SOS) was used as kaon arm. The first measurements reported a missing mass resolution of 3.5 MeV (FWHM) which was dominated by the kinematic broadening due to the Λ recoil [93]. These measurements were also limited in statistics, but triggered new activities at Jefferson Lab [103, 104]. Experiment E94-107 was performed in 2004–5 and experiment E01-011 in 2005. The former achieved an energy resolution of $\Delta E \sim 640$ keV (FWHM) in the $^{12}_{\Lambda}\mathrm{B}$ spectrum and obtained, in addition, the excitation spectra for $^{9}_{\Lambda}\mathrm{Li}$ and $^{16}_{\Lambda}\mathrm{N}$. Experiment E01-011 provided preliminary

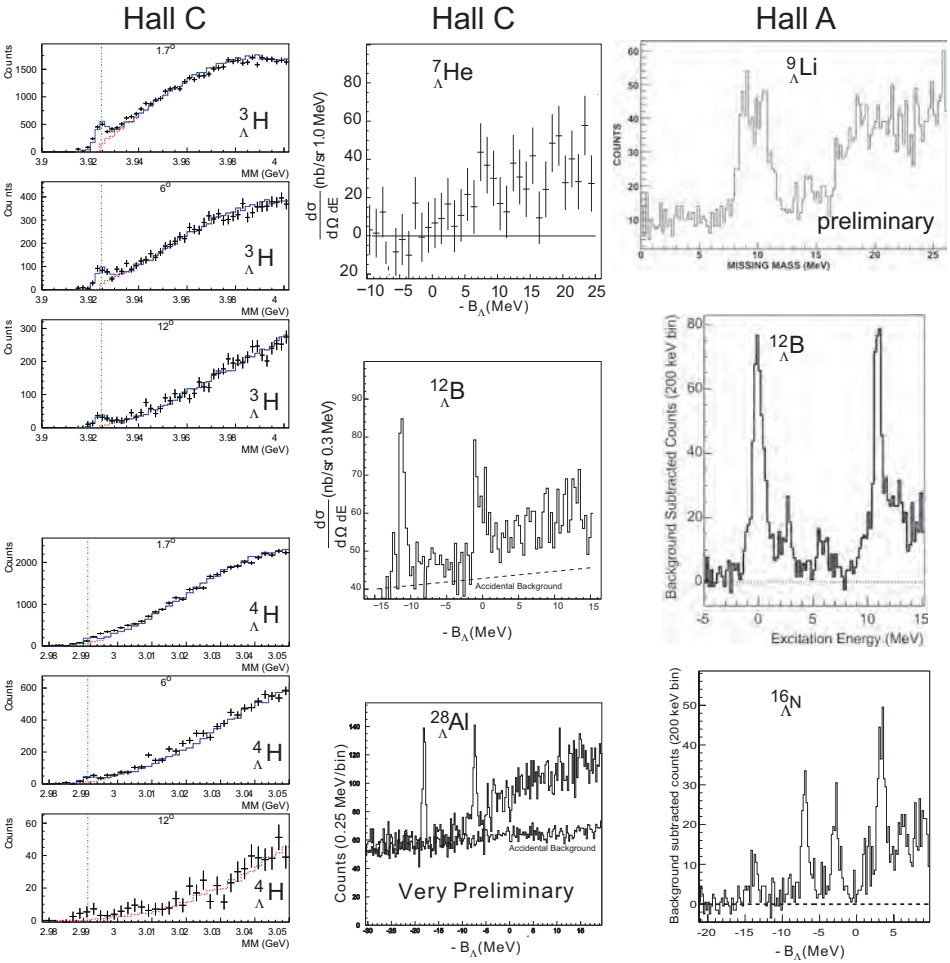

Figure 1.25.: Compilation of Λ-hypernuclei reaction spectra taken at Jefferson Lab in Hall A and Hall C experiments. Data from [83, 99–102].

excitation spectra for ${}^{7}_{\Lambda}$He and ${}^{28}_{\Lambda}$Al [105]. The experimental geometry included a new high resolution kaon spectrometer and implemented a "tilt method" for the electron spectrometer to increase the hypernuclear yield and the signal to noise ratio by avoiding the electron background at zero degrees. In the year 2009 experiment E05-115 took data on various low to medium-mass targets, which is now under analysis.

Though fifty years have already passed since its discovery, hypernuclei are still at the forefront of nuclear physics. On one hand the hyperon embedded in a nuclear system serves as a probe for the nuclear structure and its possible modification due to the presence of the hyperon. On the other hand properties of hyperons may change dramatically if implanted inside a nucleus. Thus, a nucleus serves as a laboratory offering a unique possibility to study basic properties of hyperons.

flower
under harvest sun — stranger
to bird, butterfly

Matsuo Bashō (1644–94)

2 THE KAOS SPECTROMETER

2.1. FOCUSING MAGNETIC SPECTROMETERS

Though experiments that need high-resolution spectroscopy of charged particles can be performed by means of a great number of different instruments and a large variety of complimentary techniques, the magnetic focusing spectrometer is a basic instrument, which has proved to be of greatest general use. Combined with suitable particle detectors it can resolve nuclear spectra or the energy of secondarily produced particles in considerable detail.

The magnetic design of a spectrometer is based on the fundamental equations of charged particle dynamics. The force on a particle of charge q and velocity v moving through a magnetic field B is given by:

$$\frac{\mathrm{d}\vec{p}}{\mathrm{d}t} = q \cdot (\vec{v} \times \vec{B}) = q \cdot (\vec{p}/m \times \vec{B}) \tag{2.1}$$

Since the magnetic force is always perpendicular to the direction of motion of the particle, its momentum p is conserved. The magnetic force produces a centripetal acceleration, and assuming for simplicity that the velocity is perpendicular to the magnetic field, the following equation is obtained:

$$\frac{mv^2}{\rho} = q \cdot |v| \cdot |B| \tag{2.2}$$

where ρ is the orbit radius, sometimes called the gyroradius of the particle.

Eq. 2.2 reduces to $B\rho = p/q$ which is relativistically correct with $p = \beta c\gamma m$ being the relativistic momentum. The product $B\rho$ is called the magnetic rigidity of the particle. If the particle momentum is given in GeV/c, then the rigidity, in tesla-metres, is $B\rho = 3.3356p$. Obviously, it's this relationship between the momentum and the magnetic rigidity that forms the basis for magnetic spectroscopy.

The main definition of a spectrometer is that of an instrument in which particles of different momenta (magnetic rigidities) are spatially separated on a position-sensitive detector after passing through the magnetic field region or regions. Coupled with this is the requirement that particles emitted into as large a solid angle as possible must be accepted from the source (target) in order to avoid excessive exposure times. What is required is precision optical focusing such that particles emitted into a given solid angle and having the same momentum are focused to a small spot or line on the detector. Using the terminology from light optics the momentum resolution of the instrument depends upon its optical magnification and momentum dispersion. At the same time the range of momenta covered by the spectrometer should be sufficiently large for the application. In a magnetic spectrometer with fixed geometry and B variable the quantity $R = \Delta p/p$ is constant, where Δp is a measure of the accepted momentum band.

Magnetic spectroscopy of nuclear particles is as old as nuclear physics itself. In 1899 H. Becquerel used what is nowadays known as a 180° single-focusing magnetic spectrometer to show the deflection of beta radiation. In 1910 the first determinations of the energies of electrons following nuclear decays were carried out using a narrow slit, a deflecting magnetic field, and a photographic plate. The acceptance and resolving power was very poor since no focusing was used [106].

Two basic types of focusing are obtained by means of a homogeneous field working either perpendicular to the rays, in which case the charged particles describe circles, or nearly parallel to the rays, when they describe helical paths. The transverse homogeneous field focuses charged particles only in one plane, whereas the longitudinal field is space-focusing. Historically, these two types of focusing were developed very early, and in particular the deflecting type was, except for a few preliminary trials of the helical method, the only one in use before the beginning of the 1940s [107]. In fact, the first magnetic focusing device is due to J. Danysz [108] who in 1912 suggested the so-called semicircular focusing principle.

In the 1930s strong electromagnets were used by Rutherford to make important advances in the knowledge of nuclear structure by studying the fine-structure of α-particle groups. The most powerful magnet was cylindrical in design with a homogeneous field between two annular rings, that bent the tracks into semicircles and provided first-order focusing [109]. The first spectrometer used for high resolution energy measurements of charged particles emitted in nuclear reactions were designed by R. J. Van de Graaff, W. W. Buechner, and co-workers at the Massachusetts Institute of Technology in the 1940s on the basis of Rutherford's α-particle spectrometer. It was operated with deuteron or proton beams accelerated in a 2 MeV Van-de-Graaff generator. Almost simultaneously, a double-focusing spectrometer was built by C. C. Lauritsen's group at the California Insti-

tute of Technology [110]. The instrument featured an inhomogeneous magnetic field that provided the desired focusing properties.

The popularity of high-resolution magnetic spectrometers for charged particles produced in nuclear reactions of accelerated beams with targets is due to the fact that they provide the most accurate measurement of the kinematic quantities [111]. By properly shaping the magnetic field one can reconstruct the momentum vector of the particle and the location of the interaction at the target from measurements in the focal-surface. The particle can be identified by a suitable array of detectors behind the focal-surface from which its four momentum is completely determined. These measurements can be done in a well shielded and reasonable quiet area out of the line of sight of the target. With the knowledge of the four-momenta of the measured particles and the incident beam one can determine the reaction.

Words such as focusing, dispersion, focal lengths, principal planes, resolution, resolving power, *etc.* have all the same meaning in charged particle optics as in light optics. A convex glass lens has the property that light rays passing through it are deflected towards the axis by an angle that to first order is proportional to the distance from the center of the lens. As a result, a bundle of parallel rays converges towards a point after passing the lens. Charged particle lenses, *i.e.* solenoids, quadrupole lenses and deflecting magnets, focus particles in much the same way, but with some complications relating to the fringing fields and the appearance of divergence and convergence in the same optical element. The most difficult problem, then, turns out to be to minimize aberrations in this imaging process such that the largest possible solid angle can be utilized. Any charged particle spectrometer can be treated like an optical system [110, 112].

The momentum resolution of a spectrometer is determined by the source dimensions (or the width of the beam on target), the aperture, and the focusing aberrations. A particle is assumed to be emitted from (or passing through) point x_o, y_o, in the plane $z_o = 0$. One specific choice of a coordinate system is a right-handed one in which x is pointing in the dispersive direction, z is along the particle's momentum, and y is perpendicular on both. For simplicity, in the following discussion it is assumed that the system is mechanically symmetric about a plane assumed to be the xz plane and that the magnetic field is everywhere perpendicular to the symmetry plane, *i.e.* $B_x = B_z = 0$. This then will have to be the median plane of any dipole magnet (deflecting magnet) and a symmetry plane between poles of any quadrupole or higher order multipole magnet. From this symmetry the following field properties are derived:

$$\begin{aligned} B_x(x,y,t) &= -B_x(x,-y,t) \\ B_y(x,y,t) &= B_y(x,-y,t) \\ B_z(x,y,t) &= -B_z(x,-y,t) \end{aligned} \tag{2.3}$$

The direction of the particle before entering the system is specified by the angles θ_o and ϕ_o. The coordinates are parameterised by t along the trajectory. The central ray is defined as the trajectory in the symmetry plane of the spectrometer of a particle that emerges from the central point of the target. A first-order dispersion is generated in regions where the central trajectory is deflected, *i.e.* in dipole elements. An arbitrary track is described by the functions $x(t)$ and $y(t)$, the displacements from the reference ray in median plane and perpendicular to the median plane, and the angular functions $\theta(t) = \mathrm{d}x/\mathrm{d}t$ and $\phi(t) = \mathrm{d}y/\mathrm{d}t$. A reference momentum p_o is assumed and the deviation from this momentum is given as $\delta = \Delta p/p_o$. The path-length difference to the reference ray is noted by l. The position at the exit is clearly a function of the position and direction at the entrance and of the momentum. Explicitly, the particle's trajectory is expanded around the reference ray as a function of the target coordinates x_o, θ_o, y_o, ϕ_o, δ:

$$\begin{aligned} x(t) &= \sum_{i,j,k,l,m} \langle x|x_o^i\theta_o^j y_o^k \phi_o^l \delta^m\rangle \; x_o^i\theta_o^j y_o^k \phi_o^l \delta^m \\ \theta(t) &= \sum_{i,j,k,l,m} \langle \theta|x_o^i\theta_o^j y_o^k \phi_o^l \delta^m\rangle \; x_o^i\theta_o^j y_o^k \phi_o^l \delta^m \\ y(t) &= \sum_{i,j,k,l,m} \langle y|x_o^i\theta_o^j y_o^k \phi_o^l \delta^m\rangle \; x_o^i\theta_o^j y_o^k \phi_o^l \delta^m \\ \phi(t) &= \sum_{i,j,k,l,m} \langle \phi|x_o^i\theta_o^j y_o^k \phi_o^l \delta^m\rangle \; x_o^i\theta_o^j y_o^k \phi_o^l \delta^m \end{aligned} \tag{2.4}$$

The bracketed terms are called the spectrometer matrix elements. If the exit coordinate is measured at or extrapolated to the position where $\langle x/\theta_o\rangle = 0$, which is by definition the focal-surface, one can derive the matrix elements that relate the focal-surface coordinates to those at the target. Thus,

$$x_f = f(x_o, \theta_o, y_o, \phi_o, \delta) \tag{2.5}$$

with similar expressions for y_f, θ_f, and ϕ_f. The focal-surface parameters x_f, θ_f, y_f, and ϕ_f uniquely define a track for each event. Central rays for different values

of p/B reach the focal-surface at different positions. One can then express Eq. 2.5 as a Taylor expansion in $x_o, \theta_o, y_o, \phi_o, \delta$. The quantities x_o and y_o are presumably small (relative to, for instance, the dimensions of the spectrometer) because they represent the beam-spot size at the target. The angles θ_o and ϕ_o are generally less than 100 mrad. For a broad-range spectrometer δ is not necessarily small.

One can define the first-order resolving power of the system as the inverse or the fractional change in momentum needed to displace the first-order image a distance equal to its width. The first-order image width is $\Delta x_f = M_x \Delta x_o$, where the magnification is $M_x = |\langle x_f | x_o \rangle|$. A momentum change $\delta = \Delta p / p_o$ displaces the image by $\Delta x = D\delta$ where the dispersion is $D = \langle x_f | \delta \rangle$. Hence,

$$\mathcal{R} = \frac{p_o}{\Delta p} = \delta^{-1} = \frac{D}{M_x \Delta x_o}. \tag{2.6}$$

For a large momentum acceptance spectrometer D/M_x should be treated as a function of p, often increasing with p. The best first-order resolving power is then clearly obtained at the upper end of the range. If the target spot size is small enough one can neglect any term in x_o, except the first-order term, the magnification. When the momentum also depends on quantities other than x_f, chromatic aberrations are present. Matrix calculations including second-order aberrations were introduced by K. Brown and co-workers in 1964 [113].

The inverse matrix is used to calculate the coordinates at the target from the measured focal-surface coordinates. Quantities Q, *i.e.* y_o, θ_o, ϕ_o and δ, that depend on the particle coordinates measured at the detector, can be expressed in these coordinates by the Taylor series

$$Q = \sum_{i,j,k,l} \langle Q | x_f^i y_f^j \theta_f^k \phi_f^l \rangle \; x_f^i y_f^j \theta_f^k \phi_f^l \tag{2.7}$$

The function Eq. 2.7 is not normally a determinable analytic function. The Taylor expansion is therefore not performed in the conventional way by taking analytic derivatives. Rather, it is done by numerical techniques. For magnetic spectrometers with static, homogeneous fields with median plane symmetry the first-order matrix reads as follows:

$$\begin{pmatrix} x(t) \\ \theta(t) \\ y(t) \\ \phi(t) \\ l(t) \\ \delta(t) \end{pmatrix} = \begin{pmatrix} R_{11} & R_{12} & 0 & 0 & 0 & R_{16} \\ R_{21} & R_{22} & 0 & 0 & 0 & R_{26} \\ 0 & 0 & R_{33} & R_{34} & 0 & 0 \\ 0 & 0 & R_{43} & R_{44} & 0 & 0 \\ R_{51} & R_{52} & 0 & 0 & 0 & R_{56} \\ 0 & 0 & 0 & 0 & 0 & 1 \end{pmatrix} \begin{pmatrix} x_o \\ \theta_o \\ y_o \\ \phi_o \\ l_o \\ \delta \end{pmatrix} \tag{2.8}$$

The first-order transfer matrix elements R_{ij} are called transfer coefficients and represent actually the first-order derivatives $\partial x_f / \partial x_o$. The fact that the matrix elements $R_{13} = R_{14} = R_{23} = R_{24} = R_{31} = R_{32} = R_{41} = R_{42} = R_{36} = R_{46}$ vanish is a consequence of the median plane symmetry of the magnetic field. Some of the matrix elements have a simple optical meaning. A first-order point-to-point transformation in the dispersive plane, xz, is achieved if x_f is independent of the target angle θ_o, $R_{12} = 0$, or similarly in yz. The dispersion relation between the momentum p (in fact δ) and the focal-surface position is given by the coefficient $R_{11} = \langle \delta | x_f \rangle$. A first-order parallel-to-point transformation in xz is achieved if x_f is independent of x_o, $R_{11} = 0$, or similarly in yz.

These concepts are known for a long time, see *e.g.* [114], and in the following sections on the spectrometers at MAMI there are frequent references to them.

2.2. THE SPECTROMETER FACILITY AT MAMI

The spectrometer facility at MAMI operated by the A1 collaboration offers the opportunity to electron scattering reactions on various solid-state or liquid cryogenic targets in a wide range of kinematics. Since the 1990s the spectrometer facility consisted of three vertically deflecting magnetic spectrometers (SpekA, SpekB, and SpekC) rotating around a common pivot and with deflection angles of 90° to 120° and high momentum resolution [115]. The set-up was complemented in few cases by further magnetic or non-magnetic instruments, for instance, a short-orbit pion spectrometer. The facility was used extensively for the study of electromagnetic form-factors, for meson (π and η) production, virtual Compton scattering, and other topics in hadron physics, see http://wwwa1.kph.uni-mainz.de/A1/ for information on the facility and the experiments performed there. The main spectrometer parameters are summarized in Table 2.1.

SpekA and SpekC employ a quadrupole-sextupole-dipole-dipole magnet combination in order to achieve a large acceptance. SpekB uses a single clam-shell dipole magnet. The optics of SpekA and SpekC provides point-to-point focusing in the dispersive plane which ensures the independence of the x_f coordinate measured by the focal-plane detectors from the initial angle θ_o at the target. In the non-dispersive direction the optics provides parallel-to-point focusing, meaning that the y_f coordinate measured in the focal plane is insensitive to the initial position y_o. The optics of SpekB as defined by a single dipole magnet provides point-to-point focusing in both planes. This construction design lead to a narrow spectrometer which can reach small scattering angles (down to 7°). SpekB can also be tilted for reaching out-of-plane angles up to 10°.

The standard detector package of each of the high-resolution spectrometers

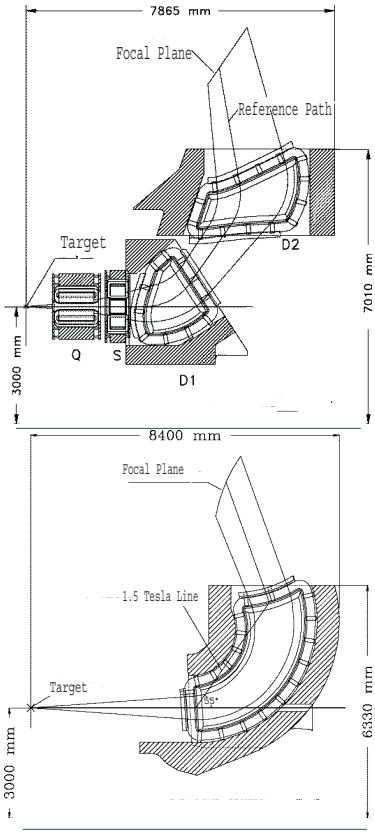

	SpekA	SpekC
configuration	QSDD	
max. mom. (MeV/c)	735	551
ref. mom. (MeV/c)	630	459
cent. mom. (MeV/c)	665	490
solid angle (msr)	28	28
momentum acceptance	20 %	25 %
momentum resolution	10^{-4}	10^{-4}
ang. res. at target (mrad)	< 3	< 3
pos. res. at target (mm)	3–5	3–5
length central path (m)	10.75	8.53

	SpekB
configuration	clam-shell D
max. momentum (MeV/c)	870
ref. momentum (MeV/c)	810
cent. momentum (MeV/c)	810
solid angle (msr)	5.6
momentum acceptance	15 %
momentum resolution	10^{-4}
ang. res. at target (mrad)	< 3
pos. res. at target (mm)	1
length central path (m)	12.03

Table 2.1.: Main parameters for the spectrometers A, B, and C and their geometrical design (Fig. from A1 Collaboration). SpekC is scaled-down from SpekA, and SpekB is a clam-shell single-dipole spectrometer. Compared to the KAOS spectrometer the maximum acceptable momenta are much lower, and the lengths of the central paths are much longer. On the other hand the momentum resolution is higher. The solid angle acceptance is comparable, but the KAOS spectrometer has a larger in-plane angular acceptance.

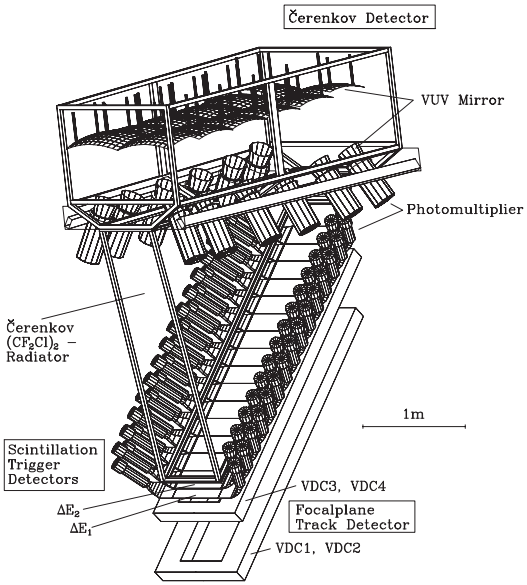

Figure 2.1.: Focal-plane detector package of the high resolution spectrometers: two vertical drift chambers, two planes of segmented scintillators and a gas-filled threshold-Cherenkov detector for electron–pion separation (Fig. from A1 Collaboration).

consists of four vertical drift chambers (VDC) triggered by a double layer of plastic scintillators, see Fig. 2.1 for a schematic drawing. Two VDC planes have wires in the non-dispersive direction, while the other two are aligned in a 40° diagonal direction with respect to the other planes. The wires (200 up to 300 depending on the plane considered), with 5 mm spacing between each other, are hold at ground potential, while the foils are set at negative potential ($U \sim 5000$ V). A gas mixture of argon and isobuthan is used.

The particles traverse the VDC with an average angle of 45° to the normal of the plane, producing 5 average hits for each plane. The VDC measure the particles coordinates in the focal plane which are then used for determining the target coordinates and the particle momentum. The resolutions reported in Table 2.1 are obtained with a spatial resolution in the drift chambers of $\sigma_x \leq 200\,\mu$m in the dispersive plane and $\sigma_y \leq 400\,\mu$m in the non-dispersive plane.

Two segmented plastic scintillator planes serve as trigger for the data acquisition system and for the drift chamber reference time. The scintillator signal is

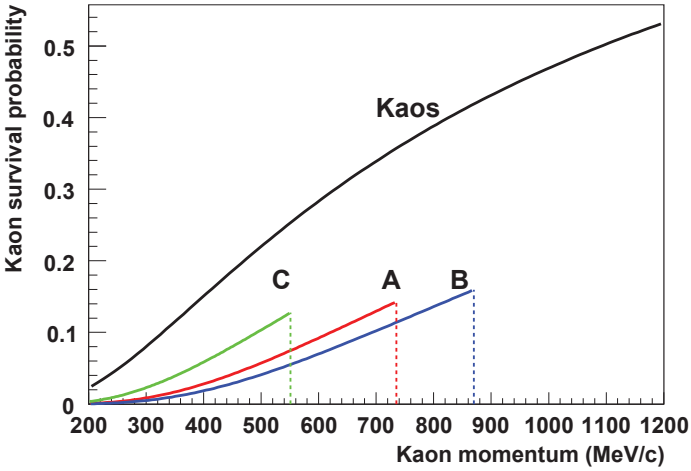

Figure 2.2.: Survival probability for kaons to be detected in the high resolution spectrometers A, B, and C as well as in the KAOS spectrometer. The momentum acceptance of the high resolution spectrometers is limited by the indicated maximum momenta.

also used for realizing the coincidence between the spectrometers. Each plane has 15 segments of dimensions $45\times16\,\mathrm{cm}^2$ for SpekA and SpekC and $14\times16\,\mathrm{cm}^2$ for SpekB. The segmentation enhances the time resolution and gives also a rough information about the particle's position. The segments are coupled to photomultipliers which are read-out by ADC and TDC. The first plane in respect to the particle's path is 3 mm thick and is primarily used for the energy-loss determination, while the second plane with 10 mm thickness is primarily used for the time-of-flight measurement. Using the correlation of the energy-losses in the two planes, particle identification can be done and minimum-ionizing particles can be distinguished from protons.

Pions cannot be separated form electrons or positrons by their energy-loss, and for this purpose gas-filled threshold-Cherenkov detectors are used. The produced Cherenkov radiation is reflected by mirrors to photomultipliers generating the signal. The detectors are placed behind the VDC and the scintillator planes inside the detector huts. Electrons (or positrons) have a momentum threshold for Cherenkov radiation of about 10 MeV/c, all pions produced with the MAMI beam have momenta below the threshold at about 2.4 GeV/c. In the typical energy ranges of the experiments, all electrons entering the volume of the Cheren-

Table 2.2.: Selected magneto-optical properties of spectrometer B (SpekB) and the KAOS hadron arm that were used for the kaon electro-production beam-times of 2008–9. The main difference of the KAOS spectrometer to the high resolution spectrometers is the short distance of 5–6 m from target to focal-surface which reduces the number of kaon decays in flight.

	SpekB	KAOS hadron arm
maximum momentum (MeV)	870	2 100
momentum acceptance (%)	15	50
solid angle acceptance (msr)	5.6	10.4
dispersive angle acceptance (mrad)	± 70	± 185
do. (°)	± 4	± 10.5
non-dispersive angle acceptance (mrad)	± 20	± 14
do. (°)	± 1.15	± 0.8
length of central trajectory (m)	12.03	5.3
angle of focal-surface (°)	47	~ 45
length of focal-surface (m)	1.8	~ 1.2
dispersion at central trajectory (cm/%)	8.22	2.4
magnification at central trajectory	0.85	2.0
dispersion to magnification (cm/%)	9.64	1.2
first-order resolving power	19 000	2 400
first-order momentum resolution	$< 10^{-4}$	$\sim 10^{-3}$

kov detector give rise to a clear signal and the detection efficiency is very close to 100 %.

Experimentally, the conservation of the strangeness quantum number in electromagnetic and strong interactions allows the tagging of baryonic systems with open strangeness, *e.g.* hyperons or hypernuclei, by detecting a kaon in the final channel. However, the detection of kaons is not effective with the high-resolution spectrometers due to the short life-time of the charged kaons and the long flight path through the spectrometers.

About ten years ago, the KAOS spectrometer was considered to be ideal for the strangeness electro-production programme at MAMI. The KAOS spectrometer is a very compact instrument suitable especially for the detection of kaons [116].

Fig. 2.2 shows the survival probability for kaons to be detected in the high resolution spectrometers SpekA, SpekB, and SpekC as well as in the KAOS spectrometer. The momentum acceptance of the high resolution spectrometers is limited by the indicated maximum momenta. The most important properties of the KAOS spectrometer as discussed in the following sections are compiled in Table 2.2 and compared to the data of SpekB, which is one of the high resolution spectrometers of the facility. It is easily seen that the KAOS spectrometer complements the existing spectrometers and is the instrument of central importance for strangeness reactions on the proton or light nuclei.

2.3. INSTALLATION OF THE SPECTROMETER

During May and June 2003 the original KaoS spectrometer at the SIS facility at GSI was dismantled and the magnets together with associated electronics and detectors were brought to Mainz. Two photographs of magnet pieces from the KAOS spectrometer are shown in Fig. 2.3. The existing support structures with a carriage on air cushions could not be used in the spectrometer hall. The re-installation of the spectrometer was based on the concept of a compact, mobile and adjustable platform with a support structure on hydraulic positioning cylinders. The platform with the spectrometer should be moved from a parking position to a measurement position via a displacement system with hydraulic pressure cylinders on segmented tracks. With this concept no support on the pivot bearing is needed and a return to the parking position enables the complete coverage of the forward region through the high-resolution spectrometers in standard operation.

The different kinematics of the proposed experiments with the KAOS spectrometer require a flexible position of the magnetic system with respect to the target that can be achieved with hydraulic positioning feet. Three cylinders (Rexroth Hydraudyne BV, The Netherlands) carry the load of the platform and allow for a precise positioning and alignment of the spectrometer. Instead of rails, very accurately grinded sliding plates for the hydraulic positioning cylinders were installed in the inner sector of the spectrometer facility. Their plunger have a double function. They lift the platform from its support, so that the skidding system (Hydrospex Cylap BV, The Netherlands) can be removed. Further, they allows a precise vertical alignment of the spectrometer on the beam-line level or up to 100 mm away from it. It is planned to lift the median plane of the magnet by 50–100 mm from the level of the beam-line to reduce the background rate in the detectors in hypernuclear experiments. The design load of the cylinders is 360 kN, making necessary a plunger diameter of 230 mm and a feet diameter of 400 mm at an oil pressure of 16 MPa. The minimum height of the cylinders is

Figure 2.3.: Photographs of magnet pieces from the KAOS spectrometer taken during the transport in June 2003.

1040 mm with a stroke of 200 mm. The cup-and-ball bearing below the plunger tolerates a tilting angle of 0.5°.

The distance from parking to target position is around 12 m and the height of the central ring being traversed is 700 mm, see Fig. 2.4. A skid-shoe is moved along a skid-track by two hydraulic push-pull cylinders. To overcome friction special PTFE coated rubber and steel blocks with less than 5% friction are placed on the skid-tracks. The full system has a capacity of 125 metric tons, the push-pull cylinders a capacity of 25 metric tons, respectively. The skid-track is segmented in 2 m long elements.

A chronology of the installation and operation of the KAOS spectrometer at MAMI is given Chapter A in the appendix. Here, some important milestones are listed: In 2003 a new access opening was cut into a concrete bunker in the spectrometer hall which now houses the power transformers. First major mechanical parts for the installation have been delivered in 2004 (displacement system and hydraulic feet), and 2005 (support beams with feet, movable platform, positioning plates). The mechanical system was completed end of 2006 (support plates and beams). The installation of the spectrometer on the platform started in mid 2006, a list of the the heavier parts mounted on the platform is given in Table C.1. Photographs of the KAOS spectrometer taken during the installation are shown in Fig. 2.5. The set-up of the refurbished vacuum system was achieved in January and February 2007. Meanwhile, a 9 m long cable girder, which can be rotated to follow the spectrometer's movement between target and parking position, was installed for the delivery of electric and cooling power to the coils. During the

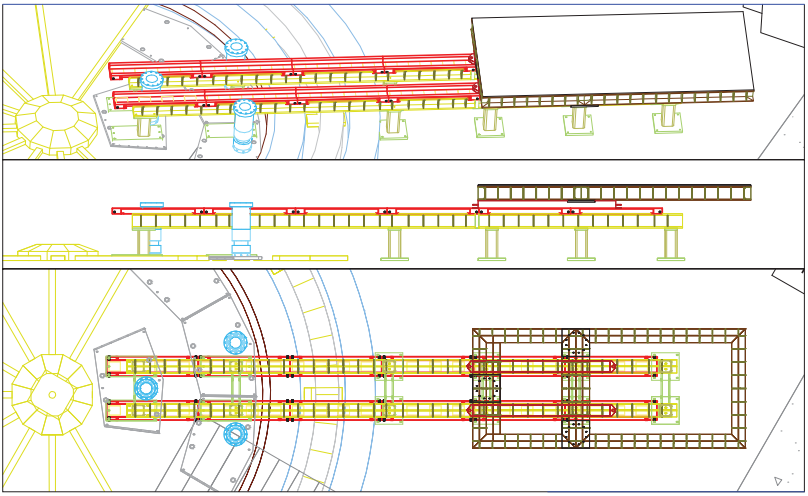

Figure 2.4.: Technical drawings of the experimental hall showing the arrangement of skid-track, hydraulic cylinders, positioning plates, and platform in the final configuration. The height of the central ring which is to be traversed is 700 mm. The distance from parking to target position is around 12 m. The spectrometers and other installations are omitted in the drawing.

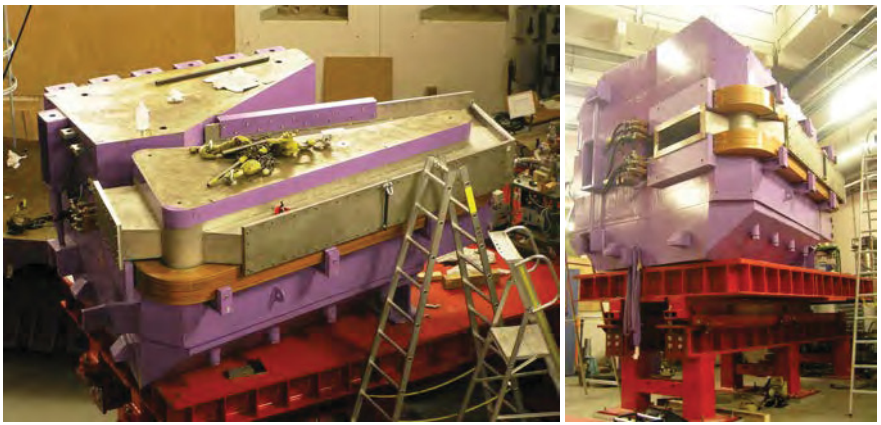

Figure 2.5.: Photographs of the KAOS spectrometer set-up taken during the installation in the spectrometer hall between February and March 2007.

years 2007–8 the commissioning of the KAOS spectrometer has been achieved during a total of five beam-times at MAMI in February, March, September, October, and November. Since 2008 the KAOS spectrometer is fully integrated into (i) the spectrometer facility and its maintenance, interlock and slow control, (ii) into its trigger distribution and blocking, coincidence logic, front-end read-out, and data acquisition and storage system, and (iii) last but not least into the security chain and control of the MAMI accelerator facility.

The pole-pieces of the dipole are curved on the exit side of the hadron arm and straight on the exit side of the electron arm. The entrance side is straight and its normal at the reference position is pointing to the target, when the spectrometer is correctly positioned. Fig. B.2 shows a technical drawing of the upper pole-piece. The reference line on the lower pole-piece is determined by two alignment holes and was marked by a white line. The procedure to line up the spectrometer with the target involves the set-up of a Bosch BC200GL rotating laser behind the vacuum chamber that is pointing along the reference line. The 635 nm light beam is rotating with a speed of 600/min.

The current is flowing through 72 turns per coil with an average length of 7.7 m per turn. The maximum current is 2500 A, that is provided at $U \sim 180$ V, corresponding to 450 kW power. The ohmic losses are cooled by water at a flow rate of 200 ℓ/min. A technical drawing of the coils is shown in Fig. B.3 The magnetic induction is measured with a temperature-compensated Hall probe (LPT-141) read-out by a teslameter (DTM-151) supplied by GROUP3. Its specifications are listed in Table C.2. The probe was calibrated twice with an NMR teslameter (PT 2025) by METROLAB positioned 40 cm from the pole edge in a uniform field region [117]. Three different probes were used to cover the full magnetic field range. The absolute precision of these probes is better than $\pm 5 \cdot 10^{-6}$. The excitation curve of the magnet is shown in Fig. 2.7.

To perform high-resolution spectroscopy it is of course essential for the particle tracks to traverse a minimum of matter thickness. A vacuum chamber was installed between the pole-faces and the magnet which is exhausted by a rotary vane pump (Pfeiffer Vacuum DUO 35) and a turbo-molecular drag pump (Pfeiffer Vacuum TMU 521) to $p \approx 9 \cdot 10^{-6}$ mbar. The specifications of the vacuum pumps installed in the KAOS vacuum system are given in Table C.3. The space between collimator and scattering chamber is not equipped with a chamber mouth because of the varying spectrometer position and target distance. This chamber was extended to cover the second spectrometer arm including the focal-surface detectors, see Section 2.6. The entrance and exit foils to the vacuum chamber are made of laminated Kapton polyimide films of $2 \times 177.8\,\mu$m. Kapton has a low out-gassing rate.

Fig. 2.6 shows a photograph of the spectrometer hall as of 2008 when the first

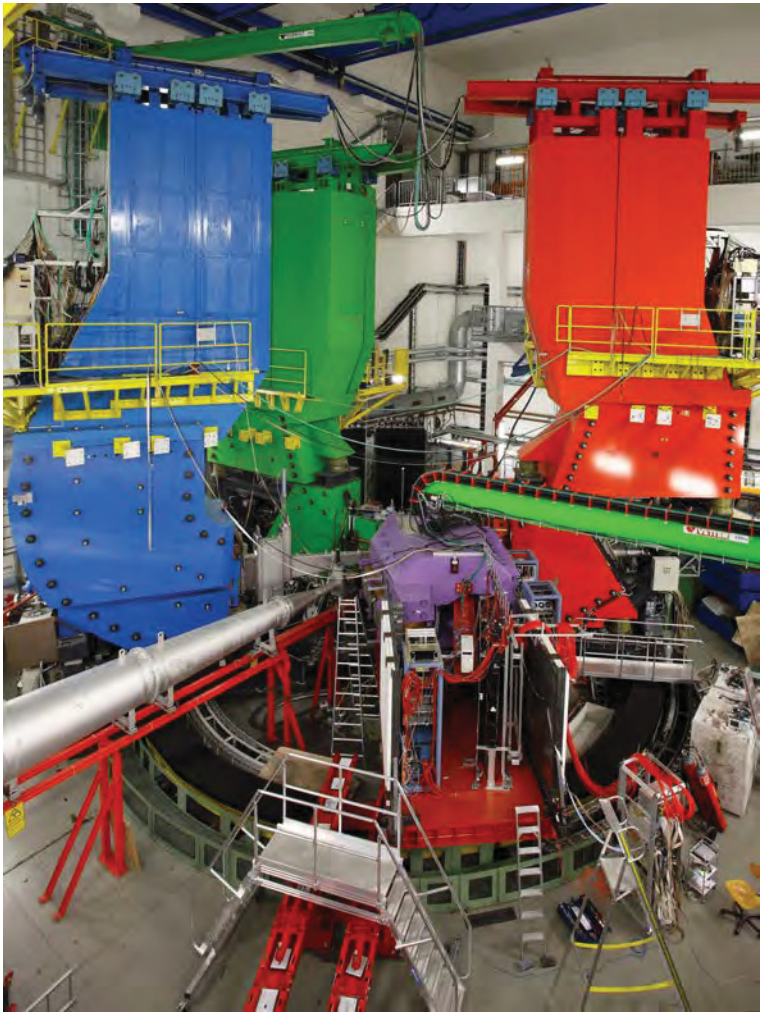

Figure 2.6.: Photograph of the spectrometer hall operated by the A1 Collaboration as of 2008. The KAOS spectrometer at the near-target position is surrounded by the high-resolution spectrometers (SpekA, SpekB, an SpekC). Significant parts of the shielding walls were removed to get maintenance access to the detectors. The kaon electro-production experiments that started in 2008 were performed using this set-up.

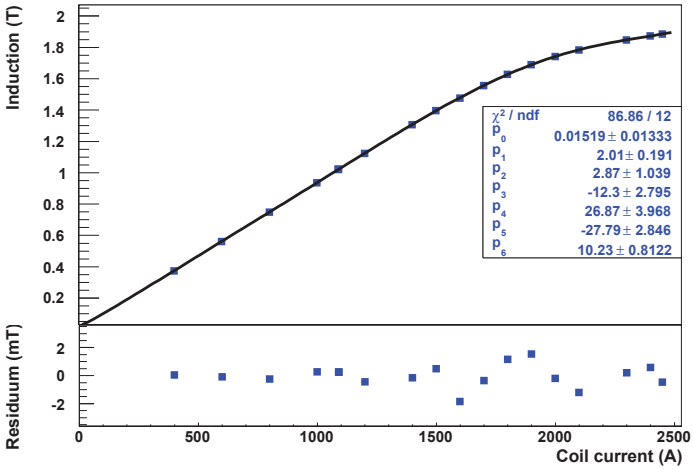

Figure 2.7.: Excitation curve of the KAOS dipole magnet as measured with a temperature-compensated Hall probe. The full line is a sixth-order polynomial fit to the data points and the bottom panel shows the residuum. The maximum coil current provided by the power supply is 2 500 A.

kaon electro-production experiments were performed. The KAOS spectrometer was operated in a near-target position, surrounded by the high-resolution spectrometers (SpekA, SpekB, and SpekC). Significant parts of the shielding walls were removed to get maintenance access to the detectors. The kaon electro-production experiments that started in 2008 were performed using this set-up.

From the point of view of background events in the detectors, the set-up of the KAOS spectrometer at forward angles is problematic. One of the main ingredients in the prospective physics potential of the KAOS experiments is the level of background shielding achievable. An investigation of background conditions in the spectrometer hall is imminent. An evaluation of the expected background was performed within our Monte Carlo simulation package [117]. The shielding of electromagnetic radiation is dependent upon the density of the shielding material. Lead has the advantage of being the densest of any commonly available and affordable materials. The highest flexibility in the geometry of the shielding was achieved by using stacked lead bricks of dimensions $50 \times 100 \times 200\,\mathrm{mm}^3$ (PbSb, $\rho = 11.3\,\mathrm{g/cm}^3$).

Fast neutrons must be slowed down before they can be captured. This can

be accomplished by elastic scattering with light nuclei. The resulting slow neutrons are then readily captured in (n,γ) reactions. Borated polyethylene (BPE, $\rho = 0.96\,\mathrm{g/cm^3}$) is a very good neutron absorber because of the polyethylene containing a high proportion of hydrogen for moderation and the boron carbide (B_4C, between 5 to 10% by weight) providing a large cross section for neutron capture. Boron oxide, also known as diboron trioxide (B_2O_3), is an alternative agent in polyethylene shields and BPE plates with 15% diboron trioxide by weight were used for the KAOS spectrometer shielding. A key point concerning neutron shielding is that the capture produces secondary γ-ray emissions in the shield material (most γ-rays in BPE are produced from the neutrons' interaction with carbon and boron, instead of hydrogen). Thus, a combined system of electromagnetic and neutron shields covering $20\,\mathrm{m^2}$ was implemented. The shielding walls comprise the neutron shielding and the electromagnetic shielding material.

A statics calculation of the mechanical aspects of a radiation shield was performed in May 2005 (Bretschneider Beratende Ingenieure, BBI, Mainz). They calculated that a symmetric set-up of side (load per unit length $\gamma = 22.8\,\mathrm{kN/m^2}$) and backward ($\gamma = 11.4\,\mathrm{kN/m^2}$) lead walls leading to tensile stresses of $\sigma_v = 18\,\mathrm{kN/cm^2}$ is already exhausting 85% of the tensile strength of the steel construction. Based on this calculation a shielding house demountable from the magnet and detector platform was installed.

The use of the KAOS spectrometer in hypernuclear physics experiments at MAMI requires the detection of both, the associated kaon and the scattered electron, at very forward laboratory angles. Both particles will be detected simultaneously by the KAOS spectrometer which will be instrumented in two arms, to either side of the main dipole. The design and construction of a new vacuum chamber and the mechanical adaption of the spectrometer platform for the two-arm operation were completed end of 2008. Fig. 2.8 shows a photograph taken during the assembly of the electron arm detectors. The vacuum chamber is seen as well as the full shielding for the hadron arm detectors. In February 2009 the spectrometer was set up for the first time in two arms, with a new vacuum chamber extending the existing vacuum system of the dipole to the electron arm focal plane region. The beam-tests for the electron arm started in 2009 and will be continued in 2010.

Because of the non-focusing magnet optics in the vertical direction, the chamber had to be of conical shape with a maximum height at the detector positions of $h = 42\,\mathrm{cm}$ and an inner volume of $V \sim 1\,\mathrm{m^3}$. A total of 7 large flanges are needed to allow for the insertion of up to 4 fibre detector planes, and for a flexible beam exit. In addition, an extension tube along the optical axis with a window and a laser system was built in to align the spectrometer. A technical drawing of the vacuum chamber is found in the appendix, see Fig. B.7. An analysis of the

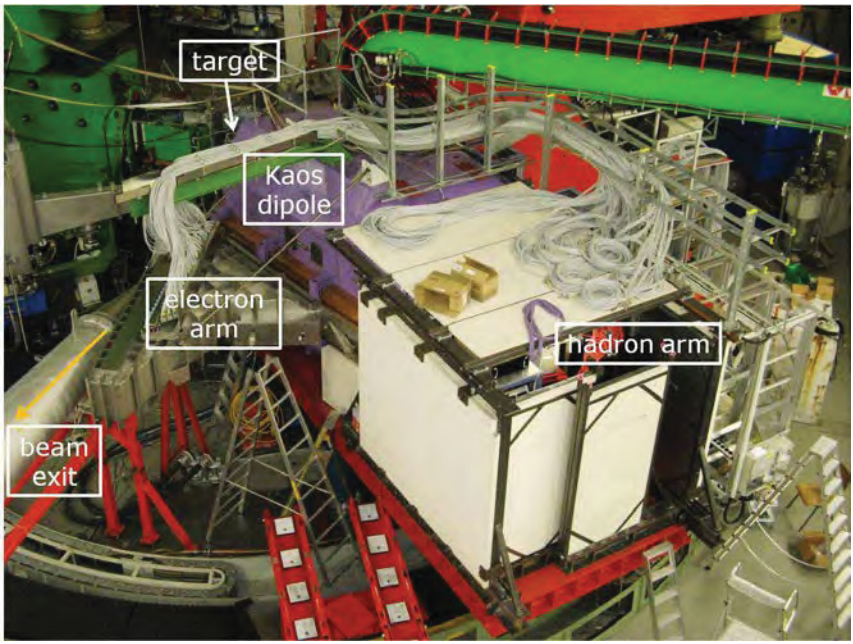

Figure 2.8.: Photograph of the spectrometer hall operated by the A1 Collaboration as of 2009. The vacuum chamber for two-arm operation of the KAOS spectrometer is seen as well as the full shielding for the hadron arm detectors. The beam-tests for the fibre detector planes that started in 2009 were performed using this set-up.

stress and displacement under vacuum was performed showing that only with additional strong support structures on the rim of the chamber the deformation of the flanges could be kept smaller than 2 mm and the stress below the permitted $\sigma_{max} < 140\,\mathrm{N/mm^2}$. A photograph of the chamber is shown in Fig. 2.9 together with a finite element analysis of displacements in the chamber under vacuum, showing (in orange colour) the outer support structures that prevent the chamber from collapsing.

When operating the KAOS spectrometer close to 0° the primary beam will pass through the dipole field of the spectrometer after impinging on a nuclear target and will be bent away from its original axis. Thus, a magnetic chicane comprising compensating magnets is mandatory. A possible solution of a chicane downstream of the target was discarded because of possible large background

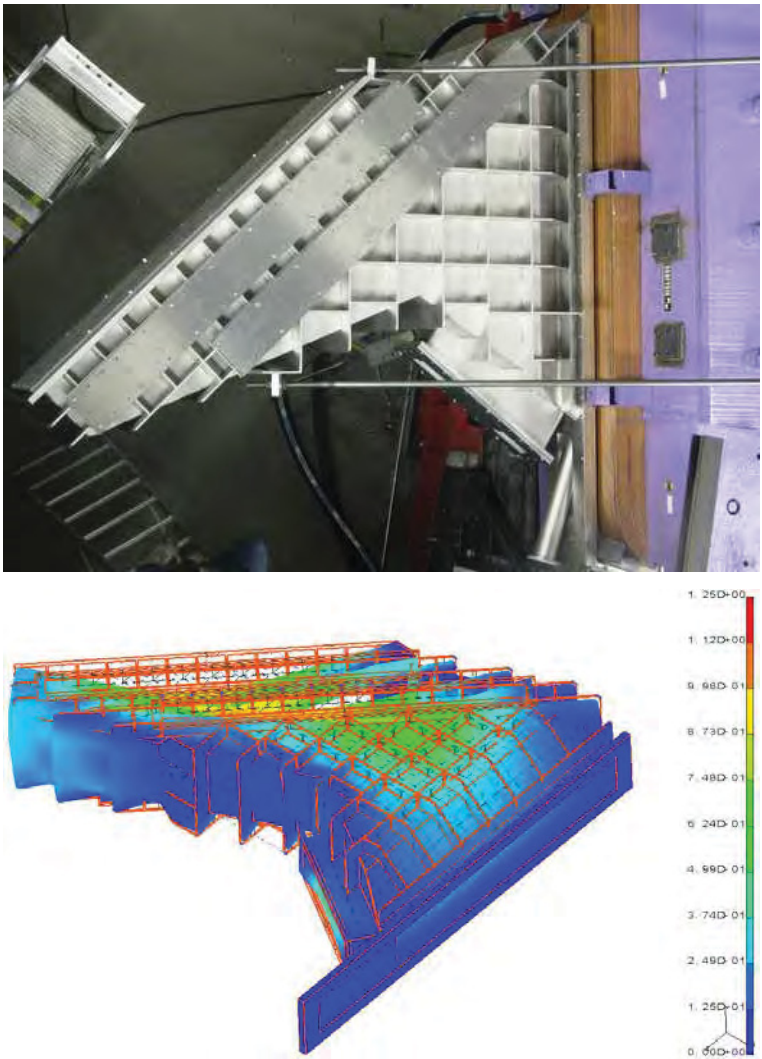

Figure 2.9.: Top: photograph of the KAOS spectrometer's electron arm vacuum chamber that extends from the dipole vacuum system to the electron arm focal-surface region. Bottom: finite element analysis of displacements in the chamber under vacuum, showing (in orange colour) the outer support structures that prevent the chamber from collapsing.

Table 2.3.: Design properties of the magnetic chicane for 1.5 GeV beam energy. The KAOS spectrometer is positioned under zero degree to the beam and the incident angle, α, at the target with respect to the entrance beam-line ranges from 10 to 22°. The momentum bites are given for the electron and kaon arm.

angle α (deg)	field B (T)	electron arm p_{min}–p_{max} (MeV/c)	kaon arm p_{min}–p_{max} (MeV/c)
22.1	1.54	420–590	720–1400
20.4	1.38	370–520	650–1320
18.4	1.20	330–470	560–1120
17.2	1.10	290–420	520–1020
13.7	0.82	220–310	390– 780
10.1	0.55	150–215	350– 510

radiation levels created in such beam-line magnets. The solution for a chicane upstream of the target comprises two dipoles which are available as spare 30° sector magnets (DCI). The properties of the DCI dipoles are described in detail in [118]. Many of them have been used at other locations before and were adapted to the new requirements, by mechanical modifications in some cases. A schematics of the experimental hall with pre-target beam chicane and the KAOS spectrometer used for the beam return is shown in Fig. 2.10. The beam transport was calculated using a Geant simulation and a range of practical solutions were found. In an overview, possible configurations of the beam transport are listed in Tab. 2.3. The angle through which the KAOS dipole bends the beam depends on the field strength. For a field of 1 T in the KAOS dipole the chicane magnet of the chicane has to deflect the beam by 13.5°, the second one by approximately twice the angle in opposite direction. With the resulting beam inclination of 16°, the KAOS dipole will deflect the beam straight into the beam-dump with an angle of only 1.47° relative to the axis. The beam angle at the target has to be varied. This can be achieved by adjusting the strength of both fields and the position of the second DCI magnet.

A group of physicists and technicians is working on the installation of the magnetic chicane with its first operation scheduled for end of 2010.

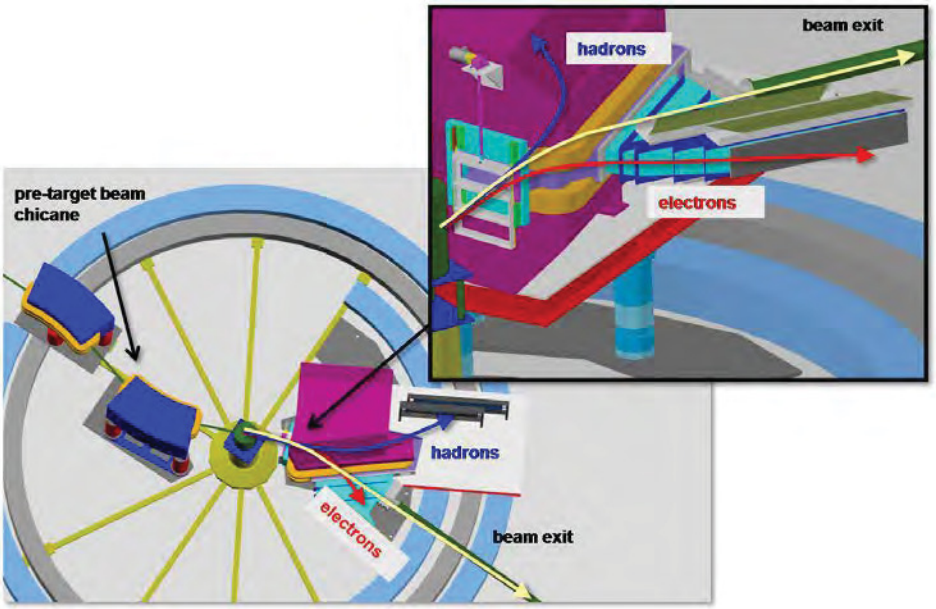

Figure 2.10.: Schematics of the experimental hall with pre-target beam chicane and the KAOS spectrometer used for the beam return.

2.4. OPTICS OF THE SPECTROMETER

The KAOS spectrometer was operated at GSI in a single-arm double-focusing *QD* configuration and is now working in a double-arm single-focusing *D* configuration. The first approach to determine the new magnet optics was determined by ray-tracing within a GEANT4 simulation [117]. The KAOS spectrometer as realised in the spectrometer hall is depicted schematically in Fig. 2.11, where ray-traced positively and negatively charged tracks for different momenta and emission angles are shown.

From the simulation a first-order transfer matrix was determined for the KAOS spectrometer as shown in Table 2.4. A comparison is made with the magnet optics of the high-resolution spectrometers of the A1 collaboration and the original KaoS spectrometer as operated at the GSI. The dispersive direction for SpekA, SpekB, and SpekC is vertical, for the KAOS spectrometer it is horizontal. The first-order focusing for the KAOS spectrometer is achieved with a bending of the central tra-

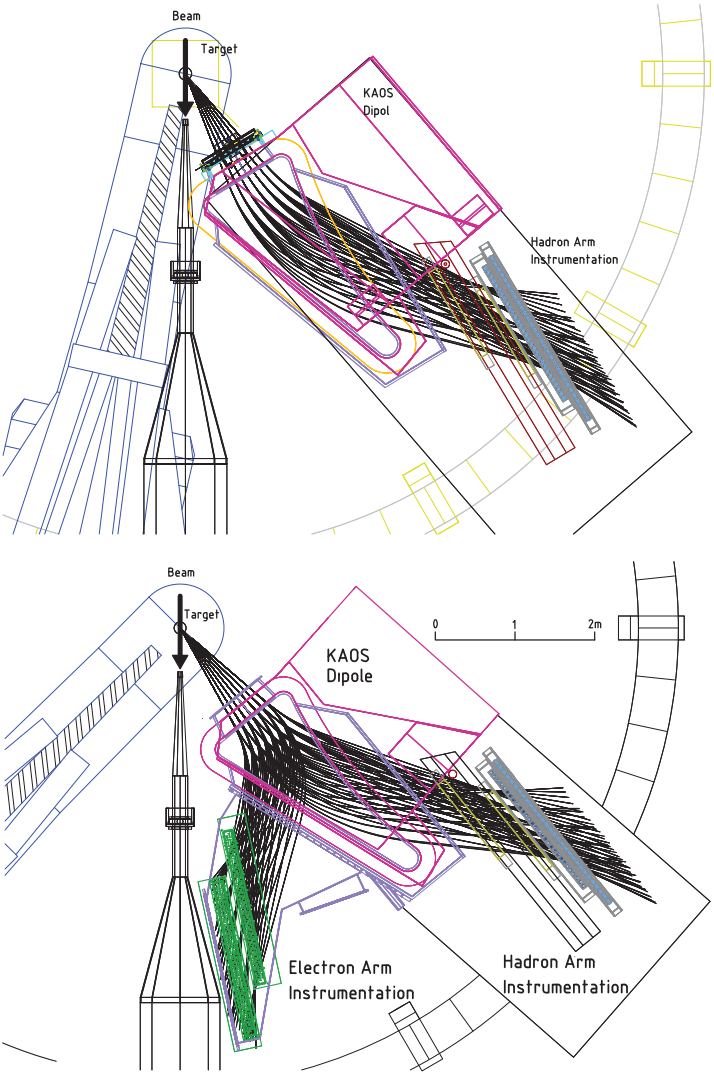

Figure 2.11.: The top figure shows the KAOS spectrometer set-up during the first kaon electro-production measurements in 2008 whereas the bottom figure shows the set-up as double spectrometer. Ray-traced negatively and positively charged particle trajectories through the spectrometer are shown by full lines from target to detection planes.

Table 2.4.: First-order transfer matrix elements of the spectrometers of the A1 collaboration. Values for the high-resolution spectrometers were taken from [115], for the KaoS spectrometer as operated at the GSI from [116]. The x and θ coordinates are pointing in the dispersive direction, y and ϕ in the non-dispersive direction.

		A	B	C	KAOS arms hadr.	KAOS arms elec.	KaoS @GSI
$\langle x_f \vert x_0 \rangle$		−0.532	−0.853	−0.526	2.02	−2.50	−0.380
$\langle x_f \vert \theta_0 \rangle$		0	0	0	0	0	0
$\langle x_f \vert \delta \rangle$	(cm/%)	5.65	8.22	4.41	2.4	4.0	1.24
$\langle \theta_f \vert x_0 \rangle$	(mrad/cm)	−9.92	−3.16	−12.70	6.0	−10.9	−19.89
$\langle \theta_f \vert \theta_0 \rangle$		−1.88	−1.17	−1.90	−1.43	−1.45	−2.64
$\langle \theta_f \vert \delta \rangle$	(mrad/%)	3.12	14.0	2.92	2.99	6.36	3.90
$\langle y_f \vert y_0 \rangle$		−0.532	−0.853	−0.526	3.2	1.93	−6.16
$\langle y_f \vert \phi_0 \rangle$	(cm/mrad)	−0.158	−0.008	−0.125	1.18	0.61	0.14
$\langle \phi_f \vert y_0 \rangle$	(mrad/cm)	6.53	−3.168	7.67	13.9	5.21	−22.18
$\langle \phi_f \vert \phi_0 \rangle$		−0.40	−1.18	−0.41	3.75	2.31	0.35

jectories on both sides by $\sim 45^\circ$ with a momentum dispersion of 2.2 cm/% for the hadron arm and 4.0 cm/% for the electron arm. The small deflection angle for the central trajectory keeps the magnet compact. The focal-surface on the electron side is almost straight, on the hadron side it is well parametrized by a parabola. The enhanced curvature of the latter focal-surface as compared to the spectrometer operation at GSI is due to the missing quadrupole strength. The dispersion to magnification ratio of the KAOS hadron arm is $D/M_x = 1.2\,\text{cm}/\%$ that leads to a first-order resolving power, $\mathcal{R} = D/(M_x\sigma_x)$, of 2 400 for a beam-spot size, Δx_o, of 0.5 mm. The first-order momentum resolution, $\Delta p/p = \sqrt{(\sigma_x^2 + M_x^2 \Delta x_o^2)/D^2}$, was determined from these values to be of the order of $\sim 10^{-3}$, where the spatial resolution in the focal-surface, σ_x, was approximated with the anode wire distance of 2 mm in the MWPC. The large momentum bite that is focused on a curved surface in the hadron arm, and that is detected by a moderately sized detector package with a mm-range position resolution, is one of the limiting factors for the momentum resolution.

In an ideal spectrometer the position along the focal surface at which a particle is detected is directly related to its momentum. In practice, however, due to kinematic broadening and spectrometer aberrations this position will also depend on

the angle of the particle trajectory with the central ray. Obviously, this will degrade the resolution if a finite aperture is used. In the KAOS spectrometer particles with given momenta or target angles leave traces in the coordinate system of the two tracking detectors that are lines of constant slopes in the central region of the acceptance and that are strongly curved at the edges. Fig. 2.12 shows the simulated traces with momenta from 350 MeV up to 600 MeV over the full angular acceptance in the coordinate system of the tracking chambers. The plot includes also the trace for particles of central target angles over the full momentum acceptance. In the regions with strong curvature the momentum depends on many higher-order terms of the transfer matrix, which need to be precisely determined. Fig. 2.13 shows the same simulated traces of particles in the focal-surface where the position along focal-surface in dispersive direction and the difference of track slope to the reference trajectory's slope are used as coordinates. The small dependence of the track slope difference on the momentum and its strong correlation to the target angle in dispersive direction is the reason for this choice as second coordinate in the transfer matrix.

If the properties of the spectrometer are known, it is possible to correct the measured position if the angles at which a particle enters the spectrometer are determined. In addition, the reconstruction of the trajectory of each particle, either electron or hadron, is mandatory in $(e, e'X)$ coincidence experiments. The missing energy and momentum in coincidence experiments can only be calculated with sufficient accuracy when the angles at which the particles leave the target are known. Furthermore, it is necessary to correct for differences in time-of-flight due to path-length differences in order to obtain a good coincidence-time resolution. Finally, background events in the detectors can be suppressed by requiring that the trajectory of a detected particle starts from the target with angles that are within the aperture of the entrance slit.

Detailed measurements with electron beams of 450 MeV and 1508 MeV energy have been performed to study the properties of the new magnet optics. Experimental ray-tracing with elastically scattered electrons off ^{12}C and ^{181}Ta foils was used to determine the transfer matrix. To select well determined angles in both planes a sieve collimator, made of 20 mm thick lead with 16 holes, 5 mm in diameter each, was installed in a distance of 1 000 mm from the target in front of the magnet. For each hole the sieve collimator defines primary angle distributions with a width of $\sigma = 2.45$ mrad. A subset of collimator holes, defining the horizontal angles $\theta \in \{-175, -130, -87, -43, 0, 43\}$ mrad, and the vertical angles $\phi \in \{0, 18\}$ mrad, was within the spectrometer acceptance. Electrons passing different holes are clearly separated in the reconstructed coordinates. The deviations to the nominal hole coordinates visualize the uncorrected optical aberrations of the system. The magnitude of the necessary correction of the transfer matrix ele-

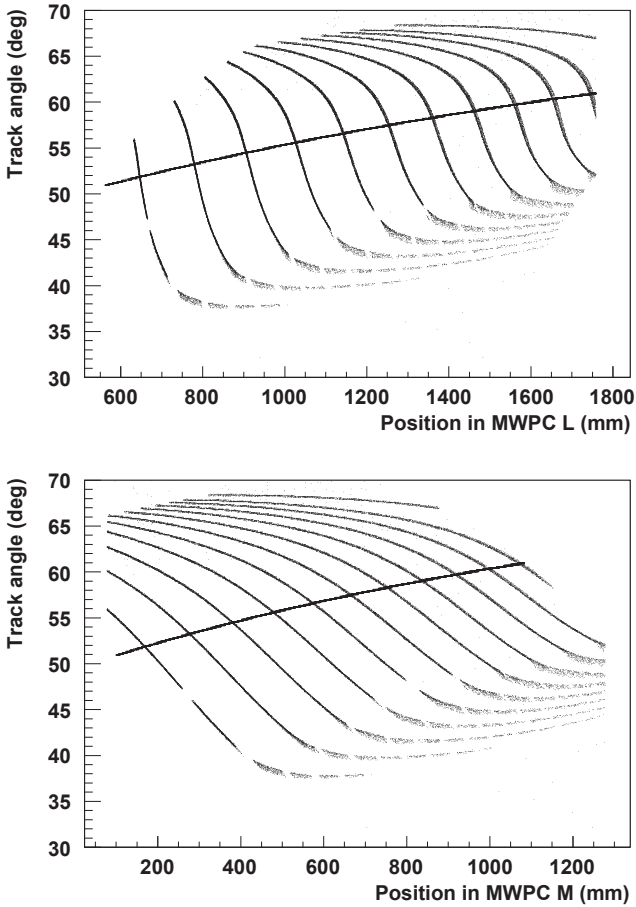

Figure 2.12.: Simulated traces of particles with momenta from 350 MeV up to 600 MeV, in steps of 25 MeV, over the full angular acceptance, and for particles of central target angles over the full momentum acceptance, in the coordinate system of the tracking chambers. Top: coordinates in tracking chamber MWPC L; Bottom: coordinates in tracking chamber MWPC M. The central momentum setting was 0.6 MeV/c. In the regions with strong curvature the momentum depends on many higher-order terms of the transfer matrix.

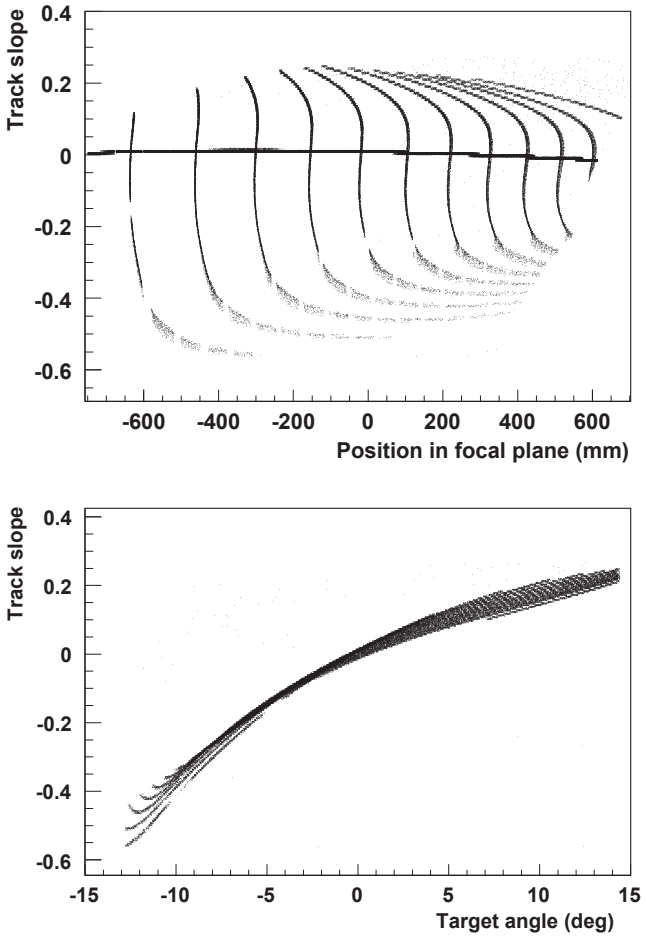

Figure 2.13.: Simulated traces of particles with momenta from 350 MeV up to 600 MeV over the full angular acceptance, and for particles of central target angles over the full momentum acceptance, in the focal-surface. Top: position along focal-surface in dispersive direction versus difference of track slope to the reference trajectory's slope detected in the focal-surface. Also the traces of particles of central target angles over the full momentum acceptance are shown. Bottom: Relation between the track slope difference to the target angle in dispersive direction. The central momentum setting was 0.6 MeV/c.

ments is of the order of 10 mrad or more, as can be deduced from the deviations of the measured hole positions to the nominal positions seen in Fig. 2.15 (top). The projections of the events to the target angles θ_o and Φ_o in the dispersive and non-dispersive plane, respectively, produced distributions of widths of $\sigma \sim 1.9$–2.7 mrad, as shown in Fig. 2.15 (bottom). A finer collimator was prepared in 2009 for an improved determination of the transfer matrix elements. It contained 53 holes in 5 different horizontal lines along the dispersive plane. Not all of these lines are within the vertical acceptance of the spectrometer. Small holes are of 5 mm diameter, several larger ones of 10 mm diameter.

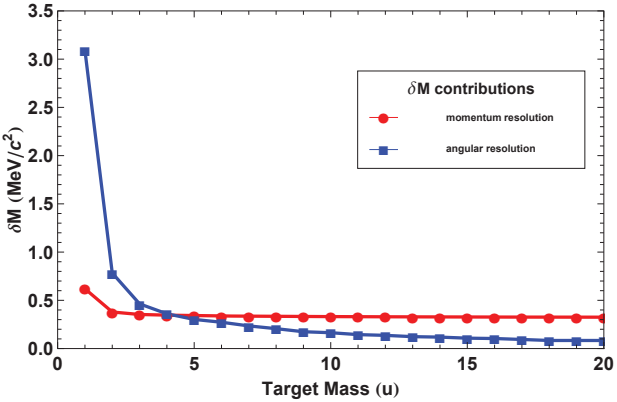

Figure 2.14.: Contributions to the experimental missing mass resolution from scattering angle and momentum resolutions of the spectrometer as a function of the target mass. For light targets (H or He) the resolution is dominated by the variance in the measured scattering angle.

The energy of a scattered electron, $E_{e'}$, off a fixed target of mass M from a beam with energy E_e is known to be

$$E_{e'} = \frac{E_e - E_x\left(1 + E_x/(2Mc^2)\right)}{\eta} \tag{2.9}$$

with the kinematic factor

$$\eta = 1 + 2E_e/(Mc^2)\sin^2(\theta/2), \tag{2.10}$$

where $\theta_{e'}$ is the scattering angle and E_x the excitation energy of the target. Electrons, scattered under different angles into the aperture of the spectrometer, carry

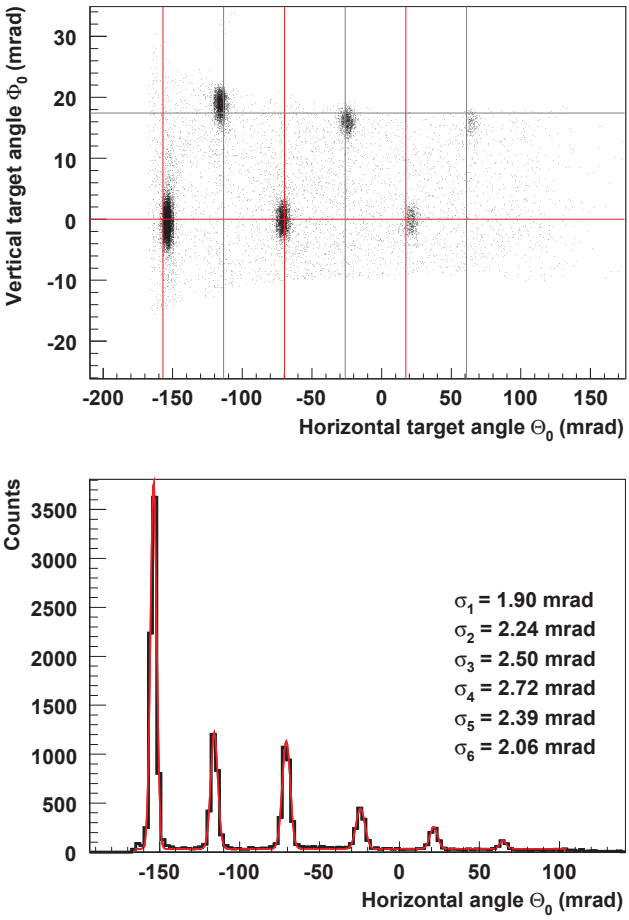

Figure 2.15.: Top: emission angles of elastically scattered electrons of 450 MeV energy, back-traced from the detector system of the KAOS spectrometer to the target, before applying any corrections of the aberrations. The sieve-slit collimator was made of a 20 mm thick lead block with holes of angular width of $\sigma \sim 2.4$ mrad at 1 000 mm distance to the target. Bottom: projection of the events onto the θ_0-axis and determination of the preliminary angular resolution of the spectrometer by fitting the peaks with Gaussian distributions, resulting in widths of $\sigma \sim$ 1.9–2.7 mrad.

different momentum due to the different recoil momentum of the target. The energy of an electron scattered by $\Delta\theta$ relative to the reference angle of the spectrometer is shifted by

$$\Delta E_{e'} \approx -E_{e'} \frac{E_e/(Mc^2)\sin(\theta)}{\eta} \cdot \Delta\theta + \ldots \tag{2.11}$$

This effect is pronounced for scattering off light targets and is called kinematic broadening. When using a H target the large angular acceptance of the KAOS spectrometer leads to a large kinematic broadening. A kinematic correction can be applied using the measured scattering angle, and the magnitude of the correction falls rapidly with increasing target mass. The contributions of momentum and angular resolution to the missing mass spectrum can be estimated using

$$M_x = \sqrt{(\omega - E_K + M_{targ})^2 + p_K^2 - 2p_K|\vec{q}|\cos\theta_K - Q^2} \tag{2.12}$$

as follows: $\frac{\partial M_x}{\partial\theta} = p_K|\vec{q}|\sin\theta_K/M_x$ and $\frac{\partial M_x}{\partial p_K} = (p_K - |\vec{q}|\cos\theta_K)/M_x$. Fig. 2.14 shows these contributions as a function of the target mass assuming preliminary values of $\Delta p/p = 10^{-3}$ and $\Delta\theta = 12\,\text{mrad}$. For light targets (H or He) the resolution is dominated by the variance in the measured scattering angle. For a ^{12}C target the missing mass resolution is expected to be one order of magnitude better than for a hydrogen target.

2.5. HADRON ARM INSTRUMENTATION

In the KAOS spectrometer's hadron arm several particle identification and tracking detectors are operated. Two large-sized multi-wire proportional chambers (MWPCs), labelled M and L, are situated behind the vacuum chamber, followed by two segmented scintillator walls, labelled F and G. A photograph of the instrumentation is shown in Fig. 2.16. A typical particle trajectory is indicated by the arrow.

2.5.1. TRACKING DETECTORS

The tracking of particles through the KAOS spectrometer's hadron arm is performed by means of two MWPCs. Despite modern alternatives like micro-pattern gas detectors, the use of MWPCs is still an economical way to cover a large area with tracking devices for charged particles. MWPCs are especially attractive when the particle track can be recorded from a single chamber in two orthogonal dimensions and when the required resolution is not significantly finer than FWHM $\sim 1\,\mathrm{mm}$.

The MPWCs were used before in several beam-times at GSI for trajectory reconstruction at relativistic heavy ion experiments, detecting successfully trajectories of pions and kaons as well as protons and heavy nuclear fragments [116, 119]. Contrary to conventional MWPCs the multiplication process in these chambers is divided into two steps, following a concept first described by Breskin and coworkers [120]. During the electron scattering experiments at MAMI the distribution of charge states of the ionizing particles as well as particle fluxes differ greatly from the situation at GSI. At MAMI, the chambers are shielded by 5 cm of lead to the external sides, however, when a continuous-wave electron beam of several μA current is delivered to solid-state or cryogenic liquid targets situated in front of the dipole the chambers experience multiple tracks in almost every event due to high electromagnetic background radiation levels.

Crucial requirements for the wire chamber operation in kaon electroproduction measurements are (i) high efficiency for minimum ionizing particles and (ii) tracking capability for luminosities above $5 \times 10^{36}\,\mathrm{cm^2 s^{-1}}$. The limit for the second requirements depends strongly on the wire chamber geometry. Modern developments aim for MWPC that resolve track coordinates with a spatial resolution of about 100 μm in a very high-rate background up to a few $\mathrm{MHz/cm^2}$. Such chambers have small chamber dimensions and are operated with low gas gain.

To determine the particle track the measured charge distributions induced on the cathode wire planes of the MWPCs are analysed. Of the several known methods for the bi-dimensional read-out of MWPCs, the induced-charge sampling is

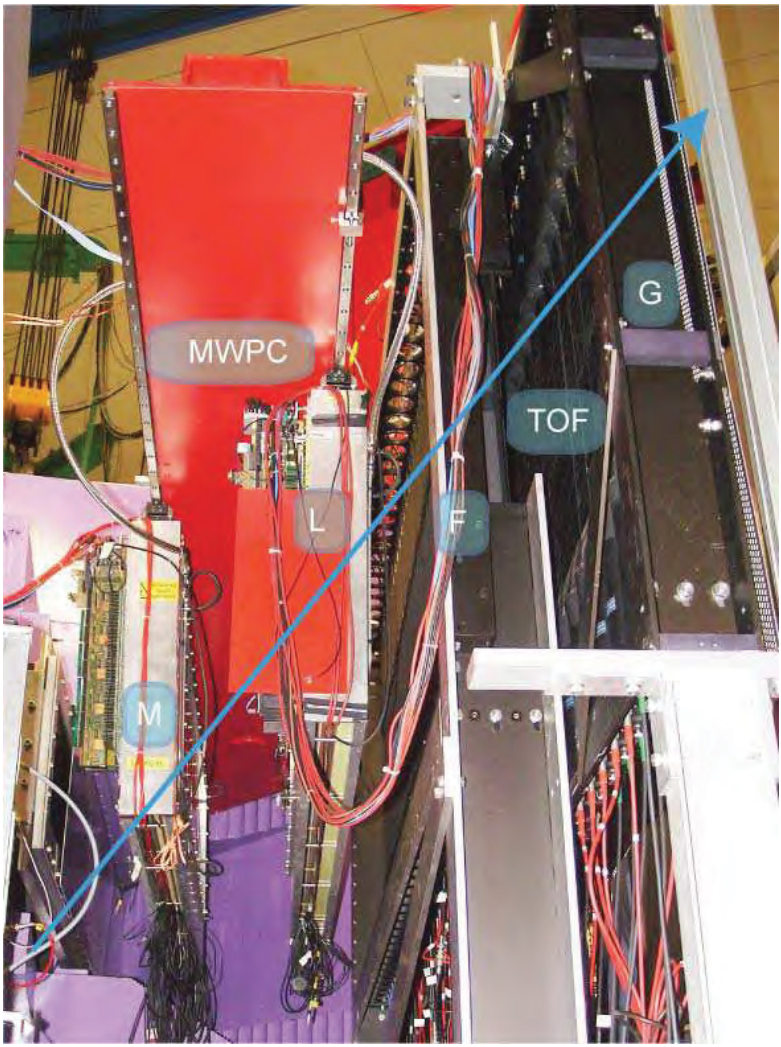

Figure 2.16.: Photograph of the detectors installed in the hadron arm of the KAOS spectrometer. The two MWPCs, labelled M and L, are situated behind the vacuum chamber, followed by the two scintillator walls, labelled F and G. A typical particle trajectory is indicated by the arrow. During spectrometer operation all detectors are protected by radiation shields.

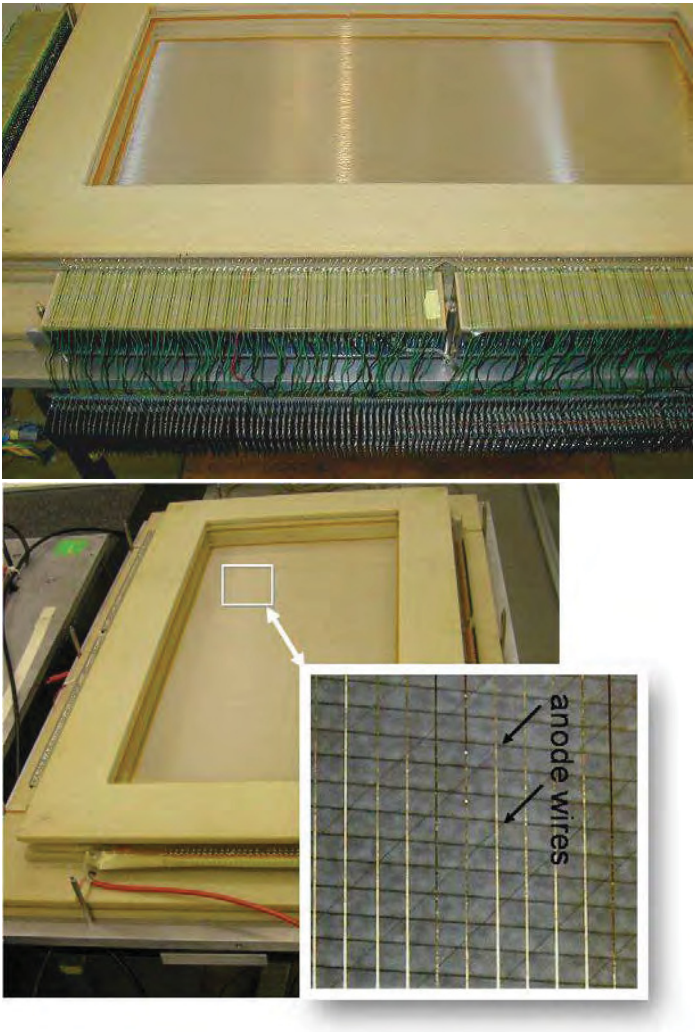

Figure 2.17.: Photographs of an exposed MWPC and its wires. The preamplifiers in their containers, and the ADC cards are seen as well as the two-stage frame structures. The anode wires with 2 mm spacing are running in diagonal direction to the two orthogonal cathode wire planes with 1 mm spacing.

well established since the 1970s [121]. However, even in single-track operation, the choice of analysis method for the induced charge distributions on the cathode strips or wires has consequences on the position resolution and the track reconstruction efficiency [122]. The method can give good spatial resolution, but is compromised for multiple particles in one event as the signals can get partially integrated, the wide charge distributions can overlap, and peaks can get distorted.

The MWPCs and associated electronics were refurbished and first set-up in 2007–8 [123], two photographs of an exposed chamber are shown in Fig. 2.17. The work also included the installation of gas pipes from the detector lab to the MWPCs on the spectrometer platform and the laying of the exhaust pipes and tubes from the MWPCs through the spectrometer hall to the top of the spectrometer hall. The gas mixer is situated close to the spectrometer. The MWPCs are triggered by the scintillator walls. The performance of the system was considerably improved in 2008 by changing the hardware, software, and trigger so that data-taking rates above 1 kHz are possible [124].

The two MWPCs have an active area of $1\,190 \times 340\,\mathrm{mm}^2$ each. The chambers are schematically depicted in Fig. 2.18. They consist of a plane of anodes ($\varnothing$ = 20 μm gold-plated tungsten wires, 2 mm spacing), symmetrically sandwiched between two orthogonal planes of cathodes in x- and y- direction ($\varnothing$ = 50 μm gold-plated tungsten wires, 1 mm spacing) along with two meshes of woven fabrics of plastic coated with a nickel layer, making up two planar electrode structures, the grid (G) and the transfer (T) plane and two gaps, the pre-amplification gap and the transfer-gap. The wires of the anode plane are running in diagonal direction, making an angle of 45° with either cathode direction. Typical potentials applied to these electrodes are: $U_G = -9.1\,\mathrm{kV}$, $U_T = -2.0\,\mathrm{kV}$, $U_A = +4.0\,\mathrm{kV}$, with the cathodes grounded. Ionizing particles which pass through the active area of the chamber produce primary electrons in the chamber gas, which will be multiplied in the high electric field of the pre-amplification gap. The gain in this first stage is about 10^2. The avalanche then drifts into the transfer gap between T and the first cathode plane where a low electric field is maintained. Finally, the avalanche reaches the anode plane and a second gas amplification by about a factor of 10^3 occurs. Due to the transverse diffusion, the electron cloud broadens on its long drift-path. Due to the exponential behaviour of the Townsend avalanche process, the very first primary electrons produced directly at the entrance gap G contribute most to the avalanche.

For the measurement of the distribution of the charges induced on the cathodes five cathode wires were connected together to one channel and are brought to one charge-sensitive preamplifier making a total of 240 analogue channels in x-direction and 70 analogue channels in y-direction. The preamplifiers provide a

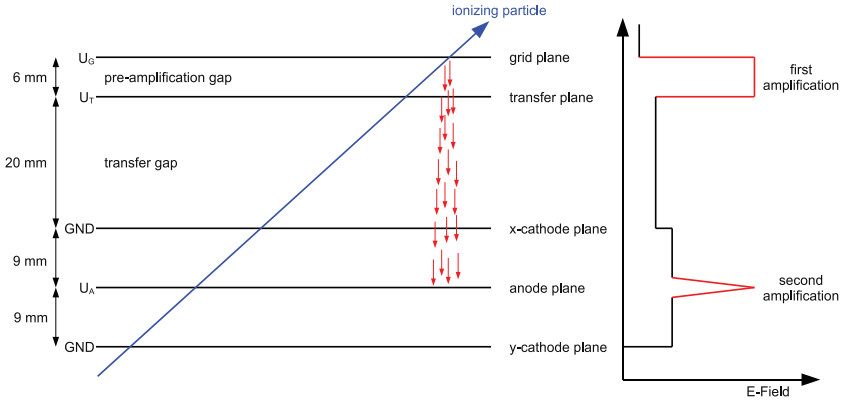

Figure 2.18.: Schematic layout of the MWPCs with two-stage gas amplification. Each chamber consists of a plane of anodes ($\varnothing = 20\,\mu$m gold-plated tungsten wires, 2 mm spacing), symmetrically sandwiched between two orthogonal planes of cathodes ($\varnothing = 50\,\mu$m gold-plated tungsten wires, 1 mm spacing) along with two conducting grids, providing two gaps in front of the wire planes. On the right side a typical distribution of the electric field is shown. Electrons liberated in the pre-amplification gap are amplified before drifting through the transfer-gap, the transferred charge is amplified a second time at the anodes.

bipolar output with a negative amplitude of up to 2.5 V. The pulse width is $\sim 2\,\mu$s. The signals are digitized by an ADC card addressed by a freely programmable transputer module, mounted directly on the chamber. The ADC converts the signal within 1.34 μs into 8 bit with an error of ± 0.5 LSB (Least Significant Bit). Sixteen of the ADC chann els are read out and processed by one transputer. The transputer network system is connected to a multi-link card inside a front-end computer. Clusters of signals in 3–5 channels were observed, consistent with the expectation for the FWHM of an induced cathode signal that is known to be nearly equal to twice the anode-to-cathode gap, 2×9 mm.

Particles from the target cross the MWPC planes with an angle of about $(50 \pm 20)^\circ$ to the normal. The peak position of charges transferred from the pre-amplification gap to the anodes is assumed to coincide with the impact point of the trajectory of the ionizing particle with the grid plane. This position does not depend on the angle of incidence of the particle's trajectory, whereas the shape of the charge distribution is influenced.

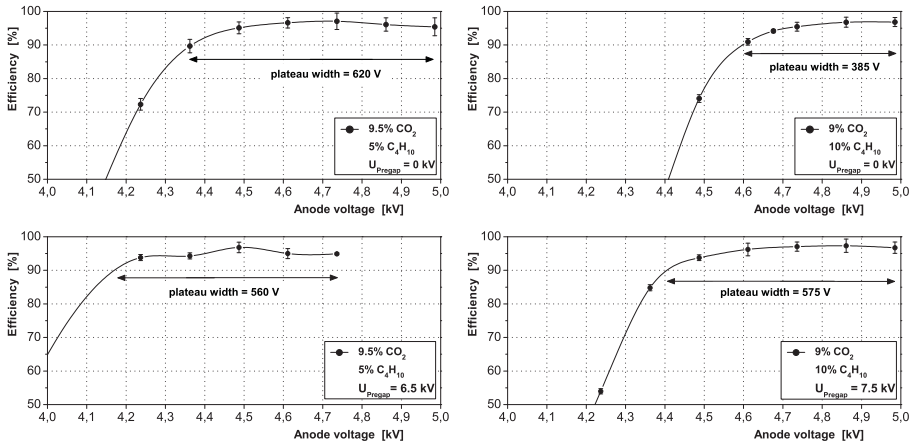

Figure 2.19.: Plateau curves from the efficiency measurements with the two argon and quencher gas mixtures {9.5% CO_2, 5% C_4H_{10}} and {9% CO_2, 10% C_4H_{10}} without a pre-gap voltage (top) and with a constant pre-gap voltage (bottom).

The chambers are filled with an ionisable gas of argon which can be mixed with one or more of quencher gases. At GSI a gas mixture of 90 % P10 and 10 % isobutane (C_4H_{10}), equivalent to 81 % argon, 9 % CO_2 and 10 % C_4H_{10}, was ini-

Table 2.5.: Efficiency plateau widths and plateau areas from laboratory measurements with the MWPC. In the measurements the anode voltage was varied whereas the pre-gap voltage was kept constant.

CO_2 admixture C_4H_{10} admixture	10 % 1 %	9.5 % 5 %	9 % 10 %	19 % 4 %
no pre-gap voltage				
plateau width (V)	600	620	385	30
plateau area (kV·Δ%)	2.86	3.43	2.07	0.01
constant pre-gap voltage				
U_{pg} (kV)	5.5	6.5	7.5	7.5
plateau width (V)	440	560	575	375
plateau area (kV·Δ%)	1.97	2.69	3.38	1.92

tially applied to the MWPCs which lead to a high detection efficiency for minimum ionizing particles. However, in a study aiming at substituting isobutane with heptane an optimum mixture of 78 % argon, 20 % CO_2 and 2 % heptane at a pressure of 1.5 atm was found. For safety reasons heptane is not used for wire chambers at MAMI. Accordingly, the efficiency of the MWPCs was tested for different gas mixtures of argon, CO_2 and C_4H_{10} in Mainz, see Table 2.5. Calibrated mass-flow controllers were used to control the amounts of the three gas components. Two important characteristic observables exist for such a test: the spark point is the voltage at which the MWPC becomes unstable against discharging inside the chamber, while the plateau width is the voltage range between reaching high efficiency and the spark point. Both depend on the gas mixture and the applied voltages. A large plateau width is desirable in order to set the working point well below the spark point. Fig. 2.19 shows in four panels the measured plateau curves for the two gas mixtures {9.5% CO_2, 5% C_4H_{10}} and {9% CO_2, 10% C_4H_{10}}. A range of high efficiency has been defined as 90 % and above, indicated by the designated plateau widths in the figure. In order to be able to compare the efficiencies of the different gas mixtures the areas between the curves and the 90 % line have been integrated. In conclusion, large plateaus of high and constant efficiency were obtained during several efficiency measurements. A mixture of {9 % CO_2, 10 % C_4H_{10}}, at an anode voltage of $U_A \approx 4.8$ kV, and a pre-gap voltage of $U_{pg} = |U_G - U_T| = 7.5$ kV was determined as a good parameter set for opera-

tion of the chambers in the electron scattering experiments at MAMI [125]. Using somewhat lower anode voltages, $U_A \approx 4.0\,\mathrm{kV}$, the amount of quencher gas was reduced to $\{9\,\%\ CO_2, 7\,\%\ C_4H_{10}\}$ in 2008.

Details of the induced charge distributions depend on experimental parameters like track angles, particle species and velocities, and multiplicities, but also on working conditions like gas mixture, high voltages, and the integration gate width and timing. Therefore it is of practical importance to apply an algorithm which gives the best position resolution and highest track reconstruction efficiency. However, the choice of the analysis method depends heavily on the experimental requirements.

Fluctuations in the primary ionisation and electron diffusion along the drift path lead to non-Gaussian charge distributions induced on the cathodes. The distributions are further deteriorated by noisy channels, by multiple tracks in the chamber, and by induced signals in the electronic chain. To relate the induced charge distributions to the avalanche position, (i) the geometrical parameters of the chamber, (ii) the signal-to-noise ratio, and (iii) physical processes of the ionization and avalanche formation had to be taken into account. Charge distributions in both MWPCs taken with $2\,\mu$A beam current on a 5 cm liquid hydrogen target are shown in Figs. 2.20 and 2.21. Peak positions as indicated by blue lines in the display were determined by the cluster algorithm discussed in this Section.

The raw data are 8-bit ADC values, Q_i, for each read-out channel, x_i, in the x- and y-plane. As preamplifiers and ADCs vary along the planes, each combination is assigned a gain factor c_i and a pedestal value p_i. In few cases, where individual channels showed misbehaviour, caused *e.g.* by wire ageing, their amplitudes were interpolated from both neighbouring channels. Then "clusters" are defined by a group of neighbouring channels with detected charges. A cluster has to consist of at least 2 channels and could include a single channel below pedestal. At first each cluster is characterized by its detected charge, $Q = \sum_n Q_i \cdot c_i$, its channel multiplicity, n, its centre-of-charge, $\bar{x} = (\sum_n Q_i \cdot c_i \cdot x_i)/(\sum_n Q_i \cdot c_i)$, its width, $\sigma = \sqrt{\sum_n |X_i - \bar{x}|^2\, Q_i/Q}$, and its largest amplitude, Q_{max}, at channel x_{max}.

Because of the two amplification regions, as shown in Fig. 2.18 (right), and the large crossing angles of the particles, the liberated charges that are drifting from the pre-amplification plane will be displaced in the anode plane with respect to the weaker direct signal. The two separated charge localisations differ by a distance $x = d \tan\theta$, d being 35 mm. For a typical angle of $\theta = 55^\circ$ this distance was $x \cong 50\,\mathrm{mm}$ corresponding to 10 channels. As the amplification of the direct signal was only partial, and the signal was induced on the cathodes at a much earlier time and thus got integrated only partially, a second peak in the charge distribution was not often observed; however, an asymmetry in the shape of the peak was

regularly present in the signals. Because the drift time was regulated by the gas mixture and the high voltages, and the integration gate could get matched to this drift time, it was possible to minimize the appearance of double peaks and to reduce variation in cluster shapes. In Fig. 2.20 the peaks in the x-plane of MWPC M show features related to the two-stage amplification.

During the experiments sometimes charge distributions were observed, where satellite peaks were accompanying the physical peak, that was produced by a heavily-ionising light particle. Fig. 2.21 shows a charge distribution in the x-plane of MWPC M with satellite charges on both sides of a needle-like peak. The source of these peaks can be understood by the anode plane construction mounted in between the cathode planes and was identified as a capacitive coupling between anode and cathode at the stesalite frame which have a dielectric constant $\epsilon_r \approx 6$, see discussion in [126]. A strong correlation exits between the vertical position of the physical peak and the relative position of the satellites in the x-plane. Typical distances between the satellites are 82–86 cathode channels reflecting the height of the frame. The satellite signals were not be present in single-track events after a fine adjustment of the integration gate, but could not be avoided in multi-track events, when the integration gate was offset in respect to the timing of the second traversing particle, and the integration became sensitive to charges induced on the cathode strips by charges flowing out of the anode wires.

Each cluster is further analysis for its internal structure to identify possible peak positions as follows: A truncated cluster is created around the channel with the charge maximum, x_{max}. It extends to the left and to the right for 2 channels, if the charge values for these channels are below a minimum of 90 % of the charge in x_{max}. The truncated cluster extends at most up to the limits of the original cluster or up to a channel with only a minimum of charge. For clusters that reach the 8-bit maximum of the ADC the counting of channels starts at the left and right limits of the saturation plateau. If no such structure is found the cluster is discarded. This procedure ensured that a truncated cluster corresponds to a peak-like structure. Next, the summed charge in the truncated cluster is compared to the charge outside the peak region. If the latter is larger than 30 % in the x-planes of the MWPC or larger than 1 % in the y-planes of the MWPC and the outside region is wider than the required minimum for a cluster, a separate cluster is created. The difference between the x- and y-planes is attributed to the different appearances of pick-up charges on the cathode wires. The extensions of the new cluster is depending on the distribution of charges. For a large charge close to the original peak, *i.e.* within 2 channels, the new cluster extends to the peak region, otherwise to the border region. This construction avoids the creation of extra clusters when fluctuations appear in the tails of the original peak.

In the analysis of the data all clusters are combined to form possible particle

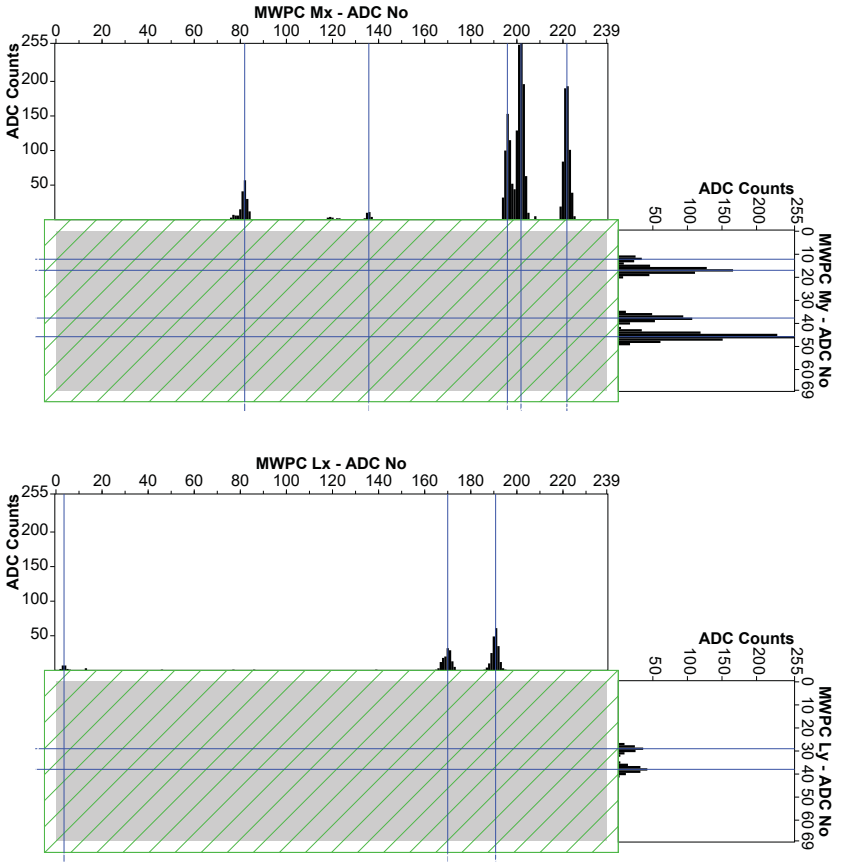

Figure 2.20.: Charge distribution in both MWPCs of an event taken with 2 μA beam current. The anode wires are shown schematically as diagonal lines, cathode wires run horizontally and vertically. The grey shaded area corresponds to the active region of a chamber. Peak positions are determined by calculating the centre-of-charge from a restricted number of cathode channels and are indicated by blue lines in the display. The peak-finding algorithm assumes a typical peak FWHM of 3–5 cathode strips and allows for asymmetric tails inherent to the chamber geometry.

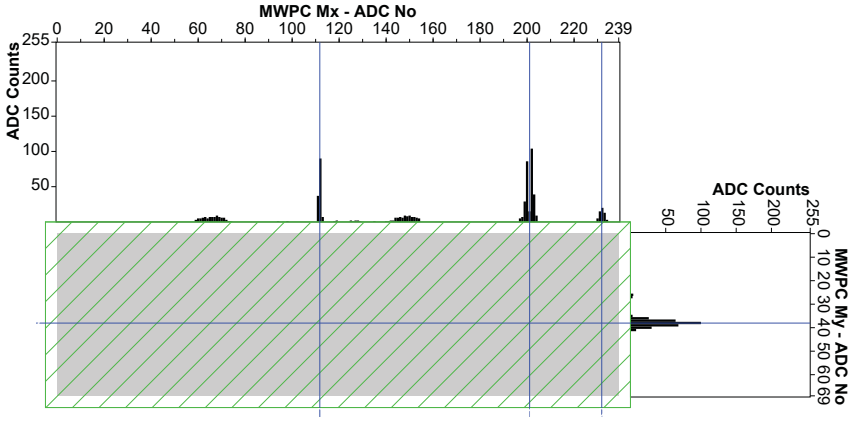

Figure 2.21.: Charge distribution in MWPC M showing satellite charges on both sides of a needle-like peak in the x-plane. Such distributions are formed by multiple particles traversing the chamber at different times, so that the integration time window is offset and the integration is sensitive to charges induced on the cathode strips by charges flowing out of the anode wires. The coupling is seen by comparing the end-points of the diagonal anode wire crossing the blue peak line of the needle to the position of the satellite peaks. The peak-finding algorithm rejects those satellites on the basis of their shape.

tracks. With n clusters n^2 possible track points and n^4 possible tracks through both chambers are generated. This ensemble is classified according to a set of track quality factors, ranging from 0 (excluded) to 1 (highest quality).

As the MWPCs were constructed with symmetric cathode planes, a correlation exists between the induced charge measured in one cathode plane to the induced charge of the perpendicular plane. Fig. 2.22 shows a large set of measured charges in MWPC L deposited by particles of different velocities. A third order polynomial function was used to parametrise phenomenologically the distribution. The non-linear response is attributed to many factors, the asymmetry in the liberated charges drifting through the two-step MWPC, the systematics in the cluster-finding, and saturation in the ADCs. In each MWPC the measured difference of a pair of clusters in x- and y-direction to the phenomenological curve is used to determine the quality factors $Q_x/Q_y|_L$ and $Q_x/Q_y|_M$. In many cases with these factors alone a correct pairing of clusters is possible, as shown in Fig. 2.20.

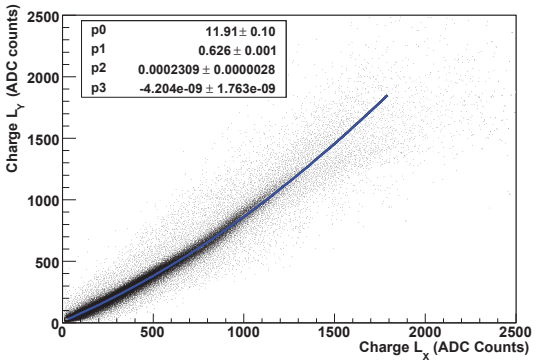

Figure 2.22.: Correlation of induced charges on the cathode planes x and y in MWPC L. A third order polynomial function (blue line) is used to parametrise phenomenologically the distribution.

Valid tracks are bound to angular limits, given by the acceptance of the spectrometer. Both MWPCs are situated in a field-free space, so that particle tracks can be extrapolated linearly to the field boundary at the end of the dipole.

Especially the relation between vertical hit positions of the two chambers provides a powerful criterion for the track finding. The target angle acceptance of the spectrometer is large in the horizontal direction and small in the vertical direction. The vertical track angles, ϕ, for particles originating at the target are strongly correlated to the vertical positions. This y *vs.* ϕ relation is caused by the magnet optics leading to diverging particles tracks.

In the horizontal direction the tracks originating at the target form a large, but limited acceptance region with horizontal track angles, θ, ranging from 35 to $\approx$ 70°, with a dependence on the horizontal position as shown in Fig. 2.23. The strip structures within the acceptance region x *vs.* θ are due to the geometry of the scintillator walls that leads to inefficiencies.

The two scintillator walls that situated behind the MWPCs in the KAOS spectrometer are segmented in x-direction. A last group of quality factors is determined by the extrapolation of the track to both scintillator walls. The spatial difference to the closest observed hit, $\Delta x|_F$ and $\Delta x|_G$, are used as well as the the spacial difference to the vertical positions, $\Delta t|_F$ and $\Delta t|_G$, as measured by the top–bottom time differences by the individual scintillator paddles. The measured time difference in a scintillator bars becomes less accurate when the particle deposits only a small amount of energy, *e.g.* for grazing incidence. To improve the quality assessment

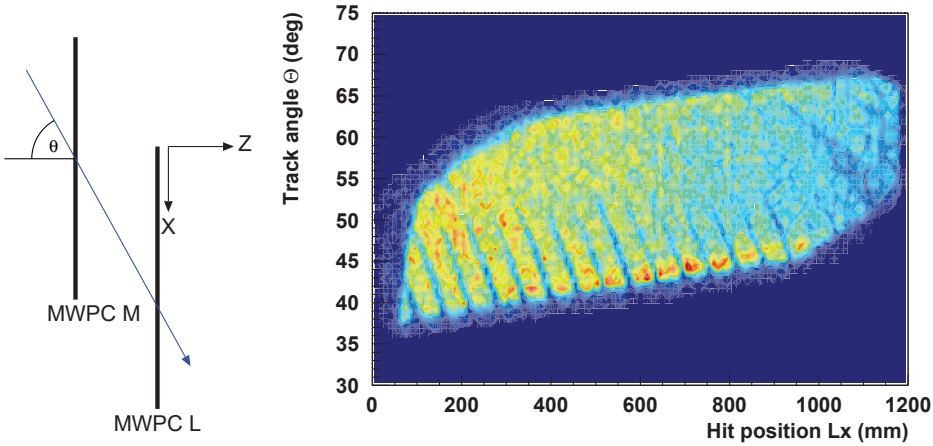

Figure 2.23.: Left: Top view of the MWPCs with the definition of the coordinate system and the horizontal track angle. Right: Distribution of events in the x *vs.* θ plane. The MWPC acceptance is formed by the bright region. The strip structures within the acceptance region are due to the geometry of the scintillator walls that leads to inefficiencies.

Table 2.6.: Track qualities for the two events displayed in Figs. 2.24 and 2.25. The quality factors Q_x/Q_y relate the charges in the two orthogonal cathode planes, the quality factors for the positions *vs.* cartesian angles x *vs.* θ and y *vs.* ϕ correspond to the acceptance, the quality factors Δx correspond to the spatial difference of the projection of the track to the hit positions in the scintillator walls F and G, and the quality factors Δt correspond to the spacial difference of the projection of the track to the vertical positions as measured by the top–bottom time difference by the scintillator paddles of the walls. It is known that track no. 0 is the proper track, as explained in the text.

Fig.	track	total	$\frac{Q_x}{Q_y}\big\vert_M$	$\frac{Q_x}{Q_y}\big\vert_L$	$x\theta$	$y\phi$	$\Delta x\vert_F$	$\Delta x\vert_G$	$\Delta t\vert_F$	$\Delta t\vert_G$
2.24	0	0.96	1	1	1	1	1	0.96	0.58	1
2.25	0	1	1	1	1	1	1	1	0.81	1
	1	0.73	0.86	0.86	1	1	1	1	0.81	1
	2	0.40	0.55	1	1	1	0.73	1	0.91	1

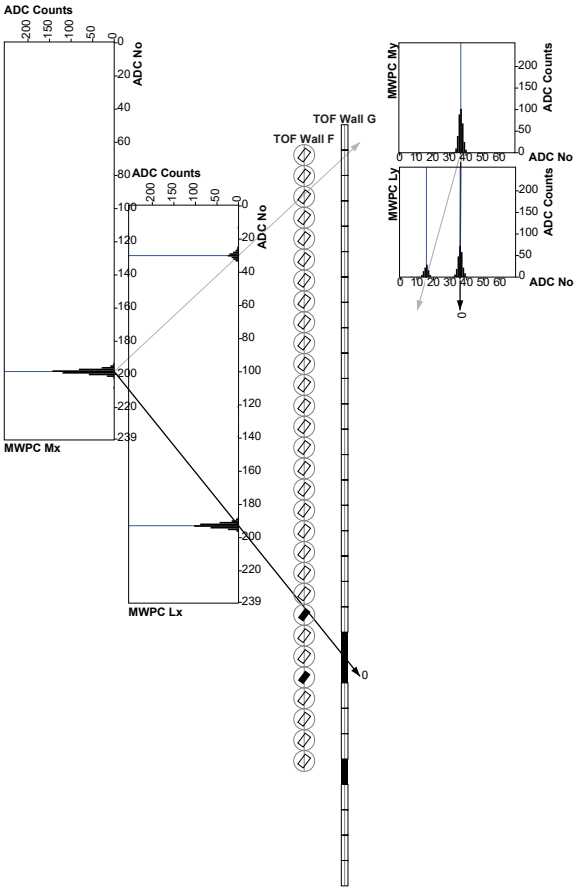

Figure 2.24.: Display of an exceptionally simple event showing in black the ADC charges read from the x-planes of the MWPCs (left), the hits in the scintillator walls (centre) and the ADC charges read from the y-planes (top right). Particles are originating in the top-left corner. One unique set of clusters in the MWPCs together with hits in the walls form the track (black arrow), the two other track combinations were excluded by the quality criteria. The track quality was close to 1, see Table 2.6.

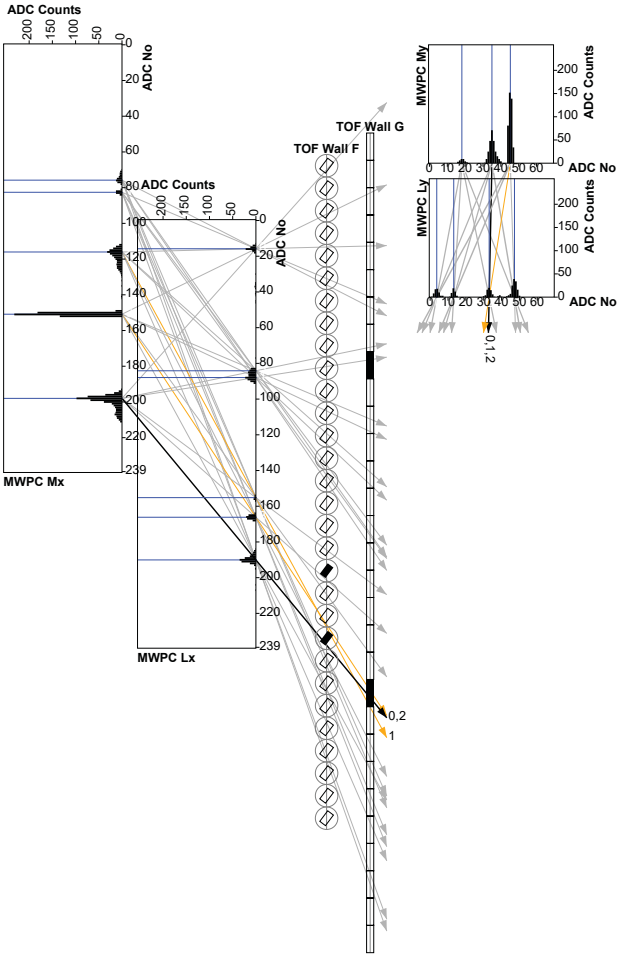

Figure 2.25.: Same as Fig. 2.24 but for a more common event topology with multiple clusters or hits in each detection plane. From the charge distribution in the x-plane of MWPC M the coincident passing of one heavily ionizing and at least one minimum ionizing particle through this chamber can be deduced. The track-finding algorithm returned three possible tracks (black and orange coloured arrows, see Table 2.6), all other cluster and hit combinations were excluded by at least one of the quality criteria.

the maximum value from both walls is used as quality factor.

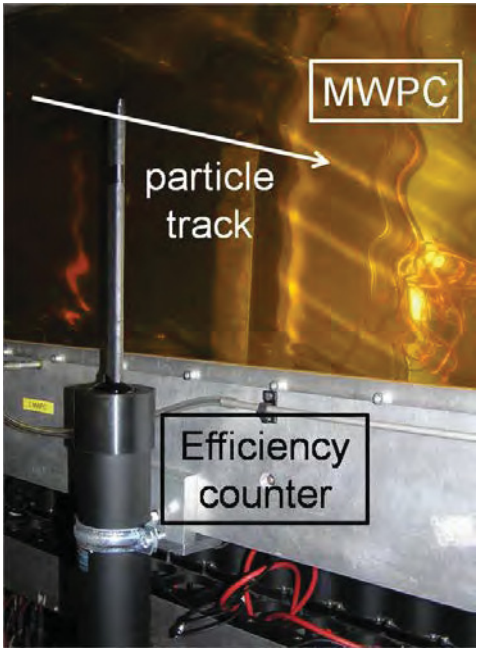

Figure 2.26.: Photograph of one of the efficiency counters that were attached to the frame of the wire chambers. The active part has an area of $\sim 2 \times 3\,\mathrm{cm}^2$. A particle track through the counters is schematically drawn (from S. Sanchez).

Figs. 2.24 and 2.25 show the event displays of two events, the first being exceptionally simple with a low occupancy of ADC charges and hits in the scintillator walls. It can be seen in this event that a strong charge correlation between the two peaks in x- and the two peaks in y-direction exits. One unique set of clusters in the MWPCs together with hits in the walls form the track, the two other track combinations were excluded by the quality criteria and assigned to background particles. The track quality was close to 1, see Table 2.6. A more common event topology with multiple clusters or hits in each detection plane is shown in Fig. 2.25. From the charge distribution in the x-plane of MWPC M the coincident passing of one heavily ionizing and at least one minimum ionizing particle through this chamber can be deduced. The track-finding algorithm returns

three possible tracks see Table 2.6), all other cluster and hit combinations were excluded by one of the quality criteria. As both events were triggered by the efficiency counters it is known that with track no. 0 a proper track assignment was achieved.

Table 2.7.: Intrinsic particle detection and tracking efficiencies as determined with the efficiency counter set-up. A track is defined as being properly reconstructed if it is found to be in the acceptance region of the respective chamber. The gain was higher in chamber L than in chamber M, so that tracking efficiencies differ by a few percent, this difference is increasing with beam current. The chamber track reconstruction efficiencies in columns 5 and 6 include all track qualities from 0 to 1 and all particle species. These efficiencies are separated into pion and proton tracks. Larger inefficiencies arise for higher beam currents and for pion tracks due to the resulting ambiguities and distortions in the charge distributions. The last 3 lines show the loss of efficiency when not all quality factors are used in the track reconstruction: [a] no $\Delta x|_{F,G}$, no $\Delta t|_{F,G}$; [b] no $x-\theta$, no $y-\phi$; [c] no $Q_x/Q_y|_{M,L}$.

I (μA)	intrinsic ϵ (%)		tracking ϵ (%)			proton ϵ (%)		pion ϵ (%)	
	L	M	any track	L	M	L	M	L	M
1	99.3	99.6	98.3	96.3	95.6	97.7	96.9	85.5	83.7
2	99.5	99.7	98.2	95.0	93.1	96.6	94.8	82.4	78.8
3	99.6	99.8	98.2	93.2	90.3	94.9	92.1	80.4	75.2
4	99.6	99.8	98.1	91.6	87.4	93.7	89.8	75.2	68.0
4 [a]	"	"	98.9	75.8	62.7	78.2	65.5	54.3	39.0
4 [b]	"	"	97.8	90.6	80.8	92.5	83.8	74.0	55.8
4 [c]	"	"	97.9	91.4	83.7	93.1	85.8	77.1	66.5

The implemented read-out principle allows for high track multiplicities; however, the track reconstruction can then become a major source of detection inefficiency, quantified by the tracking efficiencies as follows: (i) intrinsic efficiency: the percentage of events in which any charge was detected in the chamber following a charged particle, (ii) any track efficiency: the percentage of events in which a track was reconstructed from the charges, (iii) track reconstruction efficiency: the percentage of events in which the proper track was reconstructed. All efficiencies are to some extend depending on the cluster analysis and the reconstruction method. The track reconstruction efficiency is heavily depending on

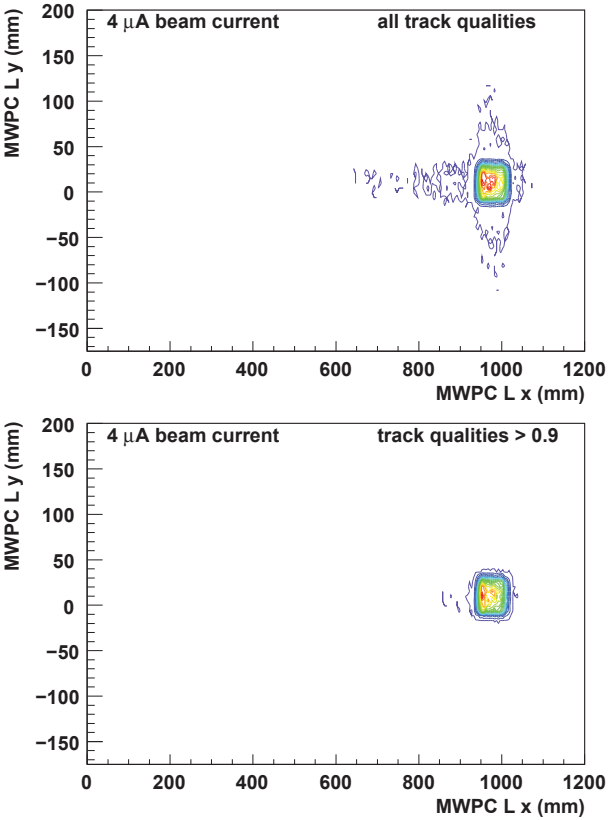

Figure 2.27.: Reconstructed track positions in MWPC L for events triggered by the efficiency counters at a beam current of 4 μA for all track qualities (top) and for track qualities larger 0.9 (bottom). The densely populated square (approx. 93 $\times$ 58 mm^2) corresponds to the projection of the position of the efficiency counters to the wire chamber coordinate system which defines the acceptance region of this chamber. Tracks found to be outside of this acceptance region were reconstructed wrongly. These tracks tend to have a low track quality.

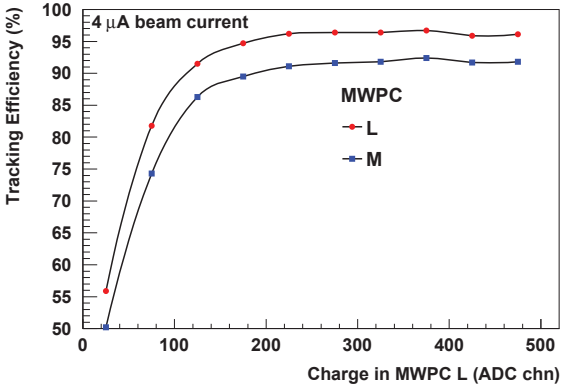

Figure 2.28.: Charge-separated track reconstruction efficiencies for a beam current of 4 μA. Efficiencies for both chambers are shown as a function of induced charge on the cathode of MWPC L. The average charge collected in chamber L for pions is $\sim$ 65 ADC counts, and for protons $\sim$ 220 ADC counts.

the particle's momentum and the beam current, or more general on the luminosity. The latter dependency is a consequence of the fast increment of the flux of background particles with the current.

There is no way of determining the tracking efficiencies from the electro-production measurements. Instead, data was taken during dedicated efficiency runs. For these runs two small scintillating detectors of type Bicron BC-408 and dimensions $L \times W \sim 30 \times 20\,\mathrm{mm}^2$ with 5 mm thickness were installed in front of each MWPC to determine intrinsic and tracking efficiencies of the chambers. The active parts were connected to optical light guides and read out by PMTs of type Hamamatsu R1828. When attached to the MWPC frames the active areas of the counters were vertically centred and horizontally at the same position relative to the corresponding MWPC, see Fig. 2.26 for a photograph of one of the efficiency counters. The detectors could easily be moved out of the spectrometer's acceptance when not in use. A coincidence of both detectors was implemented in the trigger logic for calibration studies. Event rates of $\sim$ 20 Hz at 1 muA beam current on a liquid hydrogen target were reached, sufficient to measure efficiencies in reasonable short periods.

The external counters could be used to select trajectories passing through both chambers in a small acceptance region. The histogram in Fig. 2.27 shows a typical distribution of events in the wire chamber coordinate system obtained under

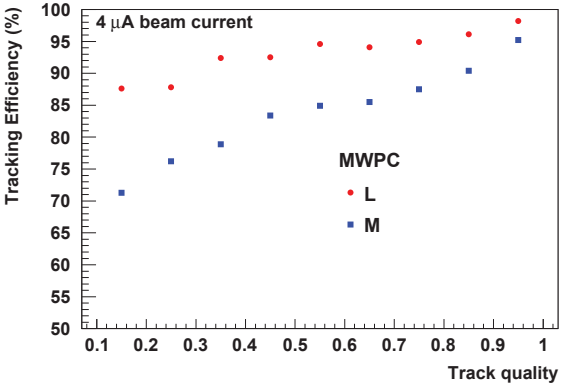

Figure 2.29.: Quality-separated track reconstruction efficiencies for a beam current of 4 μA. Efficiencies for both chambers are shown as a function of a quality factor that includes, among others, the correlation that exists between the induced charge measured in one cathode plane to the induced charge of the perpendicular plane and the relation between vertical hit positions in the two chambers. The continuous increase of the efficiency with the quality provides confidence that the quality factor is indeed a measure of the goodness-of-track.

those trigger conditions for a beam current of 4 μA. The bands in x- and y-direction correspond to wrongly reconstructed coordinates in one of the four MWPC planes, the strongly populated square corresponds to the projection of the position of the efficiency counters. When requiring a high track quality almost only properly reconstructed tracks remain in the event sample.

The spectrometer was situated under forward angles at 31° with a solid angle acceptance of $\Omega \approx 10$ msr in an in-plane angular range of $\vartheta = 21 - 43°$. The results are separated into samples taken with 1, 2, 3, and 4 μA beam current and within the samples into events where the traversing particle was identified by its specific energy-loss as proton and pion by the scintillator walls. With the spectrometer set to a momentum bite around 600 MeV/c protons, kaons, and pions loose significantly different energies in the counter gas. The intrinsic efficiencies were well above 99 % independent on the beam current. The efficiency to form a track was somewhat above 98 %. For pions track reconstruction efficiencies ranged between 86 and 68 % corresponding to beam currents of 1–4 μA, for protons the efficiencies were between 98 and 90 %, details are tabulated in Table 2.7. Several runs were taken during a period of 2 weeks showing small variations of

no more than 2 %. Charge-separated tracking efficiencies for a beam current of 4 μA are shown in Fig. 2.28. From the average charge collected for kaons track reconstruction efficiencies of 75–90 % were evaluated.

Tracks reconstructed to pass through the acceptance region on average have a higher quality factor, whereas tracks reconstructed to miss this region on average have a smaller quality factor. The continuous increase of the efficiency with the quality as shown in Fig. 2.29 for 4 μA beam current, provides confidence that the quality factor is indeed a measure of the goodness-of-track.

In general, tracks of heavily ionising particles in a low background environment have the largest probability of being properly reconstructed. Tracks of minimum ionizing particles are harder to reconstruct properly as background signals of dominantly small amplitudes are present in the chambers at any time. It is concluded that the track reconstruction in the MWPCs represents a primary source of inefficiency for high electron beam currents on typical targets of several hundred mg/cm^2 thickness. The use of information from the external detectors improves the efficiencies by 20–25 % in the case of the highest beam current that was probed. However, at these currents also the external counters register many multiply hits. The check on the spectrometer acceptance and the correlations of the coordinates improves the efficiencies by 10–15 %, and the induced cathode charge correlation has an impact of $\sim$ 5 % for the higher amplitudes. By using the introduced method and the obtained results the track reconstruction efficiencies for kaons could have been determined. These findings were applied to data taken with the KAOS spectrometer in kaon electro-production, improving the systematic uncertainties in the cross-section extraction significantly.

2.5.2. SCINTILLATOR WALLS

Particle identification in the KAOS spectrometer is based on the particle's time-of-flight and its specific energy-loss as measured with two scintillator walls.

Wall F is a segmented scintillator wall with 30 paddles of 38 cm $\times$ 3.7 cm $\times$ 2 cm size, made from material "Pilot F" (equivalent to Bicron BC-408) and read out at both ends by fast PMT (Hamamatsu R1828). The paddles are tilted by 37° around the longitudinal axis in order to achieve an almost perpendicular flight path of the incoming particles into the 3.7 cm wide lateral surface. The total length covered by the wall is 189 cm. The wall is located near the focal-surface of the hadron-arm and a momentum resolution of approximately 4 % could be obtained with this segmentation. A second wall, labelled G, is used to discriminate valid tracks against background events. It consists of 30 paddles of 47 cm $\times$ 7.5 cm $\times$ 2 cm size with a flat geometry spanning a length of 2.2 m and read out at both ends by the same type of photo-tubes. The scintillating material is Bicron BC-408. Originally,

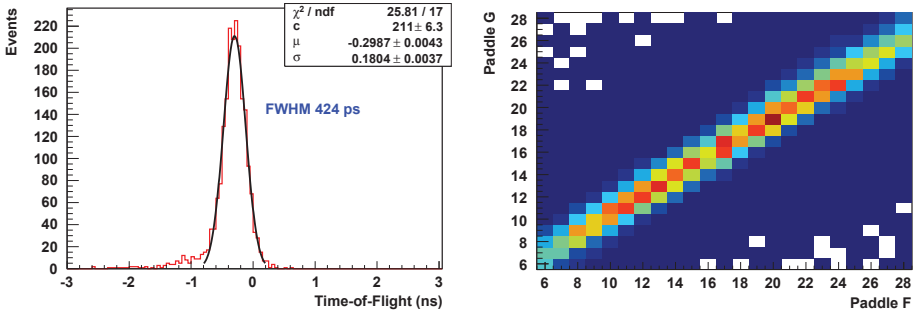

Figure 2.30.: Left: Wall-to-wall time-of-flight spectrum for pions in a given paddle combination (F19 to G19). A Gaussian distribution with a width of $\Delta t_{FWHM} = 0.42\,\text{ns}$ was fitted to the spectrum. Right: Hit distributions taken with an open trigger (any paddle in F and any paddle in G) in which a band of valid paddle combinations is seen.

the designs at the GSI were made for 60 cm long scintillators. However, due to the limited maximum size of the MWPCs (32 cm height) the walls were later built much shorter.

A top-bottom mean timing for deriving the trigger is performed by summing the analogue signals. The hadron-arm trigger of the spectrometer is generated by a coincidence of hits in the two scintillator walls. Fig. 2.30 (right) shows the hit distributions taken with an open trigger (any paddle in F and any paddle in G) in which a band of valid paddle combinations is seen. A fraction of 88 % of the individual amplitude and the summed signals are brought to constant-fraction discriminators. In total there are 60 analogue and 90 timing signals per wall. The signals from the walls are digitised with Fastbus TDC and ADC modules. An intrinsic time-of-flight resolution of $\Delta t_{FWHM} \approx 420\,\text{ps}$ could be reached for pions traversing both walls, see Fig. 2.30 (left). A set of dedicated runs were used to evaluate the energy deposition of pions and protons in the walls in relation to the CFD threshold[1]. This value is used as a crucial input to the acceptance calculation based on the Geant4 simulation.

The scintillator material features a 2.1 ns decay constant, suitable for time-of-flight measurements, and originally a bulk attenuation length of 380 cm. Both walls have been in use since the 1990s at the GSI. A complete characterization was performed in Mainz in order to decide whether they could be re-used for

[1] Conversion factor of 0.0042 MeV/unit

experiments with the KAOS spectrometer at MAMI. The time resolutions and attenuation lengths were measured for a sample paddle with a set of trigger detectors that allowed the determination of crossing particles with an accuracy of 1 cm. The study showed a clear deterioration of the optical properties of the plastic material resulting in attenuation lengths almost one order of magnitude worse than expected. As the achievable time resolution is dependent on the light yield, it was also affected.

The calibration was performed with data taken with the full spectrometer detector package, so that the track positions of charged particles were known from the tracking detectors. Using minimum ionizing particles, attenuation curves were extracted for all paddles.

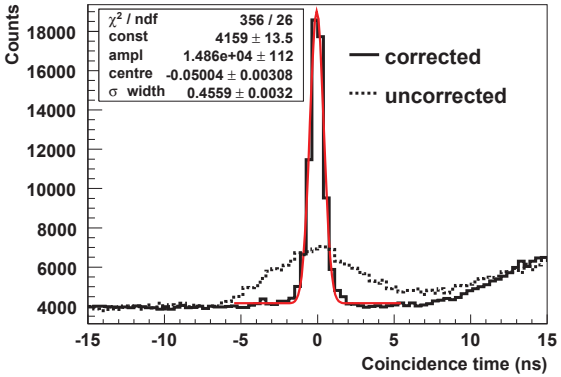

Figure 2.31.: Coincidence time spectrum for the $p(e,e'\pi)$ reaction before and after corrections for the flight-time and trigger-time jitter. A Gaussian distribution on top of a constant background was fitted to the corrected spectrum. The width of the (e',π) peak is $\Delta t_{FWHM} = 1.07$ ns, which is a typical inter-spectrometer time resolution.

The time spectrum is systematically broadened by the propagation time dispersion inside the scintillator, the time differences between different scintillator paddles and their associated electronic channels, and by the variation of the time-of-flight, being proportional to the path-length through the spectrometer.

In general, the voltage pulse of a photomultiplier (PMT), V_{PMT}, can be expressed as a linear superposition of N single photoelectron pulses, v_i. The pulses arrive at individual times due to the time spread in the energy transfer to the optical scintillator levels, t_{dep}, the decay time of the light emitting states, t_{emit}, the propagation time, t_{prop}, and the transit time, t_{TT}, being the time difference

between photo-emission at the cathode and the arrival of the subsequent electric signal at the anode. In addition, there is white Gaussian electronic noise, $w(t)$. This noise in present in the electronic front-end circuits and contribute to the time spread. One can incorporate these processes into a general description: $V_{\mathrm{PMT}}(t) = \sum_{i=1}^{N} v_i(t - (t_{\mathrm{dep}} + t_{\mathrm{emit}} + t_{\mathrm{prop}} + t_{\mathrm{TT}})_i) + w(t)$, where N fluctuates from one pulse to another. In a semi-classical model the probability for observing N photoelectrons during a time interval T is given by a Poissonian distribution $P(\overline{N}, N)$ with $\overline{N}$ being the mean number of photoelectrons per pulse.

The response time of discriminators may shift with the signal amplitude, which is called time-walk. Time-walk effects are relevant if a large range of amplitudes is discriminated. These effects can get corrected by various means, either in hardware or software. It is a standard in nuclear physics to use constant-fraction discriminators (CFD) and leading-edge discriminators (LED), the latter showing a characteristic time-walk. In many cases constant-fraction timing provides the best time resolution with scintillation counters. The timing properties of scintillators are usually defined in terms of a coincidence time resolution. In a typical laboratory measurement the time difference between the discriminated signals of two PMT placed at the extremes of a sample of scintillator is measured for minimum ionising particles crossing the scintillator at its centre. For one of the scintillators used in the KAOS spectrometer's hadron arm, 45 cm in length and 20 mm in thickness, a time resolution reduced for one PMT of the order of FWHM ≈ 150 ps has been achieved in the laboratory [127]. For long scintillators there are several effects degrading the time resolution, namely the light attenuation and the consequences of the scintillator acting as a light guide with corresponding propagation time dispersion. The raw coincidence time, being the time difference between the second spectrometer arm to the common trigger time, $t_o^{raw} = t_{coinc}^{raw} - T_o$, exhibits an additional broadening of ~ 5 ns due to the FPGA time jitter in the trigger module. The latter effect can be corrected for by subtracting the time difference between individual scintillator time and common coincidence time

$$t_{F,G} = t_o^{raw} - t_i - t_i^{offset} - L_e/v_e\,, \tag{2.13}$$

where t_o is the corrected time-of-flight, t_i^{offset} are the time offsets of individual scintillator paddle channels i, $t_i = (t_i^{bottom} + t_i^{top})/2 - T_o$ is the mean time between top and bottom PMT of the individual scintillator paddle, and the last term is the path-length correction for the scattered electron that was detected in the electron arm of the coincidence set-up. The offsets t_i^{offset} were extracted from data by using flight-time differences from one paddle in one wall to two neighbouring paddles in the other wall, thus establishing a "shoe string" pattern of corrections between the two walls. The mean timing corrects for the propagation time spread in first

order. Then, the following simple functional dependence holds for the corrected coincidence time: $t^c_{F,G} = t_{F,G} - L_{F,G}/v_{Kaos}$, with the path-length from target to wall F or G, $L_{F,G}$, being dependent on the particle momentum and its target angles, and v_{Kaos} is the particle's velocity as determined from the reconstructed momentum under the assumption that the incident particle was of type K, π, or p with mass M:

$$v_{Kaos} = |\vec{p}_{Kaos}|c/E_{Kaos} = |\vec{p}_{Kaos}|c/\sqrt{|\vec{p}_{Kaos}|^2 + M^2}. \quad (2.14)$$

The coincidence time spectrum for the $p(e,e'\pi)$ reaction before and after these corrections is shown in Fig. 2.31, where the coincidence time was determined by using the preliminary momentum and path-length reconstruction under the assumption that a pion was detected. A Gaussian distribution on top of a constant background was fitted to the corrected spectrum. The width of the (e',π) peak is $\Delta t_{FWHM} = 1.07$ ns, which is a typical inter-spectrometer time resolution achieved between spectrometers A, B, and C.

The signal amplitudes are corrected for the reconstructed path-length through the scintillator bulk material and the light absorption inside the paddle. The path-length of a track is determined by the angles θ and ϕ, given by the MWPC analysis, the thickness of the scintillator paddles, and its orientation. The scintillators of wall F are rotated by approximately 45° to the MWPC coordinate system, and the parallel alignment of the MWPC and the walls F and G is not perfect. After transformation into the scintillator coordinate system the path-length is given by

$$L_{F,G} = d_{F,G}\sqrt{1 + \tan^2\theta_{F,G} + \tan^2\phi_{F,G}}\,, \quad (2.15)$$

where $d_{F,G}$ is the thickness of the paddle. With the angular acceptance of the spectrometer the spread in path-length is dominated by the horizontal angle θ. The precise calculation of the track length inside the scintillator paddles was an important correction factor to be applied to the measured energy deposition.

Fig. 2.32 shows in red a simulation of the reconstructed energy deposition in scintillator wall F as a function of the horizontal coordinate when a continuous scintillator was assumed in the correction. A wrong correction arises from particles crossing through the corners of the paddles. The values printed in blue are the result after the proper correction factor is applied. Back lines show the *rms* widths of the energy-loss distribution.

The measured amplitudes, A_i, were first corrected to the nominal paddle thickness by $I_i = (A_i - P_i)G_i$ with P_i being the pedestal position and G_i an individual gain factor. Because of the ageing of the material the absorption of the scintillation light inside the scintillator is strong. The intensity I of the light yield, Y, has been

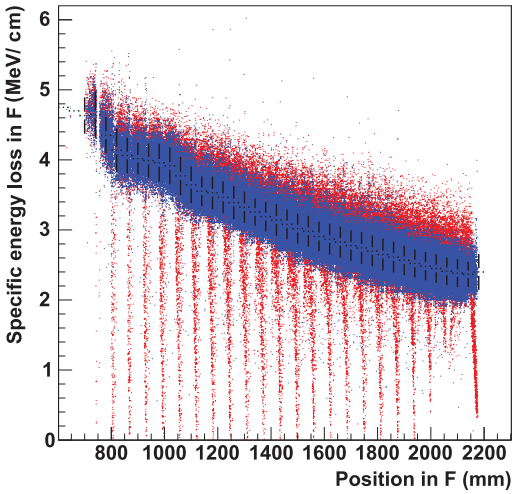

Figure 2.32.: Simulation of the reconstructed energy deposition of kaons in scintillator wall F as a function of the horizontal coordinate. When a continuous scintillator was assumed in the correction red values are obtained, the wrong correction arises from particles crossing through the corners of the paddles. The values printed in blue are the result after the proper correction factor is applied. Back lines show the *rms* widths of the energy-loss distribution (from S. Sanchez).

parametrised in dependence of the vertical hit position $y_{F,G}$ and the path-length through the scintillator paddle by an exponential form:

$$Y = L_{F,G} \cdot I_i \cdot \exp\left(-y_{F,G}/\Lambda_i\right), \tag{2.16}$$

and the top and bottom amplitudes were used to determine the geometric mean value, Q, of the amplitude in this paddle:

$$Q_i = \sqrt{Y_i^{top} \cdot Y_i^{bottom}}. \tag{2.17}$$

No two identical particles will produce the same ionization and atomic excitation because of the statistical nature of the reactions. For different particle species, the difference in energy-loss, ΔE, to a parametrised distribution was calculated,

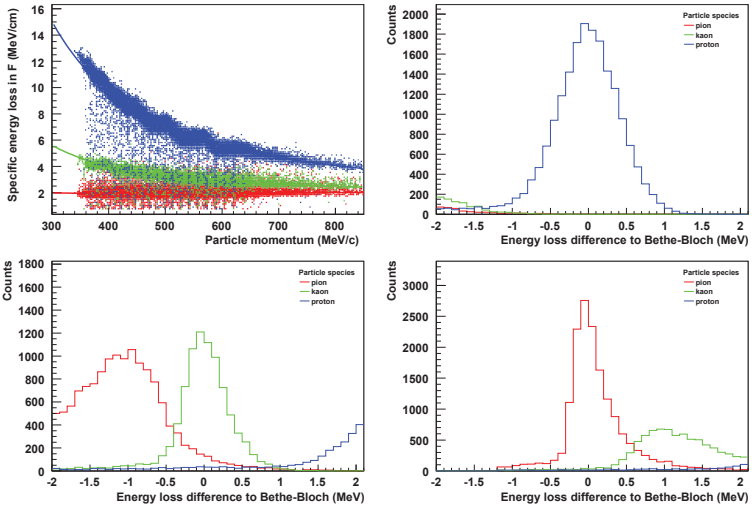

Figure 2.33.: Simulated distribution of the specific energy-loss, $\mathrm{d}E/\mathrm{d}x$, as a function of momentum and of the difference in energy-loss, ΔE, to Eq. 2.18 for protons, pions, and kaons in scintillator wall F.

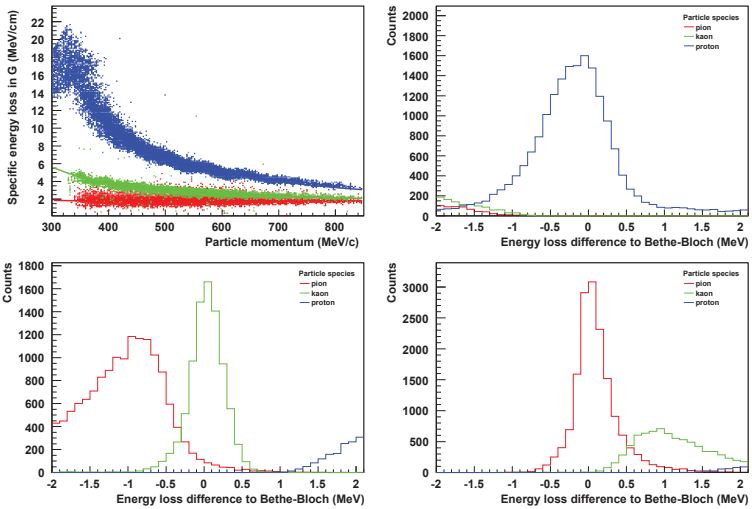

Figure 2.34.: Same as Fig. 2.33, but for scintillator wall G.

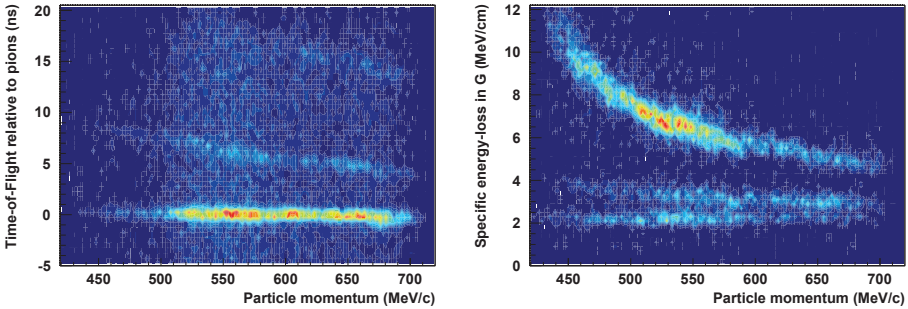

Figure 2.35.: Measured time-of-flight (left) and specific energy-loss (right) spectra in scintillator wall G as a function of particle momentum. The time-of-flight was corrected for the path-length dispersion assuming the particle was a pion. The event sample was enriched in kaon events by a cut in missing mass.

which was implemented according to the Bethe-Bloch equation [128] neglecting relativistic corrections:

$$-\frac{\mathrm{d}E}{\mathrm{d}x} = 2\pi N_A r_e^2 M_e c^2 \rho \frac{Z}{A}\frac{z^2}{\beta^2}\left[\ln\left(\frac{2M_e\gamma^2 v^2 T_{max}}{I^2}\right) - 2\beta^2\right], \qquad (2.18)$$

using $2\pi N_a r_e^2 M_e c^2 = 0.1535\,\mathrm{MeV\,cm^2/g}$, T_{max} as maximum kinetic energy to be imparted to a free electron in a collision, $\mathrm{d}E/\mathrm{d}x$ as mean rate of energy-loss (or stopping power) per unit matter thickness, A, Z as atomic mass and number of absorber, ρ as mass density of absorber, N_A as Avogadro's number, I as mean excitation energy, M_e as electron mass, r_e as classical electron radius, $r_e = 2.8\,\mathrm{fm}$, and ze, v as charge and speed of incident particle. Figs. 2.33 and 2.34 show the simulated distribution of the specific energy-loss, $\mathrm{d}E/\mathrm{d}x$, as a function of the momentum and of the difference in energy-loss, ΔE, to the Bethe-Bloch equation for protons, pions, and kaons in the scintillator walls F and G. In both walls kaons can easily be distinguished from protons, but the pion energy-loss distribution overlaps significantly with the kaon energy-loss distribution.

Measured time-of-flight and specific energy-loss spectra are shown in Fig. 2.35 as a function of particle momentum. The time-of-flight was corrected for the path-length dispersion assuming the particle was a pion. The data is dominated by background particles (p and π) because of a kaon-to-background ratio of 1 : 200 and the event sample was enriched in kaon events by a cut in missing mass (see Chapter 3) to show the position of the band of kaons in relation

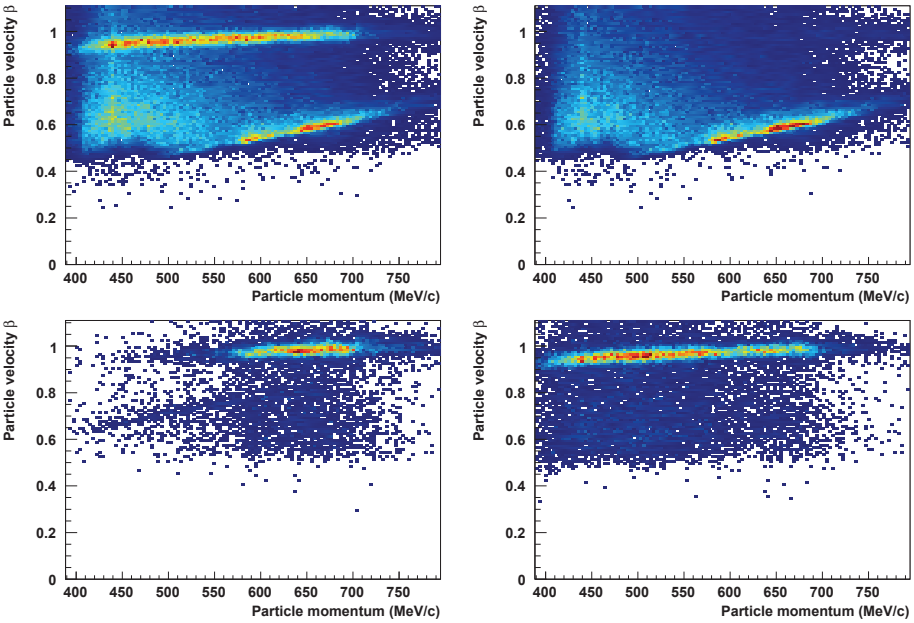

Figure 2.36.: Distribution of the velocity β as a function of momentum determined from the time-of-flight measurement and the reconstructed momentum. Top left: velocity for all valid tracks. Top right: events after a cut on high specific energy-losses in the scintillator walls. Bottom left: effect of a cut on expected specific energy-losses for kaons. Bottom right: effect of a cut on low specific energy-losses.

to the two bands from the dominant particle species. The flight-time separation between kaons and pions is 5–10 ns, between kaons and protons 10–15 ns. The energy-loss separation between kaons and pions is small, whereas the separation between kaons and protons is of the order of 2–5 MeV/cm.

The kaon identification was based on a specific energy-loss cut for the scintillator walls F and G and a subsequent cut on the coincidence time. The velocity, v, of a particle is often given as a fraction of the speed of light *in vacuo*: $\beta = v/c$. As a matter of convention, the term velocity will be used when referring to β. The

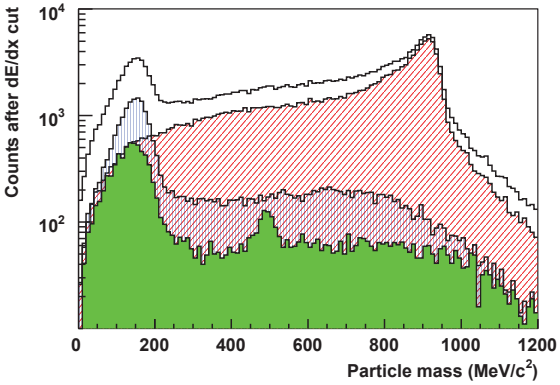

Figure 2.37.: Distribution of the mass of the detected particles determined from the time-of-flight measurement and the reconstructed momentum and path-length. The outer contour includes all events with valid tracks in the tracking chambers, the underlying curves show event samples that were cut on the specific energy-loss expectation for protons (leaning hatch), pions (vertical hatch), and kaons (solid fill).

derived particle velocity and mass are given by:

$$\begin{aligned} \beta_{Kaos} &= L_{F,G}/(c \cdot t_{F,G}), \\ \gamma_{Kaos} &= (1-\beta_{Kaos}^2)^{-1/2}, \end{aligned} \qquad (2.19)$$

and

$$M_{Kaos} = p_{Kaos}/(c \cdot \beta_{Kaos}\gamma_{Kaos}). \qquad (2.20)$$

The necessity of the pion and proton suppression is seen in Fig. 2.36 where the velocity distribution of the detected particles are shown under the effect of specific energy-loss cuts. After a cut on high specific energy-losses in the scintillator walls the protons were clearly identified. A cut on the expected specific energy-losses for kaons resulted in a kaon band at $\beta \sim 0.6$–0.8. The remaining background in this event sample is mostly due to pions. After a cut on lower specific energy-losses pions with velocities β close to unity dominate the spectrum. The particle yields in Fig. 2.37 have to be corrected for the MWPC efficiencies, the meson decay in flight and the spectrometer acceptance. The mass distribution is shown in Fig. 2.37 for the same cuts. Again, it is evident that the pion and proton suppression is necessary to identify kaons. The resolution in the mass is dependent

on the time-of-flight resolution and the accuracy of the reconstructed path-length and particle momentum:

$$\left(\frac{\delta M}{M}\right)^2 = \left(\frac{\delta p}{p}\right)^2 + \gamma^4 \left(\frac{\delta t}{t}\right)^2 + \gamma^4 \left(\frac{\delta L}{L}\right)^2 . \tag{2.21}$$

With an inter-spectrometer time resolution of approximately 1 ns and about 30 ns flight-time for kaons this contribution dominates the overall mass spectrum.

2.5.3. AEROGEL CHERENKOV DETECTOR

The clear identification of kaons with the KAOS spectrometer is one of the great challenges of the strangeness electro-production experiments at MAMI. At low momenta, $p \sim 500\,\mathrm{MeV}/c$, the discrimination between kaons and pions is possible by the *time-of-flight* method. But even with perfectly tuned scintillator walls and calibrated detectors, in such a configuration $\pi/K/p$ separation power dramatically deteriorates with momentum as $\Delta t \sim 1/p^2$, so that for the discrimination at momenta $p \geq 800\,\mathrm{MeV}/c$ a Cherenkov counter is needed as a complement. The new detector should be designed with the following restrictions:

1. have a large sensitive area to match spectrometer acceptance, with an effective area of roughly $H \times W \approx 40 \times 250\,\mathrm{cm}^2$;

2. be slim to fit in the slot in-between the second scintillator wall and the radiation shielding wall at approximately 50 cm behind the focal-surface of the spectrometer, the only readily available space in the KAOS spectrometer detector stack;

3. have reasonable time resolution and high rate capability.

The most important criterion for the design of the detector is the expected velocity distribution of kaons in the KAOS spectrometer. Fig. 2.42 shows this distribution as a function of the coordinate along the possible detector plane.

The design and the operation of Cherenkov counters is governed by the basic relations [129–131] which connect the emission angle θ_c of Cherenkov photons, the velocity of a charged particle $v = \beta c$, where c is the speed of light in vacuum, and the index of refraction n of the radiator medium. The threshold condition for Cherenkov light emission is given by

$$\beta_{min} = \frac{v_{min}}{c} \geq \frac{1}{n} . \tag{2.22}$$

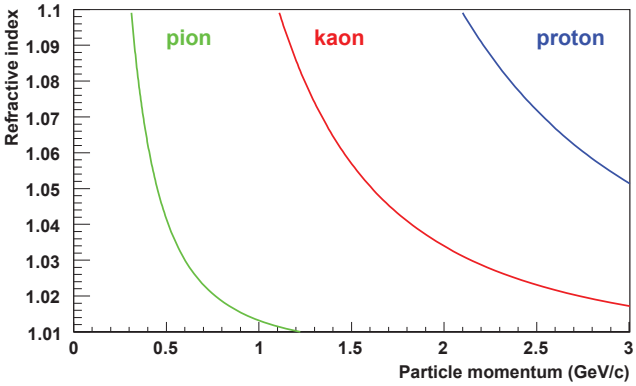

Figure 2.38.: Detection threshold for an aerogel Cherenkov counter requiring at least 2 detected photo-electrons as a function of momentum and refractive index, calculated according to Ref. [132] using an aerogel thickness $l = 4\,\text{cm}$ and a figure-of-merit $N_0 \approx 46$.

The angle of emission increases with the velocity reaching a maximum value for $\beta = 1$, namely $\theta_c^{max} = \arccos 1/n$. The minimum momentum at which a particle of mass M will exceed the phase velocity of light in the medium is simply given by

$$p_{min}c = \frac{Mc^2}{\sqrt{n^2-1}}\,. \tag{2.23}$$

The number of photons produced by a $Z = 1$ particle per unit track length in a wavelength region between λ_1 and λ_2 depends on the velocity of the particle and the refractive index $n(\lambda)$ of the radiator:

$$\frac{\mathrm{d}N}{\mathrm{d}l} = 2\pi\alpha\left(1 - \frac{1}{n^2(\lambda)\beta^2}\right)\left(\frac{1}{\lambda_1} - \frac{1}{\lambda_2}\right), \tag{2.24}$$

which is a good approximation for a weak variation of n with l. The number of Cherenkov photons scales as $L\sin^2\theta$, giving a total of N photons produced for a radiator of length L is $N = N_0 L\langle\sin^2\theta\rangle$, where $N_0 = 2\pi\alpha(1/\lambda_1 - 1/\lambda_2)$ and α is the fine structure constant. Due to the $1/\lambda$ dependence of Eq. 2.24, most of the photons are produced in the UV range. Therefore, it is an important requirement of every Cherenkov detector to have a high detection efficiency in this wavelength band.

Silica aerogel with refractive index $n \sim 1.04$–1.07 seems to be the ideal material for use as a Cherenkov radiator for pion suppression. Aerogels are trans-

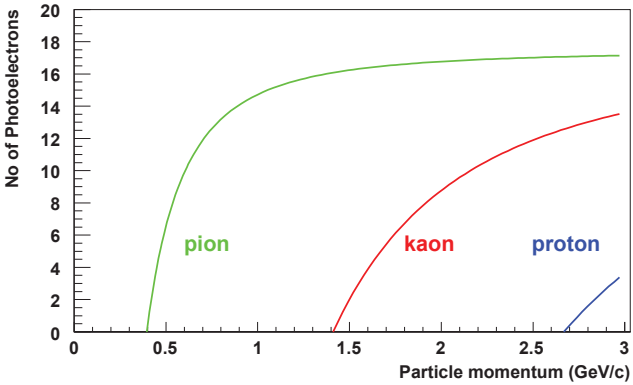

Figure 2.39.: Number of photo-electrons for two 2 inch PMT given for an aerogel thickness $l = 4\,\text{cm}$, index of refraction $n = 1.05$, and a figure-of-merit $N_0 \approx 46$, as calculated as a function of momentum according to Ref. [132]. Pions and kaons are well separated, electrons (positrons) are above threshold over essentially the full momentum range.

parent, highly porous solids of silica oxide with typical pore sizes of 10 nm and 95 % of the material's volume made by the pores. It is a silica-based substance of $n(SiO_2) + 2n(H_2O)$. It is derived from a gel in which the liquid component of the gel has been replaced with a gas. The refractive index for the various aerogel materials of density $\rho = 0.04$–$0.20\,\text{g/cm}^3$ is roughly given by $n - 1 = (0.210 \pm 0.001)\rho$.

The greatest challenge for all Cherenkov detectors is the collection of the Cherenkov radiation, which is then incident on the photodetector. Some of the strategies for an efficient light collection are the use of: (i) mirrors, that focus the light; (ii) wavelength shifters, which convert the light to a different wavelength band and transport it; (iii) diffusion boxes, in which the light gets scattered randomly until it hits on the attached PMT. The most important consideration when designing a large, diffusely reflective aerogel Cherenkov detector is how many photoelectrons will be detected per relativistic event. This photoelectron signal, typically less than ten photo-electrons, determines the detector's efficiency for detecting relativistic particles. For a diffuse light box having reflectivity η and photodetectors which cover an areal fraction ϵ of the surface, the average number of

photons hitting the PMT can be estimated by [132]:

$$N_{pe} = N_0 L \left(1 - \frac{1}{\beta^2 n^2}\right) \frac{\epsilon}{1 - \eta(1-\epsilon)} \,. \tag{2.25}$$

In Fig. 2.39, the expected yields in terms of the number of photo-electrons are given for an aerogel with index of refraction $n = 1.05$ and thickness $l = 4\,\text{cm}$, two 2 inch PMT read-out and a figure-of-merit $N_0 \approx 46$, as calculated according to this phenomenological formula. In the figure-of-merit all parameters which cannot be determined prior to construction were included.

The detection thresholds for an aerogel Cherenkov counter requiring at least 2 detected photo-electrons as a function of momentum and refractive index, calculated according to Ref. [132] using an aerogel thickness $l = 4\,\text{cm}$ and a figure-of-merit $N_0 \approx 46$ are shown in Fig. 2.38. The preferred index of refraction in the counters for the KAOS spectrometer would be $n = 1.06$, and the second best choice would be $n = 1.05$. Refractive indices below $n = 1.05$ are not possible because then the separation between pions and kaons in the momentum range $p \sim$ 600–1000 MeV/c is too small. When choosing a refractive index of 1.075 a theoretical velocity threshold of $\beta_{thr} = 0.93$ will allow to suppress pions of all momenta possible at MAMI while no kaons will leave a detectable signal, as they are limited in momentum to 1 186 MeV/c for a maximum beam energy of 1 508 MeV. Using such a high threshold very slow pions cannot be suppressed effectively, but these are distinguished easily from kaons by their time-of-flight.

Known producers of aerogels are Airglass, Sweden, the Boreskov Institute of Catalysis in Novosibirsk, Russia, and Matsushita Electric Works, Japan. The Boreskov Institute is able to produce very transparent silica aerogel with refractive indices in the range 1.005–1.05, and a larger number of tiles have been ordered to be optically characterised and tested in Mainz. Several aerogel tiles of different refractive indices were already available for studies, among them high density aerogels with $n = 1.07$ and 1.12 made by Chiba University, Japan, and tiles with $n = 1.05$ from Matsushita Electric Works.

Aerogels by themselves are hydrophilic, but chemical treatment can make them hydrophobic. If they absorb moisture they usually suffer a structural change, such as contraction, and deteriorate, but degradation can be prevented by making them hydrophobic. Available aerogel materials from the Boreskov Institute are hydroscopic, so they need baking and storage in a dry nitrogen atmosphere to maintain the initial good transmittance of the radiator. Test production of hydrophobic samples has started at the Boreskov Institute in 2010. The technology which makes the aerogel hydrophobic results in 30 % decrease in light scattering and absorption length. The Boreskov Institute claims to have very large experience with production of aerogel with $n = 1.05$, and they can also produce $n =$

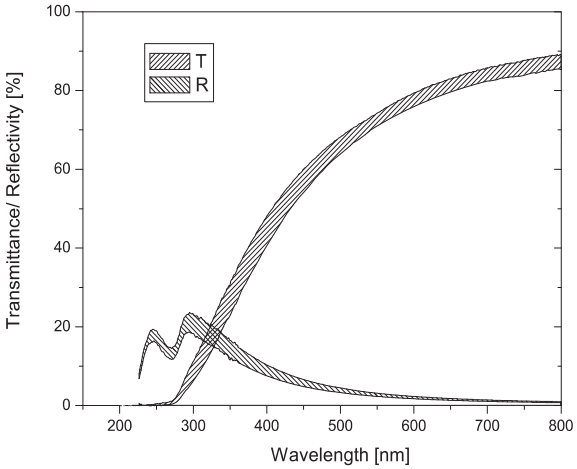

Figure 2.40.: Measured transmittance, $T(\lambda)$, and reflectivity, $R(\lambda)$, for silica aerogel with $n \approx 1.07$ (from L. Debenjak).

1.06 material with its optical parameters almost the same as for 1.05, but the yield for $n = 1.07$ will be smaller than for 1.06. In contrast, tiles made by Chiba University or by Matsushita are, in general, hydrophobic, and they are known to be of high quality.

Although the light transmittance of aerogel is relatively small, the light absorption is also rather small. Hence, a large number of photons undergo multiple scattering and lose directionality but do eventually reach a photo-detector. The transmittance between 200 nm and 800 nm of two aerogel tiles of $n = 1.07$ has been measured at different positions on the surface to scan for potential inhomogeneity and to obtain averaged values, see Fig. 2.40. From these measurements the scattering length, the absorption length and the attenuation length have been deduced by applying the following relation

$$T(\lambda) = \Big(1 - R(\lambda)\Big) \exp\left(-\frac{a}{\lambda^2}d - \frac{b}{\lambda^4}d\right). \qquad (2.26)$$

Here, d is the thickness of the aerogel tile. The parameters a and b are related to the absorption and scattering length: $\Lambda_{abs} = \lambda^2/a, \quad \Lambda_{scat} = \lambda^4/b$. The fit yields: $a = (2.48 \pm 0.04) \times 10^{-10}$ cm, $b = (5.76 \pm 0.07) \times 10^{-19}$ cm^3. These parameters have also been measured at different thicknesses of the aerogel by selecting different tile orientations. The corresponding absorption and scattering lengths at

the wavelength seen by PMT ($\lambda \approx 500\,\text{nm}$) are 8–13 cm.

Table 2.8.: Absorption and scattering lengths of $n = 1.07$ aerogel tiles of different thicknesses at wavelength $\lambda = 500\,\text{nm}$. Deviations of values at different thicknesses may indicate that the simple power-law dependence of the absorption and scattering lengths on the wavelength assumed in Eq. (2.26) is inappropriate.

d (cm)	2	4	9
Λ_{abs} (cm)	10.1	9.1	7.9
Λ_{scat} (cm)	10.8	13.7	13.5

In collaboration with a group from Ljubljana University and Jožef Stefan Institute, Ljubljana, Slovenia, an aerogel Cherenkov counter is being developed. Before the construction of the final detector several prototypes with aerogel tiles of $d = 2\,\text{cm}$ thickness were designed, mounted inside one of the spectrometers, and tested during beam-times. In a first prototype of $20 \times 10\,\text{cm}^2$ total area photons were detected by two 2 inch PMT at both ends of the light-collection box. The diffuse light collection by means of highly reflective walls, also known as a "diffusion box", was a good choice for the prototype set-ups. The inner walls were covered by Millipore paper, a highly reflecting diffusive material or alternatively by a specular reflector. The paper's light reflection is diffusive and follows LambertŠs law having 95 % diffusivity up to 400 nm, while in the UV it decreases smoothly to 80 % at 315 nm. Modifications to the basic geometry of the prototype were tried, *e.g.* different kinds of polished aluminium faces or commercial mirrors were used in the interior in order to improve the reflection of photons towards the PMT. A schematic view of the prototypes is shown in Fig. 2.41.

During the two beam-times in October and November 2008 the performance of prototypes with several refractive indices and thicknesses of the aerogel tiles were studied with electrons, pions, and protons of various momenta in the KAOS spectrometer. The absorption and scattering losses in the aerogel tiles lead to a very low number of detected photons. Detection efficiencies were determined at different threshold settings and particle momenta. In 2009, aerogel tiles with $n = 1.07$ made by Chiba University, Japan, which provide separation of pions and kaons in the momentum range $p \approx 365$–$1\,300\,\text{MeV}/c$, were tested with the beam. The detector was exposed to electrons, pions and protons. In Fig. 2.43 a

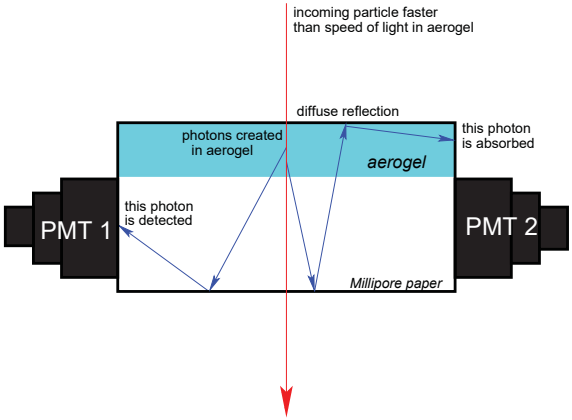

Figure 2.41.: Schematic view of the aerogel prototype detectors. During the beam-tests the detectors were placed inside the KAOS spectrometer with two 2 inch PMT aligned vertically. The inner walls of the light-collection box were covered by Millipore paper.

representative spectrum is shown for events identified by the detector package of the spectrometer as pions and protons. The number of fake photo-electrons for protons which were below the Cherenkov light emission threshold which may be a result of δ-electrons, accidental events or scintillation of particles traversing the detector

Table 2.9.: Mean number of photoelectrons measured with the prototype Cherenkov counter realised in different set-ups and compared to simulations.

p (MeV/c)	particles	mirrors	$N_{\mathrm{pe}}^{\mathrm{exp}}$	$N_{\mathrm{pe}}^{\mathrm{simul}}$
380–530	electrons	no	4.2	4.8
480	pions	yes	3.6	3.4

The detection efficiency was determined by the ratio of events with a signal above a given detection threshold to the number of events reconstructed to be passing the volume of the counter. Results for different set-ups tested during several beam-times are shown in Table 2.10. When testing with pions, the proto-

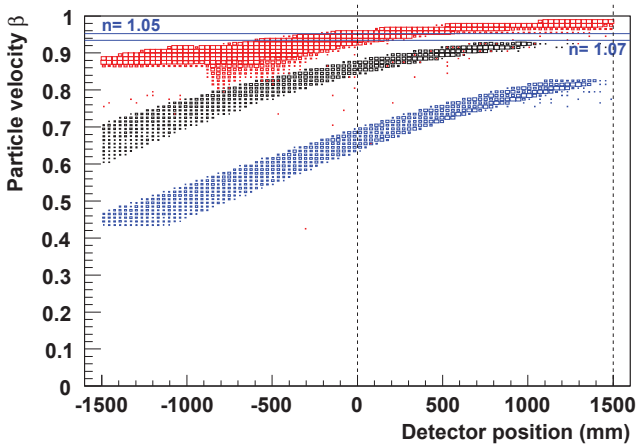

Figure 2.42.: Simulated distribution of particle velocities along the planned Cherenkov counter plane. Pions are shown in red, kaons in black, and protons in blue. A magnetic field of 1.2 T was used in the simulation, corresponding to a central momentum of 900 MeV/c. The dotted lines indicate the possible geometrical coverage of the Cherenkov detector (from [117]).

type was rotated towards the incoming particle direction.

For the simulation of such detectors, the optical properties of the aerogel were needed as input data. The behaviour of the prototype and the final detector system has been simulated with Litrani, a C++/ROOT-based program [133] using the Monte Carlo method. All beam-time set-ups of the prototype detectors were implemented in the code. The number of photoelectrons, N_{pe}, predicted by the simulation was compared to number seen in the actual experiments as shown in Table 2.9. The simulated distribution of photoelectrons for these set-ups is shown in Fig. 2.44.

Since the results from the experiments and the simulations are in fairly good agreement one can trust the simulations to predict and optimize the light yield of aerogel Cherenkov counters to be used in the final design. The study converged on the following two main scenarios: either there are no mirrors implemented (only a diffusive box coated with a reflective material, possible SpectraFlect) or there are two planar mirrors. The simulations indicate that silvered aluminium, or just ordinary mirrors improves the light collection efficiency in this geometry by about 30 %. Each cell has approximately 4 000 cm^2 inner surface, which

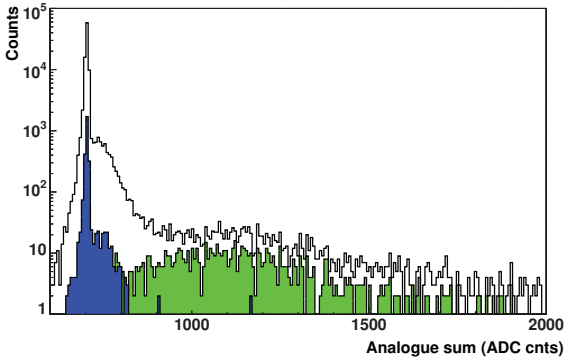

Figure 2.43.: Measured amplitude sum spectrum from both PMT of one of the prototype Cherenkov counters for events identified by the detector package of the spectrometer as pions (green) and protons (blue). The unshaded spectrum corresponds to all particles entering the Cherenkov counter. Protons were below the Cherenkov light emission threshold.

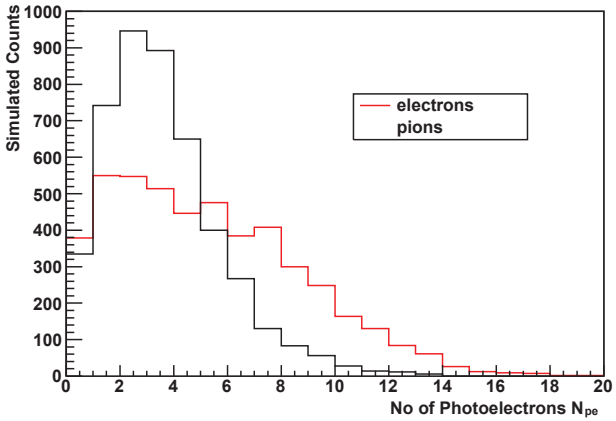

Figure 2.44.: Simulated photoelectron spectra for two different prototype Cherenkov counters. The simulated box geometries and particle momenta correspond to the measurements presented in Table 2.9 (from L. Debenjak).

Table 2.10.: Measured detection efficiencies, ϵ, for electrons and pions at various momenta, p, traversing the prototype Cherenkov counter. In one set-up the light-collection box included mirrors.

p (MeV/c)	particles	mirrors	ϵ (%)
380–530	electrons	no	88
620	pions	no	90
480	pions	yes	65

will be painted or sprayed by reflectance coating. For very high reflectivity the deposited layer might be thicker than 0.5 mm. The light-collection box was designed according the the simulation results. The photon detection probability in the case of a diffusion box is directly related to the fraction of detector surface covered by PMT. An increase in the area covered by PMT results in an increase of the number of photons detected. For the final detector 5 inch PMT from either Hamamatsu or Electron Tubes will be used.

A first cell of the final detector is under construction. The size of the tiles is $5 \times 5 \times 2\,\mathrm{cm}^3$, and 35 tiles (1.75 litres) of aerogel are used to cover the active area of this element. However, the volume that needs to be filled in each detector cell is twice as thick as one tile, $35 \times 25 \times 4\,\mathrm{cm}^3$, so that a stack of two layers is needed. The full counter array will consist of 10 such cells stacked together so that one cell touches the next cell, *i.e.* the total active area will be about $35 \times 250\,\mathrm{cm}^2$. The read-out is done two-sided by Hamamatsu super-bialkali PMT of type R877-100 with a very high quantum efficiency of up to 35 % are used. It is expected that the aerogel Cherenkov detector will be ready during the year 2010 and that it will enhance the performance of the KAOS spectrometer significantly.

2.5.4. COINCIDENCE AND TRACKING TRIGGER SYSTEM

In order to cope with the high background rates KAOS has been equipped with a new trigger system. For the hadron arm the correlation between the paddles in both walls corresponding to valid trajectories is needed for the trigger decision. The relatively high complexity of the valid patterns and the intrinsic necessity of a flexible trigger logic for a spectrometer that faces a wide experimental programme demands a programmable logic system. The VME Universal Logic

Modules VULOM and VUPROM were developed at the Experiment Electronics Department of GSI for general purpose logic operations [134]. A VULOM prototype module equipped with a VIRTEX-4 FPGA and ECL front panel inputs and outputs was tested during the first KAOS beam-time already in November 2007. Two VULOM units were necessary to cope with 90 valid combinations given by the track conditions. Beam currents up to 10 μA of 855 MeV electrons on a carbon target ($\sim$225 mg/cm^2) were used. Particle identification was carried out successfully and despite the relatively small distance from the target area to the electronics the logic modules did not show any misbehaviour. Background suppression depends on the threshold imposed on the summing discriminators. At 500 nA beam current and a sum signal threshold of 30 mV the raw trigger rate changed from 49 kHz to 1 kHz, while at 310 mV the reduction was from 1.7 kHz to 1.4 Hz [135]. During the data-taking in the kaon production experiments with 1 μA beam current on a liquid hydrogen target the raw trigger rate changed from 1 MHz to 50 kHz with minimum signal thresholds.

In 2008 the two VULOM modules were replaced by a single VUPROM module. Each so called VME Universal Processing Module (VUPROM) has 256 I/O channels in a 1-unit-wide VME 6U form-factor. The digital signals are transmitted in high speed differential LVDS standard and are combined in 8 groups of 32 channels each, where one group is reserved for output, three groups are allocated to input, and the remaining four groups are freely configurable as input or output. Such a module is equipped with one VIRTEX-4 FPGA, capable of operation at 400 MHz, and one 1 GHz DSP. The VHDL code is used for defining the logical function. A compiled program can be loaded into the FPGA via a JTAG connector or directly by means of the VME interface. A program is stored in a dedicated flash memory and it is automatically loaded after powering up.

The coincidence trigger is based on time-of-flight and is therefore generated from the KAOS VUPROM logic and from SpekB or SpekC scintillator signals. Fig. 2.45 shows the coincidence trigger system. The two single arm trigger signals are brought to the central coincidence unit together with the non-busy signals of the DAQ blocking logic. A valid trigger signal is followed by the arming and common stop signals for the TDC, the gate signals for the ADC, the interrupt signals for the front-end CPU, and additional trigger signals for the MWPC hardware. The event builder module generates event number and event type signals for the synchronisation of the data streams from the different front-end CPU.

2.5.5. DATA ACQUISITION AND EXPERIMENT CONTROL SYSTEM

Fig. 2.46 shows the simplified scheme for signals coming from the the two TOF walls (2 $\times$ 30 signals from each wall). The PMT signals are split into an energy

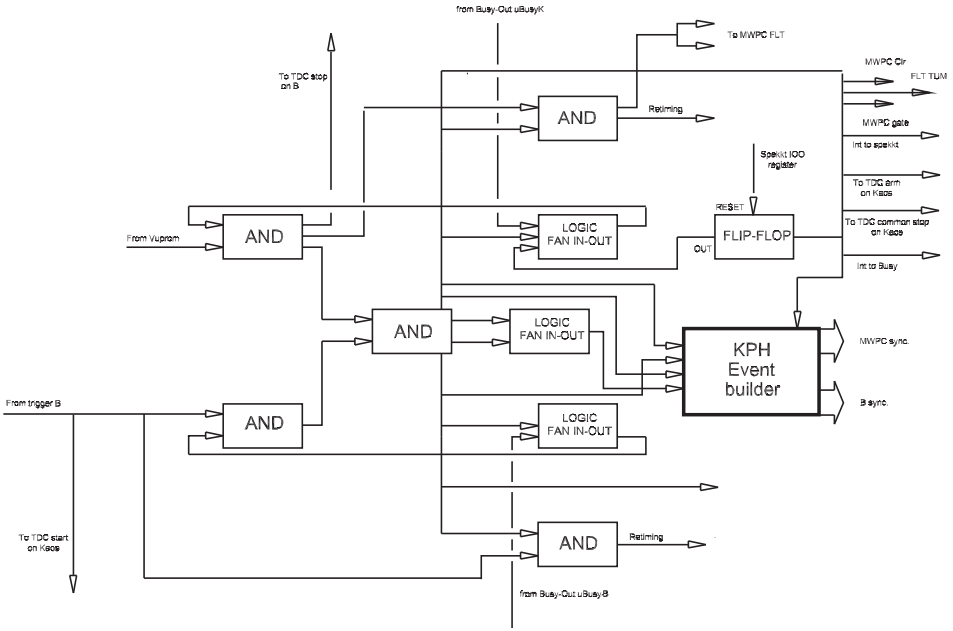

Figure 2.45.: Simplified scheme of the KAOS spectrometer's hadron arm coincidence trigger system. The two single arm trigger signals arrive from SpekB and the VUPROM logic (arrows on the left) and are brought to the central coincidence unit together with the non-busy signals of the DAQ blocking logic (arrows on top and bottom). A valid trigger signal is followed by the arming and common stop signals for the TDC, the gate signals for the ADC, the interrupt signals for the front-end CPU, and additional trigger signals for the MWPC hardware (arrows on the right). The event builder module generates event number and event type signals for the synchronisation of the data streams from the different front-end CPU (from R. Böhm).

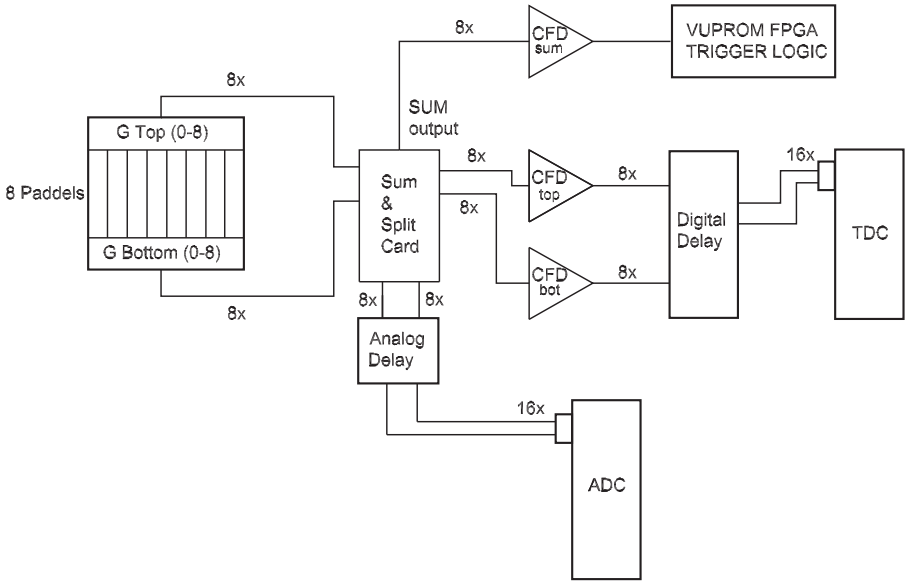

Figure 2.46.: Simplified scheme of the KAOS spectrometer's hadron arm data acquisition system for eight paddles of TOF stop detectors in wall G. Each analogue signal is split by a sum and split card (GSI SU 1601). The energy branch consists of a linear delay of 250 ns (GSI DP 1628) and an ADC (LeCroy 1885F). The time branch is digitized by a constant-fraction-discriminator (GSI CF8105), delayed by 500 ns (GSI DL 1610) and fed into a TDC (LeCroy 1875). The amplitude sum of the two PMT signals from each paddle is discriminated (GSI CF 8105) to perform a rough mean-timing and brought to the VUPROM logic modules for trigger generation. A detailed scheme is found in the appendix, Fig. B.8.

and a time branch by a sum and split card (GSI SU 1601). The energy signals are delayed by 250 ns (GSI DP1620). A timing channel consists of a Camac controlled, 8-fold, constant-fraction-discriminator (GSI CF8105) and a logic delay of 500 ns (GSI DL1610). The analogue and digital signals from the two walls are fed into ADC (LeCroy 1885F) and TDC (LeCroy 1875) in a Fastbus crate. A detailed scheme is found in the appendix, Fig. B.8. The signals from the MWPC (620 channels in total) are converted by flash ADC and read out by a transputer network as described in Section 2.5.1.

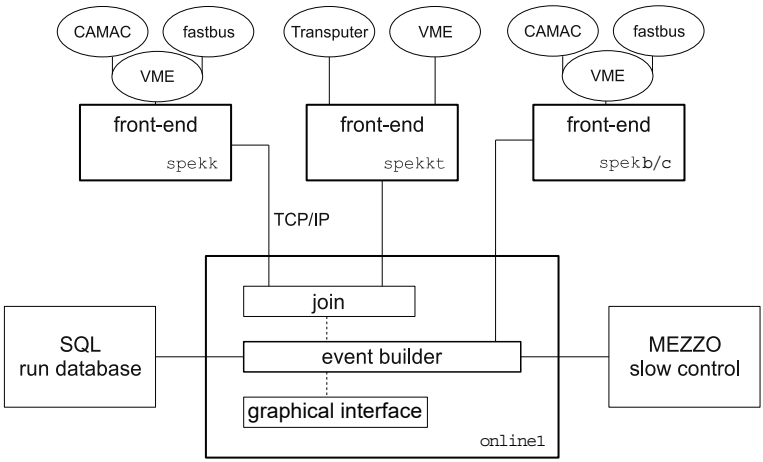

Figure 2.47.: Simplified scheme of the data streams in experiments with the KAOS spectrometer. The front-end CPU `spekk` and `spekkt` are reading the data of the MWPC and scintillator walls which are joined on the `online1` machine before they are send to the event-builder that matches the data with the stream from the participating spectrometer SpekB or SpekC.

The data acquisition and experiment control software used by the Collaboration A1 consists of three core elements, Aqua, Cola and Mezzo. While Mezzo is used to operate and monitor experimental devices, Cola to read and analyse the data, the data acquisition is actually done by Aqua (Data Acquisition for A1 Experiments). On the front-end computers, that are usually sitting on a VME bus, there are processes running which read the data from the electronic modules in Fastbus or Camac crates, pack it into Aqua-defined structures, and send it via a TCP/IP protocol through the ethernet to a central machine that collects data

streams from different spectrometer arms and stores it in run-files. This scheme is shown in Fig. 2.47. The identification of data from the same physical event is achieved by a matching a 16-bit event number which includes a 3-bit event type definition. The Aqua system is controlled though a GUI (Graphics User Interface) on a host machine, usually `online1`. Before the start of a run its conditions can be set in this interface. At the beginning of each run, the program proceeds to sets and reads the slow control diagnostics from Mezzo. Also an automatic logbook entry is made in the run database. In experiments with the KAOS spectrometer the front-end CPU `spekk` and `spekkt` are reading the data of the MWPC and scintillator walls which are joined on the `online1` machine before they are send to the event-builder that matches the data with the stream from the participating spectrometer SpekB or SpekC. The `spekkt` front-end is a standard PC that has a direct connection to the transputer system via a multi-link card. Some more details on the data-acquisition process with the KAOS spectrometer can be found in Refs. [117, 124].

Figure 2.48.: Photograph of the assembled first plane of the fibre detector taken in a clean room during assembly in 2008–9. The plane is composed of 9 216 fibres in 72 bundles and attached to the vacuum chamber flange through leak-proof fibre connectors.

2.6. ELECTRON ARM INSTRUMENTATION

A new coordinate detector has been developed for the KAOS spectrometer's electron arm [136–138]. The detector consists of two vertical planes of fibre arrays (x and θ). The package will be supplemented by one or two horizontal planes (y and ϕ) [139, 140]. The track information is used to reconstruct the target coordinates and particle momentum, and the time information used to determine the time-of-flight of the detected particle from target to the detection planes. The vertical detector system comprises a total of 18 432 fibres, covering an active area of $L \times H \sim$ 1940 mm $\times$ 300 mm. Its two planes are divided into detector segments which consist of 384 fibres in three joined fibre bundles. Each plane is composed 72 bundles and attached to the vacuum chamber flange through leak-proof connectors. The fibre arrays are made of a four-layered structure. Four fibres are coupled to one common read-out channel of a MaPMT. Particles will cross the spectrometer's focal plane with an inclination angle of 50–70° with respect to the normal of the plane. To accommodate this geometry the fibre arrays are constructed in a hexagonal packing with columns slanted by 60°. A photograph of the first plane taken in a clean room during assembly in 2008–9 is shown in Fig. 2.48. The mass production of the fibre bundles for the first detector plane was completed in early 2009, the mass production for the second plane in 2010.

For the double-arm operation of the spectrometer the electron beam must be steered through the KAOS spectrometer after impinging on the target. In such a set-up the fibre detectors will be operated close to zero degree scattering angle and in close proximity to the electron beam.

The electromagnetic background in the spectrometer is enormous and for small detection angles is dominated by Møller scattering. This background is considered to be the limiting factor for the reaction rates that can be recorded. Thus, the large number of detector channels and the high particle fluxes require a flexible and sophisticated trigger logic and a nearly dead-time free read-out scheme. To fulfil these conditions new front-end electronics with 4 608 electronic read-out and level-1 trigger channels has been developed [141, 142].

The requirements on the DAQ system are defined by this forward-angle geometry of the planned experiments. Consequently, the coincidence time resolution must be in the sub-nanoseconds range and the two-arm trigger rate must be lower than ~ 1 kHz to be handled by the slower data acquisition system of the hadron arm. The hit rate in one plane of fibre detectors is expected to be in the several MHz range. Finally, the multi-hit capability of the TDC system must allow for an unambiguous assignment of multiple hits with an off-line time separation within one channel of smaller than 10 ns. The double-arm timing resolution of the detector systems also determines the particle identification (or separation) power by time-of-flight. For high momenta the resolution needed for e/π separation can approach the electronic limit of two-arm coincidences in typical experimental conditions using standard coincidence hardware.

2.6.1. SCINTILLATING FIBRE DETECTORS

Detectors comprised of scintillating fibres that are packed together to form arrays and read out via multi-channel photo-detectors have been in use since the 1990s to track charged particles, see *e.g.* [143–145]. A fibre array is made from layers of fibres, often with alternating layers off-set relative to each other. The design of such detectors is governed by the relatively small light yield of thin ($\varnothing < 1$ mm) fibres.

The fibres used for the electron arm detector are of the standard (Non-S) type SCSF-78 (Kuraray, Japan) with double cladding and $\varnothing = 0.83$ mm outer diameter. The cladding thickness is $d_{\text{clad}} \approx 0.05$ mm, leading to a 0.73 mm thick core made of a polystyrene base with refractive index $n_{\text{core}} = 1.59$. The outer cladding is made of a fluorinated polymer with refractive index $n_{\text{clad}'} = 1.42$ and the inner cladding is made of polymethylmethacrylate with refractive index $n_{\text{clad}} = 1.49$. The emission spectrum extends from $\lambda \sim 415$–550 nm with a maximum at $\lambda \sim 440$ nm for fibres of short lengths. For a double cladding fibre the critical axial

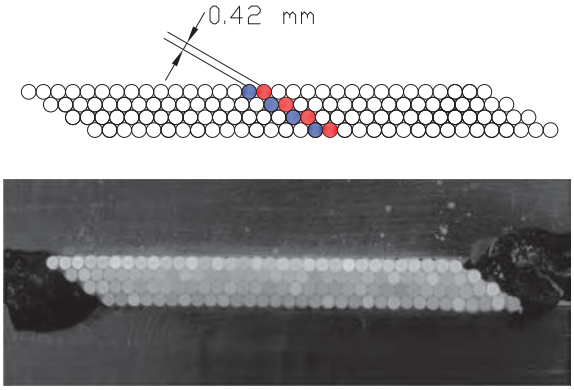

Figure 2.49.: Scheme of a fibre array with 60° column angle geometry, 4 monolayers of fibres, and a column pitch of 0.42 mm and an overlap of 0.42 mm (top). Photograph of an assembled fibre bundle of this geometry (bottom).

angle is given by $\theta_{\text{crit}} = \arccos n_{\text{clad}'}/n_{\text{core}} = 26.7°$. The trapping efficiency for photons produced close to the axis of the fibre is 5.3 %, that is 70 % higher than for single cladding fibres, where the efficiency for light trapped inside the core is only 3.1 %.

Multi-channel photomultiplier tubes are especially suitable for fibre read-out because of the good matching between the pixel size of the photomultiplier and common fibre diameters, offering a significant reduction in size and cabling with respect to conventional tubes. Since the pioneering work of Kuroda [146] such tubes have been developed in order to meet the demands on precise and reliable tracking devices under high-rate [147–149]. In recent years they have been continuously improved. The drawbacks of early devices have been greatly reduced; modern multi-anode tubes exhibit little cross-talk and a high gain uniformity between pixels. The Hamamatsu Photonics R5900 series has been chosen by many experimental groups for fibre read-out. One important parameter characterizing position-sensitive PMT concerning signal discrimination is the amount of channel-to-channel gain variations. More than 160 multi-anode PMT (MaPMT) of type HAMAMATSU R7259K featuring 32-channel linear array multi-anodes are used for the KAOS electron detector. The gain uniformity between anodes lies between 1:1.1 and 1:1.25, with the edge anodes having slightly lower gains on average.

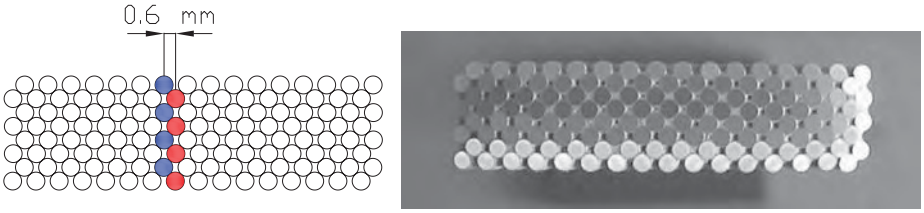

Figure 2.50.: Scheme of a fibre array with 0° column angle geometry, 4 double-layers of fibres, and a column pitch of 0.6 mm with an overlap of 0.24 mm (left). Photograph of an assembled fibre bundle of this geometry (right).

Results from laboratory measurements with a ^{90}Sr source resulted in a light yield of 4–5 photoelectrons per channel with a multiplicity of 3 channel, corresponding to 15 photoelectrons per crossing minimum ionising particle [150]. Particle detection efficiencies were determined to be well above 90 %, see [151].

In modern experiments, fibre bundles involving a rather large number of channels are easily read out via multi-channel photomultiplier tubes, while the use of single-channel photomultiplier tubes is no longer economical in terms of cost and space requirements. Accordingly, multi-layered structures of packed scintillating fibres coupled to multi-anode photomultiplier tubes became the preferred choice for some fast detectors, the fibre trackers in the COMPASS experiment [152] at CERN being one recent example.

Fibres of a "column" along the geometrical trajectory of incident particles are typically grouped — with one fibre from each layer — to one common pixel of the multi-channel read-out device. If the light yield per crossing particle is too small to be detected with the required efficiency, layers need to be added to the array. In case charged particles are crossing the fibre array at right angle to the detector base the total thickness of the array can be increased arbitrarily until a physical limit or restrictions in terms of small angle scattering are reached. This condition applies to many applications, as the angular acceptance for fibre hodoscopes is generally small, typically up to $\theta = 3°$. However, in some applications the incident particles will cross the detection plane with large angles, θ, w.r.t. the normal to the layers, and would traverse several neighbouring columns. The resultant large hit multiplicities would compromise the tracking capabilities of such a detector. For the fibre hodoscopes of the DIRAC experiment the detector response to particles with incident angles up to $\theta \sim 45°$ was studied for background issues [153]. The read-out electronics of that detector lead to a strong suppression

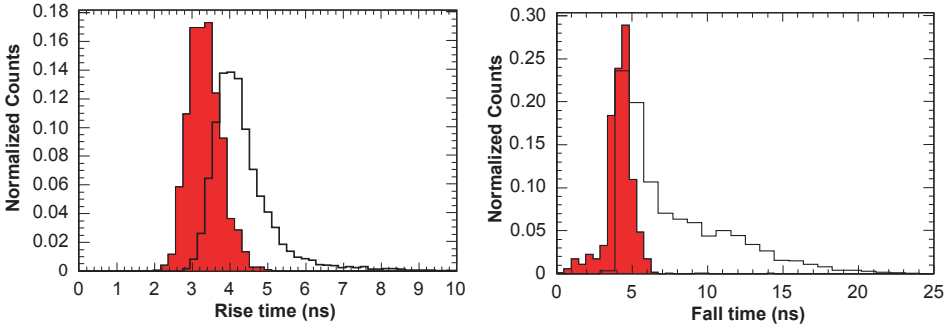

Figure 2.51.: Distributions of rise time (left) and fall time (right) in the MaPMT response. Shaded histograms: single photo-electron pulses with a mean rise time of 3.3 ns and a mean fall time of 4.2 ns. Open histograms: pulses generated by ionizing particles stopping in a coupled fibre detector.

of detection efficiency for larger angles. For restoring the original spatial resolution the packing of the fibres needs to be adapted to the incident particles' direction and the columns need to be inclined.

Only the KAOS experiment is known in which the fibre column angle, ϕ, w.r.t. the normal to the layers is adapted to large ($\theta > 45°$) incident angles of the particles for deliberately matching the geometry. In the KAOS spectrometer's electron arm, particles will cross the focal plane with an inclination angle of $\theta \sim 50$–$70°$ with respect to the normal of the plane.

As the fibre planes approximately follow the focal plane the column angles need to be matched to the track angles around 60°. Fibre arrays with a hexagonal packing of slanted columns with 60° inclination were constructed, see Fig. 2.49. Overlap and column pitch of this geometry are 0.42 mm. The fibres had a length of 300 mm. For some tests 3 bundles of 128 fibres each with an active area of $150 \times 20\,\text{mm}^2$ were constructed in a square packing geometry of 4 double-layers, see Fig. 2.50. Overlap, o, and column pitch, p, of arrays in this geometry are $o = ø\,(1 - 1/\sqrt{2}) \approx 0.24\,\text{mm}$, and $p = ø/\sqrt{2} \approx 0.60\,\text{mm}$. The constructed fibre bundles in 0° and 60° column angle geometry showed no deviations of the fibre positions by more then $0.25\,ø$. These detectors were tested in beams at the SIS facility at GSI.

By the use of a digital oscilloscope, the single thermally generated photo-electron pulses of a MaPMT assembly were analysed, whereby a mean rise time of

3.3 ns, a pulse height of −7.7 mV, and a fall time of 4.2 ns were obtained, see shaded histograms in Fig. 2.51 for the distribution of times. The distribution for pulses generated by ionizing particles stopping in a coupled fibre detector are shown as open histograms. The rise time slightly increased by ~ 700 ps for such pulses as compared to pulses from single photo-electrons. The pulse heights were distributed between −20 mV and −30 mV. For the application with the spectrometer, the detection of low photo-electron signals with high efficiency is important.

Beam-tests were also performed at MAMI with fibre detectors positioned near the focal-plane of one of the high-resolution spectrometers, where scattered electrons have an inclination of 45° with respect to the normal to the detection plane. Accordingly, bundles of 4 mono-layers with the fibre columns following the 45° inclination in square packing geometry were built.

For events in which exclusively one column is hit, one can define a theoretical spatial resolution which determined by $\sigma = (\varnothing - 2o)/\sqrt{12}$. This theoretical resolution is impaired by the internal accuracy of the fibre bundles.

2.6.2. FRONT-END ELECTRONICS

Instead of powering the photo-tubes by a voltage divider, they are powered by individual Cockcroft-Walton bases manufactured by HVSYS, Dubna [154]. The dc voltage is pulsed and converted with a voltage doubler ladder network of capacitors and diodes to the higher dynode voltages. The principal advantage of this design is that there is no need for stiff high voltage cables, since only $U \approx 140$ V has to be distributed to the first front-end board, from where the dc voltage is daisy-chained to the other boards. A drawback is that the dynode voltages can only be distributed linearly, which is acceptable for their actual use. The voltage is set with a 10-bit DAC in the base which controls the pulse height by a comparator. The modules are controlled and programmed via I^2C bus which gives a maximum number of 127 MaPMT per branch. The base modules are connected by a 10-pin flat cable to a system module. Beside the I^2C lines there is +5 V supply for the electronics and +(100–200) V for the Cockcroft-Walton network. Each system module can supply 4 branches and is controlled by RS-232 or CAN bus.

The bases of three neighbouring MaPMT are mounted directly on front-end boards of dimensions $440 \times 78\,\text{mm}^2$, see Fig. 2.53 for photographs of the front- and backside. These boards are used to provide the appropriate voltages to the MaPMT bases and to distribute the analogue signals with a minimum of time jitter to their outputs. The board hosts the low-voltage power line for the three Cockcroft-Walton bases of the MaPMT and the three times eight RJ-45 connectors

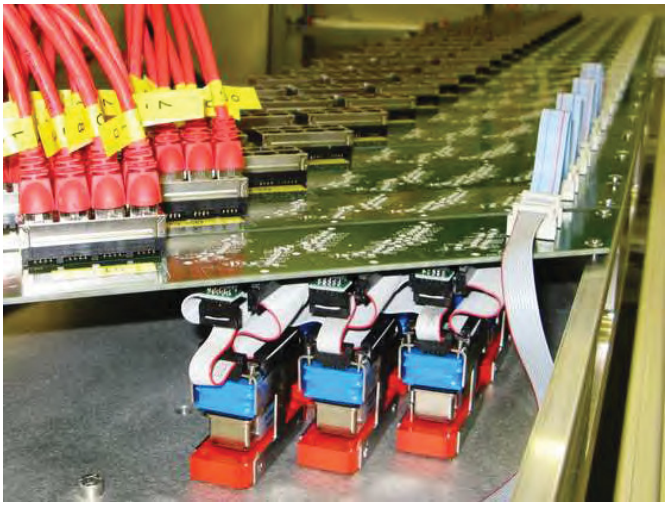

Figure 2.52.: Photograph of the assembled read-out and front-end electronics for the first plane of the fibre detector, that is mounted on top of the vacuum chamber flange which is shown in Fig. 2.48.

for the output. The form-factor of the board follows the geometry of the fibre detector that is aligned with the focal plane of the electron arm of the KAOS spectrometer. The front-end board processes analogue signals of 96 MaPMT channels that correspond to a detector segment of 384 fibres of 79 mm width. On both sides of the board holes are visible which are used for a mechanical fixation directly on the vacuum chamber flange of the KAOS spectrometer. A photograph of the assembled front-end boards for the first detector plane is shown in Fig. 2.52.

2.6.3. DATA ACQUISITION

The required timing accuracy can be achieved only if the discriminators have a correspondingly low time-walk. Since the range of signal amplitudes is large, it is not possible to have the desired level of time-walk by using leading-edge discriminators. Constant fraction discriminators have good timing properties, but they are expensive. A compromise solution is found in double-threshold discriminators (DTD).

The operation principle of a DTD is simple. Internally, two voltage ramps with slopes a_1 and a_2 are triggered by comparators at times t_1 and t_2 when the input

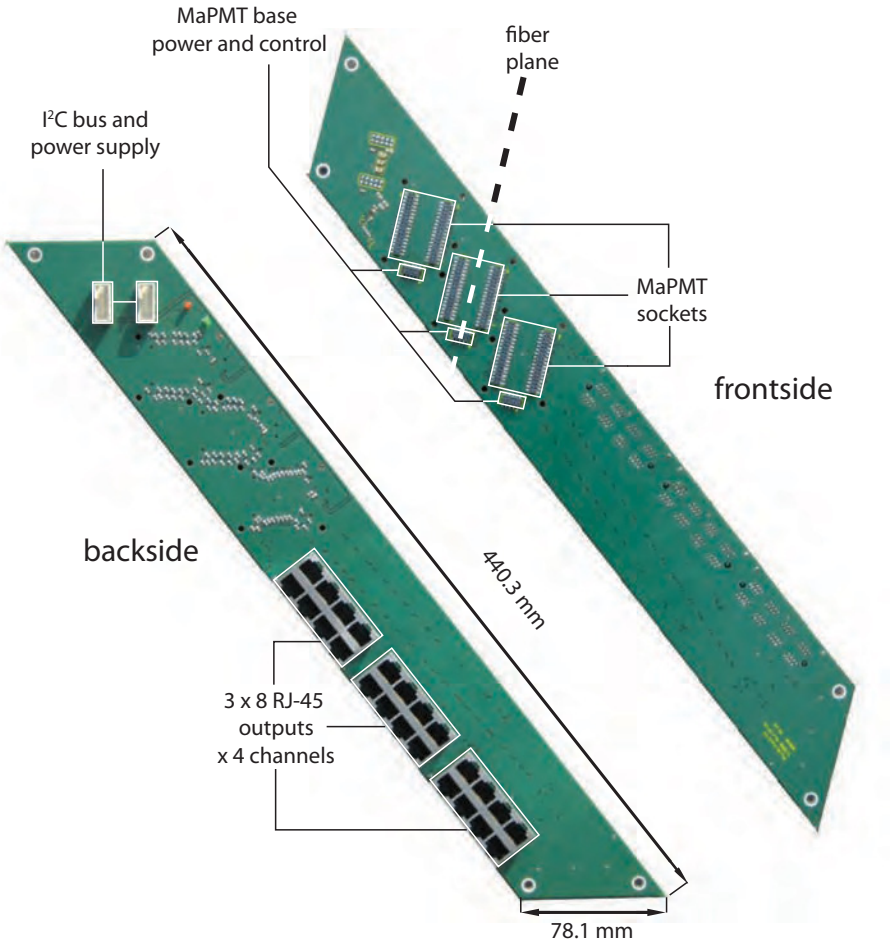

Figure 2.53.: Photograph of front-end board used in the KAOS spectrometer's electron arm showing the three MaPMT sockets on the front-side and the RJ-45 output sockets on the back-side. The Cockcroft-Walton voltage multiplier bases are controlled via I^2C lines and are powered by $U \approx 140\,\mathrm{V}$. The board width of 78 mm was determined by the corresponding fibre detector segment of 79 mm width. Detector and boards must be aligned to the indicated fibre plane that follows the focal-surface of the KAOS spectrometer's electron arm.

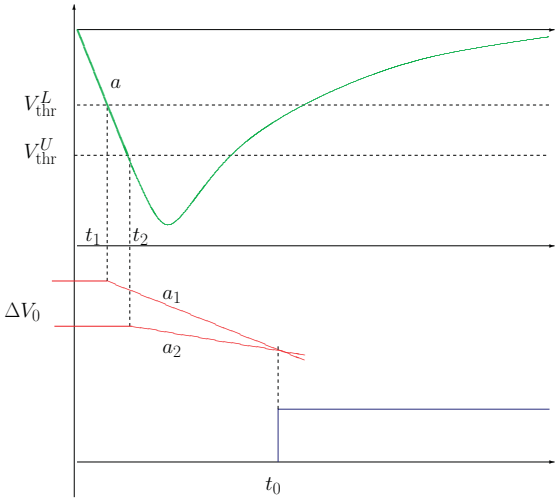

Figure 2.54.: The principle of time-walk compensation in double-threshold signal discrimination. The top signal presents the time development of the input to the DTD, the bottom part shows two internal ramps with slopes a_1 and a_2 generated at times t_1 and t_2 when the input signal exceeds the thresholds V_{thr}^{L}, respectively V_{thr}^{U}. When the potential difference between the two ramped voltages is zero, the output signal from the DTD is generated.

pulse amplitude exceeds the lower and upper thresholds V_{thr}^{L} respectively V_{thr}^{U} as shown in Fig. 2.54. A third comparator triggers the DTD output signal when the voltage difference between the two internal ramps vanishes, i.e. $\Delta V(a_1, a_2) = 0$. With the voltage difference at the last comparator given as

$$\Delta V(t) = \big(V_1 + (t - t_1)a_1\big) - \big(V_2 + (t - t_2)a_2\big) \tag{2.27}$$

the switch time of this comparator will be at

$$t_0 = \frac{\Delta V_0 + t_1 a_1 - t_2 a_2}{a_1 - a_2}\,. \tag{2.28}$$

In case one can parameterize the input signal rise time by a constant slope a, the switch time t_0 is independent on the input signal if the ratio $V_{\text{thr}}^{L}/V_{\text{thr}}^{U}$ equals

the internal parameter a_2/a_1. This condition holds because

$$t_1 a_1 - t_2 a_2 = V_{\text{thr}}^L a_1/a - V_{\text{thr}}^U a_2/a \equiv 0 \tag{2.29}$$

from which the relation $t_0 = \Delta V_0/(a_1 - a_2)$ follows. The DTD then operates with a time-zero extrapolation free of time-walk for a linear input signal of any amplitude and rise time assuming ideal comparators. Practical applications of DTD are in use since the 1990s [155].

The signals (approx. 100 mV pulse-height) of the fibre detector are transported over 15 m via Cat-7 patch cables, that are electromagnetically well shielded and that show small losses, to discriminator cards with 4-channel DTD chips, called GSI-CHIP3 [156]. The main features of the chip are the small time-walk and the high integration which has lead to our design of a 32-channel discriminator board with eight DTD chips that is shown in Fig. 2.55. The inputs are are provided to the board via eight RJ-45 connectors with 4 channels each. The cards have been developed at the Electronics Department of the Institut für Kernphysik at the Johannes Gutenberg-Universität, Mainz. The output signals are made available in LVDS standard on the front-side in a 68-pin Robinson-Nugent connector for the readout modules, and on the back-side in a VHDCI connector for the trigger generation. Up to 20 DTD boards fit into a VME 6U crate together with a controller board, see Fig. 2.56 for a photograph. The controller board is addressed from a PC via parallel port. The communication between DTD boards and the controller board is done over the VME bus through bridges implemented in complex programmable logic devices (CPLD) by LATTICE. The VME crate also provides the power supply of both boards. The voltage thresholds are set by two 8-channel 8-bit DAC relative to one tenth of a common voltage reference and are read back by a 12-bit ADC. The voltage references are set on the controller board by two 8-channel 8-bit ADC with 87 mV full scale per channel for the lower threshold and 157 mV full scale for the upper threshold. For debugging and trigger purposes two multiplexed analogue as well as OR and $\overline{\text{OR}}$ signal outputs are available at coaxial 50 Ω connectors. A dedicated 32-channel analogue output board can be attached to the DTD board for a complete signal analysis.

In practice, comparators are not ideal, and a time-walk of 15 ps peak-to-peak for an amplitude range between 70–250 mV was observed at a rise time of the input signal of 600 ps [156]. In the DTD chip the ratio $a_2/a_1 = 2$ is fixed, and the threshold ratio is set externally. Values above 2 can be used to compensate to some extent the comparator slewing.

The architecture of the following data acquisition (DAQ) system and the synchronization of the read-out units is following the set-up of the COMPASS experiment [157].

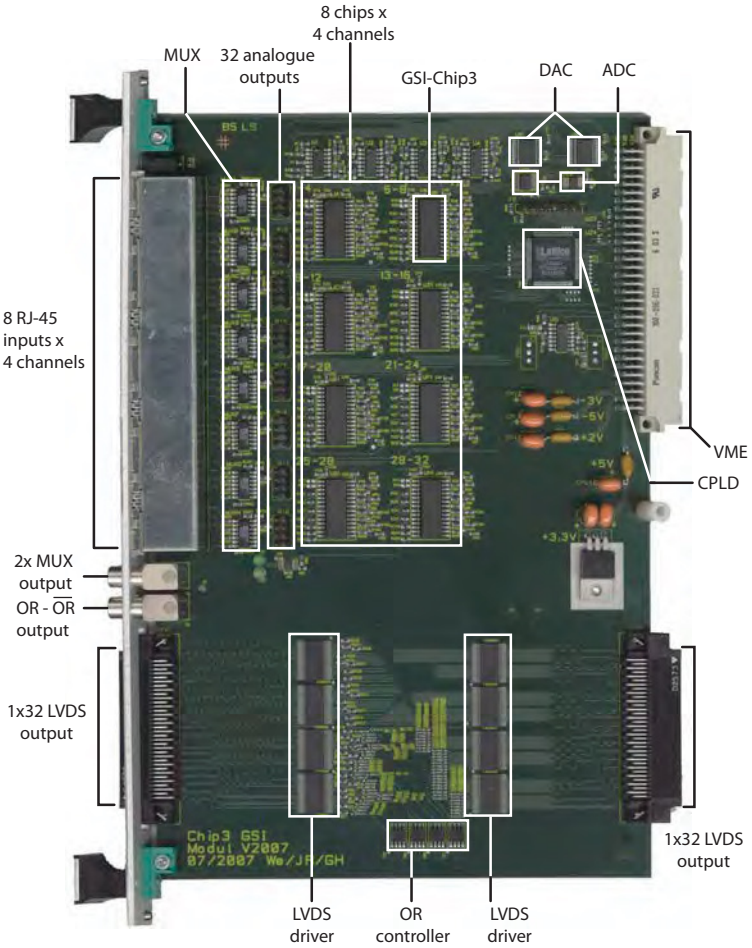

Figure 2.55.: Photograph of the double-threshold discriminator board used in the KAOS spectrometer's electron arm. The two high-density connectors and the drivers for the differential LVDS outputs are visible in the lower part. The 8 RJ-45 connectors for analogue inputs are located at the top left and the four coaxial 50 Ω outputs for multiplexed analogue signals as well as OR and $\overline{\text{OR}}$ trigger signals at centre left. The module hosts 8 GSI-CHIP3 DTD and is controlled from a CPLD device by LATTICE.

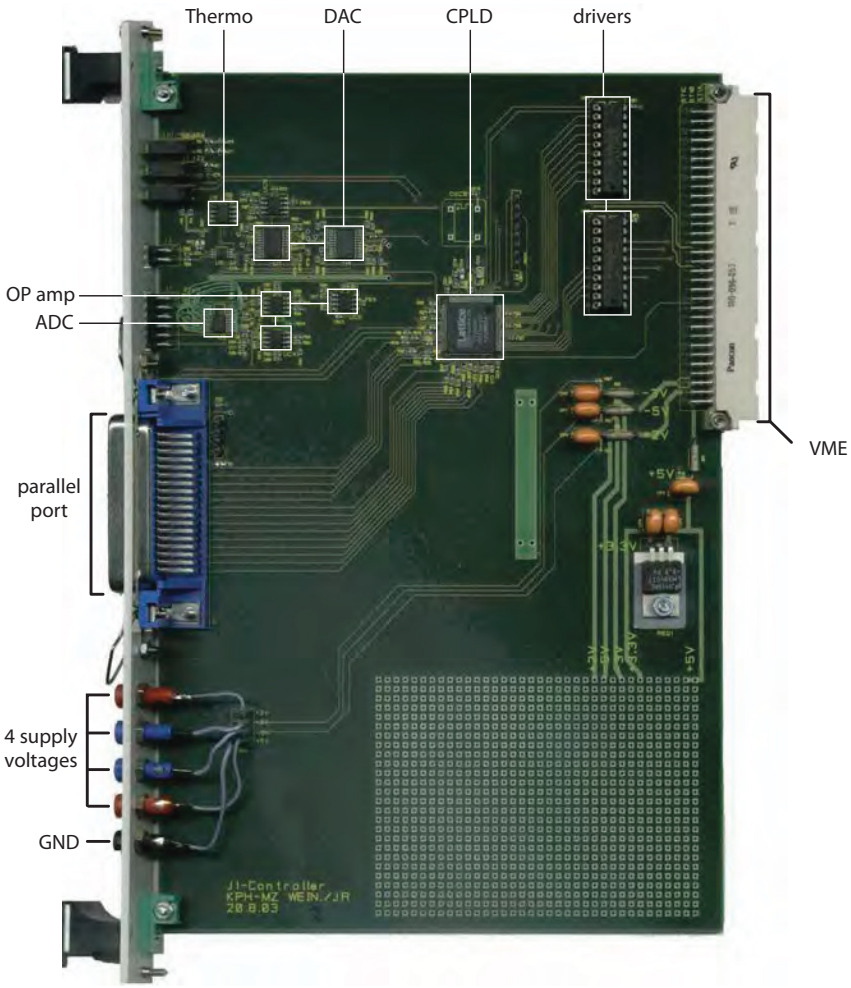

Figure 2.56.: Photograph of the controller board for double-threshold discriminators used in the KAOS spectrometer's electron arm. The CPLD device by LATTICE addresses up to 20 DTD boards in a crate via VME bus and connects to a PC via parallel port. The threshold voltages are generated from common voltage references; temperature and reference voltages are read back for diagnostics.

Upon arrival of the trigger signal the signal times are picked off by 144 TDC mezzanine boards that are plugged into the common read-out driver modules developed for the COMPASS experiment, named CATCH. These 9U VME modules are equipped with 4 slots for mezzanine cards with 32 channels each. Each TDC mezzanine card hosts 4 dead-time free $\mathcal{F}1$ chips, developed by the Faculty of Physics at the University of Freiburg [158]. The $\mathcal{F}1$ TDC performs digitization and readout asynchronously and without any dead time. The heart of the TDC is an asymmetric ring oscillator representing the actual time in a bit value. The phased-locked-loop in each of the $\mathcal{F}1$ is precisely synchronized to the 38.88 MHz reference clock provided by the TCS system. The chips accept falling, rising or both edges of the input signals, and stores them with the time-stamps in an internal memory. The measuring unit has a dynamic range of 62 054 time steps. If the measuring unit is not reset within this time, it will roll over and start again. The roll-over is not indicated by the $\mathcal{F}1$ chip. The length of an individual step is determined by the clock frequency, f, the number of delay units in the ring oscillator, $i = 19$, and the settings of two pre-scalers, $M = 23$ and $N = 2$ [159]. For the read-out of the fibre detector, the normal resolution mode with 8 channels of $\Delta t = N/(f \cdot i \cdot M) \approx 118$ ps resolution (least significant bit) has been chosen. The resolution is identical in all channels, each channel has multi-hit capability, and the double pulse resolution is typically 20 ns. With this setting a dynamic range of $62\,054 \times 118\,\text{ps} = 7.3\,\mu\text{s}$ can be used for the trigger signal generation. Individual channels need to be corrected for time off-sets introduced by the MaPMT, the front-end boards, and the discriminators. In a set-up of 288 channels the off-set values differed by $\Delta t \sim$ 1-2 ns and showed a small sensitivity to the MaPMT high voltage. Detector beam-tests have shown that hits in the TDC can be assigned to the corresponding particle track by a correlation in time and channels [137]. The time correlation is also used to link a particular particle track to the trigger.

An arriving trigger signal is digitized by the same time measurement unit as the hit-signals. A programmable trigger latency time is subtracted from the measured trigger time to account for the time needed to form and to distribute the trigger. A hit is considered to coincide with a trigger if its time stamp is within a defined trigger window following the latency corrected trigger time [159].

The 37 CATCH modules combine the data of $32 \times 4 = 128$ read-out channels each and transmit these sub-events via optical S-LINK to read-out buffer PC (ROB) located in a radiation shielded bunker. S-LINK multiplexer modules reduce the number of optical links. The fibre detector read-out system comprises three 9U VME crates. Each crate can be filled with a maximum of 16 CATCH modules providing the readout of $128 \times 12 = 1\,536$ channels. The set-up is located $\sim$ 5 m from the detector front-end, shielded from the electromagnetic radiation by the yoke of the magnet and a shielding wall.

The ROB processors receive the data, pack it into AQUA-defined structures, and send it via a TCP/IP protocol to a central machine in the counting room that collects data streams from different spectrometer arms and stores it in run-files. On this single machine, data which belong to one physical event are combined in an event building process and consistency checks are performed on the data integrity. The event identification is achieved by matching a 16-bit event number which includes a 3-bit event type definition. When using the spectrometer's electron-arm in coincidence with the hadron arm or with one of the other spectrometer, a mixture of two readout principles appears, which effects the dead time generation and the event identification information.

The scheme of the front-end, trigger, and data acquisition electronics is shown in Fig. 2.57.

2.6.4. IN-BEAM TESTS

Prior to the installation at the KAOS spectrometer's electron arm the fibre detectors were extensively tested [136, 137]. The trigger was in some cases derived from the second plane of the fibre detector (as an autonomous system) and in other cases from a reference counter (as a coincidence system). Any time jitter from the reference counter drops out when the residual time between two detector planes is determined. A simple estimator for the x-position of the form $x = \sum_{i=1}^{N} x_i/N$ was used, where x_i was the parametrised geometrical centre position of the ith channel and N the hit multiplicity. The hit multiplicity of the detector was around $N \sim 4$. The detection efficiency was determined by sandwiching the fibre detector between the external detectors. It was found to be 99 %, independent of the discriminator threshold between 3–50 mV.

In Cave C of GSI tests of a fibre detector with three bundles in a ^{12}C beam of 2 AGeV energy were performed. Two bundles of the detector were aligned to a single plane, and one bundle formed a parallel plane directly in front.

In deducing the time resolution, an iteration over all hits in a plane including multiple hits in a channel was performed, and clusters of correlated hit times were searched for. The cluster with the time closest to the trigger signal time was retained, and within the cluster the time of the first arrived signal was chosen as hit time. In the algorithm a minimum time separation of 10 ns between clusters and a hit in a coincidence window of 20 ns width were required. A time walk correction for the hit times was not needed. The hit time residual, defined as the difference between the two hit times in the two planes of fibres, was distributed with a width of $t_{FWHM} = 330$ ps for the carbon beam, see Fig. 2.58 (left). No significant dependence of the time resolution on photomultiplier high voltage

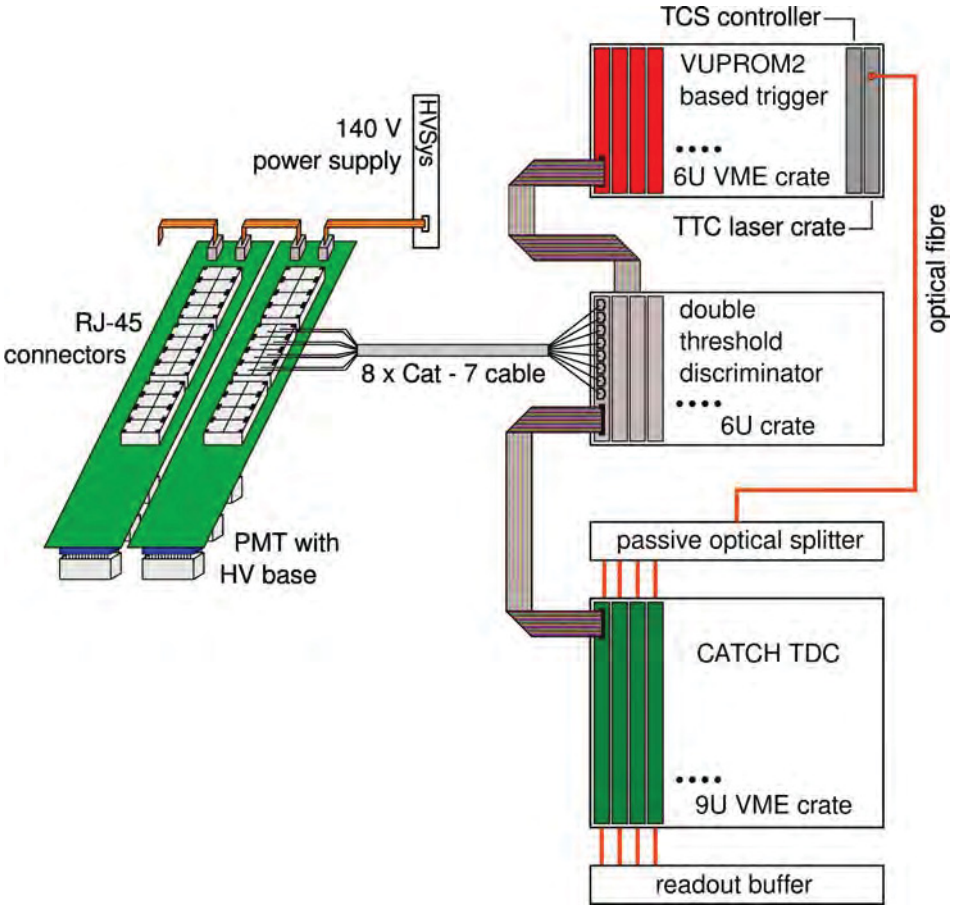

Figure 2.57.: Scheme of the front-end, trigger, and data acquisition electronics for the electron-arm of the KAOS spectrometer. The signals from three MaPMT are collected with front-end boards and transferred over 15 m to the discriminator modules (gray) which serve the VUPROM2 trigger system (red) and the CATCH TDC system (green). The trigger is distributed to the CATCH modules by a laser system via optical fibres. The data is then transferred to the readout buffer PCs. The PMT high voltage is generated in the bases and is supplied to the daisy-chained front-end boards via a 140 V line.

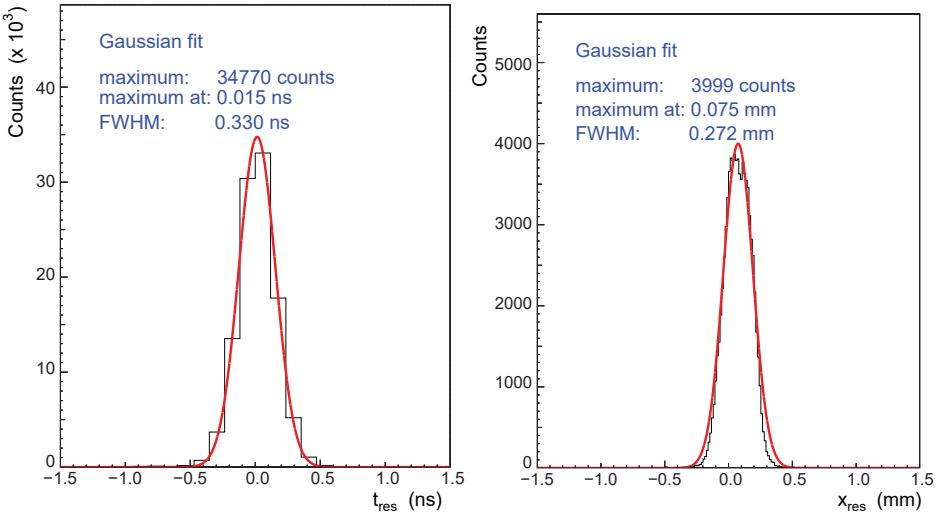

Figure 2.58.: Left: Residuals of hit times between two detector planes, $t_A - t_B$, of a fibre detector tested in a ^{12}C beam. A Gaussian fit is shown with a width of $t_{FWHM} = 330\,\text{ps}$. The time resolution of a single detector plane was derived to be $\Delta t_{FWHM} \sim t_{FWHM}/\sqrt{2} = 230\,\text{ps}$. Right: Residuals of track position estimates using the centroid of charges. A Gaussian fit is shown providing a width of $x_{FWHM} = 0.27\,\text{mm}$, however, the distribution is non-Gaussian with two overlapping peaks because of the discretisation in fibre channels.

was observed. The time resolution of a single detector plane was derived to be $\Delta t_{FWHM} \sim 330\,\text{ps}/\sqrt{2} = 230\,\text{ps}$.

The pulse height spectra for different voltages between -650 and $-850\,\text{V}$ were fitted to get the normalisation, A_i, and the pedestal position, p_i, for each ADC channel i. With these calibration values the spectra were corrected for channel-to-channel gain variations. The hit position was determined by the the centroids of charges in both detector planes. The algorithm was applied to the central area of the detector away from the edges, where the number of channels available for the averaging is restricted. The hit position residual, defined as the difference between the two track position estimates in the two planes of fibres, was measured with a $x_{FWHM} \sim 0.27\,\text{mm}$, see Fig. 2.58 (right). This accuracy was sufficient for an unambiguous identification of the hit channel, leading to a spatial accuracy

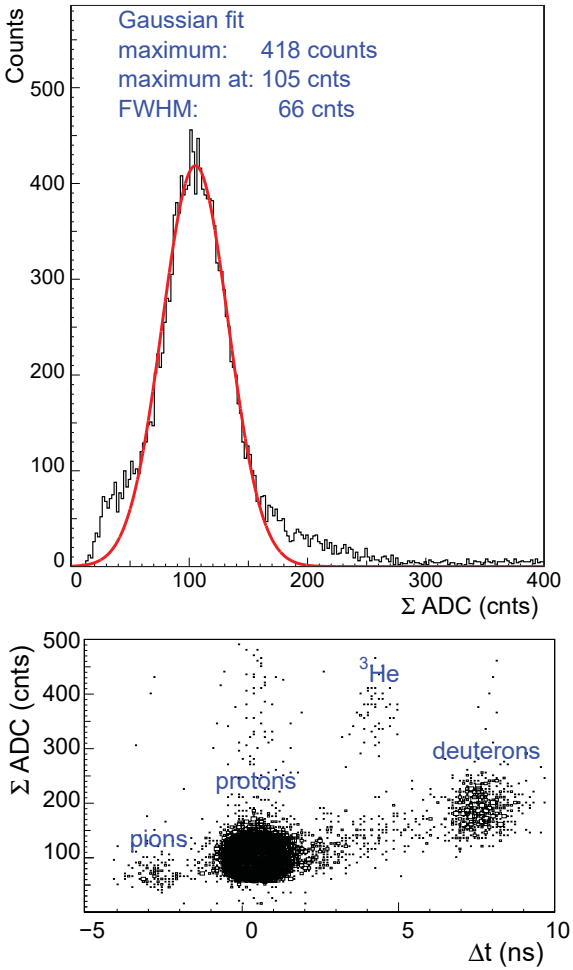

Figure 2.59.: Distribution of the pulse height sum over all channels of one detector plane for the beam of different particle species (top). From the Gaussian fit to the proton peak a relative energy resolution $\Delta E/E \sim 60\,\%$ was derived. The pulse height sum is shown *vs.* the time-of-flight so that π^+, proton, deuteron, and ^{3}He were separated (bottom).

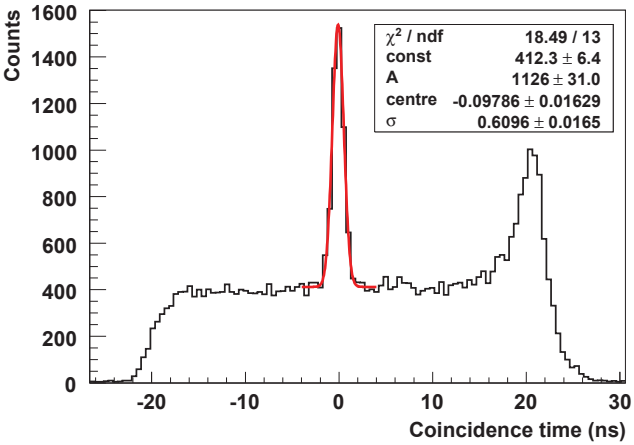

Figure 2.60.: Coincidence time spectrum from fibre detector beam-tests after corrections for the flight-time and trigger-time jitter. The coincidences in the $p(e,e'\pi)$ and $p(e,e'\mathrm{p})$ reaction were used for the calibration of the detector and the optimization of operating parameters. The FWHM of the (e',π) peak is 1.4 ns, where the fibre detector time was determined in the data analysis by the first arriving signal.

of $\Delta x \sim 0.6\,\mathrm{mm}/\sqrt{12} \approx 170\,\mu\mathrm{m}$ (rms). The channel with the pulse height maximum was strongly correlated to the hit time defining channel showing that ADC calibration constants and TDC off-set values had both been correctly determined. From the distributions of the pulse height sum over all channels a relative energy resolution of $\Delta E/E = 15$–$20\,\%$ was determined. The detection efficiency of a plane, i.e. the probability to find at least one hit in one plane provided a hit in the other plane, was above 99 %.

The energy response of another fibre detector was studied in a beam of different particle species in Cave A of GSI. In the $\mathrm{p}/\pi^+/\mathrm{d}$ beam of 3.3 Tm magnetic rigidity were dominantly protons of 1 GeV/c momentum. As was the case in the set-up for the carbon beam in Cave C, two detection planes were formed by three fibre bundles with the columns in 60° degree geometry aligned to the beam. Fig. 2.59 (top) shows the distribution of the pulse height sum over neighbouring channels of one detection plane. From the Gaussian fit to the data a relative variation in the measured energy deposition, $\Delta E/E$, of 60 % was derived for the dominant particle species. Fig. 2.59 (bottom) shows the energy loss *vs.* relative time-of-flight, in which dominant protons and sub-dominant π^+, deuteron, and

^{3}He were separated.

Since 2008 segments of the fibre detector were studied in beam-tests with the KAOS spectrometer. The aspects of mechanical compatibility, high voltage and low voltage system, and correct mapping of the whole electronics chain were verified. A successful data-taking period in a coincidence experiment provided good timing characteristics and efficient π/p particle identification by measuring time-of-flight through the spectrometer. The time spectrum after corrections for the flight-time and trigger-time jitter is shown in Fig 2.60. The coincidences in the $p(e,e'\pi)$ and $p(e,e'\mathrm{p})$ reaction were used for the calibration of the detector and the optimization of operating parameters. The FWHM of the (e',π) peak is 1.4 ns. The analysis of hit distributions has shown that each traversing particle produces a number of signals in a cluster of neighbouring channels within a time interval of a few nanoseconds. The cluster size varies with the high voltage of the MaPMT, the thresholds set in the discriminators, and the energy-loss of the particle. For electrons a typical cluster size of 3–7 channels can be expected under standard operating conditions. The fibre detector timing signal for typical events with hits in approximately 5 neighbouring fibre channels was taken from the first arriving signal. More analyses were performed in a diploma thesis related to the implementation of the fibre detector at MAMI [151].

2.6.5. TRIGGER SYSTEM

A sophisticated trigger logic to be implemented in the FPGA has been developed according to two different scenarios:

1. For the in-beam tests of the electron-arm detectors the trigger system was based on a fast clustering algorithm to define the hit positions and thus the charged particle track, and a hit multiplicity cut to reject spurious hits. The trigger was prepared to minimize accidental trigger rates and to reject background events that do not originate in the target.

2. In hypernuclei electro-production experiments the trigger decision will also include the correlation between the momenta, *i.e.* the hit positions in the focal-planes of the spectrometers. This sensitivity to the reaction kinematics allows to select a given missing-mass range by the trigger. The temporal correlation between hits is used to identify and reject pile-up and to select specific particles via time-of-flight. The possibility exists to expand the system to future additional detector components like the Cherenkov detector, which is under development.

Accordingly, the trigger must satisfy the following requirements:

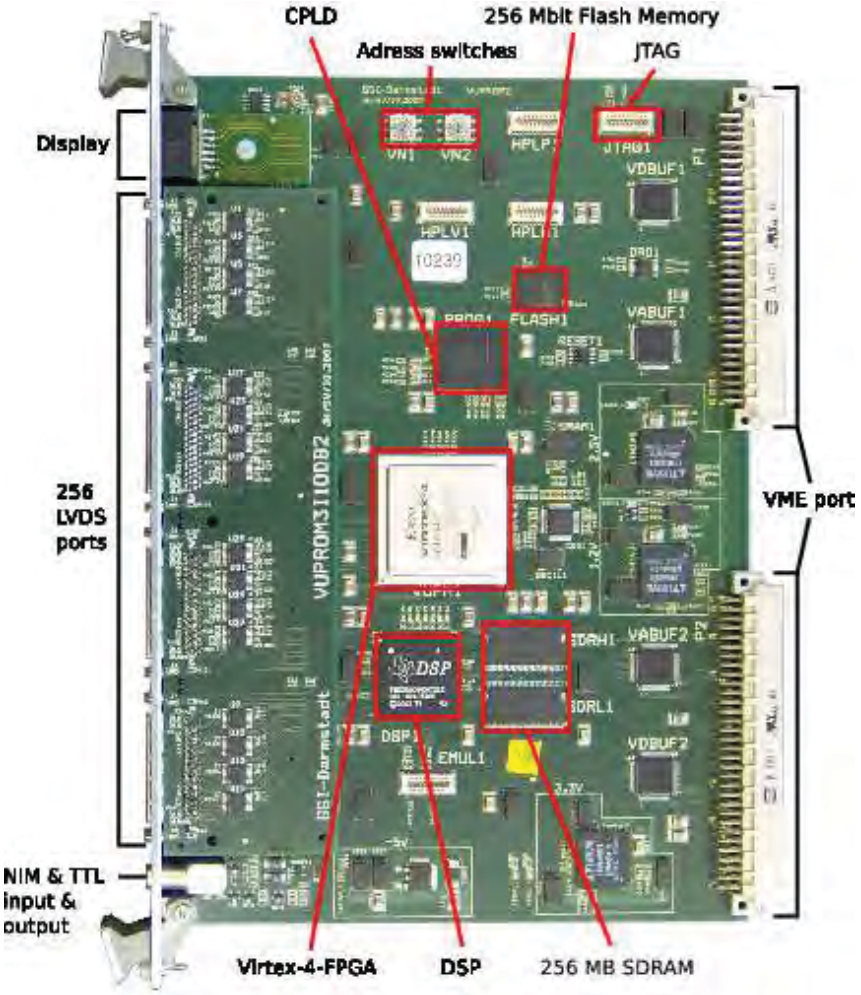

Figure 2.61.: Photograph of a second generation logic module VUPROM2 that is used in the trigger for the electron-arm of the KAOS spectrometer. The following components are marked: VIRTEX-4 FPGA chip, CPLD chip, DSP chip, flash memory, JTAG connector, input/output ports, display, and address switches.

1. detection of signal clusters in each detector plane;
2. reconstruction of particle tracks through both planes;
3. coincidence and acceptance test for all reconstructed particle tracks;
4. expandability to a missing-mass trigger by combination with the hadron-arm trigger;
5. on-line access and control of trigger parameters;
6. a fast trigger decision.

The trigger is electronically derived by VUPROM (Vme Universal PROcessing Module) boards that were developed at the Experiment Electronics Department of GSI for general purpose logic operations with 256 I/O channels each [160, 161]. A photograph of a second generation VUPROM2 module is shown in Fig. 2.61. During the last 2 years, first modules were applied as tracking triggers in experiments at GSI and at MAMI [134, 135, 162].

The first large-scale installation of a VUPROM system with several thousand input channels is now in operation for the triggering of the hadron-arm as well as the electron-arm instrumentation of the KAOS spectrometer. The electron-arm trigger set-up comprises 37 VUPROM modules.

Each 6U VME module is equipped with a Virtex-4 FPGA chip containing over 40 K logic cells, capable of operating at 400 MHz and connected to a DSP with 128 Mbytes SDRAM. The FPGA can be accessed via a JTAG connector. For fast programming of all modules the VME-bus is used to access a 256 Mbit flash memory on each board, that is divided in 8 address spaces. After start-up or restart of the module the FPGA configuration is read from two address spaces of the flash memory, so that up to four independent configurations can be stored on-board. A CPLD supports the FPGA control and the flash memory access for the FPGA configuration. The DSP is intended for complex trigger calculations. A display on the front panel is accessible from the DSP and can be used to show status information of the module. The trigger calculation results can be forwarded to front panel or to the VME backplane bus. Eight high density VHDCI connectors with 32 differential input or output channels each are implemented on the front panel, with four connectors on the VUPROM main board hard-wired as three inputs and one output and four piggyback options with free configuration. Additionally, standard LEMO in- and outputs (TTL and NIM level) are available. Thus, output and control information is accessible during trigger operation and the trigger system can be easily reconfigured and adopted to the experimental requirements.

A scheme of the trigger is shown in Fig. 2.62. The modules are arranged in four stages. The signals from both detector planes are processed in parallel and hit information is transmitted to the next stage by setting bits in an 32-bit wide output bus. The coincidence and output layers combine the signals from the two planes. A total of 37 modules is needed to satisfy the requirements on the trigger. Block diagrams of the implemented logic in all four stages are shown in Fig. 2.64. Each box represents one functional unit, thin arrows represent single logic signals, thick arrows logic signal vectors, parallel signals between components were combined to one arrow. The colour code reflects the main purpose of the component: green coloured units and signals are part of trigger signal processing, yellow coloured components are part of the trigger control, and debug or monitoring components are coloured blue.

Each detector plane has 2 304 trigger channels for which 72 VHDCI inputs in the first stage are needed. This stage uses 12 VUPROM modules with 6 VHDCI inputs each for a single plane, with every module serving 192 neighboring channels. One VHDCI output is used to transmit information to the next stage, one VHDCI output is used for debugging. Due to the geometrical arrangement of the fibres, a particle hit always causes a cluster of correlated signals in neighboring channels. Signal clusters are identified by requiring a signal in n neighboring channels and the absence of a signal in the next higher and lower channel within a given time period. This scheme, shown in Fig. 2.63 guarantees that the found cluster is exactly of the size n. Short pulses which are the result of different delays in the input signals are suppressed by a pulse-width discriminator (PWD). The PWD splits the signal into two with one part delayed. The two signals are then brought to an AND gate, so that two signals arriving with a small time difference are still accepted. An upper and lower boundary for the accepted cluster sizes is specified. Clusters with a size above the given upper boundary are vetoed to reduce background from scattered particles, hitting the detector planes under large angles with respect to the normal on the detector plane.

The second stage consists of 6 modules with the purpose of reducing the number of channels by a factor of 2 and providing the signal information on several outputs in parallel.

In the third stage the position information from the first stage of the x-plane and the second stage of the θ-plane are combined. The stage consists of 5 different logic units and a multiplexer to chose the logic for the output. A 6:1 reduction unit serves as an OR gate for all channels. One unit checks for temporal coincidences between the x- and θ-planes. A 2:1 reduction unit produces an OR output for the first 64 channels coming from the x-plane. For the θ-plane a 4:1 reduction unit is implemented. As the outputs of the reduction stage are connected to several inputs of the coincidence stage, a signal of the θ-plane can be processed

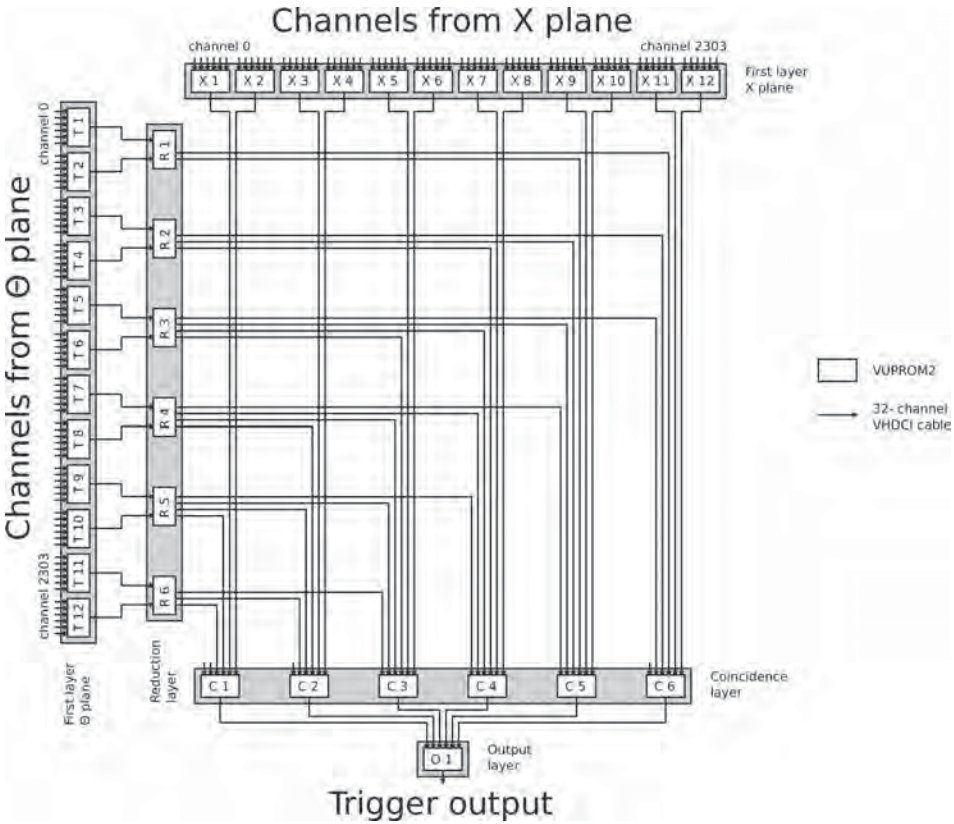

Figure 2.62.: Trigger scheme used during the beam-test of fibre detectors. Each white box represents a VUPROM2 module, gray shaded areas represent the four different stages of the trigger logic, arrows indicate 32-channel VHDCI cables. Each fibre plane has its own first layer and reduction layer, the coincidence and output layers combine the signals from the two planes. A total of 37 modules is needed to satisfy the requirements on the trigger.

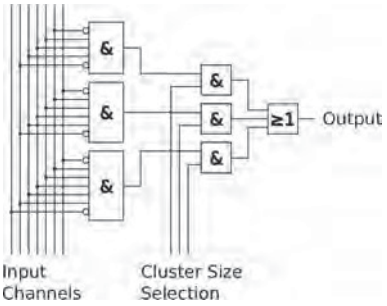

Figure 2.63.: Detail of the logic unit for finding clusters of size $n = 3$–5. The input signals are connected to AND gates, so that an output signal is only produced when a given signal size is found. Further information on the logic units is given in [151].

in different modules. If a trigger is based on coincidences independent of the hit position, this decision needs to be made by the output stage. If a correlation of the hit positions is required, a coincidence matrix is used to perform an acceptance test for the reconstructed tracks.

For performing the acceptance test, the allowed combinations of hit positions in both planes are stored in a binary matrix. This matrix is externally computed. An output signal is produced when a cluster is found on both detector planes and the corresponding matrix element is non-zero. Each VUPROM in the third stage evaluates a range of 384 channels of the x-plane and up to 1 536 channels of the θ-plane. This set-up was chosen to cover the angular acceptance known from simulations with the highest possible granularity. The position resolution for the acceptance test is 6 channels in the x-plane (4.98 mm) and 12 channels in the θ-plane (9.96 mm).

The last stage consisting of a single module that receives the information of accepted trajectories from the third stage and produces the trigger output signal. Two parallel logic units are implemented, one is a coincidence unit between signals of the x- and θ-planes, the other is an OR gate.

In our set-up the function of the Trigger Control System (TCS) is to distribute from a single source the trigger and time reference to the readout modules. The TCS is based on the COMPASS system, using a laser module and passive optical splitters, which in turn is based on the encoding method and distribution principles of the Time and Trigger Control (TTC) system developed for the LHC experiments [157]. A central component of the trigger distribution is the TCS

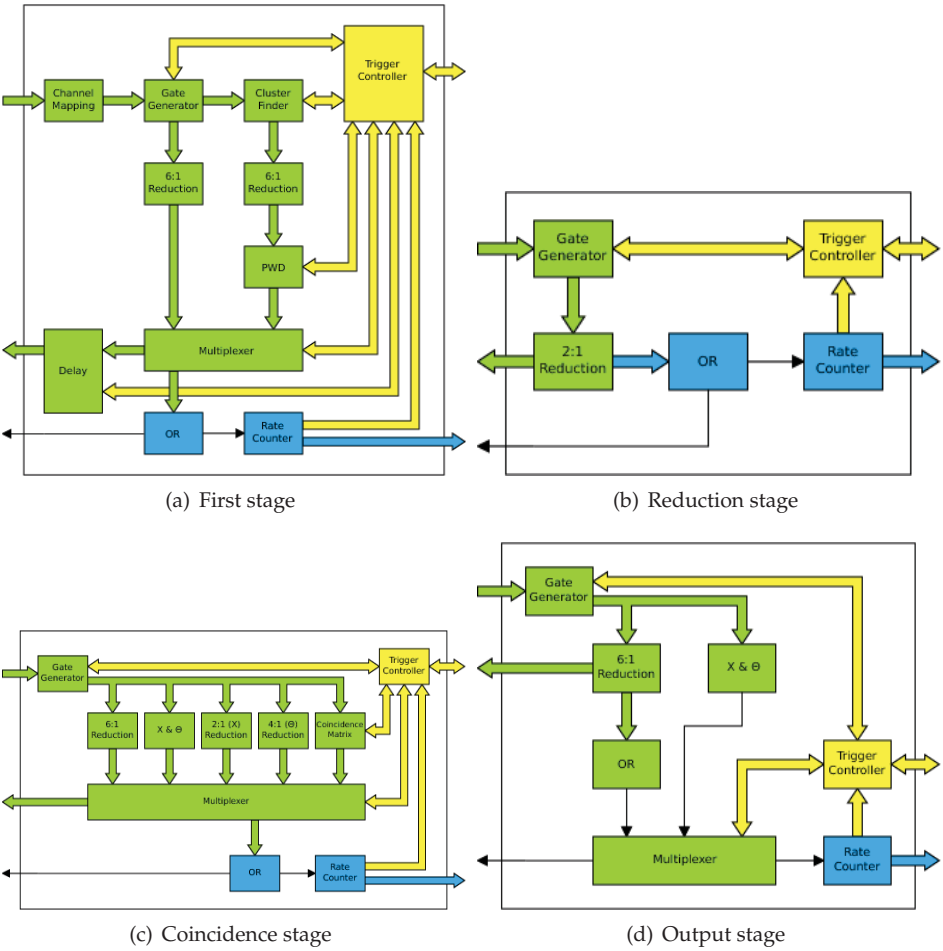

(a) First stage (b) Reduction stage

(c) Coincidence stage (d) Output stage

Figure 2.64.: Block diagrams of the trigger logic implemented in the VUPROM modules. Each box represents one functional unit, thin arrows represent basic logic signals, thick arrows logic signal vectors, parallel signals between components were combined to one arrow. The colour code reflects the main purpose of the unit: green coloured units and signals are part of trigger signal processing, yellow coloured components are part of the trigger control, and debug or monitoring components are coloured blue.

controller, a 6U VME module, that itself is triggered by a first level trigger (FLT) from the VUPROM system. Our system consists of one TTCvi encoder that operates at 155.52 MHz, two layers of optical 32-channel splitters and a total of 37 TCS receivers. The receivers are plugged to the VME-P2 back sides of the crates, that house the readout modules, decode the trigger and deliver it to the readout modules.

About half the the total read-out and trigger electronics for the electron-arm was successfully tested during two beam-times in July and August 2009. The KAOS spectrometer as realized in the spectrometer hall is depicted schematically in Fig. 2.11, where ray-traced positively and negatively charged tracks for different momenta and emission angles are shown. The solid angle from the target covered by the fibre detector was 6.4 msr. A 585 MeV electron beam was used on a CH_2 target of 1.5 mm (130 mg/cm^2) thickness, resulting in an electron–electron luminosity of $\mathcal{L} = 3.1 \times 10^{34}\,\mathrm{cm}^{-2}\mathrm{s}^{-1}$ at a current of 100 nA. Large particle fluxes, dominated by Møller scattering of the electrons, lead to high background rates in the fibre detectors at their exposed position at 8–10°. Raw signal rates of several MHz were observed, measured rates under different trigger conditions are shown in Table 2.11.

Table 2.11.: Measured trigger rates in the electron-arm of the KAOS spectrometer during beam-tests at MAMI in 2009.

trigger type	trigger rate (kHz)
raw signal rate	$1\,120 \pm 30$
clusters in x	47.0 ± 0.2
clusters in θ	37.3 ± 0.2
x OR θ	83.9 ± 0.3
x AND θ	0.49 ± 0.02
random coincidences	0.140 ± 0.001

Fig. 2.65 shows a typical event of the fibre detector taken during the in-beam tests. The data of 288 TDC channels is shown with each cross representing the leading edge time (in time steps of $\Delta t \approx 118$ ps) of a signal coming from the corresponding DTD channel. Signal types are classified into (1) single random hits, (2) signal clusters, (3) after-pulses, and (4) trigger reference time. A magnification

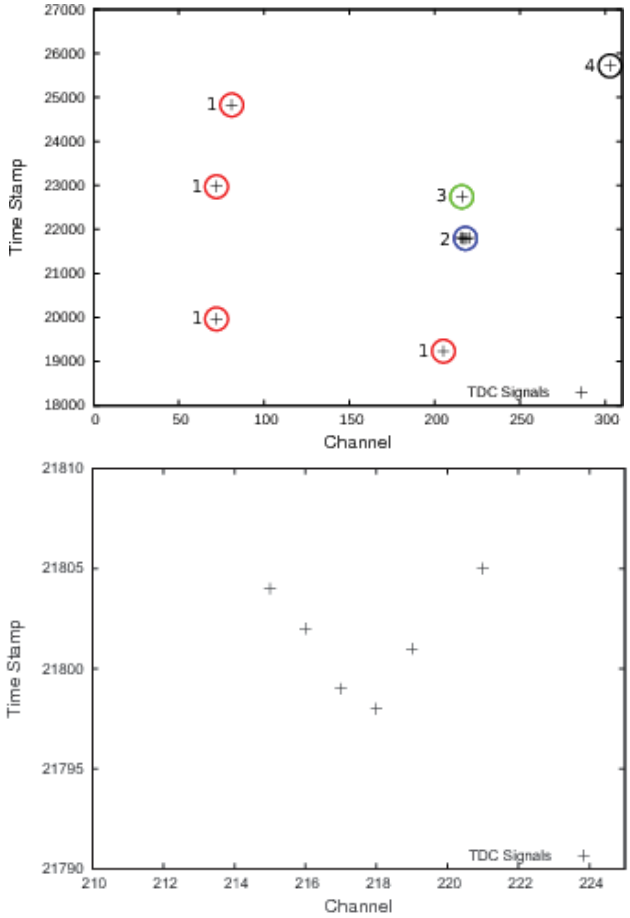

Figure 2.65.: A typical event display from the fibre detector during the in-beam tests. The data of 288 TDC channels is shown with each cross representing the leading-edge time (in time steps of $\Delta t \approx 118\,\text{ps}$) of a signal coming from the corresponding DTD channel. Different signal types are found in this event: (1) single random hits, (2) a signal cluster with (3) after-pulse, and (4) the trigger reference time. A magnification of the signal cluster produced by the charged particle is shown in the bottom panel. Further information on the cluster analysis is given in [151].

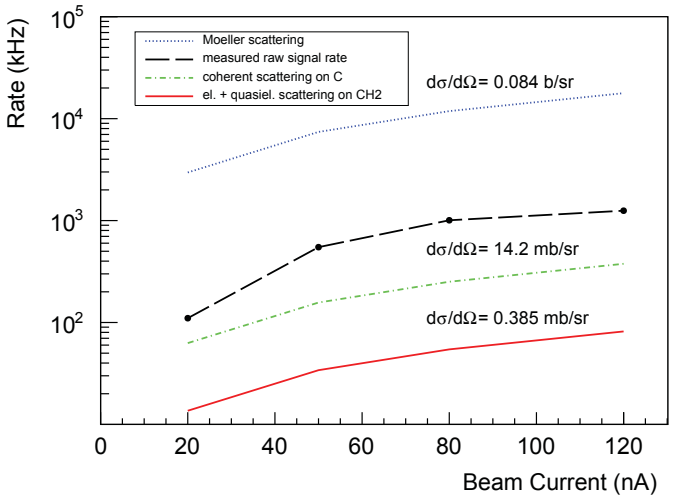

Figure 2.66.: Measured trigger rates in the x-plane of the electron-arm detector as a function of electron beam current compared to the calculated scattering rates of Møller scattering, elastic/quasi-elastic scattering at H and C, and coherent scattering at C. The used differential cross-sections are shown as well.

of the signal cluster is shown in the bottom panel. The cluster is spread over 7 channels and 7 time steps, corresponding to 0.8 ns. It is known that charged particles crossing the fibre detector produce the latter type of signals [137]. In the analysis software the clusters were identified based on a hierarchical agglomerative cluster algorithm. In deducing the hit times an iteration over all hits in a plane including multiple hits in a channel was performed, and clusters of correlated hit times were searched for. The cluster with the time closest to the trigger signal time was retained, and within the cluster the time of the leading signal was chosen as hit time. A minimum temporal and spatial distance between signals in a cluster have been defined before the analysis took place.

Signals of type (1) or (3) were filtered out by the clustering algorithm of the trigger system. In Fig. 2.66 the rate of identified type (2) signals (OR trigger rate) in the x-plane of the electron-arm detector is compared to the calculated rates of Møller scattering, elastic/quasi-elastic scattering at H and C, and coherent scattering at C. The momentum of Møller electrons scattered into the direction of the electron-arm detector was only $p \approx 40$–$50\,\mathrm{MeV}/c$, and some of the electrons were

deflected in the fringe field of the dipole, *cf.* Fig. 2.11. A good agreement between calculated and measured rates was observed. The tests have shown that a reliable triggering on signal clusters is achieved with the VUPROM boards.

ear of the pine tree
mushroom on a strange tree
with a leaf stuck to it

Matsuo Bashō (1644–94)

3 Kaon Electro-Production at MAMI

3.1. Accelerator and Experimental Set-up

The Mainz Mikrotron MAMI at the Institut für Kernphysik in Mainz is an accelerator to study the hadron structure with the electromagnetic probe.

Electrons are produced by a thermionic source with an energy gain of 100 kV. Alternatively, a polarised source can be used: the polarised electrons are produced via the photoelectric effect using polarised laser light on a GaAs crystal. Polarisations as high as 90 % have been obtained. A linear stage accelerates the beam to 3.5 MeV and injects into a cascade of three race-track microtrons [163]. These microtrons are built with normal conducting accelerating cavities resonating at a radio-frequency of $\nu = 2\,449.53$ MHz placed between two very homogeneous magnets allowing for multiple recirculation of the beam. The first stage delivers a beam of 14.9 MeV energy. Since 1991 the second and the third microtron (MAMI-B) have delivered an electron beam with high spatial and energy definition with an end-point energy of 180 MeV and 855 MeV, respectively. The extracted beam has an energy spread of only 30 keV (FWHM). As the electron beam has a micro-structure in the picoseconds-range, instead of well-separated macro-pulses, the beam is practically continuous and the duty factor of the machine is 100 %. An electron beam polarised at the photo-cathode source can be readily transported through the accelerator and delivered on target.

The machine has been upgraded to 1.5 GeV electron beam energy by a harmonic double-sided microtron with an end-point energy of 1508 MeV [164]. This fourth stage, called MAMI-C, was completed in 2007. In this machine normal conducting cavities are also used, arranged in two anti-parallel linear accelerators and the recirculation is guaranteed by four clam-shell magnets with 45° bending. For longitudinal stability reasons, one of the two linear accelerators is operated

at the first harmonic in respect to the other. With MAMI-C the threshold beam energy for associated strangeness production off protons was reached for the first time in Mainz.

The cryogenic target in the spectrometer hall that was used for the kaon electro-production experiments consists of a vacuum vessel where the scattering material, either hydrogen, deuterium or helium, can be placed. Also various solid state targets, mounted on a ladder, can be moved into the beam during experiments using remote control. The cooling and liquefying system is based on two cooling loops. The first loop is connected to a Philips compressor for liquefying hydrogen which is then transported to the target vessel by a transfer pipe. Inside the vessel there is the second cooling loop ("Basel-loop") which is closed and contains the scattering material. The liquid hydrogen of the first loop cools the second one by a heat exchanger and a fan provides continuous recirculation, see Fig. 3.1. The temperature of the liquid hydrogen is raised in the heat exchanger and it is then transported back to the Philips compressor. The scattering material is maintained in the liquid phase by the first cooling loop during the course of the experiment. The target cell inside the Basel-Loop is 49.5 mm long and is made of a 10 μm Havar walls. The geometry of the cell is optimized for enhancing the luminosity while keeping low the energy-losses. The temperature and pressure of the liquid are continuously monitored.

The beam was wobbled with a few kHz in the transverse directions in order to keep temperature oscillations as small as possible avoiding local boiling of the liquid. The stability of the liquid phase is essential for a precise determination of the luminosity. The wobbler system consists of two steering electromagnets, one vertical and one horizontal. The current through the magnets was varied sinusoidally. The typical raster size used in the experiments was $\pm$ 1 mm in both the vertical and the horizontal direction. The beam position was centred regularly using a screen and was monitored with a cavity.

3.2. COINCIDENCE MEASUREMENTS

In 2008 the first experiment on the electro-production of kaons off a liquid hydrogen target was performed [166, 167]. The reaction leads to two possible final states with either a Λ or Σ^0 hyperon, which are easily separable by a missing mass analysis. Positive kaons were detected in KAOS in coincidence with the scattered electron into SpekB. The data were taken at two different kinematic settings in $p(e, e'K)$ reactions with kaons in the momentum range of 400–700 MeV/c. The one setting with the central momentum in KAOS of 530 MeV/c and the central momentum in SpekB of 327 MeV/c was continued by a longer data-taking cam-

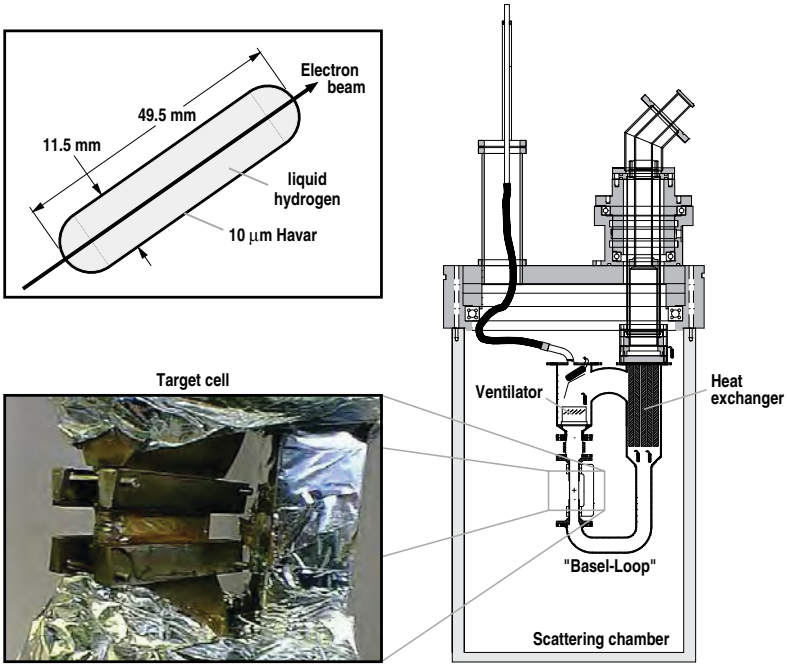

Figure 3.1.: Overview of the target cell containing the liquefied gas which is mounted in a scattering chamber. The hydrogen comes in from the top delivered by a compressor placed in the experimental hall. The target material is circulating in the "Basel-Loop". (Figs. from [165]).

Table 3.1.: Experimental settings of the kaon electro-production beam-times of 2008. The second setting was selected to acquire data from Λ and Σ^0 production channels, with the two different associated kaon momenta being simultaneously within the large momentum acceptance of the KAOS spectrometer. Measurements in this setting were continued in 2009. The beam energy was 1.508 GeV, beam intensity 1–4 μA, beam raster size $\pm$ 1 mm, and the ℓH_2 target length 48 mm.

virt. photon + target				electron arm		kaon arm	
$\langle Q^2 \rangle$ $(\mathrm{GeV}/c)^2$	$\langle W \rangle$ GeV	$\langle \epsilon \rangle$ (trans.)	$\langle \omega \rangle$ GeV	$\langle q_{e'}^{lab} \rangle$ GeV/c	$\langle \theta_{e'}^{lab} \rangle$ deg	$\langle p_K^{lab} \rangle$ GeV/c	$\langle \theta_K^{lab} \rangle$ deg
0.050	1.670	0.540	1.044	0.455	15.8	Λ : 0.466	-31.5
0.036	1.750	0.395	1.182	0.318	15.5	Λ : 0.642	-31.5
						Σ : 0.466	

paign in 2009 for a statistically and systematically improved data-set [168–170].

The central spectrometer angle of the KAOS arm was 31.50° with a large angular acceptance in the dispersive plane of $\vartheta_K = 21$–$43°$. The spectrometer setting for electron detection was fixed at the minimum in-plane angle of $\vartheta_{e'} \approx 15°$, thereby maximising the virtual photon flux. For the two studied kinematics the invariant momentum transfer, $\langle Q^2 \rangle = -\langle q^2 \rangle$, was very low, the virtual photon energy, $\langle \omega \rangle$, was near the maximum of the kaon photoproduction cross-section at 1–1.2 GeV, which excites a total energy in the virtual-photon-nucleon center-of-mass system, $W^2 = M_{targ}^2 + 2\omega M_{targ} - Q^2$, of 1.6–1.7 GeV. The kinematic conditions for the two settings are summarised in Table 3.1.

The collected data in 2008 correspond to effectively 3 days of beam-time at 1–4 μA beam current for each kinematic point with a total integrated luminosity of $\int \mathcal{L} dt \sim 284\,\mathrm{fbarn}^{-1}$. In 2009 the current was held constant at 2, respectively 4 μA. With a run-time of 244 h using 2 μA beam current (at 14 % dead-time) and 38 h using 4 μA beam current (at 45 % dead-time) the accumulated and corrected luminosity for the 2009 data-taking campaign was $\int \mathcal{L} dt \sim 2300\,\mathrm{fbarn}^{-1}$.

3.3. DATA ANALYSIS

For the data analysis, a software package is used which was specifically developed within the A1 Collaboration using the `C++` language and object oriented techniques (`Cola++`).

3.3.1. KAON AND HYPERON IDENTIFICATION

Kaon identification is based on specific energy-loss and time-of-flight, electron identification on a signal in a gas Cherenkov counter. The flight time difference between protons and kaons is 10–15 ns, between pions and kaons 5–10 ns. The energy-loss separation between kaons and pions is small, whereas the separation between kaons and protons is of the order of 2–5 MeV/cm.

The following cuts were applied to the 2009 data set taken with beam-currents of 2 and 4 μA to identify coincident $(e, e'K^+)$ events:

Electron identification: A signal in the sum of all five Cherenkov counter amplitudes to reject pions in the electron arm.

Electron arm acceptance: -4.0 ° $< \theta_0 <$ 4.2 ° and -1.2 ° $< \phi_0 <$ 1.1 ° and -7.0 % $< \delta p <$ 7.0 %

Electron arm scattered particle rejection: -15 mm $< y_0^{snout} + y_0^{colli}/8 <$ 15 mm and $y_0^{snout} <$ 30 mm

Kaon arm acceptance: $\theta_0 > -10.5\,^\circ$ and $\theta_0 < 7.3^\circ$ and $\theta_0 < 5^\circ + 0.83^\circ \times (\delta p + 17\,\%)$ and $\theta_0 > 0.2^\circ \times (\delta p - 20\,\%) - 6.5^\circ$ to restrict the acceptance in the hadron arm to a region where agreement between the Monte Carlo code and the analysed data was excellent.

MWPC track reconstruction: Track quality $> 10^{-3}$ ensuring good quality tracks in the tracking chambers.

Kaon identification: $|t_G^K| < 1.2$ ns, being the measured TOF corrected for the expected kaon flight time, and $|\Delta E_{F,G}^K| < 640$ keV, being the measured specific energy loss corrected for the expected kaon energy loss.

After electron and kaon identification the measured momenta, in magnitude and direction with respect to the incoming beam, allow for a full reconstruction of the missing energy and missing momentum of the recoiling system. The missing mass M_X is related to the four-momentum q^μ of the virtual photon and the four-momentum p_K^μ of the detected kaon according to $M_X^2 = (q^\mu + P_{targ}^\mu - p_K^\mu)^2$, where

$P^{\mu}_{targ} = (M_{targ}, \vec{0})$ is the target four-momentum. The missing energy and missing momentum can then be calculated using

$$E_X = E_e - E_{e'} + M_{targ} - E_K = \omega + M_{targ} - E_K, \quad (3.1)$$

$$\vec{P}_X = \vec{q} - \vec{p}_K, \quad (3.2)$$

and the missing mass in terms of the kinematic variables Q^2, ω, and $\vec{q}$ as well as of the reconstructed kaon energy, momentum, and scattering angle, can be written as

$$M_X = \sqrt{E_X^2 - |\vec{P}_X|^2} = \sqrt{(\omega - E_K + M_{targ})^2 + p_K^2 - 2p_K|\vec{q}|\cos\theta_K - Q^2}\,. \quad (3.3)$$

The kaon events that correspond in the missing mass to the two hyperon channels are used to extract the kaon yield. Examples of two preliminary missing mass spectra are shown in Fig. 3.2. In both spectra the mass resolution is limited by the errors in the estimated transfer matrix that was not yet corrected by the aberrations seen in the sieve slit measurements. The overlaid histograms show the missing mass distributions in two averaged (e', K) coincidence time side-bands with the appropriate weights. The large momentum acceptance of the KAOS spectrometer covers the free electro-produced hyperons Λ and Σ^0. The well-known masses of the two hyperons can serve as an absolute mass calibration.

For a description of the mass spectrum the Λ and Σ^0 peaks were fitted. Each fitting function was constructed by folding a Gaussian resolution function with an exponential function which accounts for radiative losses, ionization loss and experimental energy resolutions adjusted to the experimental distribution.

A preliminary missing mass spectrum from the 2009 beam-time is shown in Fig. 3.3 (left). Random background events in the missing mass spectra were subtracted by two averaged (e', K) coincidence time side-bands with the appropriate weights. Additional kaon background is seen in the spectrum. Since the KAOS spectrometer is operated as a single dipole with open yoke geometry a significant fraction of detected particles have scattered inside the spectrometer and need to be treated accordingly. Fig. 3.3 (right) shows the background-subtracted missing mass distribution compared to the Monte Carlo spectrum. The simulation includes radiative corrections, energy-loss in the target, and a model for the spectrometer resolutions. Figs. 3.5 and 3.4 show missing mass distributions for the $p(e, e'K^+)Y$ reaction separated in the $\cos\theta^*_K$-bins used for the extraction of cross-sections.

The dependence of the missing mass on the focal-surface coordinates is shown in Fig. 3.6. The width and the significant deviations for kaons in the $K\Lambda$-channel

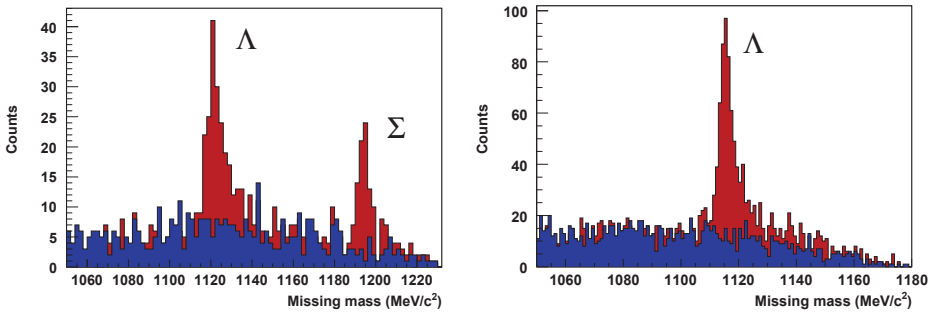

Figure 3.2.: Preliminary missing mass spectra from the 2008 beam-times in the $p(e,e'K^+)Y$ reaction at two different low-Q^2 kinematics. The overlaid histograms show the missing mass distribution in two averaged (e',K) coincidence time side-bands with the appropriate weights.

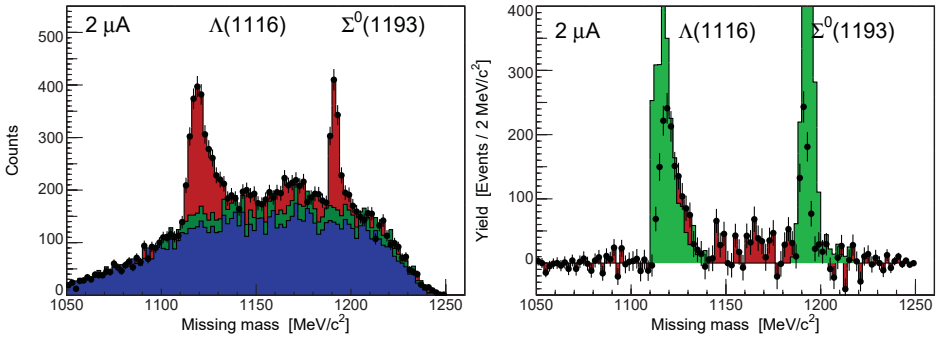

Figure 3.3.: Preliminary missing mass spectra in the $p(e,e'K^+)Y$ reaction from the 2009 beam-times. Left: Missing mass distribution with overlaid histograms showing random coincidences and additional kaon background. Right: Background-subtracted missing mass distribution compared to the Monte Carlo spectrum. The simulation includes radiative corrections, energy-loss in the target, and a model for the resolutions.

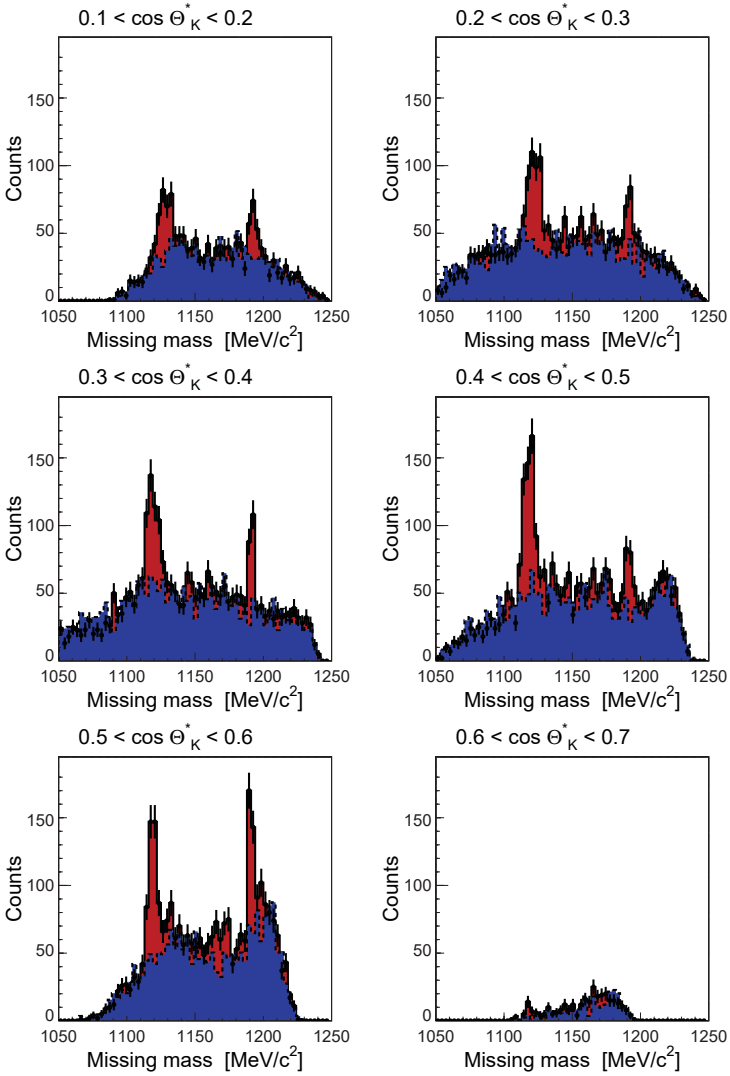

Figure 3.4.: Missing mass spectra for the $p(e,e'K^+)Y$ reaction separated in $\cos\theta^*_K$-bins.

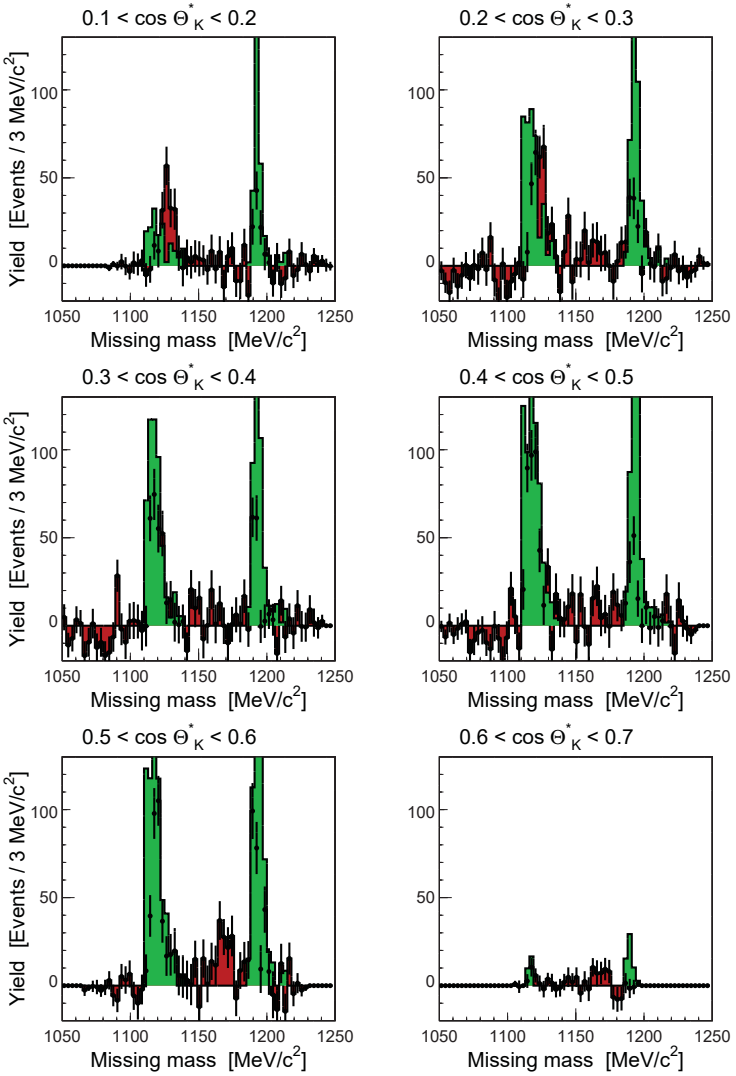

Figure 3.5.: Background-subtracted missing mass spectra for the $p(e,e'K^+)Y$ reaction separated in the $\cos\theta^*_K$-bins used for the extraction of cross-sections. The data is compared to Monte Carlo spectra.

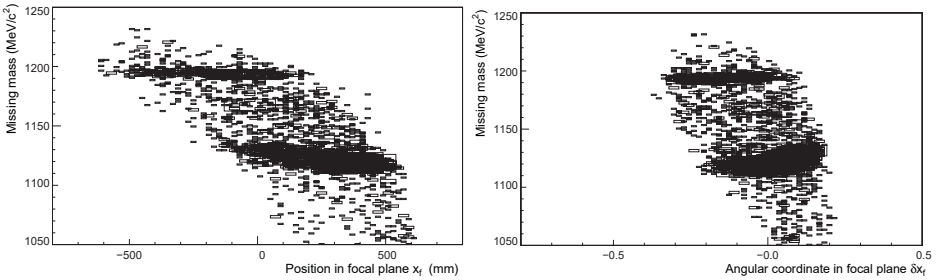

Figure 3.6.: Dependence of the missing mass on the focal-surface coordinates position x_f (left) and the track angle difference δx_f (right). The width and the significant deviations for kaons in the $K\Lambda$-channel are an indicator of wrong transfer matrix elements.

around $M_X \approx 1115\,\mathrm{MeV}/c^2$ are an indicator of wrong transfer matrix elements. Work to improve the calibrations is ongoing.

The chosen kinematics leads to two almost separated bands of kaon momenta for the production associated to the Λ- or to the Σ^0-hyperon. Fig. 3.7 (left) shows the calculated kinematic correlation between kaon scattering angle and maximum kaon momentum. The lines could be used for an absolute momentum or angle calibration of the spectrometer. The preliminary analysis of the measured kinematic correlation from the 2009 beam-time, as shown in Fig. 3.7 (left), was compared to the calculation.

3.3.2. EXTRACTION OF CROSS-SECTIONS

[1] The luminosity is calculated from the density and thickness of the target, and the beam current, and is corrected for the DAQ dead-time. It is defined by the beam current density and the number of target nuclei:

$$\mathcal{L} = j \cdot N \tag{3.4}$$

Then, the integrated luminosity is

$$\int \mathcal{L} \mathrm{d}t = \frac{Q}{e}(\rho \cdot d)\frac{N_A}{A}\,, \tag{3.5}$$

[1] This section has been updated during the course of the habilitation process following the submission of the thesis

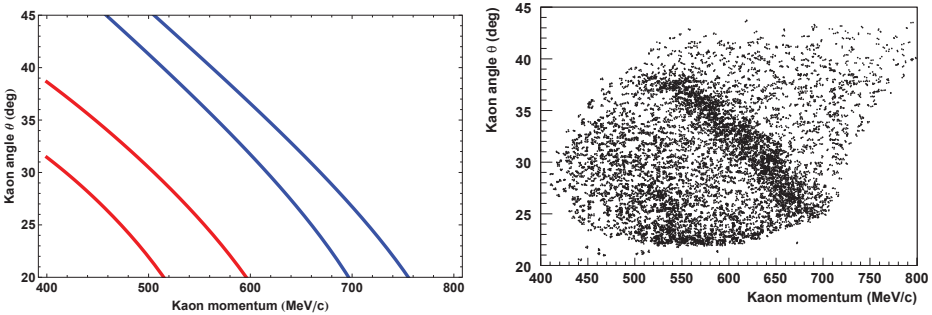

Figure 3.7.: Calculated kinematic correlation between kaon scattering angle and kaon momentum (left). Two separated bands of kaon momenta for production associated to the Λ-hyperon (blue lines for minimum and maximum) or to the Σ^0-hyperon (red lines) are seen. Preliminary analysis of the measured kaon kinematic correlation from the 2009 beamtime (right).

where Q is the total accumulated charge during the integration time, e is the electron charge magnitude, Q/e is the number of beam electrons, $(\rho \cdot d)$ is the areal density of the target, N_A is Avogadro's number, and A is the mass number of the target. For the liquid hydrogen target an instantaneous luminosity of $1.25\,\mathrm{pbarn}^{-1}$ per s and per μA is achieved.

The total efficiency $\epsilon(p,\theta,\phi)$ for the detection of kaons with the spectrometer set-up can be factored into

$$\epsilon(p,\theta,\phi,I) = \epsilon_{MWPC} \cdot \epsilon_{cut}^{total}(p,\theta,\phi) \cdot \epsilon_{trig}(p,\theta,\phi) \cdot \epsilon_{track}(I) \qquad (3.6)$$

with ϵ_{MWPC} the wire chamber detection efficiency, $\epsilon_{cut}(p,\theta,\phi)$ the analysis cut efficiency, $\epsilon_{trig}(p,\theta,\phi)$ the trigger efficiency, and $\epsilon_{track}(I)$ the tracking efficiency. In order to investigate the MWPC, tracking, and trigger efficiencies dedicated measurements have been performed in 2008 and 2009.

The trigger was generated by a combination of hits in the two scintillator walls. Particular momentum and track angle combinations allow the particle to cross the gaps between the scintillator paddles giving rise to significant detector inefficiencies. In Fig. 3.8 a simulation of these geometrical inefficiencies are shown in the tracking coordinate system. Momentum and track angle dependent trigger efficiency corrections needed to be applied to the generalized acceptance.

A cut was placed on the missing mass in order to separate the Λ and Σ^0 reaction channels. For the Λ hyperons events were selected in the $1110\,\mathrm{MeV}/c^2$

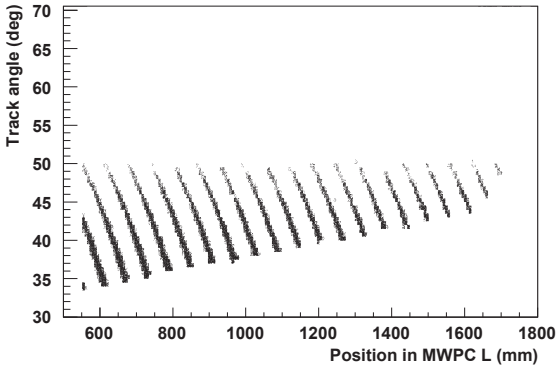

Figure 3.8.: Simulated geometrical inefficiencies in the scintillator wall defined in the coordinate system of the tracking chambers.

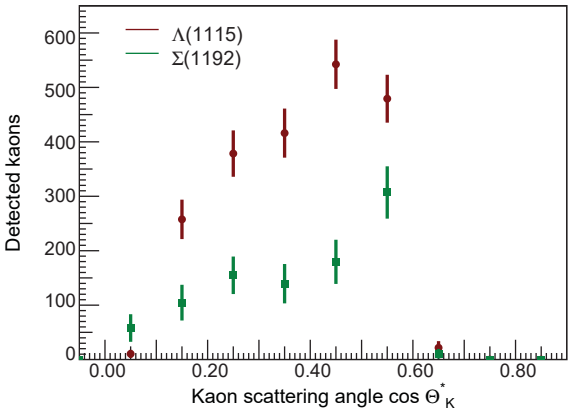

Figure 3.9.: Preliminary yield of identified $p(e,e'K^+)\Lambda,\Sigma^0$ events as a function of the cosine of the kaon centre-of-mass scattering angle. The identified kaon counts in both hyperon channels were corrected for background counts to obtain the yields. The 2009 data covered angles in the range of $\theta^*_K \sim$ 40–90° and $\phi \sim$ -20–20°.

$< M_X < 1140\,\mathrm{MeV}/c^2$ region, for the Σ^0 hyperon in the $1185\,\mathrm{MeV}/c^2 < M_X < 1220\,\mathrm{MeV}/c^2$ region. The preliminary yields of identified $\mathrm{p}(e,e'K^+)\Lambda,\Sigma^0$ events as a function of the centre-of-mass kaon scattering angle are shown in Fig. 3.9.

The data were compared to a Monte Carlo simulation using the Kaon-Maid model [21, 29] as an input for the cross-sections and a generalized acceptance function for the detector description.

The further analysis required a detailed Monte Carlo simulation of the experiment in order to extract cross-section information from the data. Following Eq. 1.18 the form of the virtual photo-production cross-section used for this analysis is:

$$\frac{\mathrm{d}\sigma}{\mathrm{d}E_{e'}\mathrm{d}\Omega_e\mathrm{d}\Omega_K^*} = \Gamma(Q^2,W)\frac{\mathrm{d}\sigma_v}{\mathrm{d}\Omega_K^*}(W,Q^2,\epsilon,\theta_K^*,\phi) \tag{3.7}$$

where the transformation between the differentials $\mathrm{d}E_{e'}\mathrm{d}\Omega_e \leftrightarrow \mathrm{d}Q^2\mathrm{d}W$ is incorporated into the virtual photon flux $\Gamma(Q^2,W)$ via the Jacobian:

$$\frac{\mathrm{d}\sigma}{\mathrm{d}Q^2\mathrm{d}W\mathrm{d}\phi\mathrm{d}\Omega_K^*} = \frac{W}{2M_pEE'}\Gamma(E',\Omega_e)\frac{\mathrm{d}\sigma_v}{\mathrm{d}\Omega_K^*} = \Gamma(Q^2,W)\frac{\mathrm{d}\sigma_v}{\mathrm{d}\Omega_K^*} \tag{3.8}$$

The experimental yield can then be related to the cross-section by

$$Y = \mathcal{L}\times\int\Gamma(Q^2,W)\frac{\mathrm{d}\sigma_v}{\mathrm{d}\Omega_K^*}A(\mathrm{d}V)R(\mathrm{d}V)\,\mathrm{d}Q^2\mathrm{d}W\mathrm{d}\phi\mathrm{d}\Omega_K^*\,, \tag{3.9}$$

where $\mathcal{L}$ is the experimental luminosity that included global efficiencies such as dead-times and beam-current dependent corrections such as the tracking efficiency, A is the acceptance function of the coincidence spectrometer set-up, and R is the correction due to radiative or energy losses.

The geometrical acceptance of the spectrometer set-up, the path-length from target to detectors, kaon decay in flight, and kaon scattering were determined by a Monte Carlo simulation using the simulation package Geant4. The kaon survival fraction varied between 0.2 and 0.35 for the range of momenta detected. Within the A1 collaboration a different simulation package (`Simul++`) for the experiments was developed in the past. This code allows to simulate, according to a chosen kinematics, the full phase-space accepted by the spectrometers. In alternative, the events can be generated sampling a distribution given by the cross-section of a specific process. The output data of the simulation are fully compatible with the real experimental data, so the same analysis and histogramming programs can be used in the two cases. The output of the Geant4 study was implemented in this simulation as a generalised acceptance map, leading to the phase-space accepted by the combination of the spectrometers with any of the

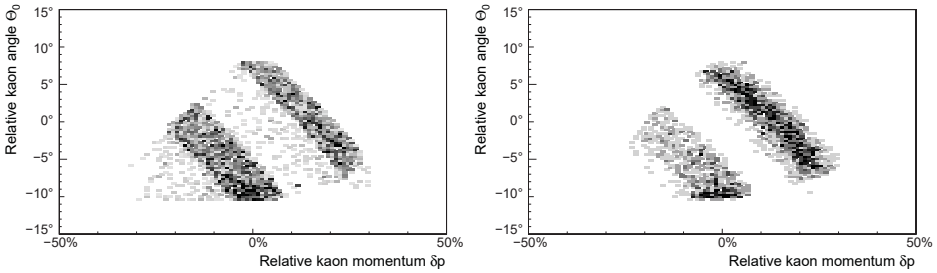

Figure 3.10.: Phase-space for kaon scattering angle *vs.* kaon momentum in the KAOS spectrometer simulated by the Monte Carlo method (left) and measured during the 2009 beam-time (right). The kaon data were extracted after particle identification and missing mass cuts. The simulation includes radiative corrections and energy-loss in the target.

high-resolution spectrometers according to a chosen kinematics together with the radiative corrections.

In the Monte Carlo for the integral events are generated within phase-space limits that extend beyond the physical acceptances of the spectrometers. The number of accepted events is then defining the phase-space accepted by the spectrometers together with the radiative corrections, absorption and decay losses as well as detector inefficiencies according to the chosen kinematics and the spectrometer models. By virtue of the Monte Carlo technique used to perform this integral the quantities A and R are not available separately or on an event-by-event basis. In Fig. 3.10 the phase-space in the target angle *vs.* momentum plane for kaon acceptance in the KAOS spectrometer simulated by the Monte Carlo integration method is compared to the data measured during the 2009 beam-time. The kaon data was extracted after particle identification and missing mass cuts. The agreement inside the fiducial volume is excellent.

The general acceptance can be written in terms of the cross-section at a given point $(d^2\sigma/d\Omega^*_K)_{0,\theta^*_K}$, called the scaling point, at $\langle Q^2\rangle$, $\langle W\rangle$, $\langle\phi\rangle$, and $\langle\phi^*_K\rangle$, when studying the dependence on the remaining variable $\cos\theta^*_K$:

$$Y = \mathcal{L}\times\left(\frac{\mathrm{d}\sigma_v}{\mathrm{d}\Omega^*_K}\right)_{0,\theta^*_K}\times \int\Gamma(Q^2,W)\frac{\frac{\mathrm{d}\sigma_v}{\mathrm{d}\Omega^*_K}}{\left(\frac{\mathrm{d}^2\sigma_v}{\mathrm{d}\Omega^*_K}\right)_{0,\theta^*_K}}A(\mathrm{d}V)R(\mathrm{d}V)\,\mathrm{d}Q^2\mathrm{d}W\mathrm{d}\phi\mathrm{d}\Omega^*_K \tag{3.10}$$

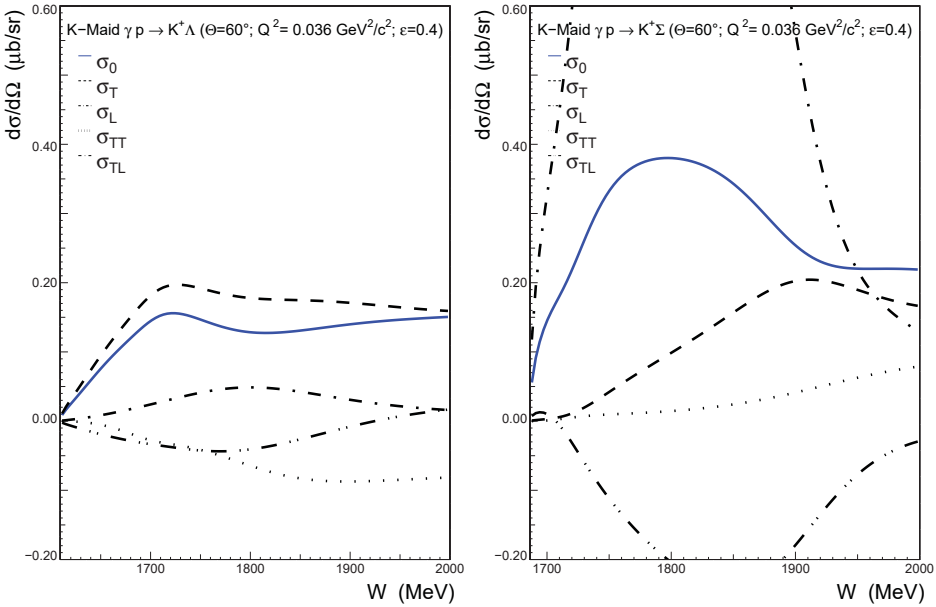

Figure 3.11.: Kaon-Maid predictions from a variant of the Kaon-Maid model without longitudinal couplings of nucleon resonances in the Λ reaction channel. The mean hadronic energy in the experiment was at 1750 MeV.

Then, the behaviour of the cross-section across the acceptance needs to be scaled according to a given theoretical description. The Kaon-Maid [21, 29] isobar model was implemented in this analysis, however, one can as well use the full (SL) and the simplified version (SLA) of the so-called Saclay-Lyon model [26]. The predictions for the cross-section dependencies on the hadronic energy from a variant of the Kaon-Maid model without longitudinal couplings of nucleon resonances in the Λ reaction channel are shown in Fig. 3.11. Fig. 3.12 shows that the predictions of the Saclay-Lyon model are not too different to the Kaon-Maid model variant in the hadronic energy range of the experiment, however, the slope of the distribution is drastically different. The scaling point for the data set from 2009 is at $\langle Q^2 \rangle = 0.036\,(\mathrm{GeV}/c)^2$, $\langle W \rangle = 1.750\,\mathrm{GeV}$, $\langle \epsilon \rangle = 0.4$.

Predictions from the phenomenological models for the kinematics studied with the KAOS spectrometer at MAMI result in relatively large discrepancies in the lon-

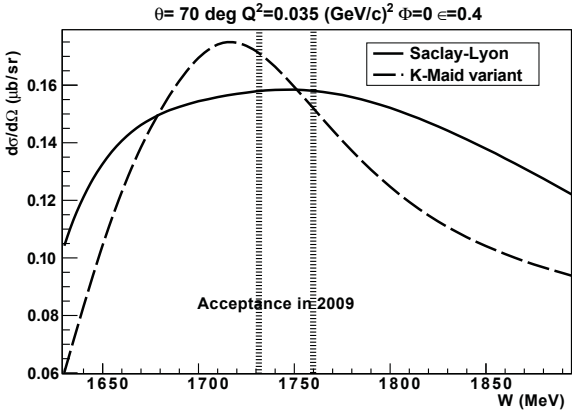

Figure 3.12.: Comparison of $K\Lambda$ cross-section predictions from the Kaon-Maid and Saclay-Lyon models for the kinematics measured at MAMI as a function of the hadronic energy. The hadronic energy acceptance of the spectrometer set-up for the 2009 beam-time is indicated.

gitudinal contributions to the cross-section. The full Kaon-Maid model including all couplings and individual dipole form-factors of baryon resonances reveals the following set of cross-sections at the centre of the acceptance in the kinematics probed at MAMI: $\sigma_T = 235\,\mathrm{nb/sr}$; $\sigma_L = 423\,\mathrm{nb/sr}$; $\sigma_{TT} = -121\,\mathrm{nb/sr}$, $\sigma_{TL} = 120\,\mathrm{nb/sr}$. The large longitudinal and the σ_{TT}, and σ_{TL} cross-sections are strongly affected by the longitudinal coupling of the $D_{13}(1900)$ resonance and the appropriate electromagnetic form-factor. With vanishing coupling the model predicts: $\sigma_T = 236\,\mathrm{nb/sr}$; $\sigma_L = 39\,\mathrm{nb/sr}$; $\sigma_{TT} = -31\,\mathrm{nb/sr}$; $\sigma_{TL} = 34\,\mathrm{nb/sr}$. The change in the σ_L, σ_{TT}, and σ_{TL} cross-sections is dramatic. Switching off also all other longitudinal couplings the variation is noticeable, but small: $\sigma_T = 192\,\mathrm{nb/sr}$; $\sigma_L = 48\,\mathrm{nb/sr}$; $\sigma_{TT} = -36\,\mathrm{nb/sr}$; $\sigma_{TL} = -51\,\mathrm{nb/sr}$. This behaviour of the model is questionable. Fig. 3.13 shows the predictions using the full version compared to a variant without longitudinal coupling of the $D_{13}(1900)$ resonance in the kinematic region of the measurements at MAMI.

Using a Kaon-Maid variant without longitudinal couplings but with electromagnetic form-factors as in the Saclay-Lyon model, the following results are obtained: $\sigma_T = 204\,\mathrm{nb/sr}$; $\sigma_L = 14.7\,\mathrm{nb/sr}$; $\sigma_{TT} = -64\,\mathrm{nb/sr}$, $\sigma_{TL} = -4.0\,\mathrm{nb/sr}$. These values differ strongly from the above, but seem to be more solid when compared to predictions from Saclay-Lyon, see Fig. 3.12.

The extension of the Saclay-Lyon model to the electro-production does not in-

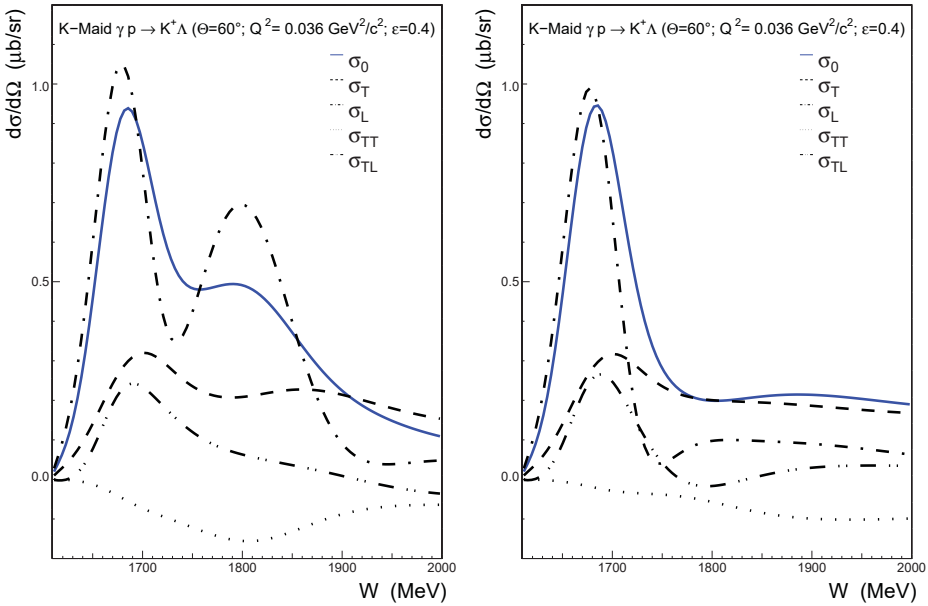

Figure 3.13.: Kaon-Maid predictions for the Λ reaction channel in the kinematics measured at MAMI using the full version (left) and a variant without longitudinal coupling of the $D_{13}(1900)$ resonance (right). The mean hadronic energy in the experiment was at 1750 MeV.

clude too many additional parameters. Predictions of the Saclay-Lyon model are reasonable ($\sigma_T = 227\,\mathrm{nb/sr}$; $\sigma_L = 7.6\,\mathrm{nb/sr}$; $\sigma_{TT} = -56\,\mathrm{nb/sr}$; $\sigma_{TL} = 9.4\,\mathrm{nb/sr}$) and are in a good agreement with predictions of the discussed variant of the Kaon-Maid model in which identical phenomenological electromagnetic form-factors are used and also with those from the original Kaon-Maid version without the longitudinal coupling of the $D_{13}(1900)$ resonance.

Finally, the cross-section is extracted dividing the yield by the luminosity and the evaluated phase-space integral. An important observable that was investigated was the stability of the results as a function of the applied cuts and their influence on the extracted cross-section. The angular distribution of the cross-section gives information on the angular dependence of the production mechanisms for each hyperon. Preliminary differential cross-sections of kaon electroproduction in the Λ and Σ^0 channels are shown in Fig. 3.14. The data points

are compared to the Kaon-Maid model, to a variant of that model, and to the Saclay-Lyon model. It is seen from the $\cos\theta^*_K$-distribution that the models predict a forward-peaked production cross-section. The absolute value of the cross-section easily differentiates between the models with small longitudinal coupling of the resonances from the full Kaon-Maid model. At the centre of the acceptance near $\cos\theta \sim 0.5$ the difference is more than a factor 2.

It is expected that the data will constrain the existing phenomenological models and generate theoretical interest. The difference between photo- and electroproduction data at small Q^2 is very important as various models predict different transitions between the photoproduction point and the electroproduction full cross-section. If *e.g.* the original Kaon-Maid model were right, then the electroproduction data would be a factor 2.5 larger than the photoproduction data at $\theta^*_K = 60^\circ$. The data could help to fix the unknown longitudinal coupling constants which appear to be important in this kinematic region.

The results presented here are coming from the data taken in 2009. Data from calibration runs is currently being analysed to improve the resolutions and to minimize the dependencies of the extracted cross-sections on the spectrometer acceptance. In the future elementary kaon electroproduction measurements with the KAOS spectrometer using the pre-target beam-chicane will be continued.

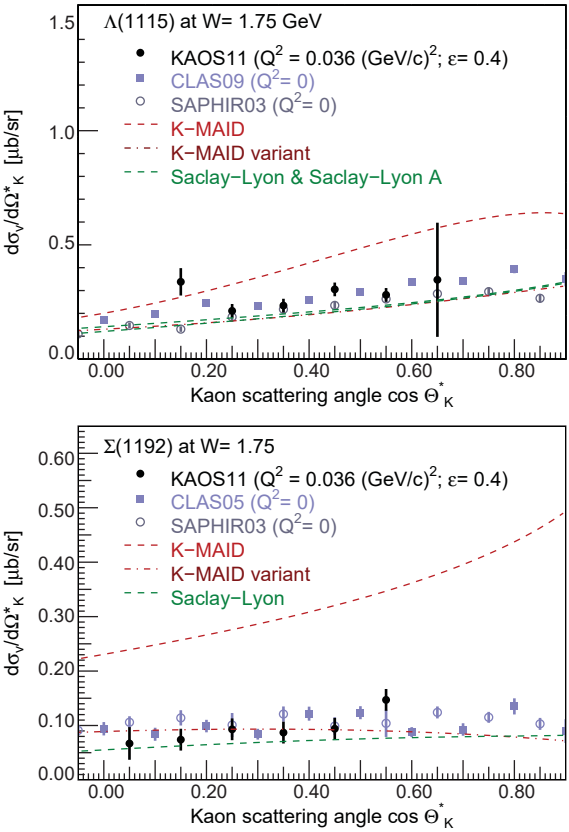

Figure 3.14.: Preliminary differential cross-sections of kaon electro-production scaled to the centre of the experimental acceptance and compared to variants of the Kaon-Maid model and the Saclay-Lyon models. Data points in light grey are from the SAPHIR and CLAS experiments, taken at Q^2= 0 [50, 58].

4 CONSIDERATIONS

4.1. RETROSPECTION

At the Institut für Kernphysik in Mainz, Germany, the microtron MAMI has been upgraded to 1.5 GeV electron beam energy, crossing the energy threshold for open strangeness production in 2007.

In analogy to the successful description of pion photoproduction in the Δ-resonance region or η photoproduction in the second resonance region, the electromagnetic kaon production amplitudes associated to Λ/Σ^0 hyperons can be described by phenomenological models. Experimental data for kaon production has been collected by ELSA, SPring8, GRAAL, and LNS Tohoku and measurements with high statistics have been performed recently at Jefferson Lab, nevertheless, there are still a number of open problems in the interpretation of the data and the description of the elementary process using phenomenological models. The data published after 1990 is inconsistent so that the experiments do not allow for a unique description of the process.

Theoretical groups have developed a particular type of effective Lagrangian model, commonly referred to as isobar approach, in which the reaction amplitude is constructed from *s*-, *t*-, or *u*-channel exchange diagrams. Most of the models use single-channel approaches, in which a single hadron is exchanged. Since several resonances may contribute in this channel, models disagree on their relative importance, and many free parameters have to be fixed. Experimental set-ups used to study the strangeness production channels are missing forward angle acceptance leading to a strong variation of the models in the forward region.

The situation clearly indicates that more experimental and theoretical work is needed in order to provide a comprehensive understanding of the elementary reaction. A number of new experiments are now addressing these issues, among them the charged kaon electro-production programme at MAMI.

An instrument of central importance for this programme is the newly installed magnetic spectrometer KAOS, dedicated to the detection of charged kaons. In 2003 it was dismantled at the SIS facility of GSI and reinstalled at MAMI during the following years. The spectrometer is now operated by the A1 collaboration to study strange hadronic systems at the spectrometer facility. Its compact design and its capability to detect negatively and positively charged particles simultaneously under forward scattering angles complement the existing spectrometers.

In 2007 and 2008 first calibration data were obtained using electron beams of 450 and 855 MeV energy impinging on liquid hydrogen as well as on solid-state carbon and tantalum targets. In the spectrometer's hadron arm there are two scintillator walls serving as timing and dE/dx and trigger detectors and two MWPC as coordinate detectors. At different kinematics the particle identification power and tracking capabilities of the hadron arm detection system was confirmed.

In 2008 kaon production off a liquid hydrogen target was studied for the first time at MAMI. Positive kaons were detected in KAOS in coincidence with the scattered electron into SpekB. Data was collected at two different squared four--momentum transfers of $\langle Q^2 \rangle = 0.050$ and $0.036\,(\mathrm{GeV}/c)^2$. The $\mathrm{p}(e, e'K)$ reaction in this energy range leads to two possible final states. Clean missing mass spectra of Λ and Σ hyperons were obtained at kaon momenta in the in-plane angular range of 400–750 MeV/c. The experimental programme was continued by a second kaon electro-production data-taking campaign in 2009 for a statistically and systematically improved data-set.

A new electron arm coordinate detector system was built in order to use KAOS as a double-arm spectrometer under zero degree scattering angle. It consists of two vertical planes of almost 20 000 fibres adapted to the shape of the focal-surface of the electron arm and serving as coordinate and timing and trigger detector. During the years 2004–8 beam-tests with fibre prototype detectors of increasing complexity and size were performed. In 2009 the KAOS spectrometer was equipped with a new vacuum chamber and was mechanically adapted for the two-arm operation. The fibre detector in its final form with its associated read-out and trigger electronics was commissioned during dedicated beams in the summer of 2009.

These first open strangeness experiments have demonstrated that the KAOS spectrometer is, in connection with the high-quality continuous wave electron beam of the MAMI-C stage, a very effective tool for investigating kaon production off nucleons and nuclei with electron scattering.

4.2. ROOM FOR IMPROVEMENT

To fully exploit the high beam currents available at MAMI and to provide the highest accuracy in the measured observables the KAOS spectrometer's hadron side should be upgraded to match the resolution and rate-capability of the newly installed electron arm. Some options exist to reach this goal:

- The 60 scintillator paddles are aged and show a strong absorption of light which complicates the energy-loss determination from the ADC spectra. Furthermore, the use of a single dipole in the spectrometer leads to optical defocussing in the vertical direction, so that some particles miss the active area of the scintillator walls, because its height was adopted to a *QD* combination with vertical focusing properties. This fact leads to complications in the acceptance determination. Finally, scintillator wall F has sizable gaps between the paddles. As paddle combinations from both walls are required by the trigger, detection inefficiencies strongly depend on the particle's angle and momentum.

  New scintillator paddles with high light output, with a geometry matched to the spectrometer optics, should be installed in both walls. That would improve many aspects of the experiment including efficiency, systematic errors, and background suppression.

- The existing wire chambers have only 2 read-out planes per chamber, making 4 planes in total for 4 coordinates to be determined. That leaves no room for inefficiencies. The MWPC reach, even under perfect conditions, position resolutions of about 0.5–1 mm. This limits the final momentum, respectively mass resolution. The read-out electronics limits the DAQ rate to something like 1 kHz.

  New wire chambers should be constructed as drift chambers with a high efficiency and some redundancy, *i.e.* several sense wire planes for each coordinate. New read-out electronics could make use of the dead-time free TDC system which is already employed for the electron arm.

- The aerogel Cherenkov counter for pion suppression should be finalized and installed soon. A possible water Cherenkov system for proton suppression should be considered as well.

- In a more rigorous approach the hadron side could be equipped with a duplicate of the electron arm fibre detector system. A final set-up using only fibre (plus Cherenkov) counters would allow for the highest DAQ rates and the best performance.

4.3. PERSPECTIVE

With regard to future experimental work it is obvious that there exists interesting topics in elementary kaon electro-production in the region $0 < Q^2 < 0.5\,\mathrm{GeV}/c^2$. However, the taking of such data is a difficult proposition for a two-arm spectrometer experiment such as the one performed in 2008–9 because of the available beam energies and physical limitations of the spectrometers. The planned two-arm operation of the KAOS spectrometer using the pre-target beam chicane provides an experimental set-up that is unique in the world and which will allow unprecedented measurements at the low Q^2-kinematics under forward angles.

The electro-production of hypernuclei offers the unique possibility to vary the energy and momentum transfer independently and to gain information on hypernuclear wave-functions. The special kinematics for electro-production of hypernuclei requires the detection of both, the associated kaon and the scattered electron, at forward laboratory angles. While the scattered electrons have to be detected at very forward angles, the kaon detector has to cover a broader range of up to 15° in order to extract dynamical information from the K^+ angular distribution. The potential of electro-production at MAMI with a sub-MeV energy resolution with reasonable counting rates up to at least medium weight hypernuclei is strong. An important goal for measuring the excitation spectra and decay properties of hypernuclei is to test the energies and wave functions from microscopic structure models and to put constraints on baryon-baryon interaction models. With the aforementioned upgrades in mind, the hypernuclei programme is one of the most promising prospects for a future activity. A roadmap to hypernuclei electro-production at MAMI was defined in 2008 which is now being pursued.

The set-up of the KAOS spectrometer and the first kaon electro-production measurements are only one of the many perspectives from which strangeness physics should be viewed, with the ultimate goal of providing a more thorough understanding of the composition of nuclear matter and sub-nuclear reaction dynamics.

A
Chronology

2002

December: First inspection of the KaoS spectrometer at GSI. Planning of dismantling and transport. Formulation of a concept for the supply of coil current and cooling power in Mainz.

2003

January: Mutual agreement between Mainz and GSI establishing power-off for KaoS at GSI and access to Cave C for dismantling.

March: Delivery of the first 10 km of scintillating fibres for the electron arm.

April: Construction of the very first prototype fibre detector.

May to June: Dismantling of the spectrometer at GSI and transport of both magnets, both power supplies, and large parts of the associated detectors and electronics to Mainz. Arrival on 11 June.

September: Cut-away of access openings into a concrete bunker in the spectrometer hall for the installation the power transformers.

Autumn: First characterization of a prototype fibre detector in terms of light yield and time resolution using radio-isotope sources.

2004

January: Production and first tests of the double-threshold discriminator cards for the electron arm. First tests of CATCH modules for the electron arm.

March: Delivery of the hydraulic displacement system comprising a 12 m long skid-track and two push-pull cylinders.

May: First beam-test at MAMI using a prototype fibre detector that was sandwiched between the drift chambers and the scintillator paddles of the focal-plane detector system of SpekA.

July: Delivery of the hydraulic positioning cylinders that support the spectrometer in measurement position.

August: Set-up of the scintillator walls and beam-tests at MAMI for background measurements. Second beam-test at MAMI using a prototype fibre detector that was characterized in terms of time and position resolution.

October: Third beam-test at MAMI using a prototype fibre detector in a geometry adapted to the focal-plane of SpekA.

October to December: Delivery and first tests of the prototype front-end boards, of the Cockcroft-Walton bases, and of the MaPMT for the electron arm.

2005

January: Final design of the spectrometer platform including the two frame structures and the base plate.

March: Final design of the support beams with feet for the skid-track.

March to May: Statics calculation of the spectrometer set-up and its movement with last changes to the steel construction.

May: Surveying and preparation work at the spectrometer's parking position in the spectrometer hall.

August to September: First aluminisation of the fibre end-faces using an evaporation chamber. First design of the sliding plates for the spectrometer positioning.

Autumn Delivery of the power supplies for the two dipoles of the magnetic chicane and of construction material for the radiation shields.

October to November: Delivery of the support beams with feet for the skid-track by Frank & Hoffmann. Delivery of the steel construction of the spectrometer platform.

2006

January: Final design of the sliding plates and definition of the spectrometer's angular coverage.

March: Delivery of the sliding plates by Blanck. Installation of the support beams and the platform for the spectrometer in the parking position.

May: Installation of the first yoke parts on the spectrometer platform.

June: Beam-tests at GSI using prototype fibre detectors in a ^{12}C beam. Start of the design and construction work on the vacuum system: chamber adjustments; blind flanges; entrance and exit windows; Kapton foil tests.

June: Rebuilding of the pre-target beam-line to accommodate the first dipole of the magnetic chicane.

August: Formulation and simulation of a tracking trigger concept using both scintillator walls. First alignment and cross-talk tests of the fibre–MaPMT coupling using a UV-laser.

September to October: First construction of a prototype fibre detector the electron arm geometry.

December: Installation of the first pole-piece on the spectrometer platform. Planning of the power cable routing through the spectrometer hall.

2007

January to February: Installation of the magnet coils and the refurbished vacuum system. Delivery of a 9 m long power cable girder which can serve the spectrometer in target and parking position.

February: Installation of the last yoke parts finishing the dipole assembly.

March: Beam-tests at GSI using several fibre detectors and measurement of their response to π^+, proton, deuteron and ^3He. For the first time a VULOM1 logic module performed on-line a cluster analysis and defined hit positions. Installation of the rotating power cable girder in the spectrometer hall at 5 m height. Installation of the cooling water supply at the spectrometer's measurement position. Installation of the scintillator walls on the spectrometer platform.

April: Installation of the power lines from the voltage distribution system to the power transformers. First (failing) tests of the vacuum system. Installation of the sliding plates on the spectrometer hall floor. Installation of trigger and read-out electronics for the scintillator walls.

May: First installation of the skid-track on support beams and first movement of the spectrometer on its platform from parking to target position. Construction of the first radiation shields. Delivery of the first multi-link cards for the MWPC read-out. Delivery of the first VULOM1 logic modules for the trigger system.

June: First tests with aerogel radiators for the Cherenkov detector. Construction of a prototype fibre detector with 2 m length for the horizontal sub-detector in the electron arm.

July: Installation of a platform extension for the trigger and scintillator wall front-end electronics racks.

Summer: Connection of the magnet coils to the cooling water and power supply. Installation of a new thyristor phase pulsing transformer for the power supply. Change of coil cooling sequence for higher cooling efficiency. Installation of an air cooling system inside the bunker for the power transformers. Installation of laminated, pressure-proof window foils at the vacuum chamber. Installation of an inspection window in the rear flange of vacuum chamber. Installation of an access tube in the vacuum chamber for field probes. Installation of a dedicated vacuum pump station on the spectrometer platform.

September: Installation of the first MWPC on the spectrometer platform.

October: Installation of side and backward radiation shields on the spectrometer platform. First movement of the spectrometer on the hydraulic positioning cylinders from target to measurement position. Installation of a Hall probe inside the dipole. First beam-tests at MAMI with the spectrometer using 855 MeV electrons: test of a VULOM1 logic module as tracking trigger, test of a cluster analysis of scintillator data; test of radiation shields. Final version of the double-threshold discriminator cards produced.

November: Final design of the mechanical support for the chicane magnets.

2008

January: Installation of a fixed collimator in front of the vacuum entrance window. Significant simplification of the spectrometer movement. Extension of the radiation shields. Installation of gas pipes from detector lab to the MWPC on the spectrometer platform.

February: First beam-tests at MAMI with an operational MWPC triggered by the scintillator walls. Data acquisition rates were limited to 5 Hz because of missing blocking circuits in the DAQ. First identification of pions, protons, and deuterons by their specific energy-loss and flight time. Various problems with the transputer chains.

March: Beam-tests at MAMI with both MWPC and improved read-out electronics installed. Installation of the ITVME system for blocking the DAQ of the MWPC, increasing the maximum possible data acquisition rate for the MPWC to 350 Hz. In-beam test of nine fibre bundles with 1 152 fibres and 288 read-out channels inside the spectrometer. Laying of the exhaust pipes and tubes connecting the MWPC with the outlets on the roof of the spectrometer hall.

March to April: First design of the mechanical support and the vacuum chamber for the electron arm.

May: Delivery of the first series of aerogel tiles for the Cherenkov detector.

June: Final design of the fibre–MaPMT connectors for the electron arm.

Summer: Installation of a laser system parallel to the optical axis of the spectrometer for the alignment with the target. Introduction of new hardware in the MWPC trigger system.

August: Delivery of the mechanical support for the chicane magnets. Final design of the collimator system. Arrival of the first aerogel prototype detector from Ljubljana in Mainz.

September: Beam-tests at MAMI with a data acquisition rate up to 750 Hz. Installation of new front-end logic to improve the MWPC DAQ. Beam-time for taking calibration data for a momentum calibration of the spectrometer. First in-beam test of an aerogel prototype detector inside the spectrometer. Implementation of a trajectory trigger for the scintillator walls using VUPROM modules. Final design of the vacuum chamber for the electron arm. Delivery of the first collimators by Röhr Stolberg. Optical characterisation of first aerogel tiles through absorption and transmittance measurements. Installation of an access platform for operating the trigger and scintillator wall front-end electronics.

October: Production beam-time at MAMI with the identification of kaons and reconstruction of Λ hyperons. Installation of a motor-driven collimator system and the first collimators. In-beam test of nine fibre bundles inside the spectrometer. Delivery of the fibre–MaPMT connectors by WEVO.

November: Production beam-time at MAMI with the identification of kaons and reconstruction of Λ and Σ^0 hyperons. Optimization of the MWPC data acquisition. Production of the final version of the front-end boards for the electron arm.

December: Design of an acceptance-matched collimator.

2009

January to May: Mass production of fibre bundles. Installation of a platform extension for the detector electronics of the electron arm. Delivery of the vacuum chamber for the electron arm by Systec. Installation of the vacuum chamber, cable bridges, and electronics for the electron arm. Installation of a radiation shielding ceiling and shields close to the vacuum chamber.

February: Measurement of the excitation curve of the dipole magnet. Delivery of the flange–MaPMT connectors by Waterjet. Delivery of the acceptance–matched collimator by JL Goslar. Final design of the cable routing and mechanical support for the electron arm.

June: Production beam-time at MAMI for kaon electro-production in Λ/Σ^0 kinematics: integrated 305 h of run-time. First use of a sandwich counter for a precise determination of the trigger, detection and tracking efficiencies. In-beam tests of Cherenkov prototype detectors with different aerogel refractive indices and tests using mirrors in the light collection box. Installation of dead-time scalers for improved luminosity determination. Completion of the first plane of the fibre detector.

July: First beam-time at MAMI with a completed fibre plane and associated electronics installed in the electron arm: tests of cascading VUPROM modules with cluster-finding algorithms and on-line debug outputs; test of a hybrid trigger synchronization using the TCS trigger control system and the A1 synchronization information; test of multiple front-ends feeding data via optical links into a single read-out buffer PC.

August: Installation of the sieve slit collimator with fine pitch. Beam-time at MAMI for taking calibration data to measure the magnet optics and to improve the momentum reconstruction. First beam-tests at MAMI with two fibre planes in the electron arm.

October: Production beam-time at MAMI for a pilot experiment on coherent ϕ-meson production in the K^+/K^- decay channel.

B

Drawings and Schemes

Table B.1.: List of technical drawings that are related to the set-up of the KAOS spectrometer. The drawings are accessible through the common directory for public drawings of the *Institut für Kernphysik*.

no.	name	date
2036	Plattform Kaos	06.01.2005
2037	Trägerrahmen 1 Kaos	06.01.2005
2038	Trägerrahmen 2 Kaos	06.01.2005
2039	Stahlplattenaufbau Kaos	06.01.2005
2040	Verschubbahn Kaos	10.03.2005
2041	Träger 1, Verschubbahn Kaos	10.03.2005
2042	Träger 2, Verschubbahn Kaos	10.03.2005
2043	Fuß Verschubbahn Kaos	10.03.2005
2044	Gleitplatten Kaos	03.08.2005
2044a	Gleitplatten Kaos	11.10.2005
2044b	Gleitplatten Kaos	10.01.2006
2045	Gleitplatten Kaos Bemaßung	03.08.2005
2045a	Gleitplatten Kaos Bemaßung	11.10.2005
2045b	Gleitplatten Kaos Bemaßung	03.01.2006
2157	Bodenplatte Strahlführung Bereich DCI-2 Kaos	27.07.2007
2158	Gleitplatte DCI-2 Kaos	27.07.2007
2158a	Gleitplatte DCI-2 Kaos	25.10.2007
2159	Positionierplatte Kaos	07.11.2006
2160	Zusammenstellung Schikane Kaos	25.10.2006
2161	Stahlfuß Schikane Kaos	24.10.2006
2162	Gleitplatte Schikane Kaos	25.10.2006

continued on next page

Continued list of technical drawings related to the set-up of the spectrometer.

no.	name	date
2163	Zwischenplatte DCI-2 Kaos	27.07.2007
2164	Stützen DCI-2 Kaos	27.07.2007
2164a	Stützen DCI-2 Kaos	25.10.2007
2165	Grabenabstützung für Kaos in A1 Halle	14.11.2006
2182	Transportwagen für Verschubbahnfüße Kaos	05.07.2007
2185	Verschubfuß für DCI-2 Kaos	05.11.2007
2192	Übersicht Kollimator Kaos	13.12.2007
2193	Kollimatorrahmen Kaos	14.12.2007
2194	Führung Kollimatorrahmen Kaos	17.12.2007
2195	Konsole für Hubgetriebe Kollimator Kaos	18.12.2007
2196	Halterung Kollimatorrahmen Kaos	19.12.2007
2197	Bleifüllung oberer Kollimatorrahmen Kaos	09.01.2008
2202	Rahmen 1 für Detektor Kaos	14.05.2008
2203	Rahmen 2 für Detektor Kaos	16.05.2008
2203	Rahmen 2 für Detektor Kaos	30.03.2009
2204	Rechtes Seitenteil für Rahmen Detektor Kaos	26.05.2008
2205	Linkes Seitenteil für Rahmen Detektor Kaos	26.05.2008
2206	Aufhängung für Detektor Kaos	27.05.2008
2207	Faserverbindung Detektor Kaos	29.05.2008
2207a	Faserverbindung Detektor Kaos	02.09.2008
2209	Faserhalterung Kaos	20.06.2008
2209a	Faserhalterung Kaos	16.02.2009
2220	Lochkollimator mit Trägerplatte Kaos	15.08.2008
2220a	Lochkollimator mit Trägerplatte Kaos	27.08.2008
2221	Vakuumkammer Kaos Gesamtansicht	18.09.2008
2222	Vakuumkammer Kaos Kammerbleche	19.09.2008
2223	Vakuumkammer Kaos Versteifungen	22.09.2008
2224	Vakuumkammer Kaos Flansche	24.09.2008
2225	Vakuumkammer Kaos Halter u. Blindflansche	26.09.2008
2226	Vakuumkammer Kaos mit oberen Detektoren	29.09.2008
2229	Halterung Rotationslaser Kaos	11.12.2008
2230	Zusatzbleiplatten Kollimator Kaos	15.12.2008
2232	Schwenkbare Kabelführung Kaos	17.02.2009
2235	Zusatzwanne für Kabelführung Kaos	15.07.2009

continued on next page

Continued list of technical drawings related to the set-up of the spectrometer.

no.	name	date
2236	Zusatzbohrungen in Lochkollimator Kaos	04.08.2009
2237	Bemaßung Bohrbild Lochkollimator Kaos	07.08.2009
2238	Zusatzhalterung Rotationslaser Kaos	14.08.2009

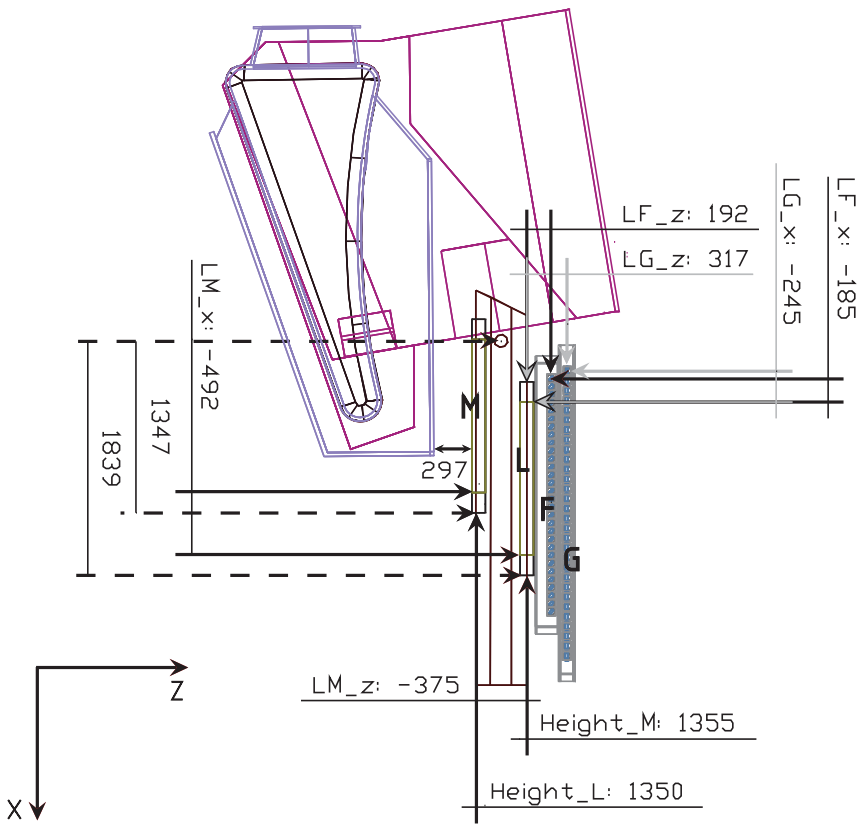

Figure B.1.: Definition of the reference frame for detector coordinates. The x-direction is along the MWPC x-plane, the y-direction is parallel to gravity direction, and the z-direction is normal to the MWPC planes. A reference detector for all relative distances is MWPC L. The wire chambers are assumed to be parallel and their absolute position is measured against a scale on the MWPC girder with the zero point close to the girder's rotation axis. Any possible misalignment of the scintillator walls against the wire chambers is corrected in the data analysis.

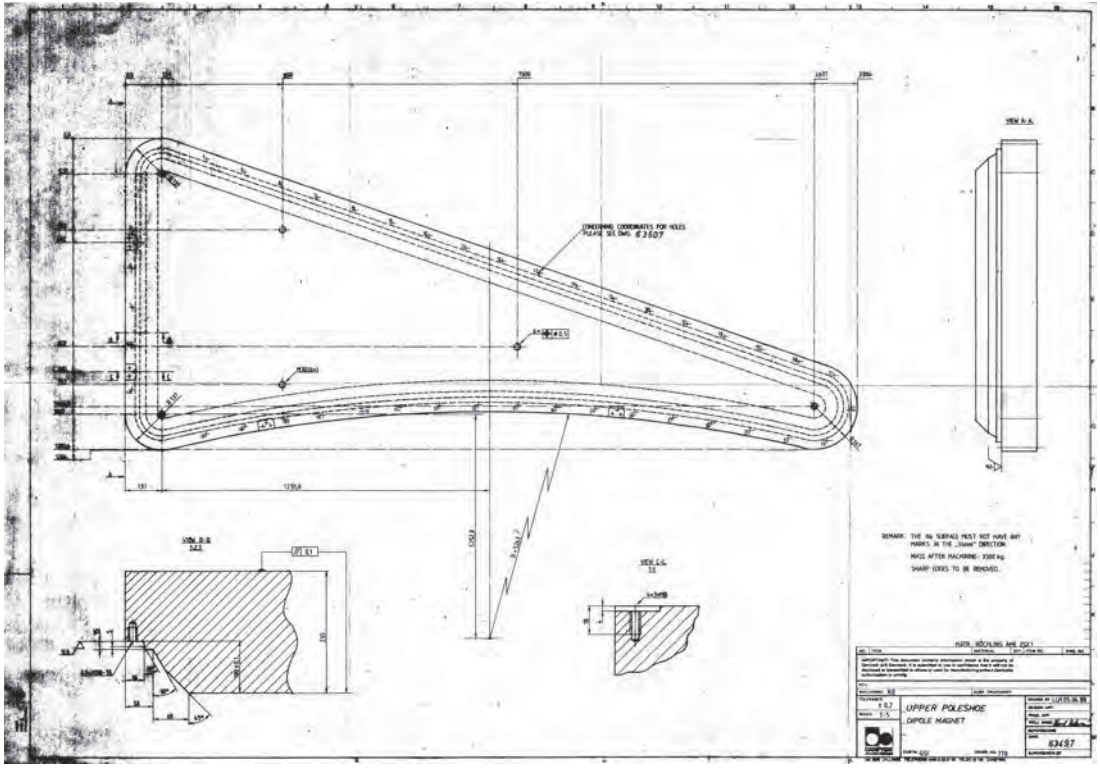

Figure B.2.: Technical drawing of the upper dipole pole-piece. The exit face of the hadron side is curved, the exit face of the electron side is straight. The entrance face is straight and its normal is pointing to the target, when the spectrometer is correctly positioned.

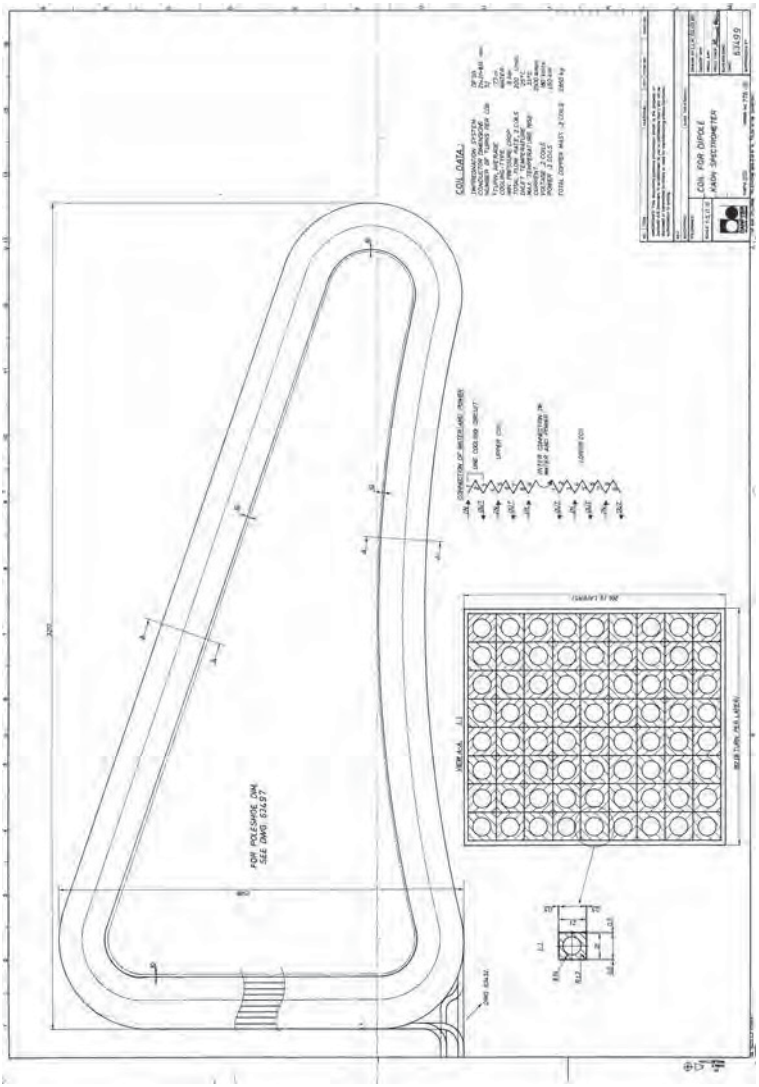

Figure B.3.: Technical drawing of the dipole coils. The current is flowing through 72 turns per coil with an average length of 7.7 m per turn. The maximum current is 2500 A, that is provided at ∼ 180 V, corresponding to ∼ 450 kW power. The ohmic losses are cooled by water at a flow rate of 200 ℓ/min.

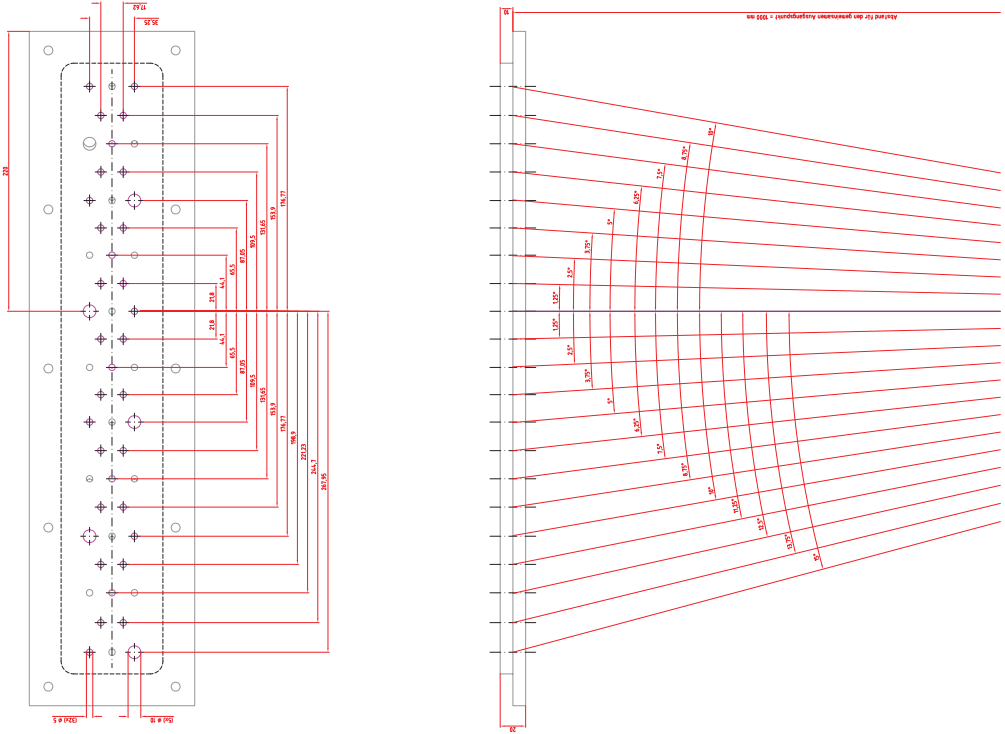

Figure B.4.: Technical drawing of the sieve-slit collimator used for the calibration measurements with the KAOS spectrometer. It contains 53 holes in 5 different horizontal lines along the dispersive plane. Not all of these lines are within the vertical acceptance of the spectrometer. Small holes are of 5 mm diameter, several larger ones of 10 mm diameter.

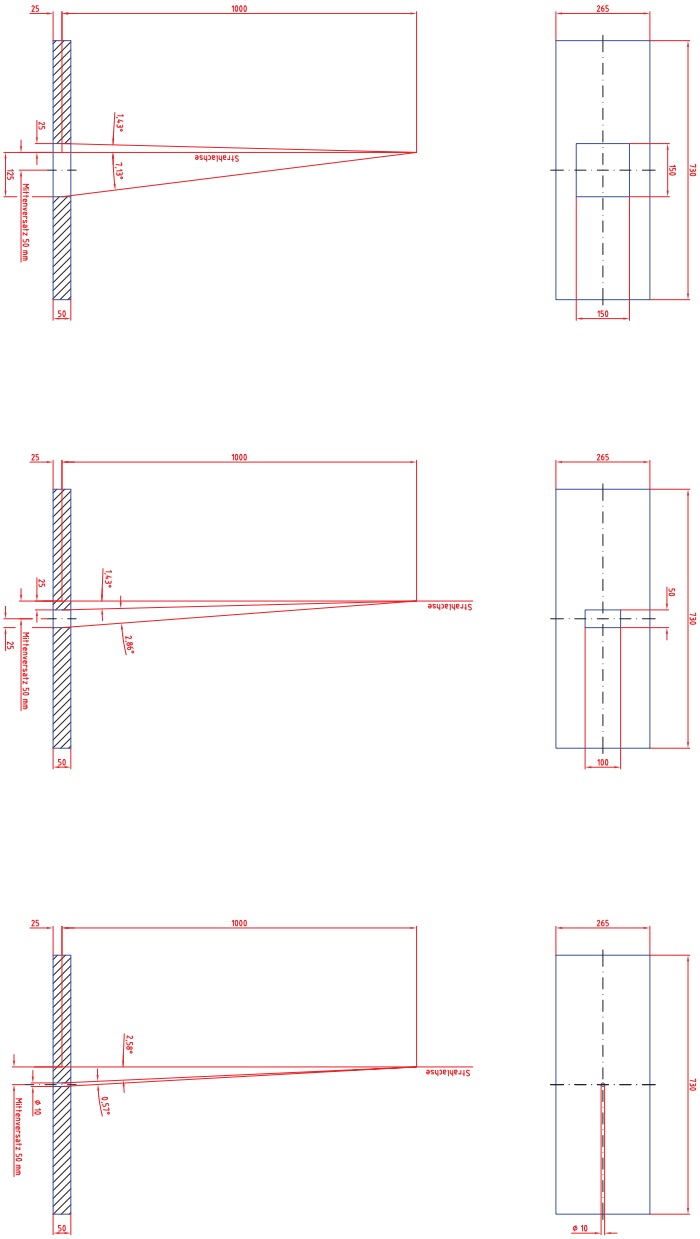

Figure B.5.: Technical drawing of the rectangular shaped upper collimator used for the kaon electro-production measurements with the KAOS spectrometer.

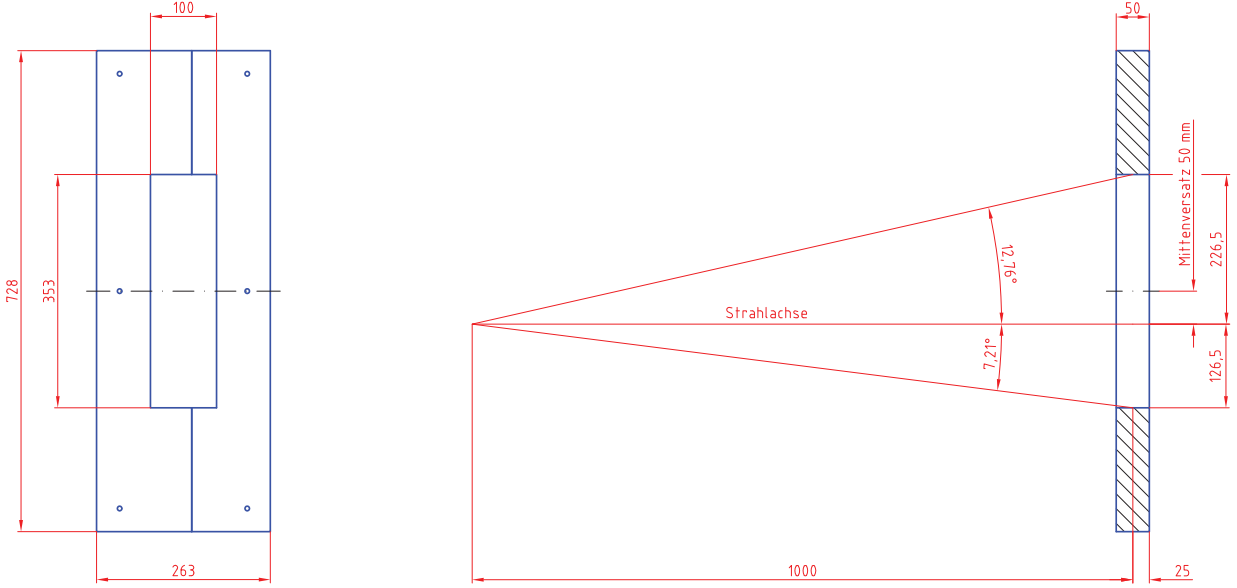

Figure B.6.: Technical drawing of the rectangular shaped lower collimator used for the kaon electro-production measurements with the KAOS spectrometer.

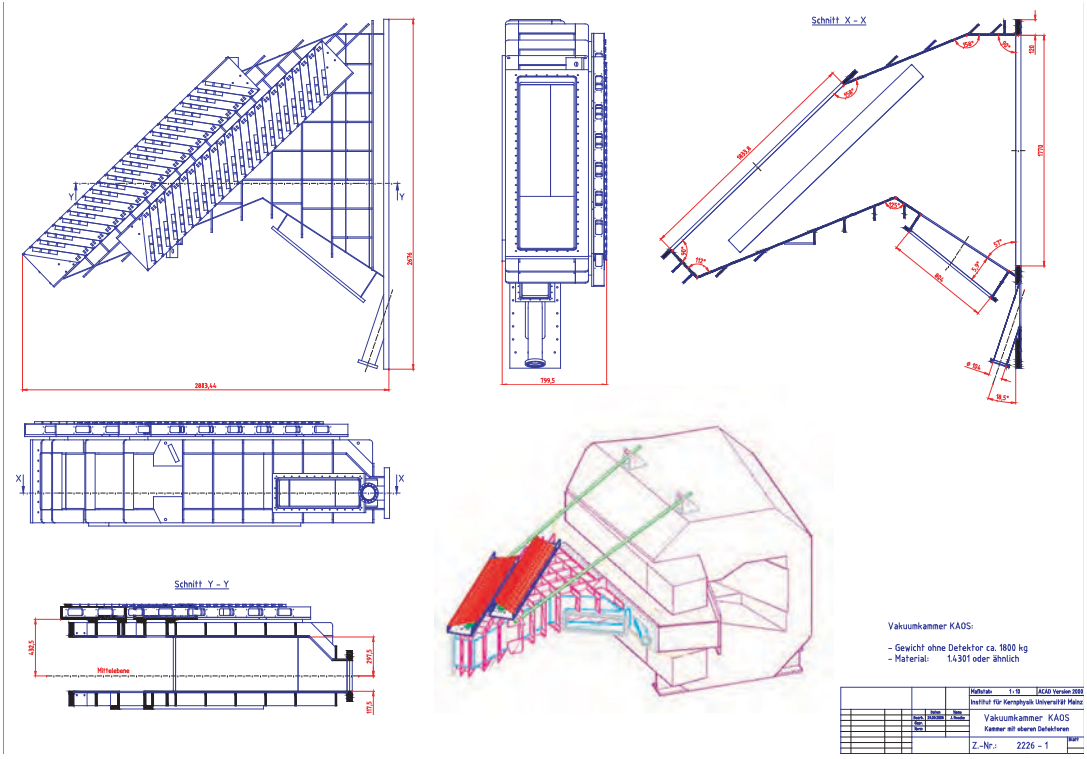

Figure B.7.: Technical drawing of the electron arm vacuum chamber used for the measurements with the fibre detector inside the KAOS spectrometer. The chamber has an inner volume of $V \sim 1\,\mathrm{m}^3$ and provides 7 large flanges that are needed to allow for the insertion of up to 4 fibre detector planes, and for a flexible beam exit.

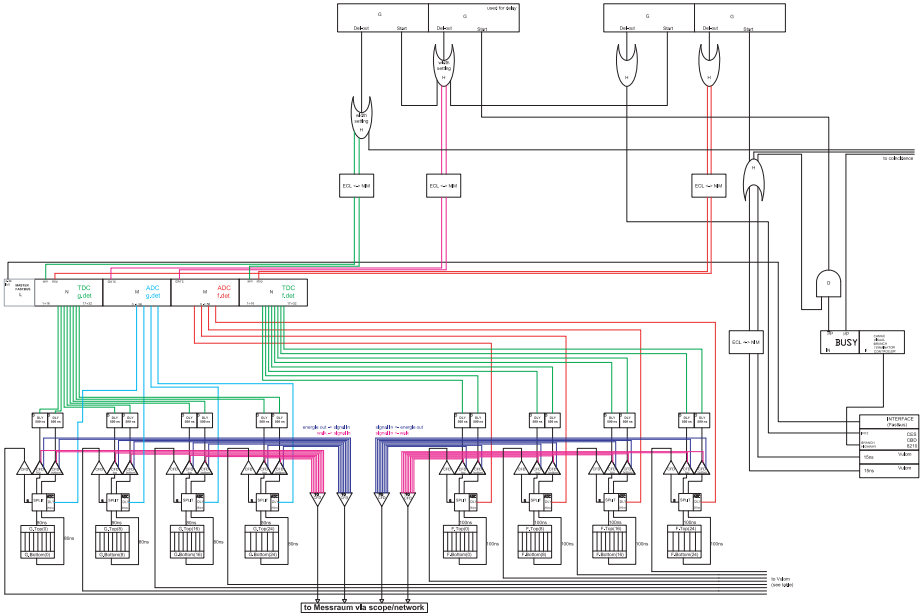

Figure B.8.: Read-out scheme for the TOF walls:
Each analogue signal is split by a sum and split card (GSI SU 1601). The energy branch consists of a linear delay of 250 ns (GSI DP 1628) and an ADC (LeCroy 1885F). The time branch is digitized by a constant fraction discriminator (GSI CF8105), delayed by 500 ns (GSI DL 1610) and fed into a TDC (LeCroy 1875). The analogue sum of the two PMT signals from each paddle is discriminated (GSI CF 8105) to perform a rough mean-timing and brought to the VULOM logic modules for trigger generation. The VULOM trigger is blocked when the data acquisition system is busy by a μbusy module. Timing modules are used to generate the ADC gate, as well as the TDC arm and common stop signals. For debugging purposes analogue as well as digital signals can be multiplexed and checked on-line in the counting room.

C

SPECIFICATIONS

Table C.1.: Heavy parts of the spectrometer that were installed between 2006 and 2007 on the spectrometer platform.

part	quantity	weight (tons)	dimensions (mm) × (mm) × (mm)
magnet yoke	1	21.3	2717 × 2400 × 540
magnet yoke	1	21.4	2777 × 2400 × 445
magnet yoke	1	12.7	1375 × 2400 × 680
magnet yoke	1	21.4	2777 × 2400 × 445
magnet yoke	1	21.3	2717 × 2400 × 540
magnet yoke	2	3.3	700 × 700 × 540
pole pieces	2	4.7	2800 × 1200 × 235
total		114	

Table C.2.: Specifications of the Hall probe with teslameter installed inside the KAOS spectrometer dipole.

DTM-151-PS	sensitive area	$1.6 \times 4.0\,\mathrm{mm}^2$
	maximum field	$3.0\,\mathrm{T}$
	resolution	$1 \times 10^{-6}\,\mathrm{T}$
	accuracy	$\pm 0.01\,\%$ at $25^\circ\,\mathrm{C}$
	calibration stability	$\pm 10\,\mathrm{ppm}/^\circ\,\mathrm{C}$
	zero stability	$\pm(1\mu\mathrm{T} + 0.0003\,\%)/^\circ\,\mathrm{C}$

Table C.3.: Specifications of the vacuum pumps installed in the KAOS spectrometer vacuum system.

DUO 35	volume flow rate	$10\,\ell/\mathrm{s}$
	maximum speed	$1800/\mathrm{min}$
TMU 521 P DN 160	volume flow rate	$560\,\ell/\mathrm{s}$
	maximum speed	$49\,980/\mathrm{min}$

Bibliography

[1] S. Janssen, *Strangeness production on the nucleon*, doctorate thesis, Ghent University, Belgium (2002).

[2] G. D. Rochester and C. C. Butler, *Evidence for the existence of new unstable elementary particles*, Nature 160 (1947) 855–857.

[3] F. Close, M. Marten, and C. Sutton, *The Particle Explosion*, Oxford University Press, New York, 1987.

[4] Particle Data Group (C. Amsler et al.), *Review of particle physics*, Phys. Lett. B 667 (2008) 1.

[5] M. Gell-Mann, *Symmetry and currents in particle physics*, in: *Nobel Lectures, Physics 1963–1970*, Elsevier, Amsterdam, 1972.

[6] T.-D. Lee, *Weak interactions and nonconservation of parity*, in: *Nobel Lectures, Physics 1942–1962*, Elsevier, Amsterdam, 1964.

[7] C. N. Yang, *The law of parity conservation and other symmetry laws of physics*, in: *Nobel Lectures, Physics 1942–1962*, Elsevier, Amsterdam, 1964.

[8] J. Cronin, *CP symmetry violation – the search for its origin*, in: S. Lundqvist (Ed.), *Nobel Lectures, Physics 1971–1980*, World Scientific, Singapore, 1992.

[9] V. Fitch, *The discovery of charge-conjugation parity asymmetry*, in: S. Lundqvist (Ed.), *Nobel Lectures, Physics 1971–1980*, World Scientific, Singapore, 1992.

[10] G. Zweig, *An SU(3) model for strong interaction symmetry and its breaking*, CERN Report 8181/Th 8419, CERN, Geneva, Switzerland (1964).

[11] G. Zweig, *An SU(3) model for strong interaction symmetry and its breaking: II*, CERN Report 8419/Th 8412, CERN, Geneva, Switzerland (1964).

[12] M. Gell-Mann, *A schematic model of baryons and mesons*, Phys. Lett. 8 (1964) 214–215.

[13] R. Hofstadter, *Nuclear and nucleon scattering of high-energy electrons*, Ann. Rev. Nucl. Sci. 7 (1957) 231.

[14] D. Drechsel and M. M. Giannini, *Electron scattering off nuclei*, Rep. Prog. Phys. 52 (1989) 1083–1163.

[15] G. Knöchlein, D. Drechsel, and L. Tiator, *Photoproduction and electroproduction of eta mesons*, Zeit. Phys. A 352 (1995) 327–343.

[16] E. Amaldi, S. Fubini, and G. Furlan, *Pion Electroproduction. Electroproduction at Low-Energy and Hadron Form-Factors*, Vol. 83 of *Springer Tracts in Mod. Phys.*, Springer, Berlin, 1979.

[17] M. Kawaguchi and M. J. Moravcsik, *Photoproduction of K mesons from single nucleons*, Phys. Rev. 107 (1957) 563–569.

[18] Z.-P. Li, *The kaon photoproduction of nucleons in the chiral quark model*, Phys. Rev. C 52 (1995) 1648–1661.

[19] R. A. Williams, C.-R. Ji, and S. R. Cotanch, *Hyperon electroproduction in a crossing and duality constrained model*, Phys. Rev. C 46 (1992) 1617–1635.

[20] S. R. Cotanch, R. A. Williams, and C.-R. Ji, *Kaon electromagnetic production and radiative capture near hyperon thresholds*, Phys. Scripta 48 (1993) 217–225.

[21] T. Mart and C. Bennhold, *Evidence for a missing nucleon resonance in kaon photoproduction*, Phys. Rev. C 61 (2000) 012201.

[22] R. A. Adelseck and B. Saghai, *Kaon photoproduction: Data consistency, coupling constants, and polarization observables*, Phys. Rev. C 42 (1990) 108–127.

[23] C. Bennhold, H. Haberzettl, and T. Mart, *A new resonance in $K^+\Lambda$ electroproduction: The $D_{13}(1895)$ and its electromagnetic form factors* (1999).

[24] T. Feuster and U. Mosel, *Photon and meson induced reactions on the nucleon*, Phys. Rev. C 59 (1999) 460–491.

[25] P. Bydžovský, M. Sotona, T. Motoba, K. Itonaga, K. Ogawa, and O. Hashimoto, *Photo- and electro-production of medium mass Λ-hypernuclei*, arXiv:0706.3836 [nucl-th] (2007).

[26] T. Mizutani, C. Fayard, G.-H. Lamot, and B. Saghai, *Off-shell effects in the electromagnetic production of strangeness*, Phys. Rev. C 58 (1998) 75.

[27] S. Janssen, J. Ryckebusch, and T. Van Cauteren, *Constraints on background contributions from $K^+\Lambda$ electroproduction*, Phys. Rev. C 67 (2003) 052201.

[28] M. Q. Tran *et al.* (SAPHIR Collaboration), *Measurement of $\gamma p \to K^+\Lambda$ and $\gamma p \to K^+\Sigma^0$ at photon energies up to 2 GeV*, Phys. Lett. B 445 (1998) 20–26.

[29] T. Mart, C. Bennhold, H. Haberzettl, and L. Tiator, *An effective Lagrangian model for kaon photo- and electroproduction on the nucleon*, online available at `www.kph.uni-mainz.de/MAID/kaon/kaonmaid.html` (2011).

[30] G. Niculescu *et al.* (E93-018 Collaboration), *Longitudinal and transverse cross sections in the $^1H(e,e'K^+)\Lambda$ reaction*, Phys. Rev. Lett. 81 (1998) 1805–1808.

[31] R. M. Mohring *et al.* (E93-018 Collaboration), *Separation of the longitudinal and transverse cross sections in the* $^1H(e,e'K^+)\Lambda$ *and* $^1H(e,e'K^+)\Sigma^0$ *reactions*, Phys. Rev. C 67 (2003) 055205.

[32] M. Guidal, J. M. Laget, and M. Vanderhaeghen, *Pion and kaon photoproduction at high-energies: Forward and intermediate angles*, Nucl. Phys. A 627 (1997) 645–678.

[33] M. Guidal, J. M. Laget, and M. Vanderhaeghen, *Electroproduction of strangeness above the resonance region*, Phys. Rev. C 61 (2000) 025204.

[34] T. Regge, *Introduction to complex angular momentum*, Nuovo Cim. 14 (1959) 951–976.

[35] T. Corthals, *Regge-plus-resonance approach to kaon production from the proton*, doctorate thesis, Ghent University, Belgium (2007).

[36] T. Corthals, J. Ryckebusch, and T. Van Cauteren, *Forward-angle* $K^+\Lambda$ *photoproduction in a Regge-plus-resonance approach*, Phys. Rev. C 73 (2006) 045207.

[37] T. Corthals, T. Van Cauteren, P. Van Craeyveld, J. Ryckebusch, and D. G. Ireland, *Electroproduction of kaons from the proton in a Regge-plus-resonance approach*, Phys. Lett. B 656 (2007) 186–192.

[38] J. F. Donoghue, E. Golowich, and B. R. Holstein, *Dynamics of the standard model*, no. 2 in Cambridge Monographs on Particle Physics, Nuclear Physics and Cosmology, Cambridge University Press, 1992.

[39] S. Steininger and U.-G. Meißner, *Threshold kaon photo- and electroproduction in SU(3) baryon chiral perturbation theory*, Phys. Lett. B 391 (1997) 446–450.

[40] V. Bernard, N. Kaiser, and U.-G. Meißner, *Neutral pion photoproduction off nucleons revisited*, Zeit. Phys. C 70 (1996) 483–498.

[41] V. Bernard, N. Kaiser, and U.-G. Meißner, *Chiral symmetry and the reaction* $\gamma p \to \pi^0 p$, Phys. Lett. B 378 (1996) 337–341.

[42] G. Ecker, J. Gasser, A. Pich, and E. De Rafael, *The role of resonances in chiral perturbation theory*, Nucl. Phys. B 321 (1989) 311–342.

[43] S. L. Adler and F. J. Gilman, *Partially conserved axial-vector current restrictions on pion photoproduction and electroproduction amplitudes*, Phys. Rev. 152 (1966) 1460–1467.

[44] T. Fuchs and S. Scherer, *Pion electroproduction, PCAC, chiral ward identities, and the axial form-factor revisited*, Phys. Rev. C 68 (2003) 055501.

[45] C. N. Brown *et al.*, *Coincidence measurements of single* K^+ *electroproduction*, Phys. Rev. Lett. 28 (1972) 1086–1089.

[46] C. J. Bebek *et al.*, *Electroproduction of K^+ mesons in the forward direction*, Phys. Rev. Lett. 32 (1974) 21–24.

[47] C. J. Bebek *et al.*, *Scalar-transverse separation of electroproduced $K^+\Lambda$ and $K^+\Sigma^0$ final states*, Phys. Rev. D 15 (1977) 3082–3084.

[48] T. Azemoon *et al.*, *Production of hyperons by virtual photons*, Nucl. Phys. B 95 (1975) 77–97.

[49] P. Brauel *et al.*, *Electroproduction of $\pi^+ n$, $\pi^- p$ and $K^+\Lambda$, $K^+\Sigma^0$ final states above the resonance region*, Zeit. Phys. C 3 (1979) 101.

[50] K. H. Glander *et al.* (SAPHIR Collaboration), *Measurement of $\gamma p \to K^+\Lambda$ and $\gamma p \to K^+\Sigma^0$ at photon energies up to 2.6 GeV*, Eur. Phys. J. A 19 (2004) 251–273.

[51] M. Iodice (E98-108 Collaboration), *Kaon electro-production on protons at JLab in Hall A*, Eur. Phys. J. A 17 (2003) 345–348.

[52] P. Bydžovský and T. Mart, *Analysis of the data consistency on kaon photoproduction with Λ in the final state*, Phys. Rev. C 76 (2007) 065202.

[53] R. Bradford *et al.* (CLAS Collaboration), *Differential cross sections for $\gamma + p \to K^+ + Y$ for Λ and Σ^0 hyperons*, Phys. Rev. C 73 (2006) 035202.

[54] T. Mart, *Role of $P_{13}(1720)$ in $K\Sigma$ photoproduction*, Phys. Rev. C 62 (2000) 038201.

[55] C. Bennhold, H. Haberzettl, and T. Mart, *A new resonance in $K^+\Lambda$ electroproduction: The $D_{13}(1895)$ and its electromagnetic form factors*, in: *2nd ICTP International Conference on Perspectives in Hadronic Physics, 10–14 May 1999*, Trieste, Italy, 1999, pp. 328–337, arXiv:nucl-th/9909022.

[56] P. Bydžovský and M. Sotona, *Kaon electromagnetic production: constraints set by new data*, Nucl. Phys. A 754 (2005) 243c–247c.

[57] D. S. Carman *et al.* (CLAS Collaboration), *First measurement of transferred polarization in the exclusive $\vec{e}p \to e'K^+\vec{\Lambda}$ reaction*, Phys. Rev. Lett. 90 (2003) 131804.

[58] P. Ambrozewicz *et al.* (CLAS Collaboration), *Separated structure functions for the exclusive electroproduction of $K^+\Lambda$ and $K^+\Sigma^0$ final states*, Phys. Rev. C 75 (2007) 045203.

[59] M. E. McCracken *et al.* (CLAS Collaboration), *Differential cross section and recoil polarization measurements for the $\gamma p \to K^+\Lambda$ reaction using CLAS at Jefferson Lab*, Phys. Rev. C 81 (2010) 025201.

[60] T. Mart, *Progress and issues in the electromagnetic production of kaon on the nucleon* (2009).

[61] T. Motoba, P. Bydžovský, M. Sotona, K. Itonaga, K. Ogawa, and O. Hashimoto, *Prospects of photoproduction of medium-heavy hypernuclei*, in: K. Maeda, H. Tamura, S. N. Nakamura, and O. Hashimoto (Eds.), *Proceedings of the International Symposium on Electrophotoproduction of Strangeness on Nucleons and Nuclei, Sendai, Japan, 16–18 June 2003*, World Scientific, Singapore, 2004, pp. 221–232.

[62] K. Tanida *et al.*, *Measurement of the $B(E2)$ of ${}^{7}_{\Lambda}Li$ and shrinkage of the hypernuclear size*, Phys. Rev. Lett. 86 (2001) 1982–1985.

[63] C. M. Keil, F. Hofman, and H. Lenske, *Density dependent hadron field theory for hypernuclei*, Phys. Rev. C 61 (2000) 064309.

[64] M. Danysz and J. Pniewski, *Delayed disintegration of a heavy nuclear fragment*, Philos. Mag. 44 (1953) 348–352.

[65] O. Hashimoto and H. Tamura, *Spectroscopy of Λ hypernuclei*, Prog. Part. Nucl. Phys. 57 (2006) 564–653.

[66] C. Samanta, P. Roy Chowdhury, and D. N. Basu, *Lambda hyperonic effect on the normal drip lines*, J. Phys. G 35 (2008) 065101.

[67] T. R. Saito *et al.* (HypHI Collaboration), *The HypHI project at GSI and FAIR*, in: J. Pochodzalla and Th. Walcher (Eds.), *Proceedings of the IX International Conference on Hypernuclear and Strange Particle Physics, Johannes Gutenberg-Universität, Mainz, 10–14 October 2006*, Springer, Berlin/Heidelberg, 2007, pp. 171–176.

[68] M. Agnello *et al.* (FINUDA Collaboration), *First results on ${}^{12}_{\Lambda}C$ production at DAΦNE*, Phys. Lett. B 622 (2005) 35–44.

[69] C. Milner *et al.*, *Observation of Λ-hypernuclei in the reaction ${}^{12}C(\pi^+, K^+){}^{12}_{\Lambda}C$*, Phys. Rev. Lett. 54 (1985) 1237–1240.

[70] P. H. Pile *et al.*, *Study of hypernuclei by associated production*, Phys. Rev. Lett. 66 (1991) 2585–2588.

[71] M. Akei *et al.*, *The (π^+, K^+) reaction on ${}^{12}C$ and ${}^{56}Fe$*, Nucl. Phys. A 534 (1991) 478–492.

[72] T. Hasegawa *et al.*, *Core-excited states of ${}^{12}_{\Lambda}C$ hypernuclei formed in the (π^+, K^+) reaction*, Phys. Rev. Lett. 74 (1995) 224–227.

[73] T. Hasegawa *et al.*, *Spectroscopic study of ${}^{10}_{\Lambda}B$, ${}^{12}_{\Lambda}C$, ${}^{28}_{\Lambda}Si$, ${}^{89}_{\Lambda}Y$, ${}^{139}_{\Lambda}La$, and ${}^{208}_{\Lambda}Pb$ by the (π^+, K^+) reaction*, Phys. Rev. C 53 (1996) 1210–1220.

[74] S. Ajimura *et al.*, *The (π^+, K^+) reaction and light Λ hypernuclear spectroscopy*, Nucl. Phys. A 639 (1998) 93c–102c.

[75] H. Hotchi *et al.*, *Spectroscopy of medium-heavy Λ hypernuclei via the (π^+, K^+) reaction*, Phys. Rev. C 64 (2001) 044302.

[76] H. Tamura *et al.*, *Observation of a spin-flip M1 transition in* ${}^{7}_{\Lambda}Li$, Phys. Rev. Lett. 84 (2000) 5963–5966.

[77] H. Tamura *et al.*, *γ-ray spectroscopy in Λ hypernuclei*, Nucl. Phys. A 754 (2005) 58c–69c.

[78] A. K. Kerman and M. S. Weiss, *Superstrange nuclei*, Phys. Rev. C 8 (1973) 408–410.

[79] H. Djapo, B.-J. Schäfer, and J. Wambach, *On the appearance of hyperons in neutron stars*, arXiv:0811.2939v1 [nucl-th] (2008).

[80] T. R. Saito *et al.* (HypHI Collaboration), *Proposal of the HypHI Phase 0 experiment*, accepted by EA 33, GSI (2006).

[81] T. R. Saito *et al.*, *Hypernuclear spectroscopy with heavy ion beams: the HypHI project at GSI and FAIR*, in: O. Hashimoto, H. Tamura, S. N. Nakamura, and K. Maeda (Eds.), *Proceedings of the International Symposium on Strangeness in Nuclear and Hadronic Systems (Sendai08), Tohoku University, Sendai, Japan, 15–18 December 2008*, World Scientific, Singapore, 2009, pp. 364–370.

[82] E. Hiyama, M. Kamimura, T. Motoba, T. Yamada, and Y. Yamamoto, *Few-body aspects of light hypernuclei*, Nucl. Phys. A 737 (2004) 138–146.

[83] L. Yuan *et al.* (HNSS/E93-018 Collaboration), *Hypernuclear spectroscopy using the $(e, e'K^+)$ reaction*, Phys. Rev. C 73 (2006) 044607.

[84] L. Tang *et al.*, *The HKS experiment on Λ-hypernuclear spectroscopy via electroproduction at JLab*, Nucl. Phys. A 790 (2007) 679c–682c.

[85] E. Hiyama, M. Kamimura, T. Motoba, T. Yamada, and Y. Yamamoto, *ΛN spin-orbit splittings in* ${}^{9}_{\Lambda}Be$ *and* ${}^{13}_{\Lambda}C$ *studied with one-boson-exchange ΛN interactions*, Phys. Rev. Lett. 85 (2000) 270–273.

[86] T. Motoba, H. Bandō, and K. Ikeda, *Light p-shell Λ-hypernuclei by the microscopic three-cluster model*, Prog. Theor. Phys. 70 (1983) 189–221.

[87] T. Motoba, H. Bandō, K. Ikeda, and T. Yamada, *Production, structure and decay of light p-shell Λ-hypernuclei*, Prog. Theor. Phys. 81 (1985) 42–103.

[88] E. Hiyama, M. Kamimura, T. Motoba, , T. Yamada, and Y. Yamamoto, *Four-body cluster structure of $A = 7$–10 double-Λ hypernuclei*, Phys. Rev. C 66 (2002) 024007.

[89] I. Filikhin, V. M. Suslov, and B. Vlahovic, *Low-lying resonances of* ${}^{9}_{\Lambda}Be$*: Fadeev calculations with Pade-approximants*, Nucl. Phys. A 790 (2007) 695c–698c.

[90] Y. Fujiwara, K. Miyagawa, M. Kohno, Y. Suzuki, D. Baye, and J.-M. Sparenberg, *Faddeev calculation of 3α and $\alpha\alpha\Lambda$ using $\alpha\alpha$ resonating-group method kernel*, Phys. Rev. C 70 (2004) 024002.

[91] H. Bandō, *Consequences of the cluster model of light hypernuclei*, Nucl. Phys. A 450 (1986) 217c–236c.

[92] H. Bandō, T. Motoba, and J. Žofka, *Production, structure and decay of hypernuclei*, Int. J. Mod. Phys. A 5 (1990) 4021–4198.

[93] T. Miyoshi *et al.* (HNSS Collaboration), *High resolution spectroscopy of the* ${}^{12}_{\Lambda}B$ *hypernucleus produced by the* $(e,e'K^+)$ *reaction*, Phys. Rev. Lett. 90 (2000) 232502.

[94] J. Pochodzalla, *Future hypernuclear physics at MAMI-C and Panda-GSI*, Nucl. Phys. A 754 (2005) 430c–442c.

[95] S. Shinmura, *Electroproductions of light* Λ *and* Σ *hypernuclei*, Prog. Theor. Phys. 92 (1994) 571–582.

[96] T. Motoba, M. Sotona, and K. Itonaga, *Photoproduction of polarized hypernuclei*, Prog. Theor. Phys. Suppl. 117 (1994) 123–133.

[97] L. Tang *et al.* (JLab E89-009 Collaboration), *First experiment to produce* Λ *hypernuclei using electron beam at JLab*, Mod. Phys. Lett. A 18 (2003) 112–115.

[98] S. N. Nakamura *et al.* (JLab E01-011 Collaboration), *Future hypernuclear program at JLab Hall C*, Nucl. Phys. A 754 (2005) 421–429.

[99] F. Dohrmann *et al.* (E91-016 Collaboration), *Angular distributions for* ${}^{3,4}_{\Lambda}H$ *bound states in the* ${}^{3,4}He(e,e'K^+)$ *reaction*, Phys. Rev. Lett. 93 (2004) 242501.

[100] J. J. LeRose *et al.* (Hall A Collaboration), *Hypernuclear spectroscopy via* $(e,e'K^+)$ *in JLab's Hall A*, Nucl. Phys. A 804 (2008) 116–124.

[101] F. Cusanno *et al.* (Hall A Collaboration), *High resolution spectroscopy of* ${}^{16}_{\Lambda}N$ *by electroproduction*, Phys. Rev. Lett. 103 (2009) 202501.

[102] O. Hashimoto, *Recent results of the JLab Hall C hypernuclear experiment E01-011*, in: J. Pochodzalla and Th. Walcher (Eds.), *Proceedings of the IX International Conference on Hypernuclear and Strange Particle Physics, Johannes Gutenberg-Universität, Mainz, 10–14 October 2006*, Springer, Berlin/Heidelberg, 2007, pp. 41–46.

[103] O. Hashimoto *et al.* (Hall C Collaboration), *Spectroscopic study of* Λ *hypernuclei up to medium-heavy mass region through* $(e,e'K^+)$ *reaction*, Exp. Proposal E01-011, Jefferson Lab (2001).

[104] O. Hashimoto *et al.* (Hall C Collaboration), *Spectroscopic investigation of* Λ *hypernuclei in the wide mass region using the* $(e,e'K^+)$ *reaction*, Exp. Proposal E05-115, Jefferson Lab (2005).

[105] S. N. Nakamura, *Future hypernuclear experiments at JLab*, in: J. Pochodzalla and Th. Walcher (Eds.), *Proceedings of the IX International Conference on Hypernuclear and Strange Particle Physics, Johannes Gutenberg-Universität, Mainz, 10–14 October 2006*, Springer, Berlin/Heidelberg, 2007, pp. 51–56.

[106] O. von Baeyer and O. Hahn, *Magnetische Linienspektren von β-Strahlen*, Phys. Zeit. 11 (1910) 488–493, cited in [107].

[107] K. Siegbahn, *β-ray-spectrometer theory and design. High resolution spectroscopy*, in: K. Siegbahn (Ed.), *Beta- and Gamma-Ray Spectroscopy*, North-Holland Publishing Co., Amsterdam, 1955, pp. 52–99.

[108] J. Danysz, *Sur les rayons β de la famille du radium*, Le Radium 9 (1912) 1–5, cited in [107].

[109] J. D. Cockcroft, *A magnet for α-ray spectroscopy*, J. Sci. Instrum. 10 (1933) 71–75.

[110] H. A. Enge, *Magnetic spectrographs for nuclear reaction studies*, Nucl. Instr. Meth. 162 (1979) 161–180.

[111] K. I. Blomqvist, *High resolution magnetic spectrometers*, Nucl. Phys. A 497 (1989) 457c–464c.

[112] K. L. Brown, *A first and second order matrix theory for the design of beam transport systems and charged particle spectrometers*, Adv. Part. Phys. 1 (1968) 71–134.

[113] K. L. Brown, R. Belbeoch, and P. Bounin, *First- and second-order magnetic optics equations for the midplane of uniform-field wedge magnets*, Rev. Sci. Instrum. 35 (1964) 481–485.

[114] H. Blok, E. A. J. M. Offermann, C. W. De Jager, and H. De Vries, *Path reconstruction and resolution improvement in magnetic spectrometers*, Nucl. Instr. Meth. Phys. Res. A 262 (1987) 291–297.

[115] K. I. Blomqvist *et al.* (A1 Collaboration), *The three-spectrometer facility at the Mainz microtron MAMI*, Nucl. Instr. Meth. Phys. Res. A 403 (1998) 263–301.

[116] P. Senger *et al.* (KaoS Collaboration), *The kaon spectrometer at SIS*, Nucl. Instr. Meth. Phys. Res. A 327 (1993) 393–411.

[117] L. Nungesser, *Aufbau und Simulation des Kaos-Spektrometers an MAMI für Koinzidenzmessungen in der assoziierten Kaonproduktion*, doctorate thesis, Johannes Gutenberg-Universität, Mainz (April 2009).

[118] K.-H. Kaiser, *Dipole der Injektion und Extraktion des HDSM*, Internal Report MAMI 12/2004, Inst. für Kernphysik, Mainz (2004).

[119] H. Stelzer, *Multiwire chambers with a two-stage gas amplification*, Nucl. Instr. Meth. Phys. Res. A 310 (1991) 103–106.

[120] A. Breskin, G. Charpak, S. Majewski, G. Melchart, G. Petersen, and F. Sauli, *The multistep avalanche chamber: a new family of fast, high-rate particle detectors*, Nucl. Instr. Meth. 161 (1979) 19–34.

[121] G. Charpak and F. Sauli, *High-accuracy, two-dimensional read-out in multiwire proportional chambers*, Nucl. Instr. Meth. 113 (1973) 381–385.

[122] N. Awaji *et al.*, *Resolution study of cathode-charge sampling on a multiwire proportional chamber for accurate particle tracking*, Nucl. Instr. Meth. 198 (1982) 243–251.

[123] M. Gómez Rodríguez de la Paz, *Strahltest und Betrieb von Vieldrahtproportionalkammern für das Kaos-Spektrometer*, diploma thesis, Johannes Gutenberg-Universität, Mainz (May 2008).

[124] M. Bösz, *Datenerfassung und Spurerkennung mit den Vieldrahtproportionalkammern für das Kaos-Spektrometer an MAMI*, diploma thesis, Johannes Gutenberg-Universität, Mainz (March 2009).

[125] J. Wellendorf Pedersen, P. Achenbach, S. Sánchez Majos, and J. Pochodzalla, *Operation of Multiwire Proportional Chambers for the kaon spectrometer at MAMI*, Technical Progress Report, Johannes Gutenberg-Universität, Mainz (2007).

[126] P. Baltes, C. Müntz, H. Oeschler, S. Sartorius, A. Wagner, and H. Stelzer, *Properties of large MWPC's at the Kaon Spectrometer*, in: *GSI Scientific Report 1991*, GSI, Darmstadt, 1992, p. 364.

[127] P. Achenbach *et al.* (A1 Collaboration), *Measurement of propagation time dispersion in a scintillator*, Nucl. Instr. Meth. Phys. Res. A 578 (2007) 253–260.

[128] H. Bethe, *Zur Theorie des Durchgangs schneller Korpuskularstrahlen durch Materie*, Ann. Physik 397 (1930) 325–400.

[129] P. A. Čerenkov, *The visible glow of pure liquids under the action of γ-rays*, Dokl. Acad. Nauk SSSR 2 (1934) 451–456.

[130] I. E. Tamm and I. M. Frank, *Coherent radiation from a fast electron in a medium*, Dokl. Acad. Nauk SSSR 14 (1937) 107–113.

[131] J. V. Jelley, *Čerenkov radiation and its applications*, Pergamon Press, London/New York, 1958.

[132] D. W. Higinbotham, *Diffusely reflective aerogel cherenkov detector simulation techniques*, Nucl. Instr. Meth. Phys. Res. A 414 (1998) 332–339.

[133] F.-X. Gentit, *Litrani: a general purpose Monte-Carlo program simulating light propagation in isotropic or anisotropic media*, Nucl. Instr. Meth. Phys. Res. A 486 (2002) 35–39.

[134] S. Minami *et al.* (HypHI Collaboration), *The trigger system for hypernuclear spectroscopy with heavy ion beams (HypHI)*, in: *Scientific Report 2007*, GSI, Darmstadt, 2008, p. 223.

[135] S. Sánchez Majos, P. Achenbach, R. Böhm, L. Nungesser, S. Minami, J. Pochodzalla, and T. R. Saito, *Application of the VME Logic Module VULOM as a trajectory trigger for the Kaos spectrometer*, in: *Scientific Report 2007*, GSI, Darmstadt, 2008, p. 170.

[136] P. Achenbach *et al.*, *New detectors for the kaon and hypernuclear experiments with Kaos at MAMI and with Panda at GSI*, in: V. Luth (Ed.), *Proceedings of the IX International Symposium on Detectors for Particle, Astroparticle and Synchrotron Radiation Experiments (SNIC06), SLAC, 3–6 April 2006*, eConf C0604032, 2006, p. 0144.

[137] P. Achenbach *et al.* (A1 and HypHI Collaboration), *In-beam tests of scintillating fibre detectors at MAMI and at GSI*, Nucl. Instr. Meth. Phys. Res. A 593 (2008) 353–360.

[138] P. Achenbach, *Probing hypernuclei at Panda and at MAMI-C*, in: J. Pochodzalla and Th. Walcher (Eds.), *Proceedings of the IX International Conference on Hypernuclear and Strange Particle Physics, Johannes Gutenberg-Universität, Mainz, 10–14 October 2006*, Springer, Berlin/Heidelberg, 2007, pp. 79–84.

[139] S. Sánchez Majos, P. Achenbach, and J. Pochodzalla, *A tracking fiber detector based on silicon photomultipliers for the Kaos spectrometer*, in: P. Sellin (Ed.), *Conference Record of the IEEE Nuclear Science Symposium (NSS08), Dresden, 20–24 October 2008*, IEEE, 2009, pp. 2220–2223.

[140] P. Achenbach, A. Sanchez Lorente, S. Sánchez Majos, and J. Pochodzalla, *Future use of silicon photomultipliers for Kaos at MAMI and Panda at FAIR*, Nucl. Instr. Meth. Phys. Res. A 610 (2009) 358–361.

[141] P. Achenbach *et al.* (A1 Collaboration), *Front-end electronics for the Kaos spectrometer at MAMI*, IEEE Trans. Nucl. Sci. 56 (2009) 316–319.

[142] P. Achenbach, *A large-scale FPGA-based trigger and dead-time free DAQ system for the Kaos spectrometer at MAMI*, in: D. Merelli (Ed.), *Conference Record of the 17th IEEE-NPSS Real-Time Conference on Computer Applications in Nuclear and Plasma Science (RT10), Lisbon, Portugal, 24–28 May 2010*, IEEE, 2010.

[143] J. Bähr *et al.*, *Test of fiber detector readout by position-sensitive photomultipliers*, Nucl. Instr. Meth. Phys. Res. A 348 (1994) 713–718.

[144] F. Bosi *et al.*, *Tests of a scintillating-fibre tracking detector based on position-sensitive photomultiplier readout*, Nucl. Instr. Meth. Phys. Res. A 374 (1996) 48–56.

[145] S. Horikawa *et al.*, *Development of a scintillating-fibre detector with position-sensitive photomultipliers for high-rate experiments*, Nucl. Instr. Meth. Phys. Res. A 516 (2004) 34–49.

[146] K. Kuroda, D. Sillou, and F. Takeutchi, *New type of position sensitive photomultiplier*, Rev. Sci. Instr. 52 (1981) 337–346.

[147] FAROS Collaboration, *Fast readout of scintillating fiber arrays using position-sensitive photomultipliers*, Nucl. Instr. Meth. Phys. Res. A 357 (1995) 78–86.

[148] FAROS Collaboration, *Scintillating fiber hodoscopes using position-sensitive photomultipliers*, Nucl. Instr. Meth. Phys. Res. A 372 (1996) 63–69.

[149] V. Agoritsas, N. Akchurin, O. Bing, A. Bravar, R. Drevenak, M. Finger, M. Finger, V. Flaminio, B. DiGirolamo, A. Gorin *et al.*, *Read-out of scintillating fibres using a weak cross-talk position-sensitive photomultiplier*, Nucl. Instr. Meth. Phys. Res. A 406 (1998) 393–402.

[150] C. Ayerbe Gayoso, *Development of a fibre detector for the Kaos spectrometer*, diploma thesis, Johannes Gutenberg-Universität, Mainz (April 2004).

[151] A. Esser, *Teilchennachweis und Spurerkennung mit dem Faserdetektor im Kaos-Spektrometer am Mainzer Mikrotron*, diploma thesis, Johannes Gutenberg-Universität, Mainz (January 2010).

[152] S. Horikawa *et al.*, *Time resolution of a scintillating fiber detector*, Nucl. Instr. Meth. Phys. Res. A 431 (1999) 177–184.

[153] A. Gorin *et al.*, *High resolution scintillating-fibre hodoscope and its readout using peak-sensing algorithm*, Nucl. Instr. Meth. Phys. Res. A 566 (2006) 500–515.

[154] *HV cells for PhotoMultiplier Tubes (PMT)*, HVSys, Dubna, Russia, online available at `www.hvsys.dubna.ru/pmt_cells.html` (2005).

[155] A. R. Frolov, T. V. Oslopova, and Yu. N. Pestov, *Double threshold discriminator for timing measurements*, Nucl. Instr. Meth. Phys. Res. 356 (1995) 447–451.

[156] *Double Threshold Discriminator (DTD) Chip*, GSI Experiment Electronics, Darmstadt, online available at `www.gsi.de/informationen/tt/Double-Threshold-1.html` (2005).

[157] P. Abbon *et al.* (COMPASS Collaboration), *The COMPASS experiment at CERN*, Nucl. Instr. Meth. Phys. Res. A 577 (2007) 455–518.

[158] H. Fischer *et al.*, *Implementation of the dead-time free F1 TDC in the COMPASS detector readout*, Nucl. Instr. Meth. Phys. Res. A 461 (2001) 508–510.

[159] G. Braun *et al.*, *F1—an eight channel time-to-digital converter chip for high rate experiments*, presented at the *Fifth Workshop on Electronics for LHC Experiments (LEB99), Snowmass, US, 20–24 September 1999*.

[160] J. Hoffmann, N. Kurz, S. Minami, W. Ott, and S. Voltz, *Programmable trigger processing module, VUPROM*, in: *Scientific Report 2007*, GSI, Darmstadt, 2008, p. 256.

[161] *VUPROM2*, GSI Experiment Electronics, Darmstadt, online available at `www.gsi.de/informationen/wti/ee/elekt_entwicklung/vuprom2_e.html` (2009).

[162] S. Minami *et al.* (HypHI Collaboration), *Development of the trigger system for the HypHI project*, in: *Scientific Report 2008*, GSI, Darmstadt, 2009, p. 52.

[163] H. Euteneuer *et al.*, *Beam measurements and operating experience at MAMI*, in: *Proceedings of the 4 th European Particle Accelerator Conference (EPAC 94), London, England, 27 June – 1 July 1994*, 1994, pp. 506–508.

[164] K.-H. Kaiser *et al.*, *The 1.5 GeV harmonic double-sided microtron at Mainz University*, Nucl. Instr. Meth. Phys. Res. A 593 (2008) 159–170.

[165] T. Pospischil, *Aufbau und Inbetriebnahme eines Protonen-Polarimeters an MAMI und Messung der Proton-Polarisation in der Reaktion $p(\vec{e},e'\vec{p})\pi^0$ in paralleler Kinematik im Bereich der $\Delta(1232)$-Resonanz*, doctorate thesis, Johannes Gutenberg-Universität, Mainz (2000).

[166] Participants in measurements with the Kaos spectrometer in 2008:
P. Achenbach[a], C. Ayerbe Gayoso[a], J. C. Bernauer[a], R. Böhm[a], D. Bosnar[b], M. Bösz[a], L. Debenjak[c], M. O. Distler[a], A. Esser[a], M. Gómez Rodríguez[a], K. Grießinger[a], M. Makek[b], H. Merkel[a], U. Müller[a], L. Nungesser[a], J. Pochodzalla[a], M. Potokar[c], S. Sánchez Majos[a], B. S. Schlimme[a], S. Širca[c,d], Th. Walcher[a], M. Weinriefer[a], and C. J. Yoon[a]
—[a]Institut für Kernphysik, Johannes Gutenberg-Universität, Mainz; —[b]Department of Physics, University of Zagreb, Croatia; —[c]Jožef Stefan Institute, Ljubljana, Slovenia; —[d]University of Ljubljana, Slovenia.

[167] P. Achenbach, *Strangeness physics with Kaos at MAMI*, in: R. A. Ricci, W. Kühn, and A. Tarantola (Eds.), *Proceedings of the XLVII International Winter Meeting on Nuclear Physics, Bormio, Italy, 26–30 January 2009*, Vol. 99 of *Conference Proceedings*, Italian Physical Society, Bologna, 2010, pp. 1–6.

[168] Participants in measurements with the Kaos spectrometer in 2009:
P. Achenbach[a], C. Ayerbe Gayoso[a], J. C. Bernauer[a], S. Bianchin[b], R. Böhm[a], D. Bosnar[c], V. Bozkurt[b], L. Debenjak[d], M. O. Distler[a], A. Esser[a], H. Fonvieille[f], I. Friščić[c], B. Göküzüm[b], K. Grießinger[a], E. Kim[b], M. Makek[c], H. Merkel[a], S. Minami[b], U. Müller[a], D. Nakajima[b], L. Nungesser[a], B. Özel-Tashenov[b], J. Pochodzalla[a], M. Potokar[d], Ch. Rappold[b], T. R. Saito[b], S. Sánchez Majos[a],

B. S. Schlimme[a], S. Širca[d,e], and M. Weinriefer[a]
−[a]Institut für Kernphysik, Johannes Gutenberg-Universität, Mainz; −[b]GSI, Helmholtz Center for Heavy Ion Research, Darmstadt; −[c]Department of Physics, University of Zagreb, Croatia; −[d]Jožef Stefan Institute, Ljubljana, Slovenia; −[e]University of Ljubljana, Slovenia; −[f]LPC INbP3-CNRS, Université Blaise Pascal, Clermont-Ferrand, France.

[169] P. Achenbach, *Status of strangeness electro-production at MAMI*, in: K. Maeda, S. N. Nakamura, H. Tamura, and O. Hashimoto (Eds.), *Proceedings of the International Symposium on Strangeness in Nuclear and Hadronic Systems (Sendai08), Tohoku University, Sendai, Japan, 15–18 December 2008*, World Scientific, Singapore, 2009, pp. 332–339.

[170] P. Achenbach *et al.* (A1 Collaboration), *First measurements of* Λ *and* Σ^0 *hyperons in elementary electroproduction at MAMI*, in: B. F. Gibson, K. Imai, T. Motoba, T. Nagae, and A. Ohnishi (Eds.), *Proceedings of the X International Conference on Hypernuclear and Strange Particle Physics (HypX), Tokai, Japan, 14–18 September 2009*, Nucl. Phys. A 835 (2010) 313–316.

List of Tables

List of Figures

List of my Scientific Works related to the Kaos Spectrometer

I. Articles in Peer-Reviewed Journals

[I] S. Sánchez Majos, P. Achenbach, and J. Pochodzalla, *Efficiency studies for a tracking detector based on square, 1.5 m long scintillating fibers read out by SiPM*, Nucl. Instr. and Meth. in Phys. Res. A 610 (2009) 502–508.

[II] P. Achenbach, A. Sanchez Lorente, S. Sánchez Majos, and J. Pochodzalla, *Future use of silicon photomultipliers for Kaos at MAMI and Panda at FAIR*, Nucl. Instr. and Meth. in Phys. Res. A 610 (2009) 358–361.

[III] S. Sánchez Majos *et al.* (A1 Collaboration), *Noise and radiation damage in silicon photomultipliers exposed to electromagnetic and hadronic irradiation*, Nucl. Instr. and Meth. in Phys. Res. A 602 (2009) 506–510.

[IV] P. Achenbach *et al.* (A1 Collaboration), *Front-end electronics for the Kaos spectrometer at MAMI*, IEEE Trans. Nucl. Sci. 56 (2009) 316–319.

[V] S. Sánchez Majos, P. Achenbach, and J. Pochodzalla, *Characterisation of radiation damage in silicon photomultipliers with a Monte Carlo model*, Nucl. Instr. and Meth. in Phys. Res. A 594 (2008) 351–357.

[VI] P. Achenbach *et al.* (A1 and HypHI Collaboration), *In-beam tests of scintillating fibre detectors at MAMI and at GSI*, Nucl. Instr. and Meth. in Phys. Res. A 593 (2008) 353–360.

[VII] P. Achenbach, L. Nungesser, and J. Pochodzalla, *Design criteria for scintillating fibre arrays with inclined columns*, Nucl. Instr. and Meth. in Phys. Res. A 591 (2008) 406–410.

[VIII] P. Achenbach *et al.* (A1 Collaboration), *Measurement of propagation time dispersion in a scintillator*, Nucl. Instr. and Meth. in Phys. Res. A 578 (2007) 253–260.

II. Contributions to Conferences, Workshops and Symposia

[I] P. Achenbach, *Strangeness physics at MAMI: First results and perspectives*, presented at the 3^{rd} *International Conference on Nuclear and Particle Physics with CEBAF at Jefferson Lab*, Dubrovnik, Croatia, 3–8 October 2010.

[II] P. Achenbach, *Overview of measurements on strange and nuclear systems at MAMI*, presented at the *Joint Workshop of the Japan Society for the Promotion of Science (JSPS) Core-to-Core Program Strangeness Nuclear Physics by Electron Beams and*

the European FP7 SPHERE Network, Villa Lanna, Prague, Czech Republic, 4–6 September 2010.

[III] P. Achenbach, *A large-scale FPGA-based trigger and dead-time free DAQ system for the Kaos spectrometer at MAMI*, in: D. Merelli (Ed.), *Conference Record of the 17th IEEE-NPSS Real-Time Conference on Computer Applications in Nuclear and Plasma Science (RT10), Lisbon, Portugal, 24–28 May 2010*, IEEE, 2010.

[IV] P. Achenbach, *New measurements on the nucleon structure with MAMI*, invited talk at the *74th Annual Meeting of the German Physical Society with the Spring Meeting of the Hadronic and Nuclear Physics Division, Bonn, 15–19 March 2010*, Verhandlungen DPG (VI) 45, 2010, p. 71.

[V] P. Achenbach, *Current issues in kaon photoelectro-production off the nucleon*, in: L. Fabbietti, W. Kühn, C. Sfienti, and A. Tarantola (Eds.), *Proceedings of the XLVIII International Winter Meeting on Nuclear Physics, Bormio, Italy, 25–29 January 2010*, PoS (BORMIO2010), 2010, art. no. 048.

[VI] P. Achenbach, *First measurements of Λ and Σ^0 hyperons in elementary electroproduction at MAMI*, in: B. F. Gibson, K. Imai, T. Motoba, T. Nagae, and A. Ohnishi (Eds.), *Proceedings of the X International Conference on Hypernuclear and Strange Particle Physics (HypX), Tokai, Japan, 14–18 September 2009*, published as: Nucl. Phys. A 835 (2010) 313–316.

[VII] P. Achenbach *et al.* (A1 Collaboration), *Associated Λ/Σ^0 production with the Kaos spectrometer at MAMI*, in: E. Epelbaum, H.-W. Hammer, and U.-G. Meißner (Eds.), *Proceedings of the 19th International IUPAP Conference on Few-Body Problems in Physics (FB19), Rheinische Friedrich-Wilhelms-Universität, Bonn, 31 August – 5 September 2009*, EPJ Web of Conferences 3, 2010, art. no. 07010.

[VIII] P. Achenbach, *Experimental aspects of hypernuclear physics with electron beams*, lecture at the *26th Students' Workshop on Electromagnetic Interactions, Bosen (Saar), 30 August – 4 September 2009*.

[IX] P. Achenbach, *A roadmap to hypernuclear physics at MAMI and Panda*, presented at the *International Conference on MAMI and Beyond, Schloss Waldthausen, Mainz, 30 March – 2 April 2009*.

[X] P. Achenbach, *Installation and commissioning of the Kaos spectrometer at MAMI*, presented at the *European Nuclear Physics Conference (EuNPC) and Spring Meeting of the German Physical Society, Hadronic and Nuclear Physics Division, Bochum, 16–20 March 2009*, Verhandlungen DPG (VI) 44, 2009, p. 69.

[XI] S. Sánchez Majos, P. Achenbach, and J. Pochodzalla, *Study on SiPM radiation hardness and low light level detection*, presented at the *European Nuclear Physics Conference (EuNPC) and Spring Meeting of the German Physical Society, Hadronic and Nuclear Physics Division, Bochum, 16–20 March 2009*, Verhandlungen DPG (VI) 44, 2009, p. 104.

[XII] L. Debenjak, S. Širca, and P. Achenbach, *Study of transmission and light yield of an $n = 1.07$ silica aerogel*, presented at the *European Nuclear Physics Conference (EuNPC) and Spring Meeting of the German Physical Society, Hadronic and Nuclear Physics Division, Bochum, 16–20 March 2009*, Verhandlungen DPG (VI) 44, 2009, pp. 83–84.

[XIII] P. Achenbach, *Status of strangeness electro-production at MAMI*, in: K. Maeda, S. N. Nakamura, H. Tamura, and O. Hashimoto(Eds.), *Proceedings of the International Symposium on Strangeness in Nuclear and Hadronic Systems (Sendai08), Tohoku University, Sendai, Japan, 15–18 December 2008*, World Scientific, Singapore, 2009, pp. 332–339.

[XIV] S. Sánchez Majos, P. Achenbach, and J. Pochodzalla, *A tracking fiber detector based on silicon photomultipliers for the Kaos spectrometer*, in: P. Sellin(Ed.), *Conference Record of the IEEE Nuclear Science Symposium 2008 (NSS08), Dresden, 20–24 October 2008*, IEEE, 2009, pp. 2220–2223.

[XV] P. Achenbach, *Strangeness physics with Kaos at MAMI*, in: R. A. Ricci, W. Kühn, and A. Tarantola (Eds.), *Proceedings of the XLVII International Winter Meeting on Nuclear Physics, Bormio, Italy, 26–30 January 2009*, Vol. 99 of *Conference Proceedings*, Italian Physical Society, Bologna, 2010, pp. 1–6.

[XVI] S. Sánchez Majos, P. Achenbach, and J. Pochodzalla, *Characterization of noise and radiation damage induced in silicon photomultipliers by 14 MeV electron irradiation*, presented at the *IEEE Nuclear and Space Radiation Effects Conference (NSREC), Tucson, Arizona, US, 14–18 July 2008*.

[XVII] P. Achenbach, S. Sánchez Majos, and J. Pochodzalla, *Future use of silicon photomultipliers for Kaos at MAMI and Panda at FAIR*, presented at the 5^{th} *Conference on New Developments In Photodetection (NDIP08), Aix-les-Bains, France, 15–20 June 2008*.

[XVIII] P. Achenbach, *Forming the hypernuclear landscape with MAMI and Panda*, presented at the *International Symposium on Heavy Ion Physics 2008 (ISHIP08), GSI, Darmstadt, 17–20 November 2008*.

[XIX] P. Achenbach, *Physics of hypernuclei as seen by an experimenter*, in: B. Golli, M. Rosina, and S. Širca (Eds.), *Proceedings of the Mini-Workshop on Few-Quark States and the Continuum, Bled, Slovenia, 15–22 September 2008*, Bled Workshops in Physics 9, 2008, pp. 1–8.

[XX] P. Achenbach, *The physics program at MAMI-C*, in: H. Machner and S. Krewald (Eds.), *Proceedings of the 11^{th} International Conference on Meson-Nucleon Physics and the Structure of the Nucleon (MENU07), Forschungszentrum Jülich, 10–14 September 2007*, eConf C070910, 2008, art. no. 111.

[XXI] P. Achenbach, *Operation of the Kaos spectrometer*, presented at the *Donnersberg Workshop 2008 on Future Prospects of Electron Scattering Experiments with MAMI, Bastenhaus, 31 March – 3 April 2008*.

[XXII] M. Gómez Rodríguez de la Paz and P. Achenbach, Betrieb von zweistufigen Drahtkammern an Kaos, presented at the *Spring Meeting of the German Physical Society, Hadronic and Nuclear Physics Division, Darmstadt, 10–14 March 2008*, Verhandlungen DPG (VI) 43, 2008, p. 114.

[XXIII] S. Sánchez Majos, P. Achenbach, and J. Pochodzalla, *Solid state photomultipliers for tracking detectors at Kaos*, presented at the *Spring Meeting of the German Physical Society, Hadronic and Nuclear Physics Division, Darmstadt, 10–14 March 2008*, Verhandlungen DPG (VI) 43, 2008, p. 69.

[XXIV] P. Achenbach, *Hypernuclear physics with Kaos at MAMI-C*, presented at the *Spring Meeting of the German Physical Society, Hadronic and Nuclear Physics Division, Gießen, 12–16 March 2007*, Verhandlungen DPG (VI) 42, 2007, p. 61.

[XXV] P. Achenbach, *Probing hypernuclei at Panda and at MAMI-C*, in: J. Pochodzalla and Th. Walcher (Eds.), *Proceedings of the IX International Conference on Hypernuclear and Strange Particle Physics, Johannes Gutenberg-Universität, Mainz, 10–14 October 2006*, Springer, Berlin/Heidelberg, 2007, pp. 79–84.

[XXVI] P. Achenbach *et al.*, *New detectors for the kaon and hypernuclear experiments with Kaos at MAMI and with Panda at GSI*, in: V. Luth (Ed.), *Proceedings of the IX International Symposium on Detectors for Particle, Astroparticle and Synchrotron Radiation Experiments (SNIC06), SLAC, 3–6 April 2006*, eConf C0604032, 2006, art. no. 0144.

[XXVII] S. Sánchez Majos, P. Achenbach, and J. Pochodzalla, *Study of time dispersion in scintillators for highly resolved Time-Of-Flight measurements*, presented at the *70th Annual Meeting of the German Physical Society with the Spring Meeting of the Hadronic and Nuclear Physics Division, Munich, 20–24 March 2006*, Verhandlungen DPG (VI) 41, 2006, pp. 55–56.

[XXVIII] C. Ayerbe Gayoso, P. Achenbach, and M. Gómez Rodríguez de la Paz, *Development of front-end electronics for the kaon spectrometer at MAMI*, presented at the *70th Annual Meeting of the German Physical Society with the Spring Meeting of the Hadronic and Nuclear Physics Division, Munich, 20–24 March 2006*, Verhandlungen DPG (VI) 41, 2006, p. 65.

[XXIX] P. Achenbach, *Strangeness electroproduction with Kaos*, presented at the *Donnersberg Workshop 2005 on Future Prospects of Electron Scattering Experiments with MAMI, Bastenhaus, 12–15 September 2005*.

[XXX] P. Achenbach, *The present and future of hypernuclei in electroproduction*, presented at the *International Workshop on Hypernuclei with Heavy Ion Beams (HypHI05), GSI, Darmstadt, 20–21 June 2005*.

[XXXI] C. Ayerbe Gayoso and P. Achenbach, *Results from a beam test of a scintillating fibre hodoscope with multianode photomultiplier read-out*, presented at the *Spring Meeting of the German Physical Society, Hadronic and Nuclear Physics Division, 4–9 March 2005*, Verhandlungen DPG (VI) 40, 2005, p. 58.

[XXXII] P. Achenbach, *The Kaos programme at MAMI-C*, lecture at the 21^{th} *Students' Workshop on Electromagnetic Interactions, Bosen (Saar), 5–10 September 2004*.

[XXXIII] P. Achenbach, *The future of Kaos at the Mainz Microtron MAMI-C*, presented at the *Symposium on Strangeness@SIS: 10 Years of KaoS at GSI, Darmstadt, 8 July 2004*.

[XXXIV] C. Ayerbe Gayoso and P. Achenbach, *Development of a scintillating fibre hodoscope with multi-anode photomultiplier read-out for use in a kaon spectrometer*, presented at the *Spring Meeting of the Hadronic and Nuclear Physics Division, Köln, 8–12 March 2004*, Verhandlungen DPG (VI) 39, 2004, p. 64.

[XXXV] P. Achenbach, *Kaon electroproduction with Kaos at MAMI-C*, in: M. Buballa, J. Knoll, W. Nörenberg *et al.* (Eds.), *Proceedings of the XXXII International Workshop on Gross Properties of Nuclei and Nuclear Excitations: Probing Nuclei and Nucleons with Electrons and Photons (Hirschegg04), Hirschegg, Kleinwalsertal, Austria, 11–17 January 2004*, GSI, 2004, pp. 137–142.

III. Published Scientific Reports

[I] A. Esser, S. Sánchez Majos, P. Achenbach, S. Minami, J. Pochodzalla, and T. R. Saito, *Development of a large-scale VUPROM system as tracking trigger for the Kaos spectrometer*, in: *Scientific Report 2009*, GSI, Darmstadt, 2010, p. 319.

[II] L. Debenjak, P. Achenbach, J. Pochodzalla, T. R. Saito, and S. Širca, *Prototype aerogel Čerenkov counter for kaon/pion separation*, in: *Scientific Report 2009*, GSI, Darmstadt, 2010, p. 320.

[III] L. Debenjak, P. Achenbach, J. Pochodzalla, T. R. Saito, and S. Širca, *Absorption and scattering lengths of high density aerogels with* $n = 1.07$, in: *Scientific Report 2008*, GSI, Darmstadt, 2009, p. 253.

[IV] S. Sánchez Majos, P. Achenbach, R. Böhm, L. Nungesser, S. Minami, J. Pochodzalla, and T. R. Saito, *Application of the VME Logic Module VULOM as a trajectory trigger for the Kaos spectrometer*, in: *Scientific Report 2007*, GSI, Darmstadt, 2008, p. 170.

[V] P. Achenbach *et al.*, *Particle identification with a fibre detector in a* $p/\pi^+/d$ *cocktail beam of 3.3 Tm magnetic rigidity at GSI*, in: *Scientific Report 2007*, GSI, Darmstadt, 2008, p. 169.

[VI] P. Achenbach *et al.*, *Performance of a fibre detector at a* ^{12}C *beam of 2 AGeV energy*, in: *Scientific Report 2006*, GSI, Darmstadt, 2007, p. 224.

[VII] P. Achenbach, J. Pochodzalla, and S. Sánchez Majos, *Measurement of photon angles for highly resolved TOF detectors*, in: *Scientific Report 2005*, GSI, Darmstadt, 2006, p. 76.

IV. Academic Seminars and Colloquia at External Institutions

[I] *Detecting strange hadrons and strange nuclei*, Invited talk at the Institute of Radiation Physics, Research Centre Dresden-Rossendorf, Aug. 2010.

[II] *Exploring hadronic degrees-of-freedom by elementary strangeness production*, Seminar of the Research Centre Elementary Forces and Mathematical Foundations (EMG), Johannes Gutenberg-Universität, Mainz, Apr. 2009.

[III] *Strangeness Physics with Kaos at MAMI*, Seminar at the Experimental Nuclear and Hadronic Physics Laboratory, University of Kyoto, Japan, Dec. 2008.

[IV] *Perspectives of hypernuclear physics*, Invited talk at the Ångström Laboratory, University of Uppsala, Sweden, Aug. 2008.

[V] *SiPM /fibre developments and the Kaos detector packages*, Seminar at the Helmholtz-Institut für Strahlen- und Kernphysik, Rheinische Friedrich-Wilhelms-Universität, Bonn, June 2008.

[VI] *Creating strange particles and nuclei with electrons and anti-protons,* Physics Colloquium at the University of Ljubljana, Slovenia, Feb. 2007.

[VII] *Ein neuer Messplatz für die Kaon- und Hyperkernforschung an MAMI*, Seminar at the Institute of Nuclear and Hadronic Physics, Research Centre Rossendorf Dresden, Jan. 2006.

[VIII] *Das Kaos-Spektrometer an MAMI-C*, Seminar of the Research Training School Gauge Theories — Experimental Tests and Theoretical Foundations, Johannes Gutenberg-Universität, Mainz, May 2003.